

AN EXPERIMENTAL RIG AND
INVESTIGATION OF STEAM
GENERATOR TUBE LOADING
DURING MAIN STEAM LINE
BREAK

*AN EXPERIMENTAL RIG AND INVESTIGATION
OF STEAM GENERATOR TUBE LOADING
DURING MAIN STEAM LINE BREAK*

By

OUAJIH HAMOUDA, B.Eng.

A Thesis

Submitted to the School of Graduate Studies

in Partial Fulfilment of the Requirements

for the Degree

Master of Applied Science

McMaster University

© Copyright by Ouajih Hamouda, February 2011

MASTER OF APPLIED SCIENCE (2011)

McMaster University

Mechanical Engineering

Hamilton, Ontario

TITLE: An Experimental Rig and Investigation of Steam Generator
Tube Loading during Main Steam Line Break

AUTHOR: Ouajih Hamouda, B.Eng. (McMaster University)

SUPERVISOR: Dr. David S. Weaver

NUMBER OF PAGES: xiv, 209, A-2, B-18, C-8, D-3, E-5, F-5, G-6

Abstract

Tubes in steam generators vibrate when subjected to cross-flow of secondary side coolant, particularly in the U-bend region. Such tube vibrations result in fretting wear at tube supports, reducing the margin of safety against failure. In the event of a main steam-line-break, the superheated water in the steam generator undergoes rapid depressurisation, resulting in a high-velocity two-phase steam-water flow across the steam generator tubes. This rapid blow-down phenomenon induces potentially catastrophic transient loading that is difficult to predict. Since the tubes represent the boundary between irradiated primary side fluids (deuterium) and the secondary side coolant, tubes in CANDU steam generators that cannot withstand the transient loading will leak irradiated primary side fluid into the secondary side, which passes outside of the containment building. The objective of this experimental study is to develop a better understanding of the transient loading and its prediction, such that structural tube failures can be avoided.

Acknowledgements

This project was supported by funding from the Canadian Nuclear Safety Commission under Contract No. 87055-09-0463, and special thanks are due to Dr. Jovica Riznic for his enthusiastic involvement and determination in ensuring project progress.

I am grateful to Dr. James Cotton and Dr. David Novog for their assistance with practical thermodynamics, heat transfer and two-phase flow design obstacles, making possible the successful completion of the commissioning phase of the project, to Dr. Hans Graf for his valuable contributions in frequency analysis and discussions of data acquisition and instrumentation difficulties, and to Dr. John Luxat for graciously lending his high-speed camera that offered invaluable flow visualisation capability.

I would like to thank Joe Verhaeghe who has made available his support in a number of ways, not least in the selection and troubleshooting of instrumentation and data acquisition methods, and installation of electronic components in the experimental set-up, as well as Ron Lodewyks, Mark Mackenzie, Jim McLaren, Dave Schick, and Jean-Paul Talon, for their helpful technical and manufacturing support, design suggestions and advice, and eagerness to be of assistance at every opportunity.

In addition, I owe special thanks to Andy Metelka of Sound & Vibration Solutions Canada for his earnest cooperation in providing instrumentation solutions.

I am indebted to my many of my colleagues, including Osama Ahmed, Ahmed Khalifa, Kevin Ng, Dr. Hossam Sadek, and Parsa Tamadonfar, who deserve particular mention for engaging me in stimulating discussions that clarified my thinking, and kindly donating their time, support, general advice, and unreserved help with my experimental set-up and procedures. Their friendship and collaboration is greatly valued and respected.

It is with immense pleasure and honour that I express my thankfulness to my parents Mongi and Emna, and sister Haifa, for their endless emotional, moral, and financial support and encouragement. They were my primary source of motivation in pursuing academic success, and it is to them that this thesis is dedicated.

I owe my deepest gratitude to my research advisor Dr. David Weaver, who fulfilled the role of being primarily responsible for my academic upbringing over the course of my Master's degree with exceptional commitment, providing optimal advice and guidance, and serving as an inspirational role model throughout my work on this project.

Table of Contents

Abstract.....	iii
Acknowledgements	iv
List of Figures.....	viii
List of Tables	xi
List of Acronyms.....	xii
Nomenclature	xiii
Chapter 1 – Introduction	1
1.1 Vibration of Tubes in a Steam Generator U-Bend.....	2
1.2 Loss-of-Coolant Accidents in Nuclear Power Generators.....	3
1.2.1 Transient Rapid Depressurisation Behaviour	5
1.2.2 Accident Consequences	7
1.3 Research Objective.....	8
Chapter 2 – Literature Review	10
2.1 Critical Flow	11
2.1.1 Single-Phase Critical Flow.....	13
2.1.2 Two-Phase Critical Flow	14
2.2 Critical Two-Phase Flow Experimental Studies.....	16
2.2.1 Large-Scale Tests.....	18
2.2.2 Code Development and Validation	22
2.2.3 Non-Equilibrium Effects.....	24
2.2.4 Working Fluid	25
2.2.5 Depressurisation Rate	27
2.2.6 Steam Generator Tube Integrity.....	28
2.3 Analysis of Predictive Models	29
2.3.1 Homogeneous Equilibrium Model.....	32
2.3.2 Non-Homogeneous Equilibrium Models	35
2.3.3 Homogeneous Non-Equilibrium Models	37
2.3.4 Non-Homogeneous Non-Equilibrium Models.....	39
2.4 Numerical Two-Phase Blow-Down Modelling.....	41
2.5 Overview of the Current State of Knowledge.....	46
Chapter 3 – Experimental Rig Design	48
3.1 Working Fluid.....	51
3.2 Pressurised Liquid Reservoir	53
3.3 Transition Sections with Sight Glasses.....	54
3.4 Test Section	58
3.5 Pressure Relief Section.....	65
3.6 Vacuum Tank	66
3.7 Support Frame.....	69
3.8 Pressurisation System	70

3.9 Instrumentation	71
3.9.1 Static Pressure Sensors.....	72
3.9.2 Dynamic Pressure Transducers.....	72
3.9.3 Dynamic Load Cells.....	73
3.9.4 Thermocouples.....	74
3.9.5 Data Acquisition Cards.....	75
Chapter 4 – Commissioning Tests.....	76
4.1 Experimental Procedure.....	77
4.2 Small-Scale Tests	78
4.2.1 First Commissioning Test.....	81
4.2.2 Second Commissioning Test.....	86
4.2.3 Third Commissioning Test.....	89
4.3 Large-Scale Tests.....	92
4.3.1 Fourth Commissioning Test.....	98
4.3.2 Fifth Commissioning Test.....	100
4.3.3 Sixth Commissioning Test.....	104
4.4 Thermodynamic Analysis	112
4.4.1 Determination of Initial Liquid Volume	112
4.4.2 Determination of Rupture Disc Burst Instant	115
4.5 Overview of Commissioning Results	118
Chapter 5 – Experimental Results.....	121
5.1 First Experiment.....	122
5.2 Second Experiment.....	130
5.3 Third Experiment.....	137
5.3.1 Third Experiment Retrieal	146
5.4 Fourth Experiment.....	152
Chapter 6 – Analysis and Discussion	162
6.1 Temperature Results	165
6.1.1 Liquid and Vapour Phase Temperatures.....	171
6.1.2 Influence of Volume to Discharge Area Ratio.....	172
6.2 Static Pressure Results	174
6.3 Dynamic Pressure Results	176
6.3.1 Dynamic Pressure Signal Oscillations	182
6.3.2 Pressure Wave Propagation Analysis	185
6.3.3 Investigation of Erroneous Pressure Measurements	187
6.3.4 Discussion of Static and Dynamic Pressure Results	192
6.4 Dynamic Load Results	194
6.4.1 Thrust Force Considerations	196
6.4.2 Alternative Load Measurement Possibilities	197
Chapter 7 – Conclusions and Recommendations.....	199
References.....	203
Appendix A – Vacuum Tank Design Drawing.....	A-1
Appendix B – Specifications and Calibration Certificates.....	B-1

Appendix C – Discharge Time Constant Behaviour.....	C-1
C.1 Quasi-Static Behaviour	C-1
C.2 Discharge Time Constant	C-1
C.3 Low Frequency Response	C-3
C.4 Description of Discharge Behaviour in the Context of Acquired Results	C-3
Appendix D – Uncertainty Analysis	D-1
D.1 Pressure Measurements Uncertainty.....	D-1
D.2 Temperature Measurements Uncertainty	D-2
D.3 Mass Measurements Uncertainty.....	D-2
D.4 Uncertainty of Calculated Quantities	D-3
Appendix E – Instrument Calibration	E-1
Appendix F – Fast Fourier Transforms.....	F-1
Appendix G – Wave Propagation Analysis Diagrams.....	G-1

LIST OF FIGURES

FIGURE 1-1. CANDU REACTOR SCHEMATIC	2
FIGURE 1-2. CANDU 600 MW(E) STEAM GENERATOR (MENELEY, 2003).....	4
FIGURE 2-1. BLOW-DOWN SYSTEM FOR PRESSURE SUPPRESSION TESTS FOR FULL-SCALE SEGMENTS OF ATOMIC POWER PLANTS (MOODY, 1966)	18
FIGURE 2-2. LIQUID LEVEL DECREASE WITH TIME FOR INITIALLY PARTLY FULL SATURATED VESSEL (ALLEMANN ET AL., 1971B)	20
FIGURE 2-3. THRUST VS. VESSEL PRESSURE (ALLEMANN ET AL., 1971B).....	21
FIGURE 2-4. EPRI STEAM GENERATOR SIMULATION FACILITY (KALRA, 1984).....	23
FIGURE 2-5. IDAHO NUCLEAR CORPORATION PIPE EXPERIMENT (HANSON AND ANDERSON, 1969).....	23
FIGURE 2-6. WEISMAN AND TENTNER (1978) CLASSIFICATION OF CRITICAL FLOW MODELS	31
FIGURE 2-7. HEM CRITICAL MASS FLUX FOR STEAM-WATER SYSTEM (WEISMAN AND TENTNER, 1978)	34
FIGURE 2-8. CRITICAL FLOW RATES FOR REVISED SLIP MODEL (WEISMAN AND TENTNER, 1978).....	36
FIGURE 2-9. HEM AND FROZEN MODEL CHOKED FLOW COMPARISON (WEISMAN AND TENTNER, 1978)	38
FIGURE 2-10. STEAM GENERATOR TRANSIENT ANALYSIS (SAUVÉ ET AL., 1996).....	45
FIGURE 3-1. EXPERIMENTAL RIG DESIGN CONCEPT	48
FIGURE 3-2. COMPLETE ASSEMBLY OF EXPERIMENTAL RIG.....	49
FIGURE 3-3. BLOW-DOWN RIG ASSEMBLY DRAWING.....	50
FIGURE 3-4. PHOTOGRAPH OF THE EXPERIMENTAL RIG ASSEMBLY	51
FIGURE 3-5. PHOTOGRAPH OF PRESSURISED LIQUID RESERVOIR	53
FIGURE 3-6. PRESSURISED LIQUID RESERVOIR ENGINEERING DRAWING	54
FIGURE 3-7. PHOTOGRAPH OF TRANSITION SECTIONS.....	55
FIGURE 3-8. TRANSITION SECTION ENGINEERING DRAWING	55
FIGURE 3-9. TRANSITION SECTION CLAMPING ARRANGEMENT	56
FIGURE 3-10. VIEWING PORT GLASS ENGINEERING DRAWING.....	57
FIGURE 3-11. SAFETY SHIELD	58
FIGURE 3-12. PHOTOGRAPH OF TEST SECTION	59
FIGURE 3-13. TEST SECTION ASSEMBLY CONFIGURATION	59
FIGURE 3-14. PHOTOGRAPHS OF TUBE BUNDLE	60
FIGURE 3-15. PHOTOGRAPHS OF TUBE BUNDLE FRAME	61
FIGURE 3-16. TUBE BUNDLE ENGINEERING DRAWING.....	61
FIGURE 3-17. TUBE BUNDLE FRAME ENGINEERING DRAWING.....	62
FIGURE 3-18. PHOTOGRAPH OF TEST SECTION TUBE BUNDLE ASSEMBLY INCLUDING O- RING	63
FIGURE 3-19. PHOTOGRAPHS OF TEST SECTION FLANGES	63
FIGURE 3-20. SCHEMATIC OF TUBE BUNDLE LOADING DESIGN	64
FIGURE 3-21. PHOTOGRAPHS OF RUPTURE DISC ASSEMBLY	65
FIGURE 3-22. PRESSURE RELIEF SECTION ENGINEERING DRAWING	67
FIGURE 3-23. VACUUM TANK PURGING PORT R-134A FILTER	68
FIGURE 3-24. VACUUM TANK THERMOCOUPLE PORT	69
FIGURE 3-25. SUPPORT FRAME	70
FIGURE 4-1. R-134A PRESSURE-ENTHALPY DIAGRAM (DUPONT, 2005).....	78
FIGURE 4-2. SMALL-SCALE TEST SECTION.....	79
FIGURE 4-3. REDUCED SCALE BLOW-DOWN RIG COMPONENTS.....	80
FIGURE 4-4. STATIC PRESSURE VS. TIME (1 ST TEST).....	83
FIGURE 4-5. TEMPERATURE VS. TIME (1 ST TEST)	83
FIGURE 4-6. TEMPERATURE VS. TIME (1 ST TEST; 0.2 S TIMESCALE).....	84

FIGURE 4-7. PHOTOGRAPH OF SMALL-SCALE EXPERIMENTAL SETUP	85
FIGURE 4-8. HIGH-SPEED IMAGES OF LOW-PRESSURE BLOW-DOWN	88
FIGURE 4-9. STATIC PRESSURE VS. TIME (3 RD TEST)	91
FIGURE 4-10. TEMPERATURE VS. TIME (3 RD TEST).....	91
FIGURE 4-11. MINERAL OIL RESERVOIR.....	93
FIGURE 4-12. COOLANT LOOP COMPONENTS	94
FIGURE 4-13. UPSTREAM COOLING SYSTEM.....	95
FIGURE 4-14. PHOTOGRAPH OF COOLING SYSTEM DESIGN	96
FIGURE 4-15. COOLING DESIGN ASSEMBLY CONFIGURATION.....	97
FIGURE 4-16. STATIC PRESSURE VS. TIME (4 TH TEST)	99
FIGURE 4-17. TEMPERATURE VS. TIME (4 TH TEST).....	99
FIGURE 4-18. SAMPLE ACCUMULATOR PRESSURISATION ATTEMPT	102
FIGURE 4-19. STATIC PRESSURE VS. TIME (5 TH TEST)	103
FIGURE 4-20. TEMPERATURE VS. TIME (5 TH TEST).....	103
FIGURE 4-21. TEMPERATURE VS. TIME (5 TH TEST; 20 S TIMESCALE)	104
FIGURE 4-22. STATIC PRESSURE VS. TIME (6 TH TEST)	106
FIGURE 4-23. TEMPERATURE VS. TIME (6 TH TEST).....	106
FIGURE 4-24. DYNAMIC PRESSURE VS. TIME (6 TH TEST).....	108
FIGURE 4-25. DYNAMIC PRESSURE VS. TIME (6 TH TEST; 0.01 S TIMESCALE)	108
FIGURE 4-26. HIGH-SPEED IMAGES OF INITIAL STAGES OF MODERATE-PRESSURE BLOW-DOWN	109
FIGURE 4-27. HIGH-SPEED IMAGES OF MODERATE-PRESSURE BLOW-DOWN.....	111
FIGURE 4-28. WAVE PROPAGATION TIMES FOR 6 TH COMMISSIONING TEST	116
FIGURE 5-1. STATIC PRESSURE VS. TIME (1 ST EXPERIMENT).....	123
FIGURE 5-2. TEMPERATURE VS. TIME (1 ST EXPERIMENT).....	123
FIGURE 5-3. DYNAMIC PRESSURE VS. TIME (1 ST EXPERIMENT).....	125
FIGURE 5-4. DYNAMIC PRESSURE VS. TIME (1 ST EXPERIMENT; 0.01 S TIMESCALE)	125
FIGURE 5-5. HIGH-SPEED IMAGES OF INITIAL STAGES OF 1 ST EXPERIMENT	127
FIGURE 5-6. HIGH-SPEED IMAGES OF 1 ST EXPERIMENT	129
FIGURE 5-7. STATIC PRESSURE VS. TIME (2 ND EXPERIMENT)	131
FIGURE 5-8. TEMPERATURE VS. TIME (2 ND EXPERIMENT).....	131
FIGURE 5-9. DYNAMIC PRESSURE VS. TIME (2 ND EXPERIMENT)	133
FIGURE 5-10. DYNAMIC PRESSURE VS. TIME (2 ND EXPERIMENT; 0.01 S TIMESCALE)	133
FIGURE 5-11. HIGH-SPEED IMAGES OF INITIAL STAGES OF 2 ND EXPERIMENT.....	134
FIGURE 5-12. HIGH-SPEED IMAGES OF 2 ND EXPERIMENT.....	136
FIGURE 5-13. STATIC PRESSURE VS. TIME (3 RD EXPERIMENT)	138
FIGURE 5-14. TEMPERATURE VS. TIME (3 RD EXPERIMENT).....	138
FIGURE 5-15. DYNAMIC PRESSURE VS. TIME (3 RD EXPERIMENT)	140
FIGURE 5-16. DYNAMIC PRESSURE VS. TIME (3 RD EXPERIMENT; 0.01 S TIMESCALE).....	140
FIGURE 5-17. LOAD VS. TIME (3 RD EXPERIMENT – INDIVIDUAL SIGNALS)	141
FIGURE 5-18. LOAD VS. TIME (3 RD EXPERIMENT – TOTAL SIGNAL)	142
FIGURE 5-19. LOAD VS. TIME (3 RD EXPERIMENT – TOTAL SIGNAL; 0.1 S TIMESCALE).....	142
FIGURE 5-20. HIGH-SPEED IMAGES OF INITIAL STAGES OF 3 RD EXPERIMENT	143
FIGURE 5-21. HIGH-SPEED IMAGES OF 3 RD EXPERIMENT.....	144
FIGURE 5-22. STATIC PRESSURE VS. TIME (3 RD EXPERIMENT – 2 ND ATTEMPT)	147
FIGURE 5-23. TEMPERATURE VS. TIME (3 RD EXPERIMENT – 2 ND ATTEMPT UPSTREAM).....	147
FIGURE 5-24. TEMPERATURE VS. TIME (3 RD EXPERIMENT – 2 ND ATTEMPT DOWNSTREAM).....	148
FIGURE 5-25. DYNAMIC PRESSURE VS. TIME (3 RD EXPERIMENT – 2 ND ATTEMPT)	148
FIGURE 5-26. LOAD VS. TIME (3 RD EXPERIMENT – 2 ND ATTEMPT).....	149
FIGURE 5-27. ACCELERATION VS. TIME (3 RD EXPERIMENT – 2 ND ATTEMPT)	149
FIGURE 5-28. STATIC PRESSURE VS. TIME (4 TH EXPERIMENT).....	153
FIGURE 5-29. TEMPERATURE VS. TIME (4 TH EXPERIMENT)	153
FIGURE 5-30. DYNAMIC PRESSURE VS. TIME (4 TH EXPERIMENT)	155

FIGURE 5-31. DYNAMIC PRESSURE VS. TIME (4 TH EXPERIMENT; 0.01 S TIMESCALE).....	155
FIGURE 5-32. LOAD VS. TIME (4 TH EXPERIMENT)	156
FIGURE 5-33. LOAD VS. TIME (4 TH EXPERIMENT; 0.1 S TIMESCALE)	156
FIGURE 5-34. ACCELERATION VS. TIME (4 TH EXPERIMENT).....	157
FIGURE 5-35. ACCELERATION VS. TIME (4 TH EXPERIMENT; 0.01 S TIMESCALE).....	157
FIGURE 5-36. HIGH-SPEED IMAGES OF INITIAL STAGES OF 4 TH EXPERIMENT	158
FIGURE 5-37. HIGH-SPEED IMAGES OF 4 TH EXPERIMENT	159
FIGURE 6-1. VAPOUR GENERATION MECHANISMS: INTERFACE BOILING (A → B), HETEROGENEOUS BOILING (C → D).....	164
FIGURE 6-2. TEMPERATURE VS. TIME (BOTTOM LOCATION).....	166
FIGURE 6-3. TEMPERATURE VS. TIME (UPSTREAM LOCATION)	166
FIGURE 6-4. TEMPERATURE VS. TIME (DOWNSTREAM LOCATION).....	167
FIGURE 6-5. TEMPERATURE VS. TIME (VACUUM TANK LOCATION).....	167
FIGURE 6-6. STATIC PRESSURE VS. TIME (UPSTREAM LOCATION).....	173
FIGURE 6-7. STATIC PRESSURE VS. TIME (DOWNSTREAM LOCATION)	173
FIGURE 6-8. DYNAMIC PRESSURE VS. TIME (BOTTOM LOCATION).....	177
FIGURE 6-9. DYNAMIC PRESSURE VS. TIME (BOTTOM LOCATION; 0.02 S TIMESCALE)	177
FIGURE 6-10. DYNAMIC PRESSURE VS. TIME (UPSTREAM LOCATION)	178
FIGURE 6-11. DYNAMIC PRESSURE VS. TIME (UPSTREAM LOCATION; 0.02 S TIMESCALE). 178	
FIGURE 6-12. DYNAMIC PRESSURE VS. TIME (DOWNSTREAM LOCATION)	179
FIGURE 6-13. DYNAMIC PRESSURE VS. TIME (DOWNSTREAM LOCATION; 0.05 S TIMESCALE)	179
FIGURE 6-14. DYNAMIC PRESSURE VS. TIME (VACUUM TANK LOCATION).....	180
FIGURE 6-15. DYNAMIC PRESSURE VS. TIME (VACUUM TANK LOCATION; 0.05 S TIMESCALE)	180
FIGURE 6-16. DYNAMIC PRESSURE VS. TIME (DOWNSTREAM LOCATION; 0.004 S TIMESCALE)	186
FIGURE 6-17. CROSS-SECTIONAL REPRESENTATION OF MODEL 2200V1 DYNAMIC PRESSURE SENSOR.....	190
FIGURE 6-18. PRESSURE VS. TIME (STATIC PRESSURE VS. DYNAMIC PRESSURE; 1 ST EXPERIMENT)	191
FIGURE 6-19. PRESSURE VS. TIME (STATIC PRESSURE VS. DYNAMIC PRESSURE; 2 ND EXPERIMENT)	191
FIGURE 6-20. PRESSURE VS. TIME (STATIC PRESSURE VS. DYNAMIC PRESSURE; 3 RD EXPERIMENT)	192
FIGURE 6-21. LOAD VS. TIME (3 RD EXPERIMENT VS. 4 TH EXPERIMENT)	195
FIGURE 6-22. DYNAMIC LOAD AND ACCELERATION POWER SPECTRA (4 TH EXPERIMENT) 196	

LIST OF TABLES

TABLE 4-1. THERMAL PROPERTIES OF MINERAL OIL	92
TABLE 4-2. INITIAL STEADY-STATE THERMODYNAMIC PROPERTIES FOR 6 TH COMMISSIONING TEST	115
TABLE 5-1. INITIAL STEADY-STATE THERMODYNAMIC PROPERTIES FOR 1 ST EXPERIMENT	122
TABLE 5-2. INITIAL STEADY-STATE THERMODYNAMIC PROPERTIES FOR 2 ND EXPERIMENT	130
TABLE 5-3. INITIAL STEADY-STATE THERMODYNAMIC PROPERTIES FOR 3 RD EXPERIMENT	137
TABLE 5-4. INITIAL STEADY-STATE THERMODYNAMIC PROPERTIES FOR 3 RD EXPERIMENT – 2 ND ATTEMPT	150
TABLE 5-5. INITIAL STEADY-STATE THERMODYNAMIC PROPERTIES FOR 4 TH EXPERIMENT	152

List of Acronyms

AEC:	United States Atomic Energy Commission	HFC:	Hydro-Fluoro-Carbon
AECB:	Atomic Energy Control Board	HRAI:	Heating, Refrigerating, and Air conditioning Institute of Canada
ASME:	American Society of Mechanical Engineers	IEPE:	Integrated Electronic PiezoElectric
CANDU:	CANada Deuterium Uranium	LIVM:	Low Impedance Voltage Mode
CFC:	Chloro-Fluoro-Carbon	LOCA:	Loss-Of-Coolant Accident
CFD:	Computational Fluid Dynamics	MSLB:	Main Steam-Line-Break
CSE:	Containment System Experiment	PHWR:	Pressurised Heavy Water Reactor
DAQ:	Data AcQuisition	PVC:	PolyVinyl Chloride
DBA:	Design Basis Accident	PWR:	Pressurised Water Reactor
DTC:	Discharge Time Constant	RPM:	Revolutions Per Minute
EPRI:	Electric Power Research Institute	SGTR:	Steam Generator Tube Rupture
EVET:	Equal Velocity Equal Temperature	SLB:	Steam-Line-Break
EVUT:	Equal Velocity Unequal Temperature	UTSG:	U-Tube Steam Generator
FFT:	Fast Fourier Transform	UVET:	Unequal Velocity Equal Temperature
HCFC:	Hydro-Chloro-Fluoro-Carbon	UVUT:	Unequal Velocity Unequal Temperature
HEM:	Homogeneous Equilibrium Model		

Nomenclature

A :	Flow Area [m^2]	K :	Bulk Modulus [N/m^2]
a :	Sonic Velocity [m/s]	k :	Thermal Conductivity [$\text{W}/\text{m}\cdot\text{K}$]
C :	Total Shunt Capacitance [F]	L :	Length [m]
C_D :	Coefficient Dependent on Reynolds Number	m :	Mass [kg]
C_d :	Damping Matrix [$\text{N}\cdot\text{s}/\text{m}$]	M :	Mass Matrix [kg]
c_p :	Specific Isobaric Heat Capacity [$\text{J}/\text{kg}\cdot\text{K}$]	M_{R134a} :	Molar Mass [kg/mol]
c_v :	Specific Isochoric Heat Capacity [$\text{J}/\text{kg}\cdot\text{K}$]	P :	Pressure [N/m^2]
D :	Pipe Diameter [m]	p :	Tube Pitch [m]
d :	Tube Diameter [m]	R :	Ideal Gas Constant [$\text{J}/\text{mol}\cdot\text{K}$]
F :	Force [N]	r :	Radius [m]
f_c :	Corner Frequency [Hz]	Re :	Reynolds Number
g :	Gravitational Acceleration [m/s^2]	R_G :	Gate Resistance [Ω]
G :	Mass Flow Rate [kg/s]	s :	Entropy [J/K]
g_c :	Universal Gravitational Constant [$\text{m}^3/\text{kg}\cdot\text{s}^2$]	S :	Hoop Stress [N/m^2]
h :	Enthalpy [J]	T :	Temperature [K]
H :	Height [m]	t :	Wall Thickness [m]
J :	Thermal Energy to Mechanical Energy Conversion Factor [$\text{s}^2\cdot\text{m}$]	u :	Fluid Velocity [m/s]
		v :	Instantaneous Gate Voltage [V]
		V :	Volume [m^3]
		V_O :	Initial Voltage [V]

Greek Symbols

β :	Vapour Quality
δ :	Measurement Uncertainty
Δ :	Overall Uncertainty
v :	Specific Volume [m^3/kg]
ξ_T :	Thrust Coefficient
ρ :	Density [kg/m^3]
τ :	Time Constant [s]
ν :	Kinematic Viscosity [m^2/s]

Subscripts

0 :	Upstream
b :	Break Location
c :	Critical
CT :	Calculated, Thrust
ext :	Externally Applied Vector
f :	Fluid-Elastic Vector
g :	Vapour
i :	Inside
int :	Non-Linear System
l :	Liquid
min :	Minimum
sat :	Saturation
TH :	Theoretical
$under$:	Undershoot

Superscripts

t :	Time [s]
-------	----------

Chapter 1 – Introduction

Nuclear technology has been the subject of intensive industrial and academic research for the past sixty years, as manufacturers strived to improve the reliability of the designs of the various components that make up a nuclear power plant and to enhance economic and energy efficiencies. A departure from standard working conditions in nuclear power plants may occur as a result of several events such as chemical explosions, earthquakes, air crashes, sabotage, operational transients, cooling system failures and operator errors (Riebold, 1981). One of the phenomena that must to be analysed and addressed during the licensing procedure for water-cooled nuclear reactors is the postulated Loss-Of-Coolant Accident (LOCA).

The LOCA behaviour resulting from a guillotine break of a main steam line in a Canadian Deuterium Uranium (CANDU) power plant, particularly due to external events such as seismic activity and sabotage, forms the motivation of this research investigation. A major piping rupture of this type is one of many ‘limiting fault condition occurrences’ (Riebold, 1981). These faults fall under the category of accidents that are highly improbable, yet are studied often, due to the severity of their consequences. The worst possible outcome in this case would be the release of significant doses of radioactive material that bypass the reactor containment walls of a nuclear power plant. In general, flow dynamic behaviour is calculated numerically using specialised numerical computer codes. A satisfactory numerical assessment of a particular accident event constitutes a requirement for licensing the operation of the reactor (Banerjee and Hancox, 1978).

CANDU steam generators contain tubes that carry irradiated heavy water, also known as deuterium oxide, which is the neutron moderator fluid in CANDU core reactors. Heat is transferred from the heavy water to the light water in the secondary side of the steam generator, which eventually leaves the generator as steam, powering conventional turbines that generate electrical power. A simplified schematic of a

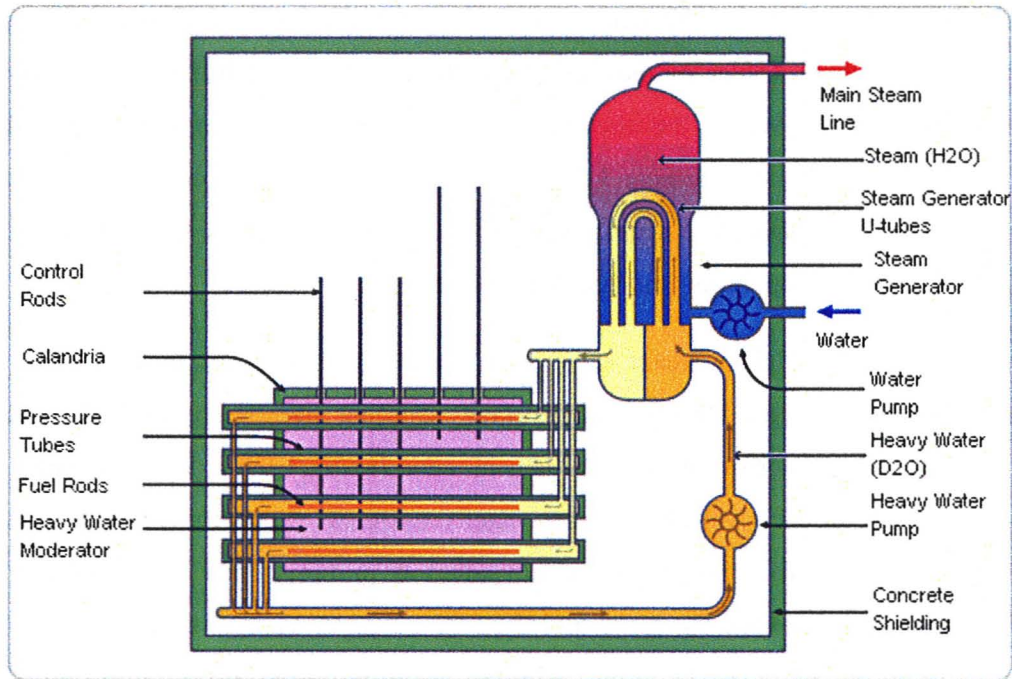


Figure 1-1. CANDU Reactor Schematic

CANDU power reactor is shown in Figure 1-1. As can be seen in Figure 1-1, U-tube rupture in a steam generator due to a main steam line LOCA would leak highly radioactive reactor coolant, D_2O , into the main steam system, which can breach the containment boundary since the steam lines extend beyond the containment walls (Wu and Chuang, 1984).

1.1 Vibration of Tubes in a Steam Generator U-Bend

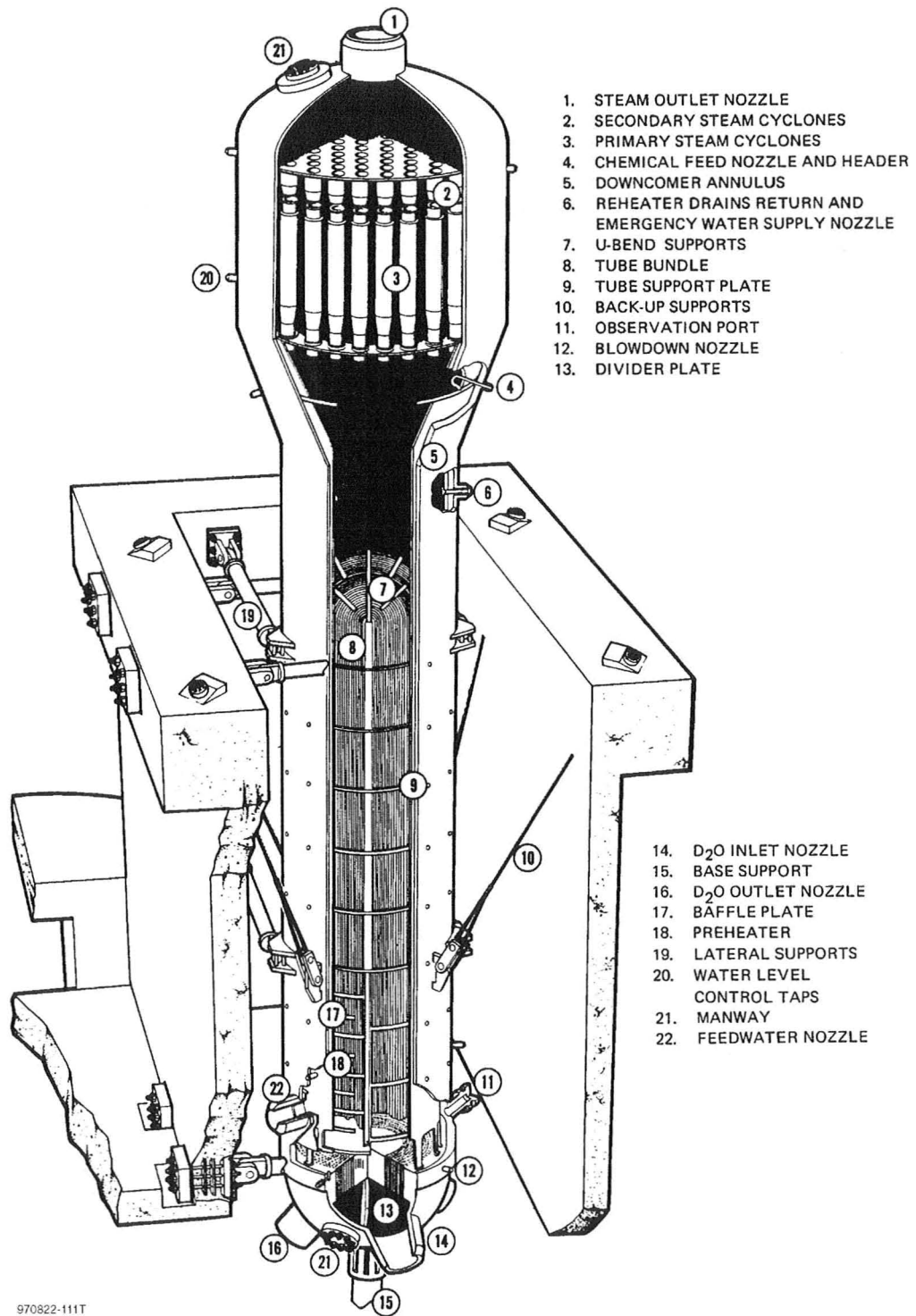
A main concern of reactor safety is to ensure that radioactive materials produced by nuclear fission reactions during reactor operation are safely contained (Ybarrondo et al., 1972). In Pressurised Water Reactor (PWR) power plants such as CANDU, the steam generator provides the required heat sink capability in the reactor loop, and plays a very important role in the safe and secure plant operation since it represents the dynamic

connection between the reactor core and the turbine generator (Chappidi et al., 1993; Kalra, 1984). Under normal operation, the circulation of the boiling two-phase steam-water flow governs the thermal hydraulic behaviour of a typical CANDU U-tube generator, shown in Figure 1-2. A thorough understanding and prediction capability of normal and off-normal steam generator behaviour are of prime importance with respect to evaluation of operation and accident transients.

In CANDU steam generators, steam rises parallel to the tubes, driven by buoyancy forces. During their normal operating life, steam generator tubes can be damaged by corrosion and mechanical wear (Kalra, 1990). In the U-bend region, the tubes experience two-phase steam-water cross-flow, which can produce tube vibrations. Typically, anti-vibration bars are installed to minimise this vibration response. Small clearances between the tubes and the tube supports exist in order to allow for thermal expansion and manufacturing assembly. Fretting wear due to impacting and sliding contact at the tube supports reduces the tube wall thickness, and naturally, the tube's margin of safety against mechanical failure. It is critical that failures are avoided in normal and off-normal situations, since, as previously discussed, the steam generator tubes provide the safety barrier between the radioactive primary side coolant, and the non-radioactive secondary side fluid.

1.2 Loss-of-Coolant Accidents in Nuclear Power Generators

One of the most important events considered in the design and licensing stage of nuclear safety assessments is the sudden rupture of a major coolant line, which triggers a LOCA. In PWRs, a large-break LOCA is considered to be the worst-case scenario, and is characterised as the hypothetical Design Basis Accident (DBA). The largest break is proposed wherein the pipe is instantaneously separated to allow flow out both ends, and this is termed a 'guillotine double-ended pipe break' (Ybarrondo et al., 1972). Reviews of



970822-111T

Figure 1-2. CANDU 600 MW(e) Steam Generator (Meneley, 2003)

available thermal hydraulic analyses indicate that the most critical transient from a steam generator tube integrity perspective is the guillotine large-break Main Steam-Line-Break (MSLB). Basically, the DBA represents the postulated, most severe, but highly unlikely condition against which reactor safety systems must be designed (Riebold, 1981). Research in the nuclear safety field has targeted the identification of the full thermo-hydraulic behaviour associated with LOCAs in a manner that permits exploration of safety margins, in order to provide an adequate foundation for quantification of existing design conservatism.

A double-ended guillotine pipe break in the main steam-line of a CANDU steam generator is almost instantaneously succeeded by a rapid blow-down, where liquid water in the steam generator is brought to a superheated state by means of a very rapid depressurisation, and suddenly flashes to vapour. This phenomenon produces a huge increase in the flow rate and hence pressure drop, resulting in considerable transient drag loading on the tubes in the U-bend region. The United States Atomic Energy Commission (AEC) stated in the Report of the Advisory Task Force on Power Reactor Emergency Cooling that “*the key phenomena during loss-of-coolant ... are the hydraulic effects of blow-down on the core and other components within the primary coolant system*” (Allemann et al., 1970). For the design of steam generators, investigation of the conditions at the onset of the phase transition provides important physical insights to the processes that lead to such explosive liquid flashing (Elias and Chambré, 1993).

1.2.1 Transient Rapid Depressurisation Behaviour

Depressurisation LOCAs caused by a loss of system integrity may give rise to violent phase change effects, classified as blow-downs. A blow-down can be defined as the “*seemingly explosive phase transition which occurs as a result of suddenly lowering the pressure in a vessel or piping network initially containing high-pressure high-*

temperature liquid, to a level substantially below the saturation pressure corresponding to the initial liquid temperature' (Winters and Merte, 1978). The liquid temperature decreases quickly as a result of a blow-down. Physically speaking, because of the sudden pressure drop, the whole energy in the liquid cannot be contained as sensible heat, and the surplus heat is converted into latent heat of vaporisation (Saury et al., 2005).

When a component of a nuclear power reactor system is subjected to a rapid depressurisation due to a pipe rupture, the resultant behaviour of the system depends on the initial conditions (Elias and Chambré, 1984; Krotiuk, 2004). If the fluid is initially saturated liquid and the break pressure is below the saturation pressure, the decompression produces liquid flashing, and a two-phase mixture of vapour and superheated liquid results. In the case of subcooled liquid, the flashing also produces a two-phase mixture, similar to the saturated liquid initial conditions. If the fluid is initially saturated steam, an isentropic decompression produces 'wet' steam. Finally, if the fluid is initially a two-phase mixture, it remains as a two-phase mixture following decompression, and the continued flashing increases the quality of the mixture. For normal CANDU operating conditions, the secondary side steam generator can be subcooled liquid, saturated liquid, two-phase flow, or saturated steam, depending on the location considered inside the steam generator.

The nature of blow-downs is very complex, and is influenced by vessel or pipe geometries and sizes of pipe rupture, among other factors (Winters and Merte, 1978). Essentially, a sudden pipe rupture produces a depressurisation wave at the break, which propagates in both directions into the system (Barták, 1990). The pressure in this wave falls from the initial value and may reach a pressure well below the saturation pressure corresponding to the initial temperature. This phenomenon is widely termed the 'pressure undershoot' (Alamgir and Lienhard, 1981). The pressure undershoot plays a vital role in the ensuing vapour generation and pressure recovery processes (Elias and Chambré, 1993). There is a finite time between the superheated state of the liquid and the first appearance of detectable bubbles, and the coolant is temporarily in a meta-stable state

before the onset of nucleation triggers the sudden expansion of the liquid (Kendoush, 1989). The extremely rapid growth of vapour bubbles in the superheated coolant gives the blow-down its explosive character. The pressure then recovers slightly, but never reaches the initial saturation value (Edwards and O'Brien, 1970). In nuclear safety LOCA studies, the pressure undershoot plays a significant role, and in most relevant experimental studies, bulk boiling as well as heterogeneous wall boiling occur throughout the entire depressurisation process (Gühler et al., 1979).

1.2.2 Accident Consequences

Inside a nuclear reactor vessel, following a large primary pipe break, decompression waves and transient pressure forces produce dynamic loading on the surfaces of the vessel internals, such as fuel rods and calandria tubes (Organisation for Economic Co-operation and Development, 2008). Similarly, Steam-Line-Break (SLB) transients in steam generators produce high velocity flows that affect thermal and hydraulic loads on the internal components (Kalra and Adams, 1980). As far as nuclear safety is concerned, transient phenomena in steam generators are second in importance only to transients in the reactor vessel (Kalra, 1984). Due to the pronounced boiling effect, the liquid level on the generator secondary side depletes rapidly, which eventually leads to dry-out of the steam generator (Chappidi et al., 1993). Furthermore, the increased pressure imbalance produces a transient loading on the tubes carrying the primary fluid, potentially jeopardising their structural integrity.

Severe accident induced Steam Generator Tube Rupture (SGTR) is a major concern since tube failure due to transient forces caused by a MSLB can lead to nuclear fission products escaping from the primary circuit to the secondary side, and ultimately bypassing the containment (Auvinen et al., 2005; Bhasin et al., 1993; Liao and Guentay, 2009; Wu and Chuang, 1984). It is common for steam generators to operate with certain

minimal tube flaw conditions, a situation that is remedied during routine maintenance procedures. Detailed inspection, fitness-for-service and life cycle management programs are performed in order to ensure that no tubes reach a state at which postulated accidental events pose a risk towards their integrity, and that any leakage produced from accidents will be of no significant consequence (Revankar and Riznic, 2009). It is important to study events associated with the decompression of a steam generator initially operating at high pressure as this can lead to improved understanding of loading on steam generator tubes (Edwards and O'Brien, 1970). The passage and reflection of acoustic waves into the interior of the steam generator from the rupture location takes place during the first few milliseconds of the transient, and the resultant forces must be identified and properly modelled in order to evaluate the integrity of steam generator tubes in the aftermath of a LOCA (Allemann et al., 1970).

1.3 Research Objective

The objective of this research project is to address the potential for steam generator tubes of increased vulnerability, due to fretting wear or corrosion degradation, to rupture because of transient loading during a postulated MSLB accident. The overall purpose of this project is to perform an experimental investigation of the transient blow-down loading of steam generator tubes in order to provide some physical insights and guidance for the development of predictive modelling tools. The experiments were conducted using a purpose design and built experimental blow-down rig that implements a CANDU design model tube bundle.

The introduction of a test section to study the transient loads on steam generator tubes represents the experimental novelty of this study, and the author is not aware of any experimental studies of this kind having previously been carried out for CANDU steam generators. A series of blow-down experiments were performed in which the pressure

drop was increased from relatively low values to scaled CANDU steam generator operating conditions. The effects of initial volume of liquid and location of the liquid free surface relative to the model tube bundle test section were investigated to assist in understanding the nature of the transient behaviour and the generation of tube loading. This thesis presents the design of the purpose built experimental rig, a description of the experimental procedure, including commissioning, and an analysis of the results of the dynamic thermal-hydraulic behaviour during a simulated main steam pipe rupture.

Chapter 2 – Literature Review

The need for adequate performance margins for nuclear power plants, including the safety systems, is constantly increasing. High levels of safety can be designed for, but excessive requirements come with a rapid cost increase (Meneley, 2003). This results in increasing demands for quantitative measurability in design and safety assessment methodologies, completeness in codes and standards, and rigor in their application (Ybarrondo et al., 1972). Despite a knowledge of the basic principles governing the main physical phenomena, serious efforts are undertaken in an attempt to accurately describe the depressurisation in terms of mathematical equations, incorporate the equations into numerical computations, and evaluate the margins of conservatism inherent to incorporated assumptions.

Design information requirements are related to operating license requirements, since the design must be deemed acceptable by licensing authorities. Licensing calculations have generally focused on being more conservative rather than realistic, over-predicting expected defined accident consequences, in order to assure regulatory authorities that the protection of the public is maintained during plant operation and under off-normal accidental situations.

Normally, in studying accidental behaviour of industrial products, such as those in the automotive and robotics fields, full-scale demonstration experiments are available. In the case of nuclear power plants however, it is generally not practical to obtain full-scale tests. The diversity of reactor system designs and the large variety of potential events to be assessed make the necessary huge number of full-scale experiments exorbitantly costly (Jackson et al., 1980). The commonly adopted theoretical approach in steam generator performance assessment is to solve the appropriate conservation equations in two-phase flow, with constitutive relationships empirically formulated, usually from simple tube experiments (Kalra, 1984).

The majority of the work available in the published literature investigates guillotine breaks of coolant circuits, and the implications are extended towards studying the safety considerations in the sudden depressurisations of vessels containing subcooled or saturated liquids. The phenomenon has been theoretically and experimentally modelled by a vast number of researchers (Deligiannis and Cleaver, 1996). Experimental investigations have generally been set-up with the hope of achieving improved knowledge of the physics governing rapid flow depressurisation, conceiving theoretical models, and providing data to compare the models through numerical simulations (Drai et al., 1998).

2.1 Critical Flow

Following the rupture of coolant piping, the coolant discharge rate from the break becomes one of the main issues to be analysed for the overall safety of water-cooled nuclear reactors. The desire to obtain realistic predictions of transient mass discharge rates from postulated breaks has driven much of the research activity towards understanding critical two-phase flow. The main reason for this is that the condition of critical flow sets the maximum possible escape rate of a high-pressure fluid from the system in which it is contained. For instance, the critical flow specifies the highest rate at which light water can be lost from the steam generator of a Pressurised Heavy Water Reactor (PHWR) under LOCA conditions (Levy, 1965). As the coolant decompresses to the ambient pressure level, given the initial high-pressure, high-temperature operating conditions, the discharge rate is governed by the compressible behaviour of the ensuing two-phase mixture during blow-down (Henry, 1970; Sozzi and Sutherland, 1975). Advances in nuclear technology stimulated extensive research activity focussing on two-phase critical flow of one-component mixtures, and many analytical and experimental investigations were performed, signifying the fundamental importance and relevance of the phenomenon with regards to blow-down safety analysis in nuclear power plants

(Ardron, 1978; Faletti and Moulton, 1963; Henry and Fauske, 1971; Hutcherson et al., 1983).

For a postulated LOCA, the critical flow at the break location determines the discharge rate, and therefore has a direct strong influence on the subsequent system depressurisation. The sudden pipe rupture generates a rarefaction wave that travels through the system, away from the break, at sonic velocity relative to the flow. At the same time, the newly imposed pressure difference accelerates the fluid towards the break. When the fluid velocity and the sonic velocity become equal and opposite to each other, the wave becomes stagnant with respect to an observer (Weisman and Tentner, 1978). At this stage, the flow is considered 'critical' or 'choked', and downstream pressure signals can no longer be transmitted to the upstream fluid. Thus, for critical flow through an outlet, the flow rate reaches a maximum and ceases to depend on conditions downstream of the break (Dobran, 1987). Further reductions in receiver pressure no longer cause flow acceleration, and merely result in a steeper pressure gradient at some location in the outlet passage (Ardron and Furness, 1976). Hence, the critical flow rate through a broken pipe depends on upstream fluid conditions, and local conditions determined by the pipe break characteristics, but not on the downstream conditions.

The critical flow rate of a blow-down transient limits the two-phase mixture discharge to a maximum value, and an accurate evaluation of this flow rate is fundamental towards predicting the system behaviour (Sami and Duong, 1989; Weisman and Tentner, 1978). Reliable modelling of the two-phase fluid characteristics of the critical mass flow rate through a ruptured pipe is important not only for predicting the fluid decompression rate, but also for calculation of the receiver pressurisation rate, vessel thrust reaction, and impingement forces produced by the expanding jet on nearby surfaces that come in contact with the fluid flow (Dobran, 1987; Moody, 1975). During the first several hundred milliseconds of the blow-down, vessel internal structures are exposed to significant hydrodynamic forces, and the impingement loads are estimated by application of the critical flow theories (Schneider and Whipple, 1978; Ardron et al.,

1977). Allemann et al. (1971b) presented some rough preliminary analysis to illustrate thrust effects in blow-down phenomena. Equation (1) was used to calculate the thrust force, F_{CT} :

$$F_{CT} = \frac{G_c^2}{g_c} A_b v_c + P_c A_b \quad (1)$$

where G_c is the critical mass flow rate, g_c is the universal gravitational constant, A_b is the break location flow area, v_c is the critical specific volume, and P_c is the critical pressure. The main factors affecting the two-phase critical flow rate are the fluid properties, break geometry, degree of superheat, and exit quality (Gühler et al., 1979).

2.1.1 Single-Phase Critical Flow

The concept of single-phase critical flow is fairly simple and well understood, and widely accepted analytical models are available in the published literature (Riznic and Ishii, 1989; Wallis, 1980). Critical flow occurs when fluid velocity is equal to the sonic velocity of the propagation of the pressure wave (Isbin et al., 1957). The sonic velocity, a , is represented in Equation (2) (Weisman and Tentner, 1978):

$$a^2 = \frac{g_c v^2}{\left(\frac{dv}{dP}\right)_s} \quad (2)$$

where s is the entropy. The critical mass flow rate, G_c , can then be found using Equation (3):

$$G_c^2 = a^2 \rho^2 = \frac{g_c}{\left(\frac{dv}{dP}\right)_s} \quad (3)$$

where ρ is the density.

2.1.2 Two-Phase Critical Flow

In two-phase flow, the physics of the situation are considerably more complicated. The reason for this is that the mechanical and thermal non-equilibrium effects due to liquid flashing, which are not encountered in single-phase flow, significantly influence two-phase critical flow (Riznic and Ishii, 1989; Weisman and Tentner, 1978). Mechanical non-equilibrium refers to unequal phase velocities in a two-phase critical flow, and thermal non-equilibrium concerns change in local void fraction due to pressure change. Since blow-down flow does not involve external heating, the vapour generation mechanism is mainly due to the flashing effect (Tain et al., 1995). In fact, the non-equilibrium vapour generation process related to pressure reduction is one of the most important features of flashing liquid flow (Downar-Zapolski et al., 1996). Because of the finite rate at which the void fraction can change, flashing initiates with some delay. This leads to meta-stable conditions where the actual void fraction does not equal the equilibrium value corresponding to the local pressure. In order to determine the critical flow rate, an accurate description of the flashing phenomena is clearly required.

The Homogeneous Equilibrium Model (HEM) and various non-equilibrium models are used to model two-phase critical flow. For a homogeneous two-phase mixture, the sonic velocity and critical flow can be related by the change in specific volume with pressure, in a similar approach as that for single-phase critical flow (Weisman and Tentner, 1978). The relationship is more complex than single-phase however, since the change in specific volume depends on the amount of vaporisation that occurs during the wave passage. The HEM assumes thermodynamic equilibrium between the phases and provides good results for critical flow rate for long tubes, in which there is sufficient time for the two phases to reach equilibrium (Dobran, 1987). In short tubes however, this condition is not satisfied, and the HEM usually under-predicts the mass flow rate (Gühler et al., 1979; Ju et al., 1982). For such cases, a non-equilibrium model is commonly employed instead. The non-equilibrium models consider relative velocity and

temperature differences between the phases, and are usually functions of flow regime. They are generally more successful than the HEM, but so far, no single model has been successful for all quality regimes and discharge nozzle geometries.

In nozzle, venturi, orifice, and short pipe geometries, the two-phase mixtures are subjected to extremely high accelerations, not allowing the vapour-liquid interface enough time to achieve equilibrium mass transport or flashing rate (Levy, 1965). Thus, it has generally been accepted that non-equilibrium effects need to be accounted for in nozzles and short pipes (Fraser and Abdelmessih, 2002). The effects of flow length and diameter on the critical flow rate for long pipes are not fully understood. This poses important questions concerning the suitability of experimental observations in small laboratory test sections, which are typically used to simulate large nozzles and pipes in industrial power plants (Isbin, 1980). The following three points characterise the problem (Hutcherson et al., 1983):

- *Does the critical flow in large pipes differ from that in small nozzles?*
- *Does the transient two-phase critical flow in large diameter ducts differ from steady-state critical flow in smaller geometries?*
- *What role do the internal flow area and meta-stable thermodynamic states play in determining the flow regime, and thus the system compressibility?*

The suppression of nucleation by non-equilibrium phenomena, which can occur if the coolant temperature is low enough, is another challenge that researchers aiming to model two-phase critical flow have faced (Wallis, 1980). In this case, the transition from single-phase to two-phase choking flow in the early blow-down stages requires some consideration. Furthermore, the flow pattern can also influence both thermal and mechanical non-equilibrium (Weisman and Tentner, 1978). Usually, critical mass flow-rates are very high and dispersed flow is the dominant regime. Thermal non-equilibrium effects in this case will differ between liquid droplets dispersed in vapour and bubbles entrained in liquid flow. Thus, a modelling assumption based on a particular flow pattern may not be appropriate when applied to a different flow pattern.

2.2 Critical Two-Phase Flow Experimental Studies

This section presents some of the most significant pioneering studies that have investigated two-phase critical flow. Isbin et al. (1957) conducted the first explicit experimental investigation published in the literature that measured critical flows of steam-water mixtures over a wide range of quality. Faletti and Moulton (1963) studied critical flow of steam-water mixtures in an annulus configuration. They plotted measured critical mass velocities as a function of mixture quality, and the results were correlated against theoretical homogeneous critical mass velocities. They found that exit pressures were generally lower than what had previously been reported in the literature.

The first experimental blow-down study was conducted by Edwards and O'Brien (1970). They performed high-pressure high-temperature pipe blow-down experiments in a 3-inch nominal bore horizontal pipe about 13 feet long, initially filled with subcooled water. The rapid depressurisation was initiated by the rupture of a glass disc located at one end of the pipe, suddenly exposing the water to the atmosphere. Edwards and O'Brien made qualitative observations pertaining to bubble growth and the ejection process induced by rapid depressurisation, and recorded transient pressure and temperature histories at seven axial locations. The pressure decreased from the initial level to a value much lower than the saturation pressure that corresponds to the initial liquid temperature at each measurement location. It was noticed that when the liquid was decompressed below its saturation pressure, vapour formed at a finite rate until a new equilibrium state was achieved. The duration of the non-equilibrium state was about 0.5 milliseconds.

Edwards and O'Brien indicated that theoretical predictions closely matched the initial stages of depressurisation. Despite the existence of non-uniformities and uncertainties in the initial liquid temperatures, these experiments are regarded as the classical blow-down tests in the literature, since they were performed at high pressures up to PWR conditions. This experiment has been the point of reference for a great deal of

subsequent analysis, and the experimental data has been used to a large extent as a standard against which various blow-down models were verified and validated (Malnes and Rasmussen, 1974).

Henry et al. (1970) investigated the critical flow phenomenon in one-component, two-phase, liquid-vapour mixtures with respect to processes in steam turbines, boilers, and nuclear reactors. Aided by the experimental studies, Henry and Fauske (1971) formulated 'frozen' flow theoretical models that are still used to predict two-phase critical flows. Sozzi and Sutherland (1975) conducted critical flow tests with saturated, subcooled and boiling water. They were particularly interested in the effects of fluid enthalpy, entrance geometry and flow length. They showed that critical, two-phase flow at high pressure and low quality is strongly dependent on upstream stagnation quality. The dependence faltered with increasing flow lengths for two-phase upstream conditions.

Barták (1990) investigated the early stage of flashing flow in horizontal pipes connected to pressure vessels. The experimental test facility consisted of a scaled PWR model vessel and its internal structures, and the horizontal test pipe was 1.7 metres long and 88 millimetres in diameter. Pressure and temperature was measured at 200 millimetre intervals, and depressurisation rates ranging from 10,000 to 40,000 MPa/s were achieved using an assembly of two rupture discs. The pressure transients displayed a different trend from Edwards and O'Brien's (1970) results. In contrast to the previous experiments, in which the test pipe was closed off at one end, the presence of the pressurised vessel in this study influenced the reflection of the pressure waves. For experiments with initial temperatures greater than 220 °C, significant pressure undershoot behaviour produced non-equilibrium two-phase flow conditions along the entire length of the discharge pipe. For lower initial temperatures, the pressure undershoot was negligible, and oscillatory high-amplitude reflected waves were obtained.

2.2.1 Large-Scale Tests

Moody (1966) presented a vessel blow-down critical flow model that was compared with two pressure suppression tests for full-scale segments of atomic power plants. In one test, the simulation consisted of a 1/112 segment of an atomic power plant, and in the other, the model reactor vessel was a 1/48 segment. Figure 2-1 displays a basic primary system schematic of the tests. The initial pressure of the saturated steam-water mixture in the model vessels was 1250 psi. The blow-downs were initiated using a double rupture disc assembly, and transient pressure measurements were obtained.

Allemann et al. (1970) conducted Containment System Experiment (CSE) blow-down tests to provide an experimental database for verification of modelling assumptions

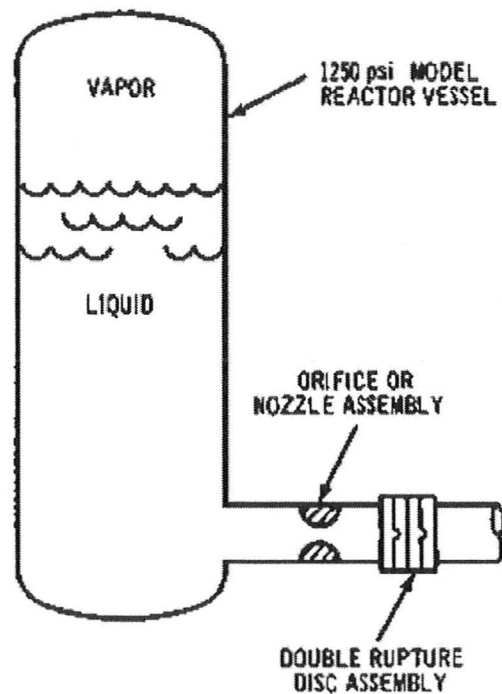


Figure 2-1. Blow-Down System for Pressure Suppression Tests for Full-Scale Segments of Atomic Power Plants (Moody, 1966)

and calculations with regards to full-scale reactor plants, and to build on existing models and develop improvements where predictions of experimental results were unsatisfactory. The CSE of Battelle-Northwest was a large-scale program for evaluation of the success of containment systems in nuclear electric power plants in reducing the release of radioactive fission products as a result of severe accident conditions. A rapid pressure loss at the break location produced a pressure difference that accelerated flow towards the break.

Transient and dynamic pressures, temperatures, liquid levels, stresses, flow rates, fluid masses remaining, fluid void fractions in the exit duct, thrust reactions and hydraulic forces resulting from sudden rupture of high temperature water systems were studied, and measured values were compared to predictions of available analytical models. Hypothetical piping breaks from a bottom outlet were simulated in a 150 ft³ vessel, and high-enthalpy water blow-downs up to 2100 psi and 600 °F were investigated with orifice diameters of 1.5 to 6.8 inches. The pipe breaks were simulated using rupture discs. Most of the initial depressurisation was achieved within one millisecond. Nitrogen gas was used for pressurisation, and Allemann et al. commented that nitrogen dissolved in the water might have caused abnormal subcooled behaviour. The nitrogen solubility had a pronounced effect on blow-down in the subcooled regime, by reducing the severity of pressure oscillations and the rate of subcooled decompression. As a result, the authors concluded that the data gathered using gas pressurisation without special provisions was not directly applicable to typical DBA situations.

In a continuing effort, Allemann et al. (1971a) studied high-pressure water blow-downs using orifice diameters of 0.9 to 5.2 inches at three different locations on the vessel. For these tests, a sieve plate separator was used to divide the vessel into two volumes. The plate was intended to simulate the reactor core, but was more representative of smaller components such as mixer, support and grid plates in nuclear reactors. The same group of researchers later conducted further tests through 1.5 to 6.8 inches diameter side nozzles (Allemann et al., 1971b). The experiments were conducted

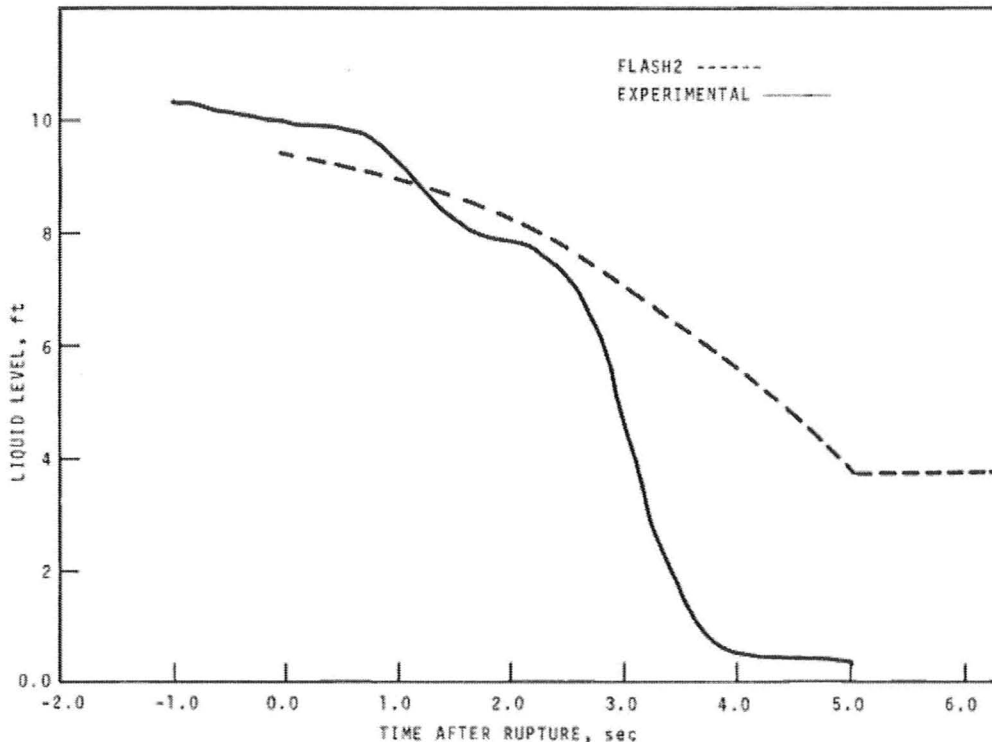


Figure 2-2. Liquid Level Decrease with Time for Initially Partly Full Saturated Vessel (Allemann et al., 1971b)

for two types of initial conditions: hot subcooled water, and saturated water surmounted by a vapour region of high quality steam. Figure 2-2 shows the non-linear decrease of liquid level with time for an initially partly full saturated vessel. The thrust force generated by the blow-down was measured using load cells, and Figure 2-3 shows thrust as a function of vessel pressure. The authors attributed the low force values to meta-stable flow conditions, deciding that the flow must have a large slip ratio.

The Marviken power plant in Sweden was originally designed as a boiling heavy-water direct cycle reactor, but served as a large-scale test facility for critical flow experiments instead, from 1972 to 1985. Critical flow tests were performed to investigate the effect of parameters such as upstream conditions and nozzle dimensions on the critical mass flow rate. A series of blow-down experiments were also carried out on a test facility in the Battelle-Institute in Frankfurt in 1975. The simulated pressure vessel with

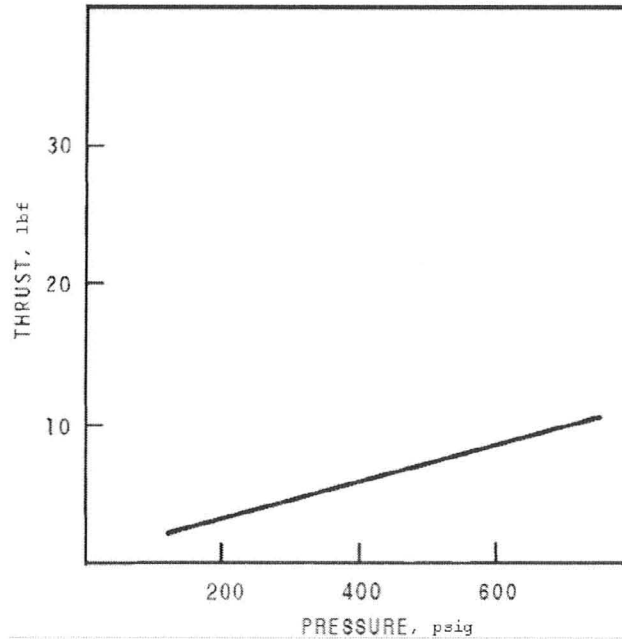


Figure 2-3. Thrust vs. Vessel Pressure (Allemann et al., 1971b)

internal components stood 11.3 metres high, and had a diameter of 0.8 metres. The purpose of the experiments, referred to as the RS-16B experiments, was to study blow-down loads on PWR internals. The Heiß Dampf Reaktor in West Germany is another example of a research reactor that was used as a test facility for large-scale experiments. The main objective of these tests was to explore the effects of multidimensional fluid-structure interaction phenomena during the blow-down phase of a LOCA for code validation purposes.

Kalra and Adams (1980) performed SLB simulation experiments in a 1/7 scale PWR U-tube Electric Power Research Institute (EPRI) steam generator simulation facility. The general-purpose EPRI facility was specially designed for the investigation of the thermal-hydraulic behaviour of a prototypical PWR U-tube steam generator, employing conventional fluid-to-fluid modelling (Freon-to-water) and flow visualisation techniques. Because design-specific vendor data are usually proprietary and not available

to the general public, Kalra (1984) identified the need to set up a general facility of this type for performing the wide variety of steady state and transient steam generator safety tests. The scale-model of a prototype U-Tube Steam Generator (UTSG) was built for experimental work, and a large database was established. The main concepts of the facility included preservation of geometric similarity, modelling the global steam-water behaviour in steam generators, enabling visual observations of flow pattern development inside the steam generator to be made, and performing normal operational and off-normal accidental conditions transient experiments.

Figure 2-4 depicts a schematic of the EPRI steam generator simulation facility. The experimental design preserved geometric similarities through incorporating the major features of industrial UTSGs and employing the underlying principles of fluid-to-fluid scaling. For scaling purposes, the prototype was based on a compromise standard commercial design that did not involve vendor-specific details. Classic transients such as the SLB were studied and reported. Furthermore, flow visualisation provided a better fundamental understanding of flow behaviour and contributed towards the improvement of analytical models and code validation efforts.

2.2.2 Code Development and Validation

Many experimental results were obtained over the years in order to validate available computer behaviour prediction codes and develop code improvements that allow for more accurate representation of observed response characteristics. For example, Hanson and Anderson (1969) carried out simple pipe blow-down tests to compare the magnitude of the thrust forces predicted by the computer codes BURST and WHAM. The experimental configuration is shown in Figure 2-5.

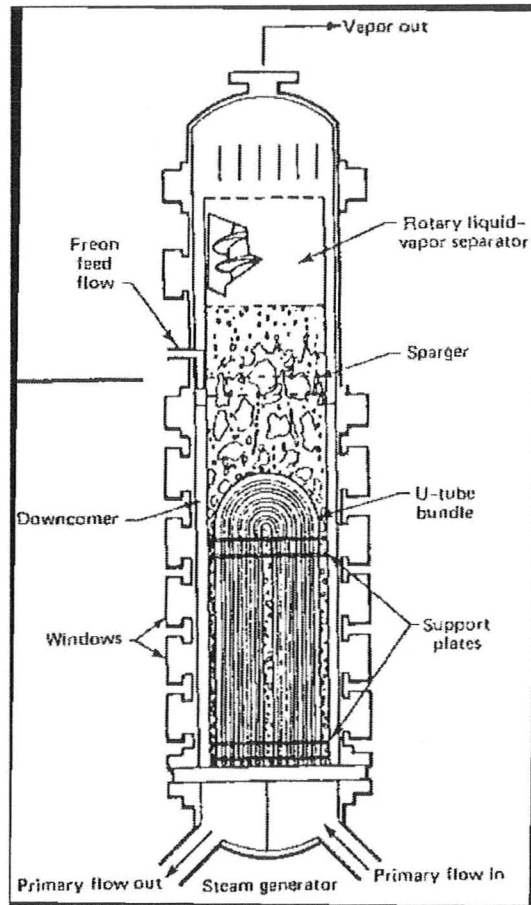


Figure 2-4. EPRI Steam Generator Simulation Facility (Kalra, 1984)

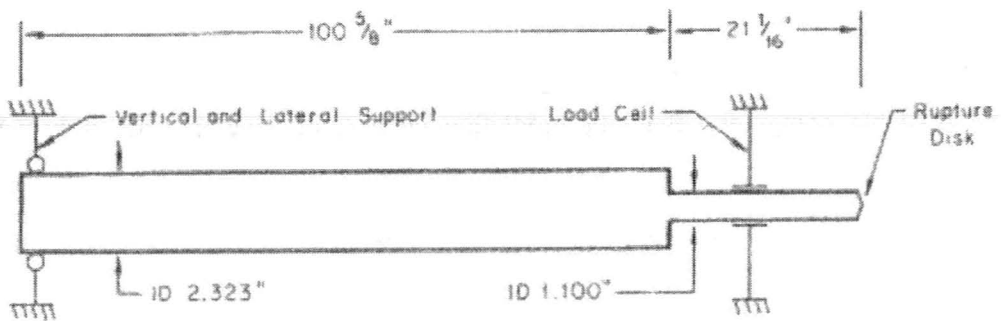


Figure 2-5. Idaho Nuclear Corporation Pipe Experiment (Hanson and Anderson, 1969)

Having stated that experiments were required to improve the mathematical models and provide benchmarks that validate whether or not the models adequately represent the pertinent physical phenomena, Banerjee and Hancox (1978) presented a strategy for the development of LOCA analysis codes. They focussed mainly on developing procedures that determine benchmark and computationally efficient solutions to the various models. The experiments by Hall and Hall (1979) are another example of high-pressure steam-water blow-down tests carried out to supplement the available database for code validation. More recently, Mignot et al. (2004) presented experimental supercritical water depressurisation results as well as calculations for validation of current computer models used in reactor design codes such as RELAP. Pinhasi et al. (2005) state that more experimental blow-down data is needed for complete validation of pertinent models and evaluation of physical mechanisms. They argue that benchmark experiments should be extended to provide data on a wider range of parameters that have not been properly considered so far, such as mass flow rate and void fraction.

2.2.3 Non-Equilibrium Effects

Non-equilibrium effects such as slip ratio (mechanical non-equilibrium) and delayed phase transition (thermal non-equilibrium) were investigated by a large number of researchers, and several analytical models were developed to account for the observed trends in mathematical terms. Klingebiel and Moulton (1971) experimentally studied the nature of two-phase choking and the validity of describing the physical processes through a separated model. They were specifically interested in assessing the contribution of the slip between the two phases. Winters and Merte (1979) performed pipe blow-down experiments with dichlorodifluoromethane (R-12), in which prominent two-phase non-equilibrium behaviour was also manifested. The blow-down transients were highly influenced by the initial temperature and the pipe geometry, but not by the initial pressure level. Hutcherson et al. (1983) noticed a significant non-uniform fluid quality distribution

during the early stages of blow-downs in their tests. Choking only occurred at the exit of the exhaust duct that was used, and it was determined that the initial pressure decrease inside the vessel was due to the vapour volume production rate being lower than the initial volume exhaust rate. In experiments performed by Nakamura et al. (1984), dynamic characteristics associated with the flashing phenomena of saturated water contained in vessels also displayed similar features.

Hanaoka et al. (1990) performed blow-down experiments triggered by a quick opening solenoid valve. A test piece rod was placed inside the vessel as a source of nucleation cavities, and the flashing phenomenon was compared with and without the test piece under identical conditions. They discovered that for the same initial conditions, the test piece resulted in an increase in the heterogeneity of the flashing nucleation, and the limits of superheat were reduced. The presence of the test piece essentially decreased the time available for pressure relaxation, and produced more explosive flashing behaviour. After the inception of flashing, the pattern of the pressure recovery was dependent mainly on mass discharge flux through the orifice and the rate of vapour formation. Fraser and Abdelmessih (2002) investigated one-component, critical two-phase flow of saturated and subcooled water in long pipes. They introduced a new method, involving a cavitating ring that could be positioned in axial locations along the pipe length, which allowed them to control the location of flashing inception. They carried out a systematic study of the effects of flashing inception, and using the information gained from the experimental analysis, developed a computer model for predicting critical two-phase flow rates over a wide range of conditions.

2.2.4 Working Fluid

Using working fluids such as R-12, as realised by Winters and Merte (1978), has more experimental advantages than merely providing blow-down data for a fluid other

than water. The advantages are mainly associated with its relatively low vapour pressure. This makes it possible to use thinner rupture diaphragms than the thick tempered glass membranes required for high-pressure water blow-down experiments. Also, because the saturation temperature of R-12 is close to that of ambient temperature conditions, it is easier to maintain uniform initial temperatures. Winters and Merte used a cellulose triacetate rupture membrane that shatters when pierced under stress, and almost always provides no blockage of flow area at the exit of the duct. In the experiments conducted by Edwards and O'Brien (1970), the thick glass discs left non-yielding obstructions in the path of the exiting flow and undesirably reduced the break area significantly. Clegg and Papadakis (1986) studied the evaporation of saturated liquid Freon-11 in a small glass tank, and stated that direct visual liquid observations during evaporation were facilitated because of the proximity of the boiling point to ambient temperature conditions.

Deligiannis and Cleaver (1996) carried out pressurised Freon-12 blow-down experiments from a partially full vessel with a vent pipe. They provided several justifications for their selection of R-12 as a working fluid. Most of the literature work had been previously performed for water, and given that the thermodynamic properties of saturated Freon-12 are well known, it was regarded beneficial to provide data for a fluid different from water. The low vapour pressures associated with R-12 permitted the use of a thin Melinex film as a rupture diaphragm. Problems that arise due to high pressures, such as safety concerns and leakage issues, were avoided. The use of thermal insulation was also unnecessary since initial temperatures were fairly uniform. Reinke and Yadigaroglu (2001) released up to 2 litres of meta-stable propane, butane, refrigerant-134a and water to atmospheric pressure from initial superheats through rapid depressurisation from glass receptacles without nucleation sites. The velocity of the two-phase flow produced at the boiling front was significantly lower than that predicted by isentropic phase change theory.

2.2.5 Depressurisation Rate

In order to accurately represent instantaneous pipe ruptures and other very sudden accidents, the rapidity with which the experimental configurations replicate this phenomenon is of paramount importance. Lienhard et al. (1978) studied extremely high speeds of depressurisation that had not been previously attained in published laboratory experiments. Subcooled water was released from 10.8 metre long horizontal pipes of one-half and two inches internal diameter equipped with a novel quick-opening mechanism, at thermodynamic parameters typical for PWR conditions. The very high depressurisation rates, up to 200,000 MPa/s, allowed the water to reach superheated states at pressures, P_{min} , much lower than the saturation pressure, P_{sat} . The magnitude of the pressure undershoot, ΔP_{unders} , from Equation (4), was highly dependent on the initial fluid temperature, and showed a weaker dependence on the blow-down depressurisation rate.

$$\Delta P_{unders} = P_{sat} - P_{min} \quad (4)$$

The authors noticed that the initial pressure had no significant influence on the pressure undershoot, and that the speed of propagation of pressure rarefaction waves in water could be higher than the speed of sound when the water is contained in a heavy pipe. Several other authors experimentally concluded for other fluids that increasing break exit sizes result in higher rates of depressurisation (Gühler et al., 1979; Hanaoka et al., 1990; Nakamura et al., 1984).

Hanaoka et al. (1990) conducted blow-down experiments from a Pyrex glass vessel through a top orifice initiated by electro-magnetic quick-opening valves. Similar phenomena were observed, in that the pressure decreased below saturation pressure, after which the pressure recovered due to inception of flashing. The authors concluded that the liquid superheat limit depends mainly on the experimental depressurisation rate. More recently, Saury et al. (2005) analysed the effects of initial water level and depressurisation rate on the flash evaporation of a water film. Qualitative descriptions were made possible using high-speed camera visualisations. Up until then, studies that

involved high depressurisation rates usually focussed on flowing pressurised liquid (Alamgir et al., 1980; Alamgir and Lienhard, 1981; Deligiannis and Cleaver, 1990; Elias and Chambré, 1993; Reinke and Yadigaroglu, 2001), and not much was available in the literature regarding stagnant liquid pool depressurisation. Saury et al. acquired visualisations that showed a very violent initial mechanism of flashing, where the liquid was completely disrupted and bubble nucleation occurred everywhere in the liquid volume. After a short period of intense liquid boiling, the magnitude of the phenomenon decreased, and boiling approached the free surface. It was concluded that the maximum amplitude of flash evaporation, the flashing time, and the final evaporated mass were all increasing functions of the initial liquid level. In modelling flashing two-phase flow, the depressurisation rate is treated as an independent parameter, as it is very difficult to accurately describe its dependency on various parameters and conditions such as initial thermodynamic conditions, test channel geometries, and sudden depressurisation mechanisms (Pinhasi et al., 2005).

2.2.6 Steam Generator Tube Integrity

There is very little in the published literature pertaining to experimental studies on steam generator tubes exposed to rapid blow-downs. Tubes in nuclear steam generators under normal operating conditions experience significant degradation such as denting, stress corrosion cracking, fretting and fatigue, due to various chemical and thermal-hydraulic circumstances. Although such degraded steam generator tubes may be acceptable for normal operation, their vulnerability in accident conditions may be increased. The Atomic Energy Control Board (AECB) carried out an experimental program to determine the tolerance of steam generator tubes with various defects to high cross-flow velocities (Forrest, 1995). Tube bundles were placed in water tunnels in which high cross-flow velocities were established. The tubes were tested at steady state up to failure, either due to a leak or complete rupture, and the failed surfaces were then

inspected. During four of the tests, a dummy tube in the first or second row was found to have failed, and all tubes showed scuff marks associated with tube-to-tube impacts.

2.3 Analysis of Predictive Models

The behaviour of heat exchangers, and specifically steam generators, is fundamentally nonlinear due to coupling effects between energy transport (heat transfer coefficients) and mass transport (velocities) (Kalra, 1984). Models that describe transient steam generator flow during sudden large deviations from initial conditions are essential for realistic quantification of PWR plant response. This requirement to model two-phase flow has driven the majority of the technical developments (Jackson et al., 1980). The theoretical models for predicting two-phase critical flow rate range from the simple HEM, which is really a single-phase flow technique, to very sophisticated, elaborate mechanistic models that attempt to represent approximately all the non-equilibrium phenomena (Fraser and Abdelmessih, 2002; Tain et al., 1995; Wallis, 1980). In between are the hybrid models that are based on equilibrium models and treat some of the non-equilibrium aspects through various assumptions and empirical correlations.

The critical flow rate of a one-component two-phase mixture is a function of the degree of inter-phase heat, mass, and momentum transfer as the fluid travels between its stagnation state, which is the thermodynamic state of a fluid particle brought isentropically to rest, and the exit plane (Ardron and Furness, 1976). The different assumptions that have been made with respect to these processes have led to the variety in the formulation of analytical models. The number of partial-differential mass, momentum and energy conservation equations used in the various one-dimensional models varies from three equations written for the homogeneous mixture to six conservation equations written for each phase separately (Bouré, 1975). The more conservation equations exist in the formulation, the more detailed the laws of the

transfers between the phases and between each phase and the containment walls are. Usually, existing models involve empirically adjusted quantities such that the number of conservation equations is governed by a compromise between the requirement to adjust the empirical correlations and the requirement to detail the transfer laws.

A subject of debate is the trade-off between simple, often highly empirical, models and more complex models that rely on fundamental principles. Although empirical models are usually more economical especially when applied to computer simulation codes, they may not be confidently extrapolated to new untested regimes as reliably as the more elementary theoretical models (Jackson et al., 1980). Early non-equilibrium models were largely empirical in nature, and extrapolation of the critical flow parameters gave inaccurate predictions (Dobran, 1987). More successful modelling was achieved using separate phase conservation and balance equations. This approach is advantageous in that very elaborate descriptions of the thermal and mechanical non-equilibrium could be made, albeit at the expense of a huge amount of information required to complete the model formulation, such as initial nucleation site density, bubble diameter, inter-phase friction and heat transfer, and flow regime transitions. It is argued that it is possible to reach a point of diminishing returns from increased theoretical complexity. In practical applications, the problem is usually not sufficiently well defined to warrant a sophisticated approach, and the results are sometimes worse than those obtained from simpler models that require less input information (Wallis, 1980).

Weisman and Tentner (1978) classified critical flow rate predictive models as shown in Figure 2-6. Researchers generally classify two-phase one-dimensional critical flow models into the following categories: HEMs, Non-Homogeneous Equilibrium (Slip) Models, Homogeneous Non-Equilibrium Models, and Two-Fluid (Separate Flow) Models (Kim and O'Neal, 1995; Tain et al., 1995; Wallis and Richter, 1978). Alternatively, these models can be referred to as Equal Velocity Equal Temperature (EVET) models, Unequal Velocity Equal Temperature (UVET) models, Equal Velocity

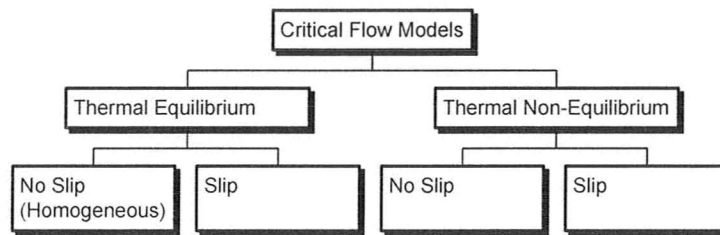


Figure 2-6. Weisman and Tentner (1978) Classification of Critical Flow Models

Unequal Temperature (EVUT) models, and Unequal Velocity Unequal Temperature (UVUT) models respectively.

The HEM treats two-phase flow using single-phase flow analysis methods. The phases are assumed to be well mixed and to have equal velocities and temperatures, and the flow evolution is taken to be isentropic (Fraser and Abdelmessih, 2002). Slip flow models, such as those developed by Levy (1965) and Moody (1975), attempt to incorporate non-equilibrium effects by allowing the vapour and liquid phases to have different velocities in thermodynamic equilibrium. The ratio between these velocities, defined as the slip ratio, is specified in different ways, often without any physical consideration of the flow. Non-equilibrium models range from attempts to represent non-equilibrium with a single empirical correction function, such as Henry's (1970) correction factor in terms of thermodynamic equilibrium quality, to a complete set of one-dimensional mass, momentum and energy conservation equations for each phase, supplemented with criteria for nucleation and phase transition (Wallis, 1980). In separate flow modelling, one-dimensional conservation laws are written for each phase, and the equations include inter-phase heat, mass and momentum transfer terms. Average phase temperatures and velocities are considered to be unequal, and some elaborate models contain formulations for bubble nucleation and growth.

Whenever a reduced model is used, the reduction in the number of conservation equations is due to implicit assumptions on the interfacial transfer laws, as emphasised by Bouré (1975). A restriction on the enthalpy of a single phase affects the mass transfer law and restrictions on both enthalpies affect both mass and energy transfer laws, whereas

slip restrictions affect the momentum transfer law. Because there is no completely general theory of two-phase critical flow, each model can only satisfactorily predict critical two-phase flow rates for particular well-defined conditions (Ardron and Furness, 1976; Fraser and Abdelmessih, 2002). For large vessels with relatively small discharge openings, it may be sufficient to treat the expanding two-phase flow as a homogeneous mixture in thermodynamic equilibrium (Winters and Merte, 1978). The pressure can be modelled to follow the saturation temperature corresponding to the mixing temperature, and the discharge flow can be described using a suitable slip choked flow model. Thermodynamic non-equilibrium is more significant however when the size of the discharge opening is large compared to the vessel volume.

Non-equilibrium models can be divided into empirical models (Henry, 1970) and mechanistic models (Ardron, 1978; Malnes, 1975; Winters and Merte, 1979). The first approach accounts for non-equilibrium vapour generation by introducing one or more empirical coefficients to keep the flow quality below its equilibrium value. The coefficients are usually fitted to experimental data without attempting to physically describe the mechanism of vapour formation. In the second approach, the modelling is performed from an analytical perspective. Vapour generation is typically modelled as a bubble growth process that is dependent on the superheat level. The relation between the vapour density and pressure is significant, since the vapour temperature and density do not remain constant in a liquid undergoing decompression (Pinhasi et al., 2005). Usually, the diffusion-controlled rate of bubble growth depends on transient conduction in the liquid surrounding each bubble, without considering the effects of neighbouring bubbles.

2.3.1 Homogeneous Equilibrium Model

In the early choked flow models, mechanical and thermodynamic equilibrium between the vapour and liquid phases were commonly assumed (Yoon et al., 2006). In

the HEM, the two phases are everywhere at equilibrium with equal velocities and temperatures. The approach is to treat the two-phase mixture as a pseudo-fluid that can be described as an equivalent single-phase flow (Wallis, 1980). Several system codes for nuclear loss-of-coolant analysis, such as early versions of RELAP, are based on the HEM. The HEM is the simplest analytical model that can be postulated (Weisman and Tentner, 1978), and it incorporates the following assumptions (Isbin, 1980; Kim and O’Neal, 1995; Yang et al., 1986):

- The vapour and liquid phases are thoroughly mixed and uniformly distributed such that there is no slip present
- Heat and mass transfer rates are infinite such that thermodynamic equilibrium exists at all times
- Body forces, chemical reactions, and obstruction effects are all negligible
- The flow is isentropic, steady and quasi-one-dimensional in that no radial distribution effects are included

The single-phase theory may be applied to a flowing two-phase mixture if it is regarded as a homogeneous fluid, and the specific volumes of vapour and liquid are additive. The theoretical critical mass velocity in this case may be found from Equation (5) (Faletti and Moulton, 1963):

$$G_{TH} = \left[-g_c \left(\frac{\Delta P}{\Delta v} \right)_s \right]^{\frac{1}{2}} \quad (5)$$

As the fluid flows through the pipe, the pressure drops, the fluid vaporises, and the velocity increases. Since the increase in kinetic energy decreases the fluid enthalpy, from application of simplified assumptions to the continuity and energy conservation equations, the mass flow rate can be related to enthalpy and specific volume by Equation (6) (Weisman and Tentner, 1978):

$$G = \left[2g_c J \cdot (h_0 - h) / v^2 \right]^{\frac{1}{2}} \quad (6)$$

where J is the thermal energy to mechanical energy conversion factor, and h is the enthalpy. For fixed stagnation conditions the critical mass flow rate can be obtained by finding the downstream pressure at which the mass flow rate is a maximum. Figure 2-7 shows the results of critical mass flow rate calculations for steam-water systems.

As previously discussed, blow-down in long pipes approaches thermal equilibrium, whereas thermal non-equilibrium effects are more significant in short pipes. Accordingly, the HEM provides better predictions for long pipe blow-down experiments (Weisman and Tentner, 1978). The HEM assumption is valid for ideal conditions such as a long pipe where there is sufficient time for equilibrium to be achieved and when the

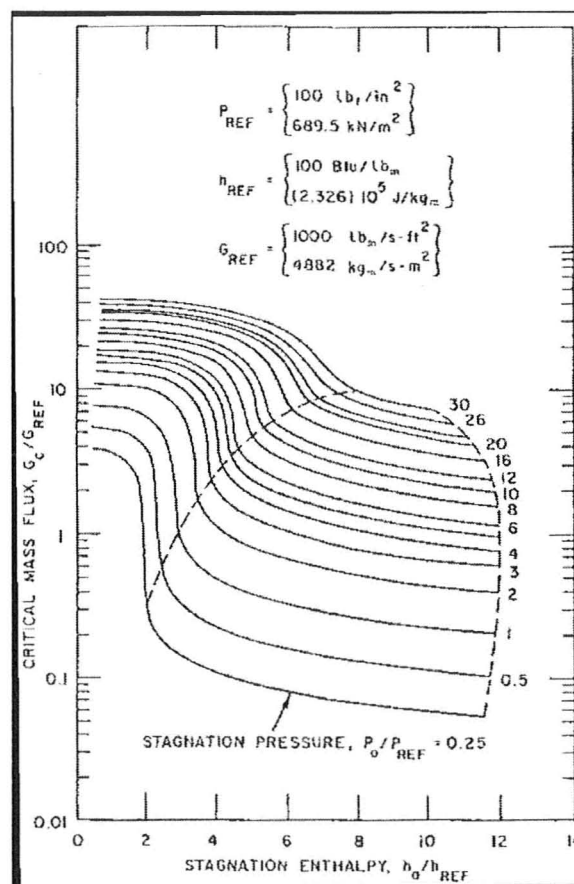


Figure 2-7. HEM Critical Mass Flux for Steam-Water System (Weisman and Tentner, 1978)

flow pattern produces inter-phase forces that are large enough to suppress significant relative motion, such as in bubbly flow (Yoon et al., 2006). Errors can be large however, for short pipes where vapour formation does not proceed to equilibrium, and in longer pipes where the flow regime, such as annular flow, permits deviations in phase velocities (Henry, 1970; Isbin et al., 1957; Sozzi and Sutherland, 1975). Also, when the break area is relatively large compared to the container volume, the liquid becomes superheated with respect to the system pressure due to rapid depressurisation and expansion of fluid, and the thermodynamic non-equilibrium renders the homogeneous assumption inaccurate (Winters and Merte, 1978; 1979). Meta-stability due to rapid flashing reduces the effective compressibility of the mixture, producing an increased critical flow rate. Slip also results in higher flow rates, since the vapour is accelerated at a much higher rate than the liquid, due to its lower density (Ju et al., 1982).

2.3.2 Non-Homogeneous Equilibrium Models

Several models have been presented that are based on the assumption of complete inter-phase thermal equilibrium. This could be expected to be valid for flows where the fluid flow path is long relative to the timescale of the evaporation process, such as the case of very long, or very large diameter pipes (Ardron and Furness, 1976). These models are identified as the ‘slip models’, because an expression for the slip ratio is required in order to predict the choked mass flow rate at the critical location (Downar-Zapolski et al., 1996). Slip models assume that both liquid and vapour exist at a saturated condition, and the additional closure law for velocity ratio is added. Levy (1965) proposed a model for two-phase critical flow rate wherein a theoretical formulation for the slip ratio based on inter-phase momentum exchange was incorporated. In an extension of the HEM, Moody (1965) developed a non-homogeneous equilibrium model that permits different vapour and liquid velocities. The slip ratio was treated as a variable determined by the condition of maximum kinetic energy flux at the exit (Yoon et al., 2006).

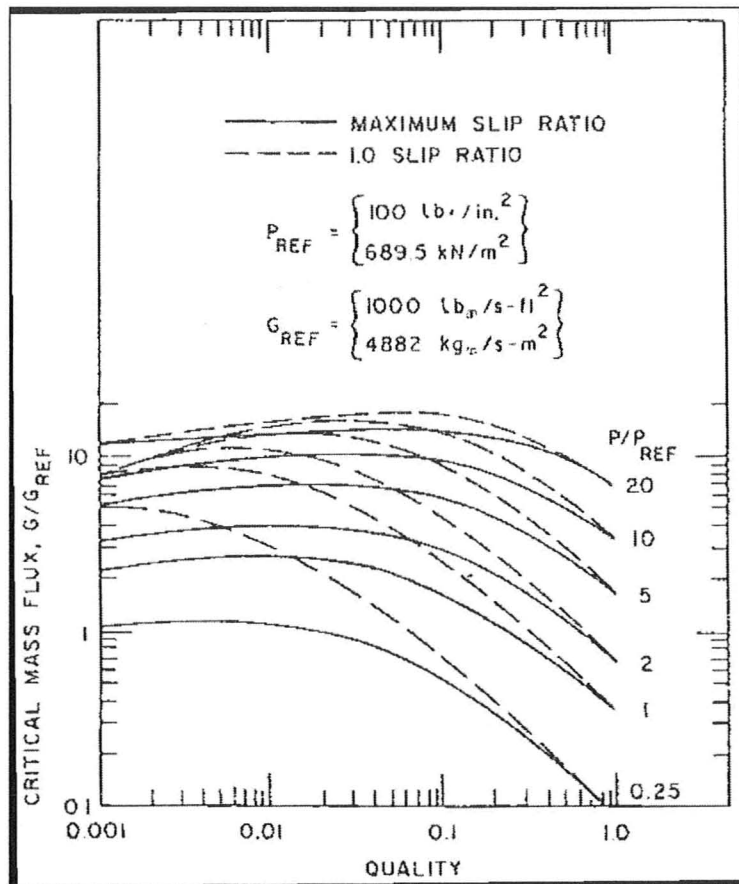


Figure 2-8. Critical Flow Rates for Revised Slip Model (Weisman and Tentner, 1978)

Moody (1975) argued that the models of his own earlier work as well as Levy's were not consistent since they were based on either the energy or momentum conservation, but not both. He then formulated a new more sophisticated slip model based on the mass, momentum and energy conservation laws and the second law of thermodynamics. Figure 2-8 shows the critical mass flow rates obtained from the revised slip model.

Through an analysis of the characteristics of the conservation equations, Weisman and Tentner (1978) demonstrated the unrealistic nature of the high slip ratios in several slip models, despite improved predictions of critical flow when break properties were

used. The slip ratio is expected to be close to unity at the large mass flow rates encountered under critical flow conditions. Critics of slip models point out that they are based on ideal flow regimes (annular or separated flow) and that the energy or momentum maximisation and minimisation assumptions are not based on any theoretical grounds whatsoever. Ju et al. (1982) performed high quality steam-water experiments and obtained slip ratios much higher than those predicted by slip models since the flow pattern changed continuously throughout the test section instead of remaining the same. In most slip models, the slip ratio is assumed to be independent of quality (Yoon et al., 2006).

2.3.3 Homogeneous Non-Equilibrium Models

Thermal non-equilibrium is believed to be one of the main sources of deviations between model predictions and experimental data, especially when the fluid enters the critical point in a subcooled state or the critical flow path is very short, such as in short pipes or nozzles (Yoon et al., 2006). The non-equilibrium exists due to the finite rate of vapour generation during the depressurisation process and can significantly increase critical flow rates and rarefaction wave propagation velocities (Weisman and Tentner, 1978).

For flows in short pipes and nozzles, the time associated with phase change may be assumed to be very short, and the assumption of ‘frozen’ (constant quality) flow holds (Dobran, 1987). Homogeneous frozen models assume that the two phases are homogeneous, the average phase velocities are equal, and there is no mass or heat transfer occurring between the two phases (Kim and O’Neal, 1995). Each phase need not be in thermal equilibrium and the non-equilibrium effects are accounted for in an empirical manner (Fraser and Abdelmessih, 2002). Henry and Fauske (1971) derived a fairly complex non-equilibrium model for critical discharge of initially subcooled water

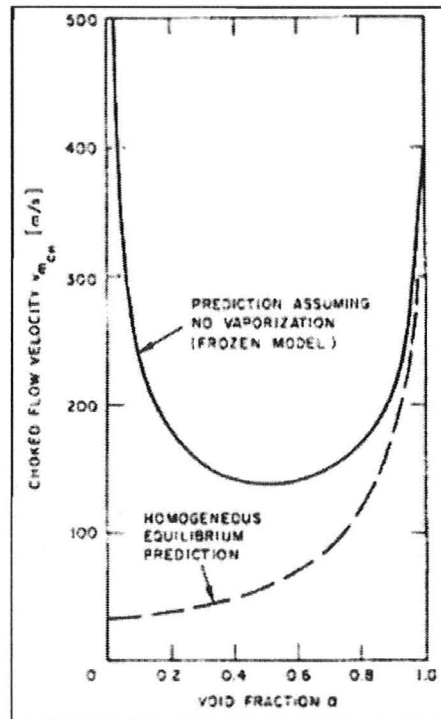


Figure 2-9. HEM and Frozen Model Choked Flow Comparison (Weisman and Tentner, 1978)

from a nozzle in which non-equilibrium vapour generation is handled entirely through an empirical coefficient. Figure 2-9 shows the difference in predictions obtained by the HEM and the frozen model.

Critical discharge through short pipes is substantially influenced by thermodynamic non-equilibrium. Significant non-equilibrium effects have been observed for pipes less than ten diameters long, even when the bore diameter was very large (Ardron, 1978). The increase in the flow rate is greatest when the fluid is initially subcooled, since this subcooled condition may prevail until just upstream of the break location. When the upstream liquid is sufficiently subcooled such that qualities at the break location are very low, non-equilibrium effects play an important role regardless of the pipe length (Weisman and Tentner, 1978). In such cases, the flow rate predictions are significantly higher than the HEM or slip model predictions, as illustrated in Figure 2-9.

2.3.4 Non-Homogeneous Non-Equilibrium Models

While the previously discussed models provide useful tools for calculations, none of them provide a true description of the physical mechanisms involved in critical two-phase flow (Weisman and Tentner, 1978). The main non-equilibrium phenomena that are neglected in the HEM are the vapour bubble nucleation and the inter-phase transfer terms, while multi-dimensional effects and two-phase flow regime transitions are also ignored (Wallis, 1980). In bubbly two-phase flow regimes, the number density of bubbles is a key parameter affecting the interfacial area concentration (Pinhasi et al., 2005). Some theoretical developments have attempted to incorporate these effects, and they all feature at least some form of empiricism.

A mathematical approach that is in principle capable of representing most of the recognised non-equilibrium phenomena is the ‘two-fluid’ or ‘separated flow’ model (Wallis, 1980). Using this model, the mechanical non-equilibrium and the thermal non-equilibrium can be considered simultaneously with the aid of proper constitutive interfacial transfer terms (Yoon et al., 2006). These equations specify the rate of phase change, momentum exchange, and heat transfer between the phases (Riznic and Ishii, 1989). Malnes (1975) developed a model based on vapour bubbles, which serve as heterogeneous nucleation sites, dissolved in liquid, and Ardron (1978) developed another non-equilibrium model for blow-down of saturated or subcooled water. Despite their potential superiority, two-fluid models pose severe closure problems (Downar-Zapolski et al., 1996). Accurate representation of the constitutive relations, particularly for choked flow with large depressurisation and convective acceleration, is very difficult (Riznic and Ishii, 1989; Wallis, 1980). For instance, in order to model interfacial drag and apparent mass effects, knowledge of the flow pattern and entity size (such as bubble volume) is required. Assumptions must be made relating to applicability of steady-state drag correlations in accelerating flow and the effect of interfacial geometry changes on these

forces. Such simplifications often result in quite arbitrary assumptions that compensate for lack of knowledge (Downar-Zapolski et al., 1996).

The main difficulty associated with developing reliable non-equilibrium critical flow models is properly modelling the volumetric rate of vapour generation (Weisman and Tentner, 1978). The volumetric vapour generation term is used in the constitutive equation for closure of the two-phase conservation equations. It is evaluated based on non-equilibrium dynamic and thermodynamic considerations of different flow regimes, or through ‘relaxation’ phase change models, by means of empirical coefficients. Relaxation is defined as ‘*the transition of a thermodynamic system from non-equilibrium to equilibrium*’ (Pinhasi et al., 2005). The rate of change of quality is assumed to be proportional to the difference between the actual quality and the equilibrium quality (Downar-Zapolski et al., 1996). Once the initial inhibiting effects of surface tension are overcome, the rate of vapour generation is usually assumed to depend on transient conduction in the liquid surrounding each bubble (Ardron, 1978). The effects of neighbouring bubbles are neglected, and this ‘thermal boundary layer’ method is only valid for very low qualities (Wallis, 1980). Hence, the increase in realism gained by introducing bubble nucleation is offset by uncertainties in the mechanisms involved.

Models that predict the onset of flashing usually contain adjustable parameters such as the nucleation site density and the degree of superheat at flashing inception. These parameters have not been sufficiently investigated, and in most of the models (Edwards and O’Brien, 1970; Ferch, 1979; Winters and Merte, 1979), the arbitrary specification of either the initial bubble size or the number density of the bubbles is necessary (Pinhasi et al., 2005). Practically speaking, in industrial systems, homogeneous nucleation is unlikely, and a heterogeneous nucleation factor must be introduced and provided a priori (Deligiannis and Cleaver, 1996). The values of such parameters are chosen to fit experimental data rather than represent physical characteristics.

Wallis (1980) states that “*if any improvement to this situation is to be achieved we need a concerted effort to measure independently the various components of the model*

such as bubble size, interfacial area and heat transfer, number of nuclei of a given size, and evolve a theory that is compatible with this detailed evidence.” Wallis believes that the sophistication of a theoretical analysis should match the degree to which the physical phenomena can be specified. Nucleation characteristics and upstream flow conditions in industrial systems are not usually sufficiently well known to allow for very precise definition of the problem. For LOCA analysis for instance, break location and geometry can vary significantly. Small changes in break location and geometry, however, can produce changes in the critical flow rate that are comparable in magnitude to the improvement in accuracy gained from using the more sophisticated theories rather than the simpler ones.

2.4 Numerical Two-Phase Blow-Down Modelling

Due to the extent of the complexity involved in analysing the physical phenomena associated with nuclear power plant accident events, it has effectively become compulsory to employ computer codes for such analysis (Winton, 1974). For a postulated LOCA, the calculation of the critical mass discharge that initiates from the break location, as well as the local pressure following rapid depressurisation, is industrially evaluated through computer codes that contain simple physical critical flow models and correlations (Isbin, 1980). Reliable and elaborate system codes such as RELAP-5, TRACE and SATAN-VI have evolved over the years and are commonly used in the analysis of primary circuit and component system transients.

The pressure circuit is usually represented by a number of control volumes, and the conditions are linked by one-dimensional thermal equilibrium conservation equations (Hall and Hall, 1979). These computational codes usually model a very general thermal-hydraulic network without including the detailed local behaviour within each of the segments comprising the system (Kalra, 1984). Confidence in the codes is developed

through comparison of the numerical predictions with wide ranges of experimental data, and for over 30 years, computational methods have complemented results from scaled model experiments and prototypic tests for reactor systems safety analysis and licensing purposes (Organisation for Economic Co-operation and Development, 2008). The one-dimensional two-fluid modelling codes have generally satisfied the minimum needs of the nuclear energy technology, and the success of such codes is usually the result of empirical local adjustments that allow proper representation of certain limited cases (Downar-Zapolski et al., 1996).

The application of Computational Fluid Dynamics (CFD) codes in nuclear reactor safety analysis is not as well established. Incorporation of CFD methods in various safety assessments is attracting increasing interest however (Scheuerer et al., 2005). CFD codes can potentially include three-dimensional flow effects, which are not properly predicted by one-dimensional system codes. For the time being, CFD codes are difficult to use in the evaluation of nuclear accident events due to the huge degree of sophistication inherent to transient two-phase phenomena.

Bhasin et al. (1993) numerically studied the effects of a MSLB on steam generator internal components of a CANDU reactor. They evaluated the possible release of radioactivity due to rapidly varying pressure and drag forces. The loading analysis was performed with 100% SLB at 0% power using a simplified dynamic load factor method. This method was judged to be conservative compared to other more realistic methods such as modal superposition or direct time integration. It was concluded that all components were safe as per the American Society of Mechanical Engineers (ASME) allowable limits. Leakage due to MSLB was ruled out, as the maximum primary stress in the U-tubes was found to be 1,900 psi, which is negligible compared to the allowable stress levels of about 75,000 psi. The maximum drag force per tube was calculated as 21.9 lbs per tube for the MSLB transient.

Sauvé et al. (1996) studied tubes with postulated initial flaws under transient blow-down conditions following a 100% MSLB using a fatigue crack growth assessment

based on the tube force and moment time histories obtained from transient vibration analysis. The work was performed as part of the justification for continued operation of Bruce “B” tubes with fret scars under postulated blow-down conditions. The effect of the transient and flow-induced vibration on the tube response was considered in detail. First, a thermal-hydraulic analysis was carried out to estimate transient conditions that exist in the U-bend. The forcing functions were then derived and applied to a non-linear time domain analysis. A fatigue evaluation followed, which was concluded by the tube crack growth assessment. The forcing functions included steady-state turbulent excitation as well as instantaneous transient blow-down forces and corresponding fluid-elastic force components. The computer code SOPHT was used for the thermal-hydraulic analysis.

A two second duration of steady-state turbulent excitation was implemented prior to activating the blow-down transient in order to establish steady-state conditions. The pressure drop was considered by evaluating the forces on the tube at each instant of the blow-down transient based on the fluid properties. As such, the problem was reduced to the calculation of the instantaneous forces in the tubes and estimating the tube responses from the equations of motion following Equation (7):

$$\bar{F}^t = 0.5\rho^t d C_D^t \left[|u^t| u^t \right] \quad (7)$$

where F is the force per unit length of tube, d is the tube diameter, C_D is the coefficient dependent on Reynolds number, and u is the velocity of the fluid. In calculating the coefficient C_D , the quality of the fluid is used to estimate the kinematic viscosity from which the Reynolds number is obtained. Using correlations of the coefficient with Reynolds Number, the coefficient can be evaluated at a certain point in time. Once the time-dependent forces are evaluated, the response of the tubes under blow-down conditions is obtained by direct integration of the equations of motion (8):

$$M\ddot{x}^t + C_d\dot{x}^t + F_{int}^t = F_f^t + F_{ext}^t \quad (8)$$

where M is the mass matrix, C_d is the damping matrix, F_{int}^t is the non-linear system force that includes non-linear supports (contact force discontinuities arising from loose

supports including normal impact and friction), F_f is the fluid-elastic force, and F_{ext} is the externally applied force. The gap velocity is found using Equation (9):

$$u^t = \left(\frac{p}{(p-d)} \right) \frac{\dot{m}^t}{\rho^t A} \quad (9)$$

where p is the tube pitch, and m is the mass. The kinematic viscosity, ν , and the Reynolds Number, Re , are found using Equations (10) and (11):

$$\nu^t = \nu_l(1 - \beta^t) + \nu_g \beta^t \quad (10)$$

$$Re = \frac{u^t d}{\nu^t} \quad (11)$$

where β is the vapour quality. Figure 2-10 shows a sample force time history evaluation.

The flow conditions obtained from the one-dimensional blow-down analysis were conservatively applied uniformly to the U-bend. A traditional approach was used to assess the fatigue crack growth rate, which is a linear-elastic fracture mechanics flow model used together with a fatigue crack growth rate model. The evaluation indicated that the tubes met all the fatigue requirements. The final crack depth following a postulated blow-down transient for initial notch depths equivalent to 40% and 60% of the tube wall thickness was below the allowable crack depth of 80%.

Krotiuk (2004) performed detailed thermal-hydraulic calculations and sensitivity studies using three-dimensional hydraulic components of TRAC-M to assess a generic Westinghouse PWR steam generator tube loading during a MSLB. Only the primary system tube wall was modelled as a heat transfer structure, and heat transfer effects were neglected. The model divides the steam generator into one-dimensional flow paths and cannot predict radial flow conditions around the primary system tubing. The predicted loadings were used in structural assessment of the primary tubes to determine the potential for increased tube leakage. It was concluded through computer code simulations that a guillotine rupture of a steam-line at hot standby conditions produces the largest forces. The study revealed that the short-term thermal-hydraulic and acoustic effects

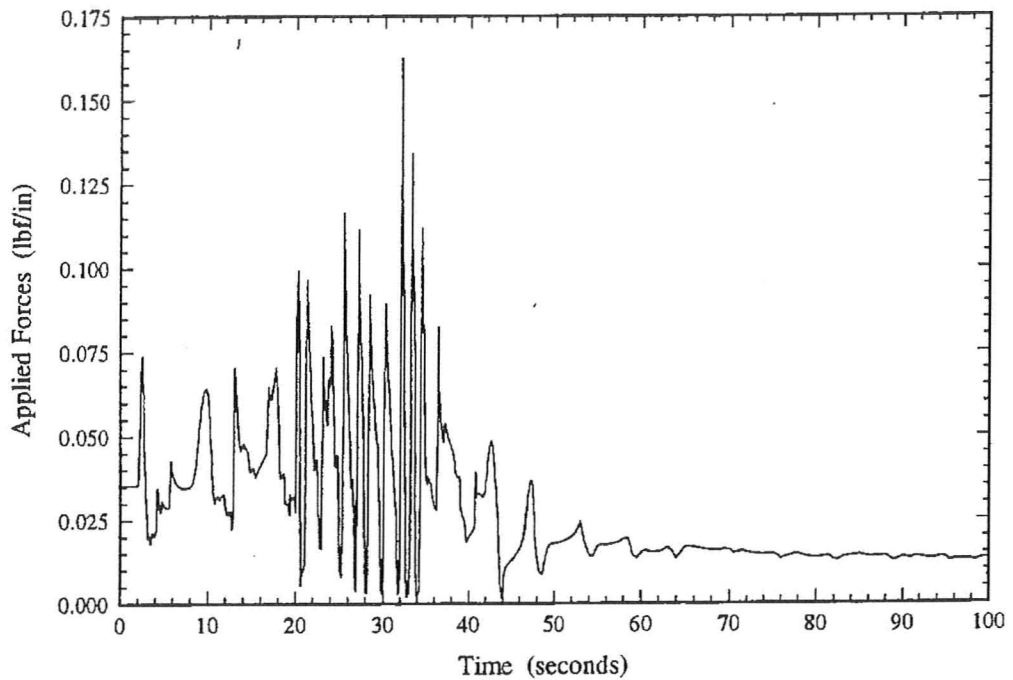


Figure 2-10. Steam Generator Transient Analysis (Sauvé et al., 1996)

produced the primary loads during the first few seconds following the break. Flow-induced vibration loading due to the quasi-steady flow present following the initial short-term effects was determined to be smaller than the short-term loading. Consequently, no long-term loading analysis was performed. At the U-bend, the primary tubing peak pressure differential obtained using TRAC-M was 1.05 psi.

Majumdar et al. (2007) conducted sensitivity studies on the failure of flawed steam generator tubes in a Westinghouse steam generator during MSLB using TRAC-M. The objective was to evaluate the assertion that dynamic loads induced on the tubes could lead to crack growth and increased leakage or tube rupture. The axial loads were calculated from pressure drop analysis, and the calculations were compared with similar previous analyses. Comparisons with RELAP5 calculations displayed similar results, although the RELAP5 predictions were slightly larger. The TRAC-M pressure drop predictions were multiplied by an uncertainty factor of 1.5. The effect of tube bending on burst pressure was shown to be negligible, and analysis of the tubes under transverse

pressure loading showed inertia effects to be negligible for the calculated rise time of the pressure pulse. The study also revealed that the dynamic loads associated with a MSLB have little impact on steam generator tube integrity unless extensive circumferential cracking is present.

2.5 Overview of the Current State of Knowledge

Although one-dimensional formulations restrict the use of system codes in simulations of complex geometries, the physical models are relatively well understood, and can be reliably implemented provided that they are applied within the specified ranges of validity (Organisation for Economic Co-operation and Development, 2008). The general trend is to continue with such approaches, and operate within the geometrical limitations. There appears to be a trade-off between system codes and CFD models. System codes contain limited geometrical capabilities and numerical errors that are sometimes uncontrollable, but they incorporate sophisticated and consistent physical models, which are often run in real-time for reactor transients. Geometric complexity is no real issue for CFD codes, with the modern numerical schemes available, however, for two-phase applications, the physical models are in need of further development. During the initial blow-down stages, before flashing of the liquid begins, single-phase CFD models have been used to provide behaviour predictions. Once flashing starts happening, a proper two-phase model is absolutely essential for the description of the decompression process, due to the predominance of non-equilibrium two-phase effects.

The common approach to practical licensing issues from a regulatory perspective has been the use of simplified modelling, coupled with conservatism to account for the unknown factors, such that sufficient safety margins are guaranteed (Organisation for Economic Co-operation and Development, 2008). The degree of conservatism required to cover up for the lack of physical understanding is a key issue that needs to be determined.

Information is usually obtained from laboratory experiments, but extrapolation to full-scale applications is not a straightforward task. Furthermore, the experiments themselves usually contain simplifications. Currently, the only way to increase conservatism is to increase the safety margins, which places bigger constraints on plant effectiveness.

Chapter 3 – Experimental Rig Design

In order to carry out the steam generator blow-down simulations, an experimental rig was designed and built. A computer rendering of the design can be seen in Figure 3-1. The basic concept of the design is to have a static fluid reservoir containing liquid R-134a at the appropriate temperature and pressure conditions, a sectional model test section including a bundle of steam generator tubes, a pressure control device to suddenly release the pressure on the fluid reservoir, and a vacuum tank of sufficient volume that the blow-down transient is not controlled by rising downstream pressure. The pressure upstream and downstream of the pressure release device is monitored, as are the temperatures and the load on the tube bundle during the transient. Sight glasses upstream and downstream of the test section permit visual observation of the blow-down event as well as its recording using high-speed imaging techniques.

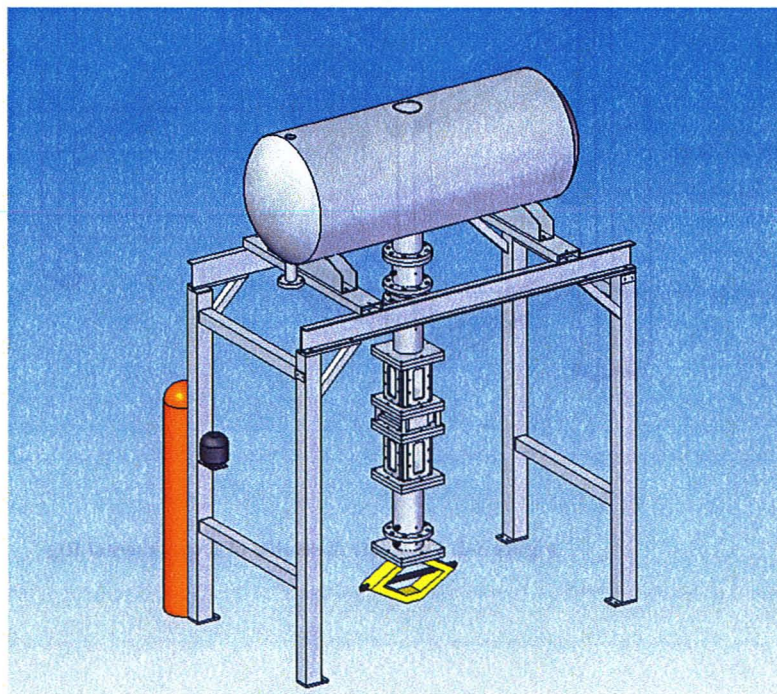


Figure 3-1. Experimental Rig Design Concept

Figure 3-2 provides a pictorial view of the overall test facility with each of the significant components labelled. An assembly drawing is shown in Figure 3-3 and a photograph of the assembly is shown in Figure 3-4. Since US suppliers had to be used for some specialised components and others used standard US components (such as structural steel), most of the dimensions in the text and drawings are in Imperial rather than Metric units.

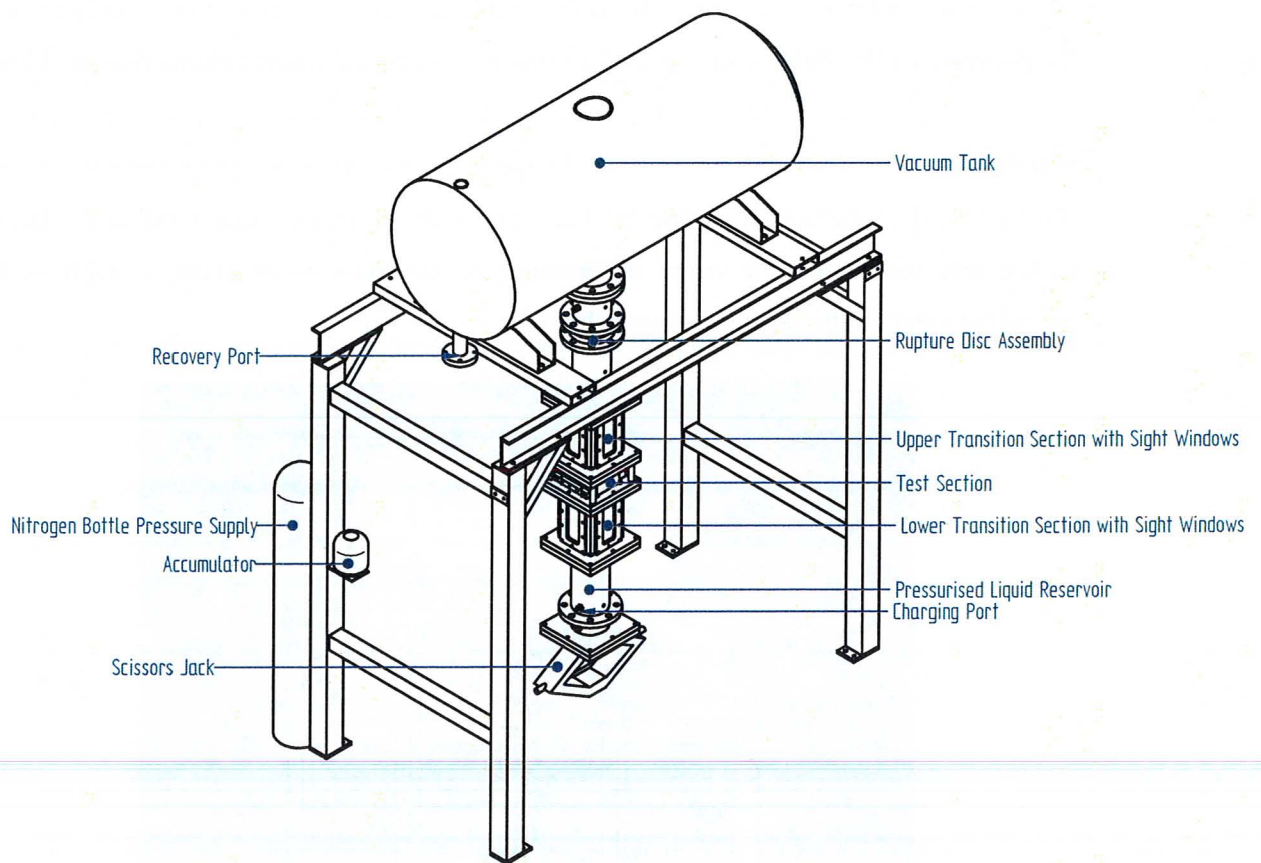


Figure 3-2. Complete Assembly of Experimental Rig

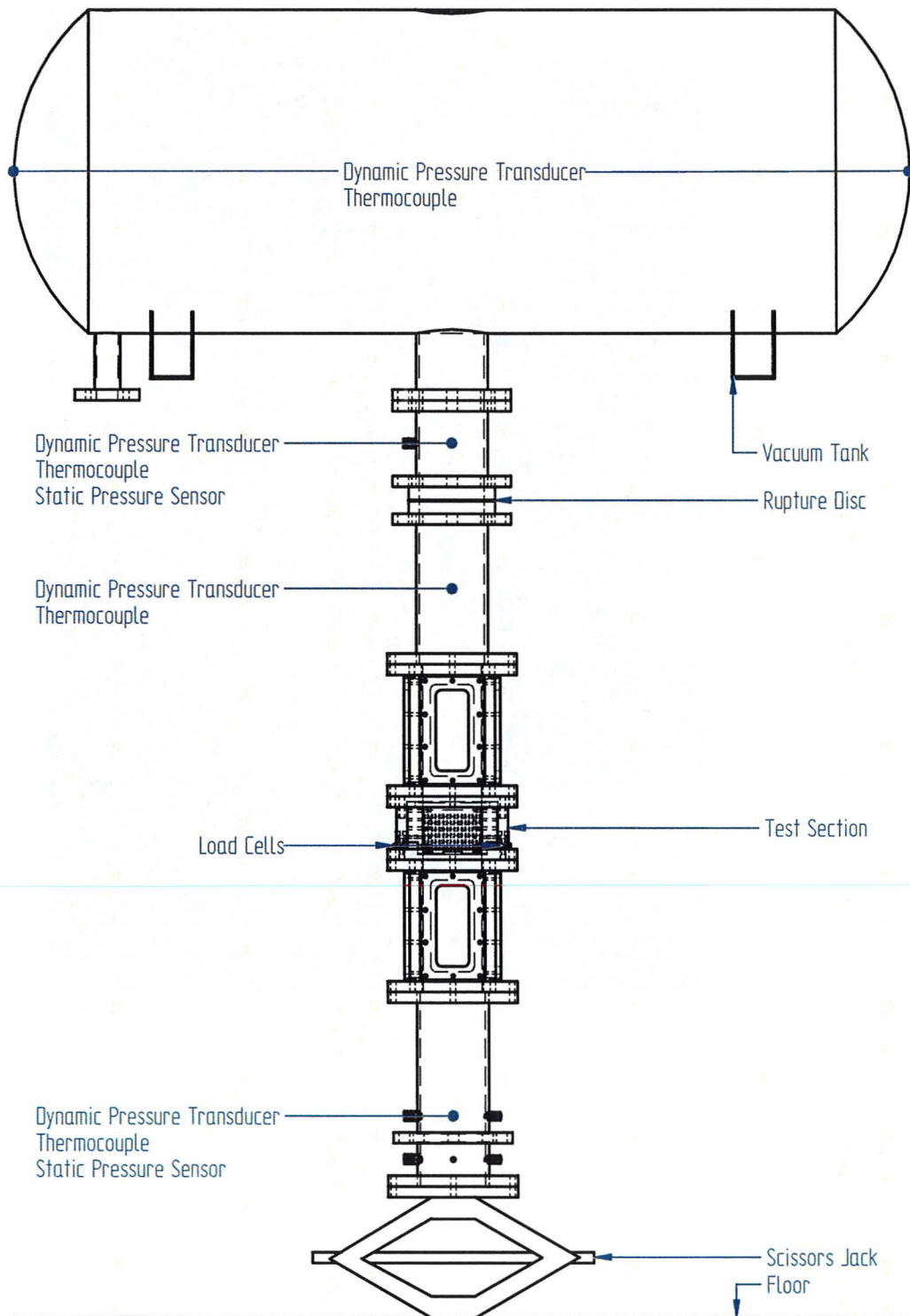


Figure 3-3. Blow-Down Rig Assembly Drawing



Figure 3-4. Photograph of the Experimental Rig Assembly

3.1 Working Fluid

Experiments with water at typical high-temperature, high-pressure nuclear reactor conditions require large-scale facilities, high electrical power, and high testing costs, due

to the large magnitudes of latent heat and critical pressure (Akhtar et al., 2006). It is very difficult to satisfy such requirements in an ordinary test laboratory. Modelling fluids that have lower boiling points and latent heat of vaporisation compared to water, such as Freon fluids CFC-11, CFC-12, and HCFC-22, are often used in thermal-hydraulic analysis experiments in order to reduce the associated costs and technical difficulties (Leung and Dimayuga, 2007; Chun et al., 2007). However, the release of Freon CFCs and HCFCs to the atmosphere poses environmental issues as it contributes towards ozone depletion and global warming effects. Therefore, CFC-11 and -12 have gradually been phased out and replaced by the more environmentally friendly HCFC-123 and HFC-134a. In this study, refrigerant-134a was used as the working fluid in order to keep the costs down and simplify the required experimental facility.

Tain et al. (1995) systematically studied factors limiting fluid-to-fluid scaling accuracy and quantified these factors for modelling fluids such that a range of application for the scaling technique could be defined. In fluid-to-fluid modelling, the geometric, thermodynamic and hydrodynamic similarities should all be satisfied for both fluids (Chun et al., 2007). Akhtar et al. (2006) determined that R-134a is a good modelling fluid to scale high-pressure steam-water flows except for very low flow conditions. The loading on the steam generator tubes during a blow-down is basically a fluid drag force and is expected to scale with the dynamic head. Thus, fluid density and velocity are important scaling parameters and, in two-phase flows, the ratio of liquid-to-vapour densities is important. The liquid-to-vapour density ratio can be matched by setting the pressure of the working fluid. R-134a has a density ratio of about 35 at 26 °C and a pressure of 690 kPa, which is very close to that of steam-water at 257 °C and 4.5 MPa boiler pressure. For the sectional model tube bundle, the tube diameter and pitch ratio are also important in partially determining the bubble size. The model used in these experiments has essentially full sized tubes with the full-scale pitch ratio, in compliance with the requirement for geometric similarity. Thus R-134a was chosen as a reasonable operating fluid for these blow-down simulation experiments.

3.2 Pressurised Liquid Reservoir

The pressurised liquid reservoir is made from standard 6-inch Schedule 40 pipes and stress relieved, blanchard-ground steel flanges. The total height is 18 inches with a blanking flange dividing the pipe into 4-inch and 13-inch long sections. In this way, the capacity of the liquid reservoir can be changed by about 4.6 litres by simply turning the reservoir over. A photograph of the reservoir is shown in Figure 3-5 and an engineering drawing is shown in Figure 3-6. The steel pipes (items 3 and 5 in Figure 3-6) were chamfered and welded to the custom designed steel end flanges and the blank pipe flange in between (items 2 and 4 respectively in Figure 3-6). Circular 0.125-inch deep grooves matching the steel pipe wall thickness were machined into the blank round flange on both sides in order to secure the pipes before welding. The end flanges are square to connect with the transition sections and the bottom blanking flange (item 1 in Figure 3-6). Mating surfaces on all flanges were machined flat to 0.001 inches, and neoprene gaskets were placed in between for sealing. Mounting holes were machined in both the small and large volume sections to accommodate for pressure sensors and thermocouples, as well as R-134a charging ports. For the static pressure sensor and charging ports, the appropriate hex couplings were welded into the proper locations (items 6 and 7 in Figure 3-6), whereas the thermocouple and dynamic pressure sensor ports were drilled and tapped directly into the pipe walls (not shown in Figure 3-5 as they were yet to be machined).

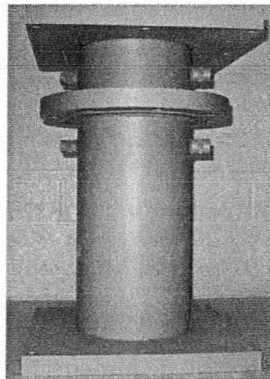


Figure 3-5. Photograph of Pressurised Liquid Reservoir

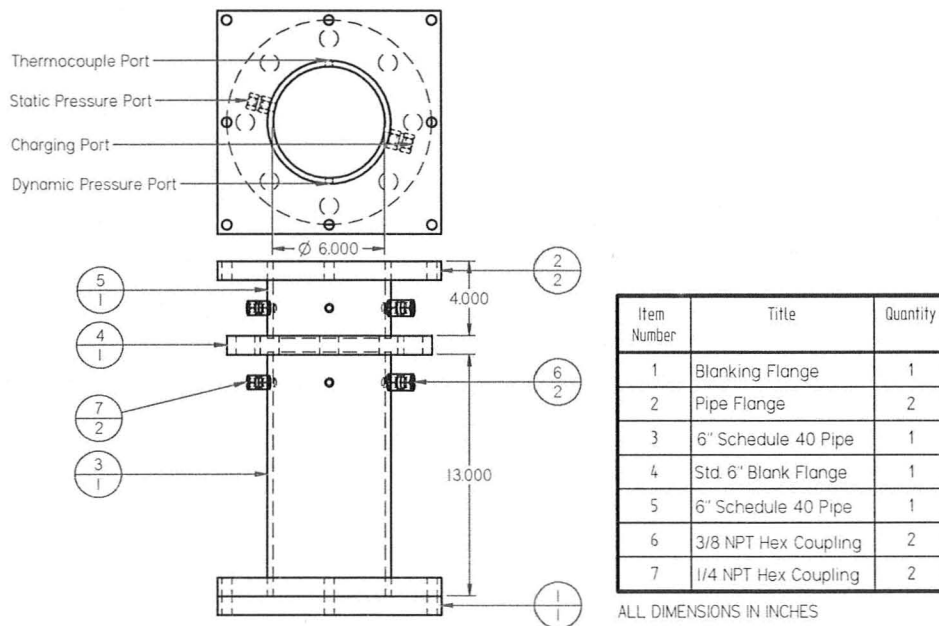


Figure 3-6. Pressurised Liquid Reservoir Engineering Drawing

3.3 Transition Sections with Sight Glasses

The transition sections above and below the test section are identical. The inside dimension of these sections is 5.4 inches square which gives the same cross-sectional area as the 6-inch standard pipe. A photograph of the transition sections is shown in Figure 3-7 and an engineering drawing is shown in Figure 3-8. Figure 3-9 displays all the custom designed steel components of the transition section, as well as an assembly drawing illustrating the clamping arrangement. The steel transition flanges (item 1 in Figure 3-9) have the same bolthole pattern as the pressurised liquid reservoir, the test section, and the pressure relief section flanges. The inside square hole was rounded so as to create a press fit around the side plates. The side plates were designed in two different shapes, identified as large and small side plates (items 2 and 3 in Figure 3-9). Both designs have identical holes that accommodate the glass windows and bolts for the clamping plates (items 4 and 5 respectively in Figure 3-9). The difference between the

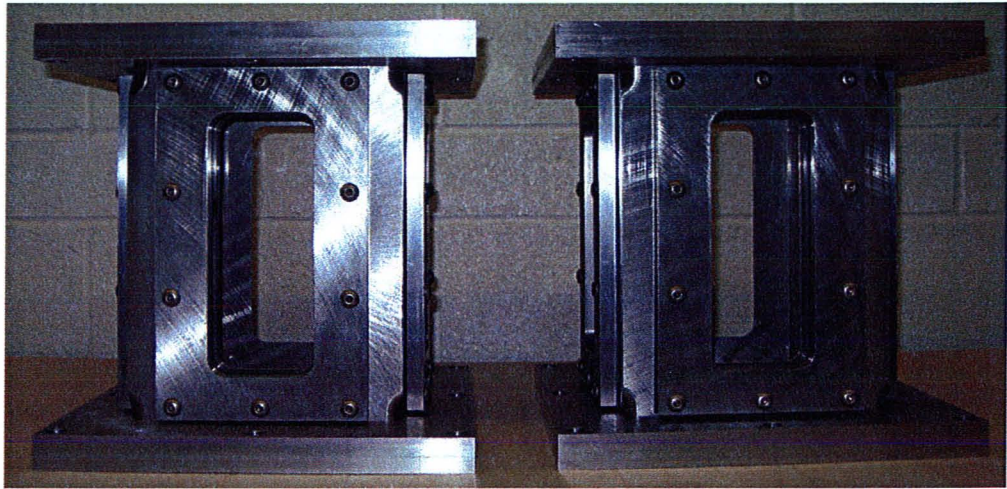


Figure 3-7. Photograph of Transition Sections

two side plates is that the large plates are wider, rounded at the outside corners, and slightly recessed along the inner surface that is in contact with the small plates. The purpose of the recess was to locate the small side plates such that a perfectly square flow area along the height of the transition section is produced by welding the plates to each other and to the top and bottom transition flanges, as shown in Figure 3-8 and Figure 3-9.

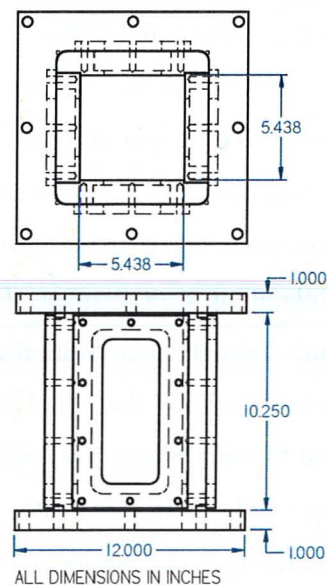


Figure 3-8. Transition Section Engineering Drawing

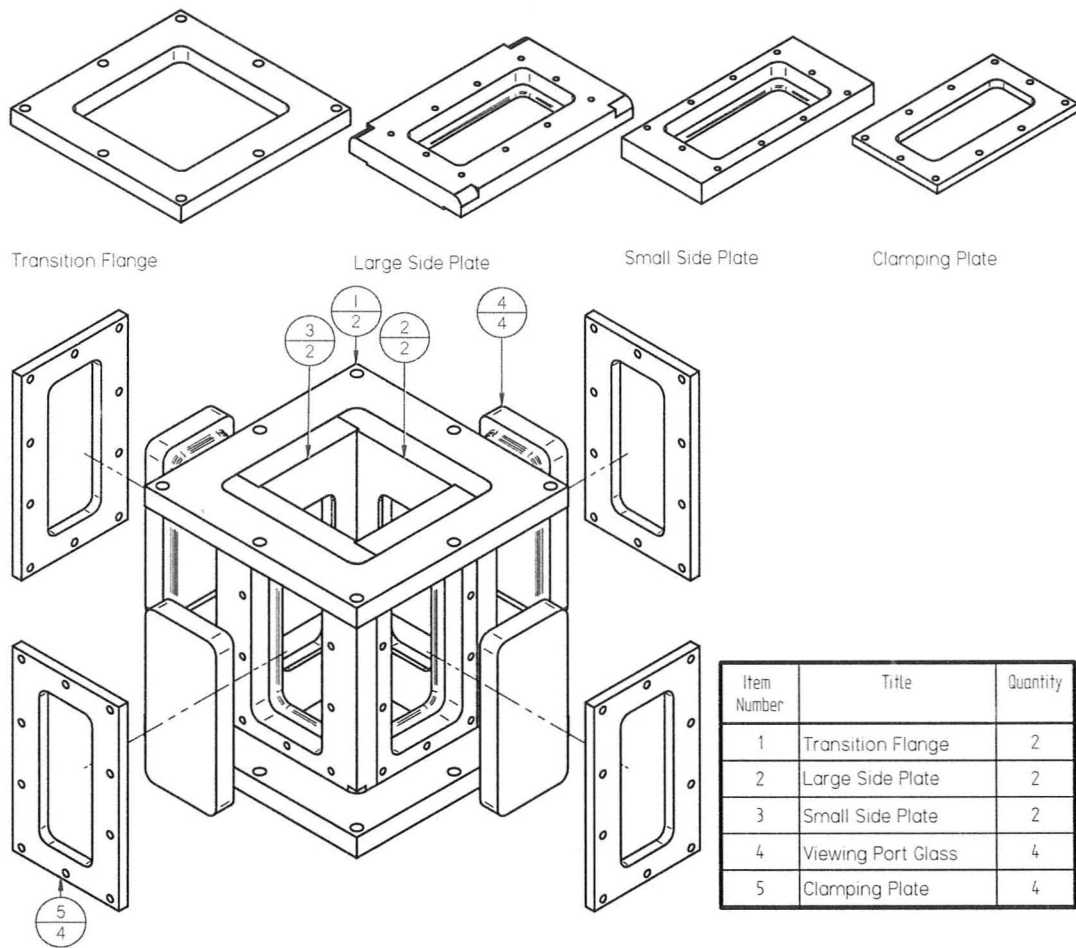


Figure 3-9. Transition Section Clamping Arrangement

The side plates are 1.25 inches thick, and are each fitted with a 1.25-inch thick tempered quartz glass window with a sighting area of 3×7.5 inches. An engineering drawing of the viewing port glasses is shown in Figure 3-10. The sighting area protrusion fits into the frame of the side plate such that the surface of the glass is flush with the inside surface of the side plates, producing no change in the flow area. The shoulder of each window is intimately fixed against the ledge of the enclosing side plate, and the larger glass surface is flush with the outside surface of the side plate. The windows are secured in place by bolting the flat clamping plates onto the side plates. The inside hole

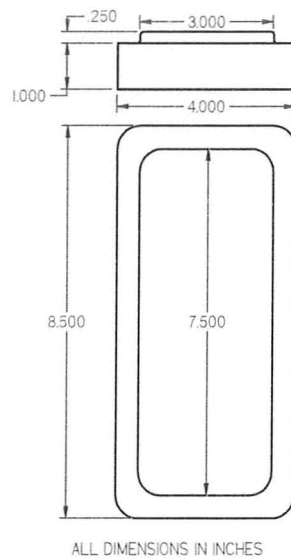


Figure 3-10. Viewing Port Glass Engineering Drawing

of the clamping plate has the same dimensions as the sighting area of the viewing glasses. There are 8 windows in total, each of which is sealed with neoprene gaskets between the windows and side plates and between the windows and clamping plates.

The sight glasses were special orders produced by Specialty Glass Products of Willow Grove, PA, USA. A couple of the delivered glasses contained visible manufacturing defects; small spalls in the corners. Since there is a small risk that cracks might propagate from these locations under pressure, it was decided that a safety shield should be constructed, in order to contain any shards of glass projected in the unlikely event of cracking and complete failure of the glasses. The frame of the shield consists of structural steel tubing, and the 0.25-inch thick sheets were manufactured from a fully transparent Lexan brand of polycarbonate resin thermoplastic. Lexan is known for its remarkable toughness and bullet resistant properties. A schematic of the safety shield design is shown in Figure 3-11.

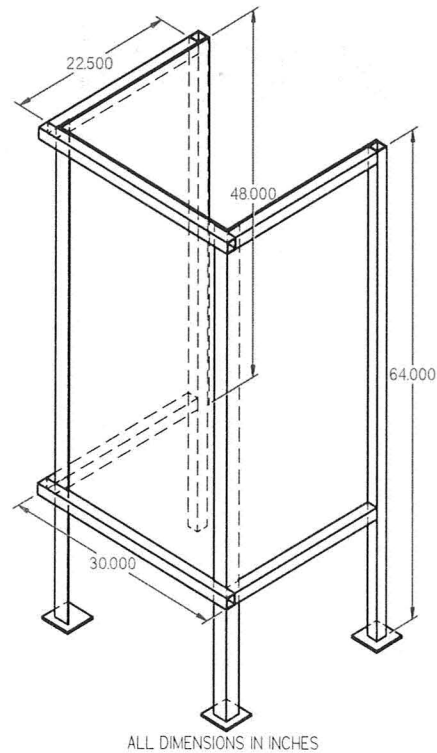


Figure 3-11. Safety Shield

3.4 Test Section

The test section contains a tube bundle consisting of 6 rows of 0.5-inch diameter tubes in a normal triangular geometry with a pitch ratio of 1.36. The tube array geometry, pitch ratio and tube diameter are similar to those used in CANDU steam generators. It was necessary to ensure that the load cells, which measure the dynamic load on the tube bundle during the blow-down, were sealed from the working fluid, since the manufacturer would not guarantee their instrument performance and durability when submerged in or exposed to any liquid. This condition posed a significant challenge from a design perspective, and the constructed test section is the product of several design



Figure 3-12. Photograph of Test Section

iterations and intricate machining work. A photograph of the test section is shown in Figure 3-12, and an illustration of the assembly configuration is provided in Figure 3-13.

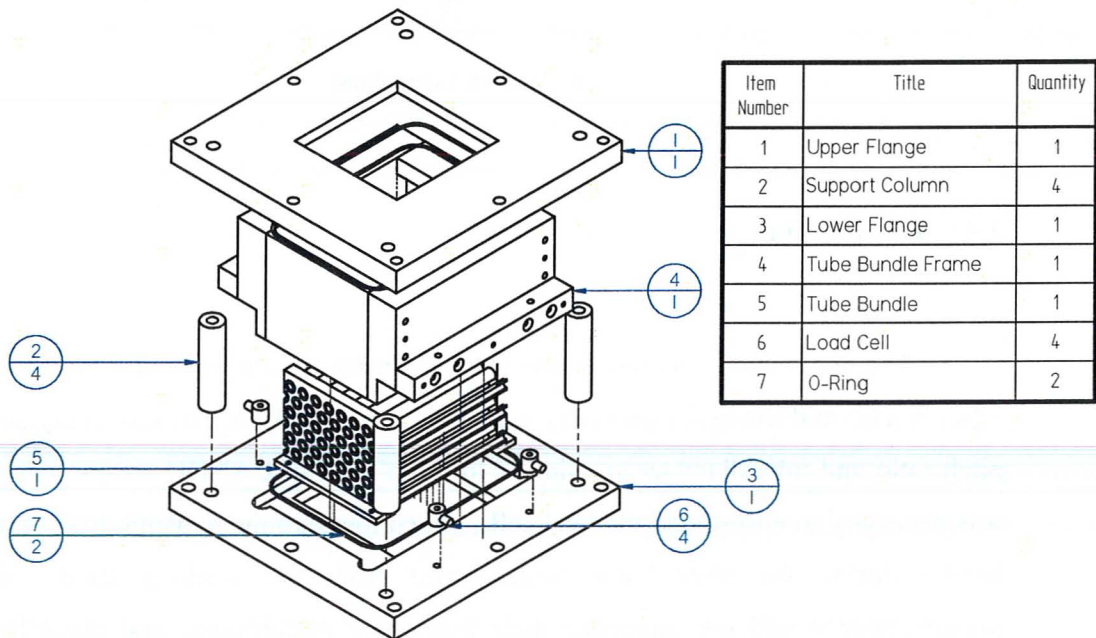


Figure 3-13. Test Section Assembly Configuration

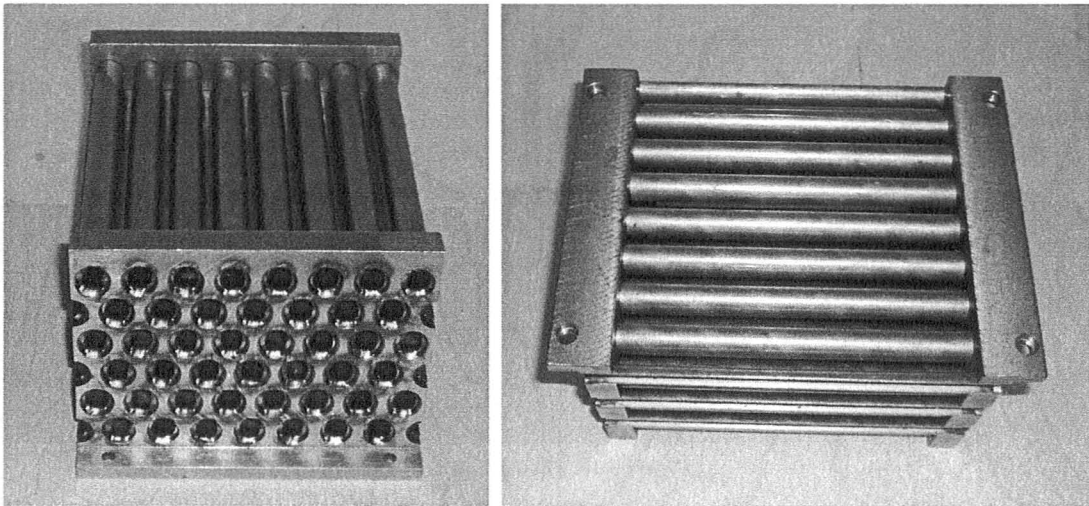


Figure 3-14. Photographs of Tube Bundle

The tube bundle (item 5 in Figure 3-13) is securely bolted into the tube bundle frame (item 4 in Figure 3-13), which is supported by four load cells (item 6 in Figure 3-13). Photographs of the tube bundle and the tube bundle frame are displayed in Figure 3-14 and Figure 3-15, and engineering drawings are provided in Figure 3-16 and Figure 3-17 respectively. The tube bundle consists of two drilled steel walls (item 1 in Figure 3-16), hydraulic steel tubing modelling CANDU steam generator tubes (item 2 in Figure 3-16), and half tubes of the same diameter (item 3 in Figure 3-16) that maintain the correct flow path area along the walls. All of the tubes were welded in place, forming a single tube bundle unit that is bolted into the tube bundle frame, as shown in Figure 3-18. The frame consists of a pair of short and long side walls (items 1 and 2 respectively in Figure 3-17), and a load cell block (item 3 in Figure 3-17) on either side. All mating surfaces were machined flat, and a sealed flow path area was formed by attaching the individual parts to each other using a set of bolts and dowel pins for positioning accuracy.

The upper and lower flanges (items 1 and 3 respectively in Figure 3-13) are rigidly held apart by four circular columns (item 2 in Figure 3-13), and the tube bundle frame effectively ‘floats’ in between the flanges, the surface area of the compressed O-rings (item 7 in Figure 3-13) being the only location of contact on either side. Photographs of the flanges are shown in Figure 3-19. The arcs at the corners of the

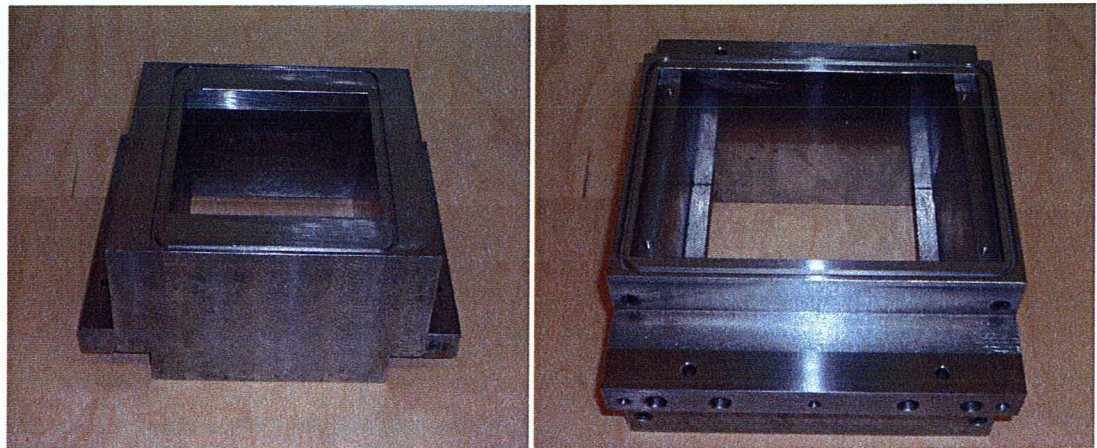


Figure 3-15. Photographs of Tube Bundle Frame

recesses were necessary in order to create the rectangular profiles that accurately position the tube bundle frame inside the flanges. The O-ring grooves were machined onto the top and bottom surfaces of the tube bundle frame after it was assembled. The load cells are mounted onto the lower flange and attached to the test section frame at the four lower corners, using finely threaded bolts. The test section casing was designed so that the load cells are sealed from the R-134a using the O-rings.

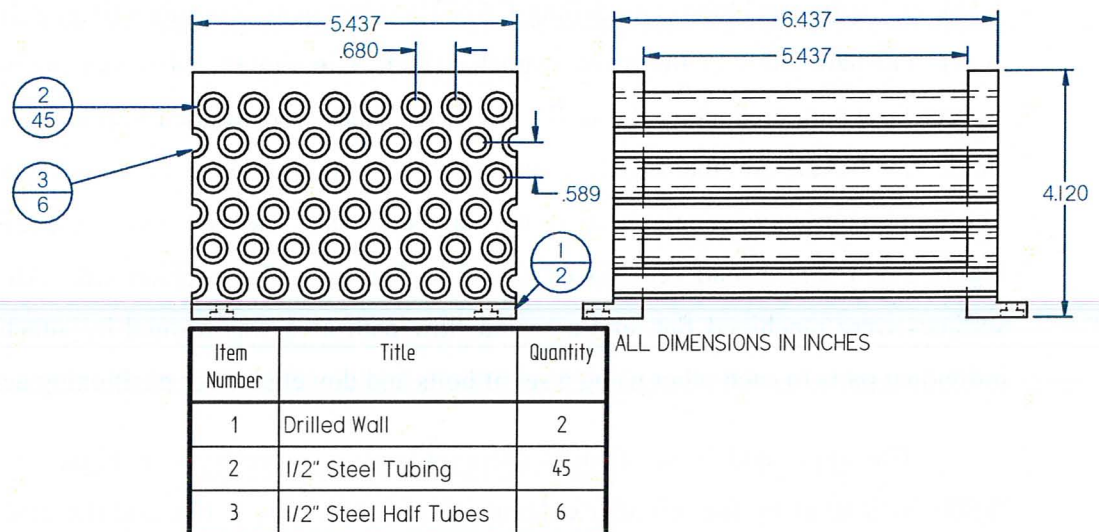
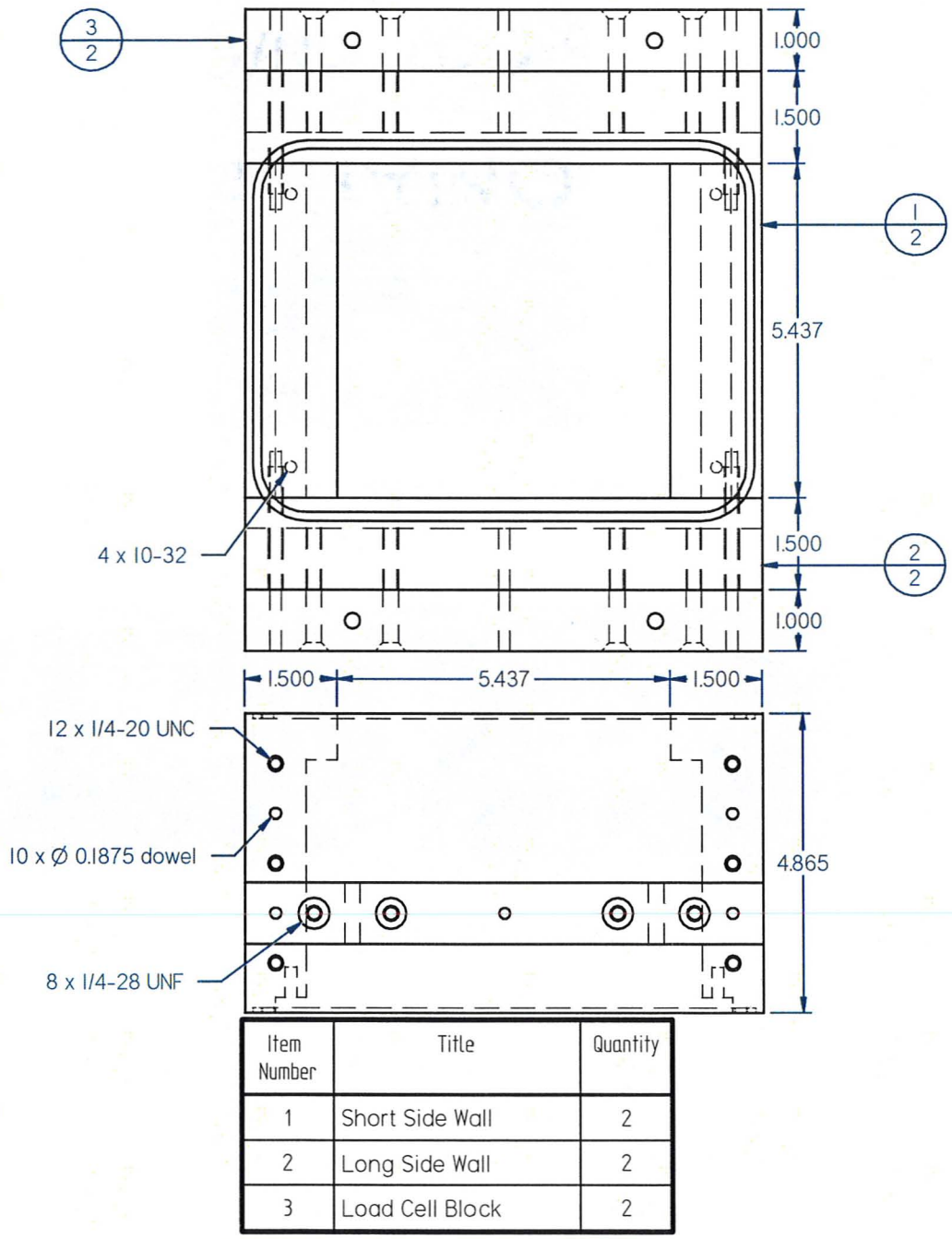


Figure 3-16. Tube Bundle Engineering Drawing



ALL DIMENSIONS IN INCHES

Figure 3-17. Tube Bundle Frame Engineering Drawing

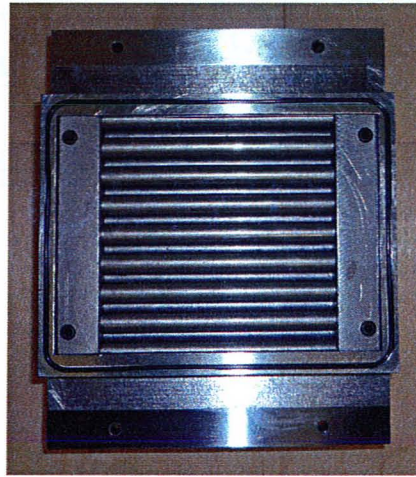


Figure 3-18. Photograph of Test Section Tube Bundle Assembly Including O-Ring

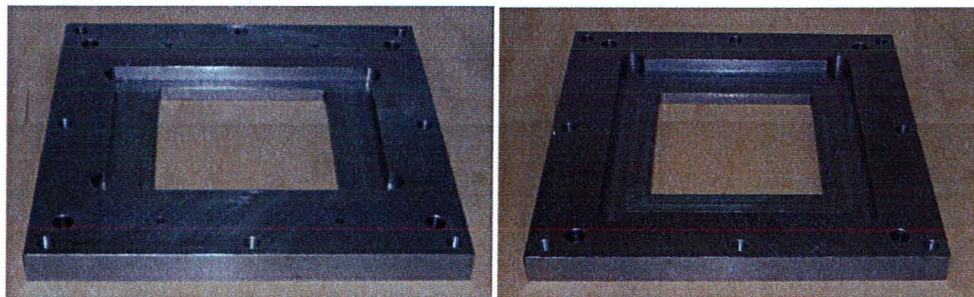


Figure 3-19. Photographs of Test Section Flanges

Figure 3-20 depicts a schematic of the load on the tube bundle and the transfer of the load to the load cells, including the O-ring design and clearances. Basically, the design transfers the entire blow-down drag loading on the tube bundle to the force sensors while sealing the latter from contact with the R-134a. The basis of the O-ring design was that it should be compatible with R-134a and fit smoothly within the walls on the bottom surface of the tube bundle frame. This led to the selection of Neoprene O-rings number 2-173, with a nominal cross-section of $3/32$ inches and internal diameter of 8.5 inches. The actual cross-section of the O-ring is specified as 0.103 ± 0.003 inches.

With the groove width machined to 0.140 inches, and the gland depth machined to 0.081 inches, a clearance of 0.005 inches is needed in order to provide the 0.017 inches squeeze for the O-ring to seal effectively. In order to achieve this clearance, the support columns were machined to a length of 3.875 inches. Given that the flange recesses are both 0.500 inches deep, the columns maintain the top and bottom inside flange surfaces at 4.875 inches apart, 0.010 inches greater than the height of the tube bundle frame, as illustrated in Figure 3-20. Manufacturing tolerances dictated that the actual dimensions deviated from the design dimensions by a few thousandths of an inch, and the necessary corrective measures were taken to ensure overall functionality of the design.

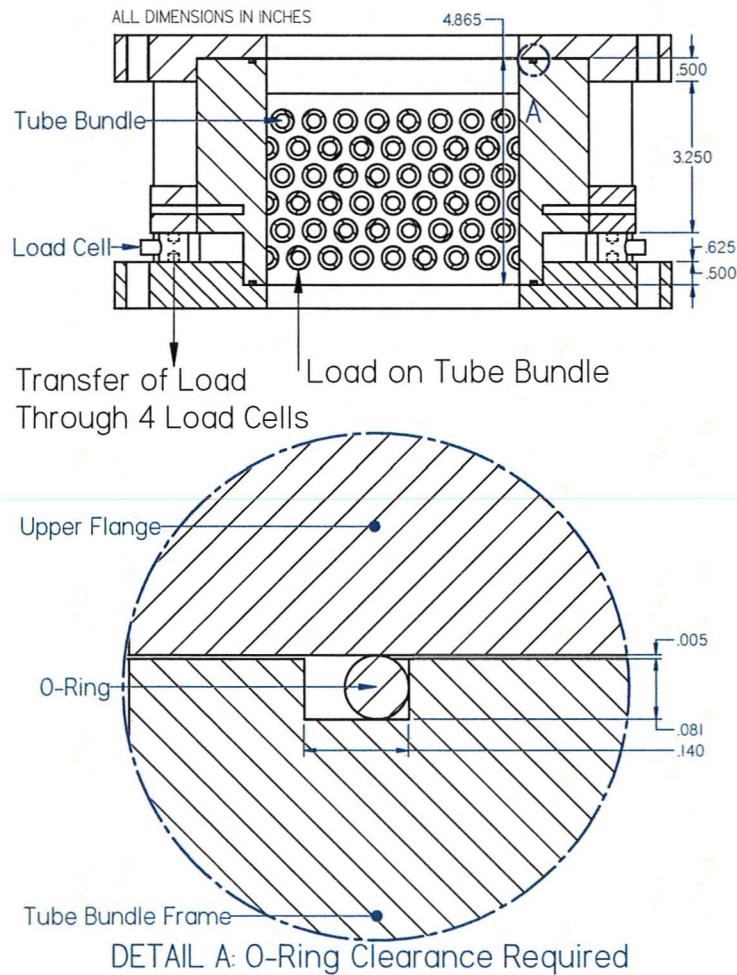


Figure 3-20. Schematic of Tube Bundle Loading Design

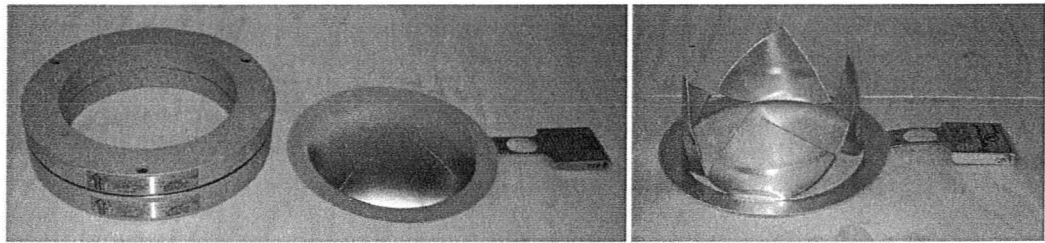


Figure 3-21. Photographs of Rupture Disc Assembly

3.5 Pressure Relief Section

The device used for suddenly releasing the reservoir pressure to create the simulated blow-down is clearly a very important part of the design. The design criteria were that the flow area should be as close as possible to that of the 6-inch diameter pipe serving the device, that the pressure difference across the device at which pressure release occurs should be controllable, and that the device should go from closed to fully open in as short a time as possible. After much deliberation, it was decided that a rupture disc assembly (model 6" Poly-SD) supplied by Fike Canada Inc. was the best choice. Aluminium rupture discs are available that are set to rupture at various prescribed pressure differences and are non-fragmenting with a predictable opening pattern. The acquired rupture discs are rated at 44.7 psid, 64.7 psid, and 84.7 psid, and will be referred to in this text as the low-pressure, moderate-pressure, and high-pressure rupture discs respectively. The downside of this device is that the replacement of ruptured discs requires opening up the system to atmosphere and, therefore, purging of the entire system after each test. The determining factor however, was the opening time of the order of milliseconds, more than ten times faster than quick opening valves of the same size. Figure 3-21 shows photographs of the rupture disc assembly before and after rupture.

An engineering drawing of the pressure relief section is shown in Figure 3-22. The assembly configuration of the pressure relief section is very similar to that of the

pressurised liquid reservoir. The pipe flange (item 1 in Figure 3-22) is identical to the pipe flange shown in Figure 3-6. The instrumentation ports, including the static pressure sensor hex coupling (item 6 in Figure 3-22), are also identical to those described for the pressurised liquid reservoir. The rupture disc holder (item 4 in Figure 3-22) is fixed between standard 6-inch flanges (item 3 in Figure 3-22) welded to standard pipes (items 2 and 5 respectively in Figure 3-22), connecting to the upper transition section and the vacuum tank. Six standard bolts and two threaded rods 11 inches long, placed in opposite holes on the flanges, provide the compression necessary to create the seal between the flanges, gaskets, and rupture disc holder. The rupture discs can be replaced by simply lowering the entire upstream section of the rig and suspending it temporarily on the scissors jack, using the threaded rods for positioning guidance. This eliminates the need to completely disassemble all of the upstream components whenever a rupture disc needs replacement, which is the case after every blow-down experiment.

3.6 Vacuum Tank

The volume of liquid in the reservoir determines to some extent the length of the blow-down transient and also the required volume of the vacuum tank receiver. Calculations and practical considerations such as available space and cost led to the design based on 6-inch standard Schedule 40 pipes and a 240-gallon capacity vacuum tank. The primary design criteria for the vacuum tank receiver were that it should provide an expansion ratio of 60 or greater for liquid refrigerant in the reservoir and that it should withstand dynamic pressures at least equal to the maximum design pressure in the reservoir of about 100 psi. Steel Fab in Oakville, Ontario built the tank to ASME Code with a volume capacity of about 910 litres and design pressures from a vacuum to 200 psi. This provides an adequate expansion ratio of 65:1 for 14 litres of liquid refrigerant in the reservoir and a factor of safety on pressure of greater than 2.

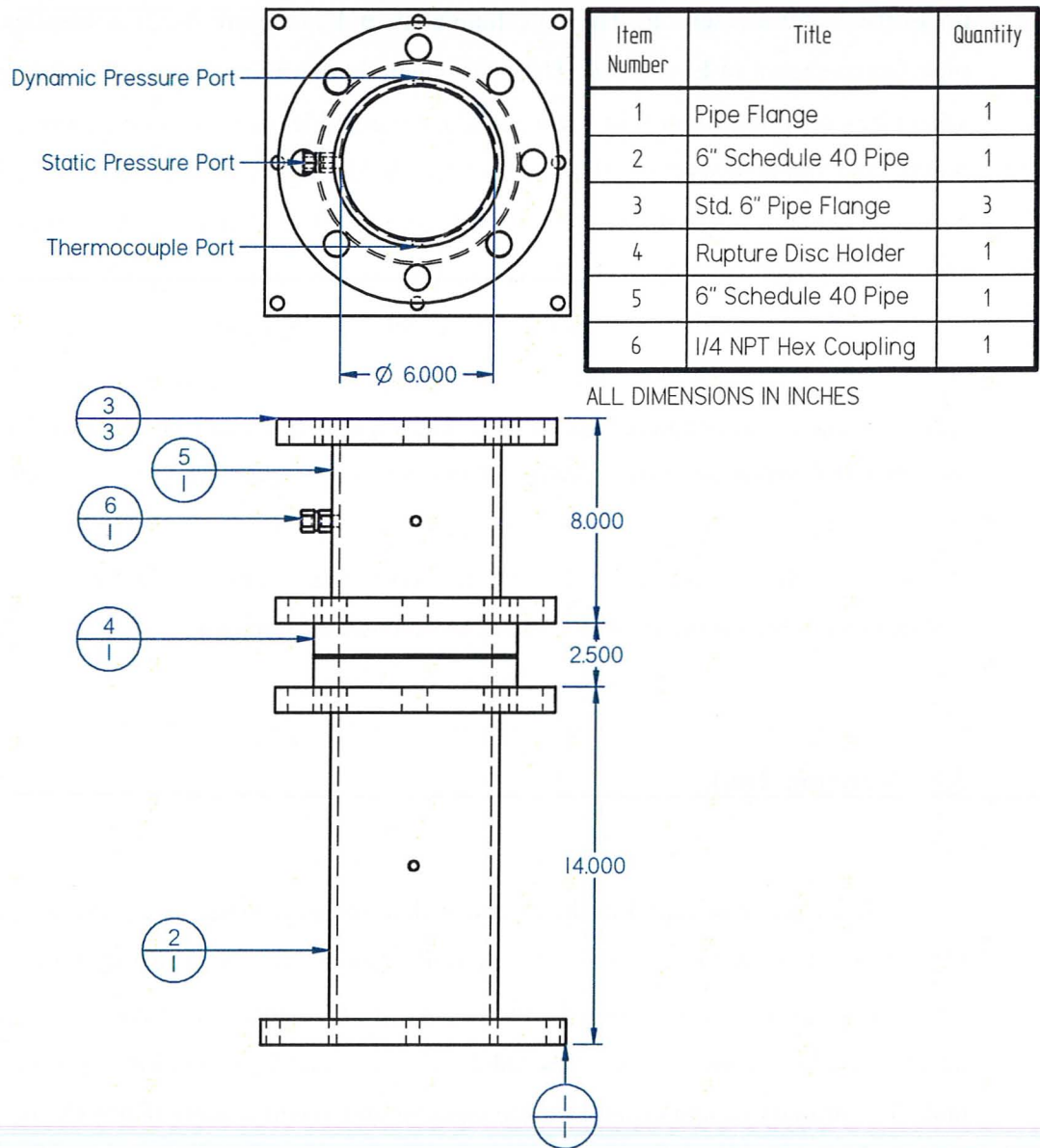


Figure 3-22. Pressure Relief Section Engineering Drawing

Two channelled feet at opposite ends transfer the weight of the tank onto the support frame. A standard 6-inch pipe flange at the bottom of the tank serves as the downstream exit area of the blow-down flow, leading towards the interior of the tank. A standard 2-inch pipe flange at one end of the tank is connected to an R-134a filter and



Figure 3-23. Vacuum Tank Purging Port R-134a Filter

closed off by a 300-psi rated diaphragm line valve. After every blow-down, the R-134a is recovered from here using an oil-less refrigerant recovery system, which extracts R-134a from the experimental rig down to a vacuum. The R-134a is stored in a recovery cylinder and reused in subsequent experiments. A photograph of the purging port is shown in Figure 3-23. Three hydraulic plugs were installed to seal the sides and top of the tank. The hydraulic plugs were all prepared such that a dynamic pressure sensor and thermocouple could be mounted at opposite ends, and a 125-psi pressure relief valve inserted at the top of the tank. A photograph of the thermocouple port is shown in Figure 3-24. A design drawing of the vacuum tank provided by the manufacturer is included in Appendix A.

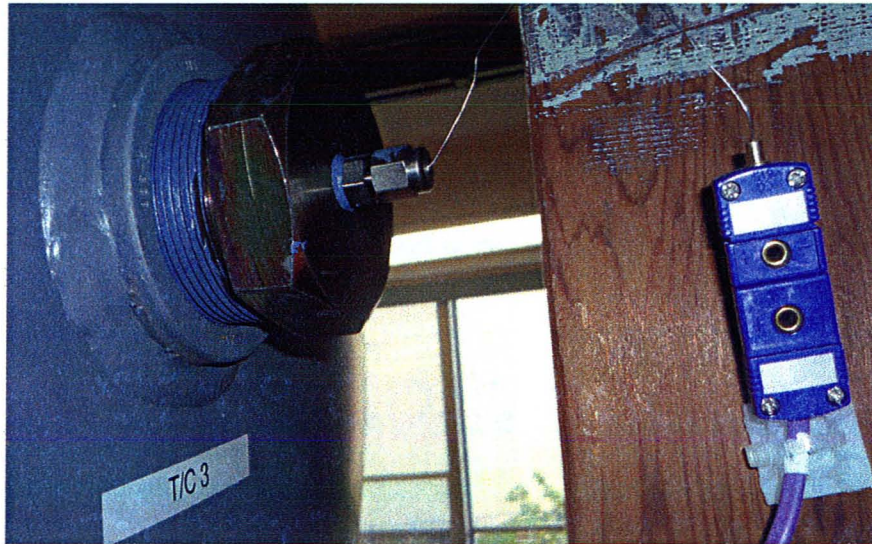


Figure 3-24. Vacuum Tank Thermocouple Port

3.7 Support Frame

The entire blow-down rig is supported on a stiff steel support structure such that the pipe from the vacuum tank to the fluid reservoir is suspended above the floor with sufficient space to insert a scissors jack. The support frame was bolted to the floor and braced to the walls at two locations for increased stiffness. Levelling screws were inserted at the base of each leg to ensure horizontal alignment. The design is comprised mainly of welded structural steel channels and tubing, and a drawing of the frame is provided in Figure 3-25. The scissors jack is loaded against the fluid reservoir such that the vertical transient load from the blow-down is carried largely by the floor rather than by the vacuum tank. The jack also permits the blow-down pipe assembly to be lowered for rupture disc replacement.

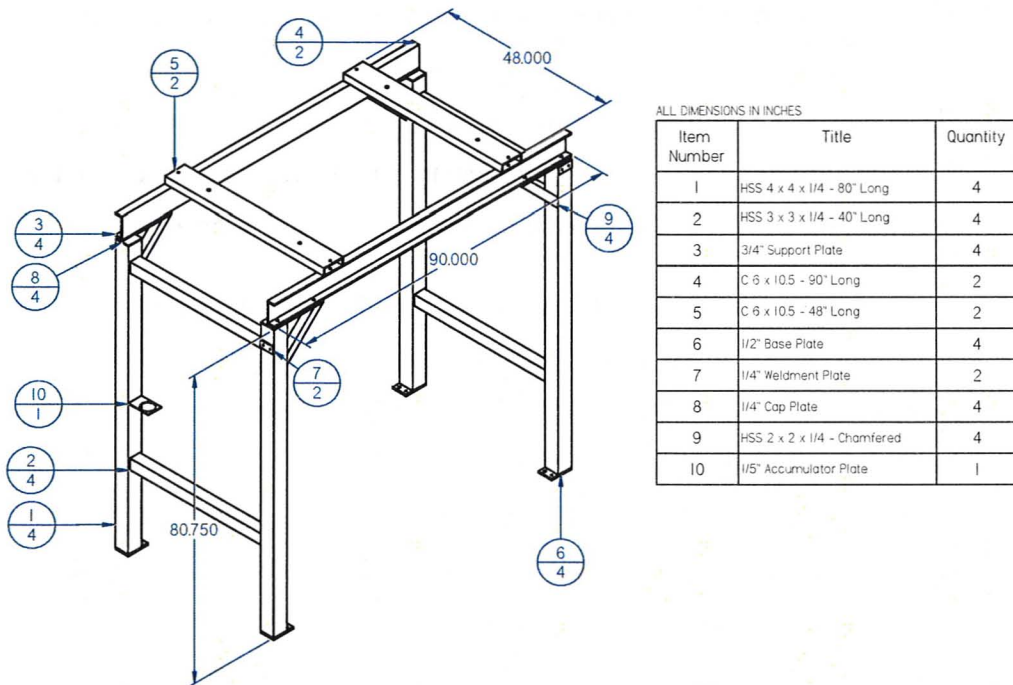


Figure 3-25. Support Frame

3.8 Pressurisation System

The purpose of the nitrogen gas cylinder and accumulator system illustrated in Figure 3-2 is to produce the required pressurisation to trigger the blow-down. The hydraulic diaphragm accumulator of 170 cubic inches capacity is divided into two compartments horizontally separated at the centre by a Hydrin elastomeric diaphragm. The bottom section of the accumulator is connected by a 0.375-inch internal diameter R-134a compatible hose to the pressurised liquid reservoir, and is initially purged to a vacuum and isolated with a bi-directional diaphragm line valve. The top section is connected to the nitrogen gas cylinder, with a bleed valve in between to relieve any excess pressure build-up. In order to activate the blow-down, the bottom compartment of the accumulator is first allowed to fill up with R-134a by opening the line valve, with the

top section of the accumulator at atmospheric pressure. The top compartment is then pressurised using the nitrogen cylinder until the required pressure is achieved. The advantage of using this system is that it permits precise control of reservoir pressure, and therefore disc rupture, without introducing any foreign substance to the system. In particular, the problems associated with nitrogen contamination are avoided.

In order to assist in reducing and preventing refrigerant emissions and ensure that the pressurised system does not pose any safety hazards, leak testing of the blow-down rig was necessary prior to the experimental phase. A high strength, pipe joint sealant supplied by Highside Chemical Inc. was used to seal most of the potential leakage pathways in the blow-down rig. The sealant, Leak Lock, adheres to mating surfaces and forms a chemically resistant flexible fluid-tight seal after joints are assembled. The sealant can be applied to threaded joints, flanged joints, gasket surfaces, and all mating surfaces where a fluid-tight seal is required, and is compatible with most refrigerants including R-134a. Leak testing was performed by pressurising the entire system using the nitrogen gas cylinder and then applying a soapy solution to various areas to detect the leak locations, until all leaks were eventually eliminated. A compressed gas pressure regulator was used to prevent over-pressurisation of the system.

3.9 Instrumentation

During the initial experimental stages, which involve bringing the entire blow-down rig down to a vacuum, to purge any gases and create the necessary low pressure in the vacuum tank, and then pressurising the upstream section with R-134a, the pressure is monitored using static pressure sensors. This way, the pressure can be adequately controlled to ensure that the blow-down does not occur unexpectedly, and is triggered by adjusting the pressure to the prescribed rupture disc pressure difference. Throughout the blow-down transient, measurements are taken upstream and downstream of the test

section of temperature and pressure as well as the dynamic drag load on the test section tube bundle. The following sections discuss the selection of the instruments used to acquire data in these experiments. Detailed manufacturer's specifications for all of the instruments are included in Appendix B.

3.9.1 Static Pressure Sensors

High-Accuracy Pressure Sensors supplied by Measurement Specialties Inc. (model U5100) were chosen for static pressure measurements in this experimental study. The sensor is suitable for the mildly corrosive environments encountered in refrigeration systems. It employs a silicon-based strain gage isolated by an oil-filled capsule and a stainless steel diaphragm designed to provide wide temperature range stability performance. The sensor measures down to zero absolute pressure and is therefore appropriate for the entire range of experimental pressures, starting from the vacuum point.

3.9.2 Dynamic Pressure Transducers

The dynamic pressure transducers chosen for this study were high-sensitivity, acceleration compensated LIVM (Low Impedance Voltage Mode) dynamic pressure sensors (model 2200V1) supplied by Dytran Instruments Inc. with a 100-psi capacity and 50-mV/psi sensitivity. Dynamic pressure sensors respond to very rapid changes in pressure, and cannot measure static pressures. The selected pressure sensor measures pressure perturbations at frequencies from 0.08 Hz to 200 kHz and pressure pulses to 2 μ s rise time. It is acceleration compensated in the axial direction to minimise the effects of acceleration during measurements where the sensor may be subjected to vibration. The importance of the acceleration compensation is that the sensor does not pick up vibration

signals from the rig during the transient blow-down, and is sensitive to pressure changes only.

The sensor was ordered with a mounting adaptor (model 6502) and was pre-installed and sealed in the adaptor at the factory. This facilitated the installation of the sensor since the port required for the adaptor was less complicated than that required for direct installation of the sensor. A brass seal was supplied with each sensor, ensuring that no fluid leaks past the sensor when mounted in place. The sensors were calibrated at the factory using dynamic hydraulic calibration methods, and the exact calibrated sensitivities are included on individual calibration certificates supplied with each sensor. Since the sensor was being used in a thermally active environment, the diaphragm was thermally shielded with a silicone rubber insulating coating to prevent erroneous pressure readings due to transient temperature effects. Due to the high relative stiffness of the sensor element compared to the coating layer, the silicone rubber does not significantly alter the sensitivity of the sensor. The specifications and calibration certificates for the sensors are included in Appendix B.

3.9.3 Dynamic Load Cells

The load cells chosen to measure dynamic loading on the tube bundle are LIVM force sensors (model 1051V4) supplied by Dytran Instruments Inc. with a 500-lbf capacity and 10-mV/lbf sensitivity. A quartz crystal inside the load cell held under very high compressive preload provides a voltage output when stressed by input force. The output polarity is positive for compression and negative for tension. The discharge time constant for this model of load cell is long enough to allow load measurements to be performed over a very wide frequency range, from quasi-static to 50 kHz. The sensor features a radially protruding connector, which allows the sensor to be mounted between two flat smooth parallel surfaces to measure tensile and compressive loads. In order for

the load cell to provide accurate results, it is important that the mating surfaces meet squarely and intimately. The surface areas at the top of the flange on which the load cell was mounted and the bottom of the test section load cell block area in contact with the load cell were surface ground. This way, smooth polished mounting surfaces (0.625 inches diameter) were prepared, flat to less than 0.0005 inches total indicator run-out.

The stiffness of the load cells is 11.4 lb/ μ in, which is almost comparable to a solid piece of steel of similar dimensions. This high stiffness, coupled with the relatively negligible stiffness of the O-rings used to seal the test section tube bundle, allows practically the entire load applied onto the tubes during the transient blow-down to be registered by the sensors. The load cell signals are monitored individually but summed to determine the total transient load on the test section. Specifications and individual calibration certificates were supplied with each sensor and are included in Appendix B.

3.9.4 Thermocouples

There is evidence of fast response temperature measurements obtained for blow-down experiments in the literature. Winters and Merte (1979) obtained transient fluid temperature measurements using calibrated fine-wire (0.025 mm) Chromel-Constantan thermocouples, and concluded through tests and calculations that the thermocouples had a time constant of less than 1 ms. Deligiannis and Cleaver (1996) performed temperature measurements using 25 μ m copper-constantan thermocouples, and cite a response time of the order of 80 kHz. Thus, for this experiment, Quick Disconnect Chromel-Constantan (type E) thermocouples supplied by Omega were chosen. The sheathed thermocouples come with a 6-inch long 0.25 mm diameter stainless steel sheath, and an exposed junction of 25- μ m diameter wires.

The most significant challenge associated with the thermocouples was to create a seal at the mounting location in the walls of the blow-down rig. Due to the fragility of the

thermocouple sheath and the exposed junction, the regular sealant could not be used. In order to achieve the required seal, 0.125-inch stainless steel Swagelok tube fittings were mounted onto the walls of the rig, at the temperature measurement locations. The fitting threads were sealed normally using the pipe joint sealant. Blank Teflon ferrules for 0.125-inch compression fittings were used instead of the regular stainless steel bored ferrules supplied with the fittings. These blank ferrules were drilled using a 0.27-mm drill to provide minimal clearance in order that the thermocouple sheath could be inserted carefully all the way through, such that the tip of the exposed junction is just beyond the end of the compression fitting inserted into the rig. The tube fitting was then tightened with the thermocouple in place, causing the Teflon ferrule to compress evenly onto the sheath, creating a non-destructive press fit that prevents leakage flow.

3.9.5 Data Acquisition Cards

Two separate cards were used for Data Acquisition (DAQ) in this experiment. The dynamic pressure and load signals were obtained using an 8-channel dynamic signal acquisition card (model PCI-4472) supplied by National Instruments. This model has 24-bit resolution and 102.4 kHz maximum simultaneous sampling rate for eight analogue channels. The input channels incorporate built-in Integrated Electronic Piezoelectric (IEPE) signal conditioning for dynamic measurements. For temperature and static pressure measurements, a 16 analogue input DAQ (model PCI-6221) with a connector block (model SCC-68) supplied by National Instruments was used. This model has 16-bit resolution and 250 kHz sampling rate, divided over the 6 channels that were needed for the thermocouples and static pressure sensors. The connector block has an embedded temperature sensor with an accuracy of ± 0.3 °C that is used for cold-junction compensation of the thermocouple measurements. Signal processing for all captured measurements was performed using LabVIEW and data analysis was performed using MATLAB software.

Chapter 4 – Commissioning Tests

Because of the somewhat unpredictable nature of sudden depressurisations and possible resultant shockwaves in the experimental blow-down rig, it was decided that the safest measure was to carry out a series of blow-down experiments in which the pressure drop from the liquid vessel to the vacuum tank was increased from modest values to scaled CANDU steam generator conditions. Thus, it was desired to perform the commissioning experiments first at reduced pressures. This was a necessary step intended to demonstrate proof of concept, and is essentially a simple pipe blow-down, without any internal blockage to the flow in the shape of a tube bundle or other component included.

The benefits of performing these commissioning tests extend beyond mere safety precautionary measures. One of the main purposes was the familiarisation with the charging and purging processes of R-134a. The Heating, Refrigerating, and Air conditioning Institute of Canada (HRAI) regulates the handling of refrigerant fluids, and strict measures are placed concerning refrigerant recovery, reuse and reclamation. Thus, it was important to gain familiarity regarding R-134a charging and purging in order to prevent loss of substantial volumes into the surroundings, and establish correct procedures for subsequent experiments. Another objective of commissioning was the testing of the instrumentation and DAQ system. Commissioning also provided valuable experience with pressurisation using the nitrogen gas cylinder and accumulator system, and testing of the rupture disc behaviour to determine the required pressure difference accuracy for rupture.

Finally, results obtained from commissioning experiments could be compared with available results in the literature. Winters and Merte (1978) made a clear distinction between ‘vessel blow-downs’ and ‘pipe blow-downs’. Pipe blow-downs refer to cases where the size of the discharge opening is large in comparison to the volume of the vessel in which the fluid is stored. Thermodynamic non-equilibrium effects play a significant

role in such situations, and need to be considered in the modelling. When the discharge opening is small with respect to the vessel volume, the depressurisation is classified as a vessel blow-down. In this case, the pressure follows the saturation pressure corresponding to the homogeneous temperature, and the critical flow can be modelled using a non-homogeneous equilibrium (slip) model. Therefore, the commissioning tests are expected to represent pipe blow-down phenomena and display a deviation from equilibrium conditions. However, for later experiments in which the test section is inserted, the flow is expected to choke due to the significant restriction in flow cross-sectional area, and the depressurisation is expected to demonstrate vessel blow-down characteristics.

4.1 Experimental Procedure

The starting point of all of the experiments is the insertion of the appropriate rupture disc in the pressure relief device. The entire system upstream and downstream of the disc is then purged to a vacuum. Next, the fluid reservoir is charged with the desired volume of R-134a. Since there is no direct indicator of the quantity of R-134a inserted into the rig, the R-134a bottle is placed on top of a digital scale throughout the charging process. The readout on the scale displays the mass of R-134a discharged, and the corresponding volume of R-134a can then be calculated. The R-134a charging proceeds to a desired upstream pressure just below the rupture disc burst pressure. The final pressure is produced in a controlled fashion using the nitrogen gas cylinder and accumulator system as described in Section 3.8.

4.2 Small-Scale Tests

In order to model a two-phase steam generator blow-down, the fluid must initially be in a subcooled state. Therefore, the temperature of the fluid in the pressurised liquid reservoir must be less than the saturation temperature corresponding to the required rupture pressure. For the rupture disc pressures of 85, 65, and 45 psi, which correspond to 586, 448, and 310 kPa respectively, the saturation temperatures can be determined from Figure 4-1. Since the downstream vacuum tank is purged to vacuum for each experiment, the prescribed pressure drop for each rupture disc represents the actual absolute R-134a pressure required to trigger the blow-down. Thus, the saturation temperature is 20.8 °C for the high-pressure, 12.3 °C for the moderate-pressure, and 1.8 °C for the low-pressure blow-downs. Consequently, for the lowest pressure, the R-134a needs to be cooled to about -1.5 °C to be in a subcooled state outside the tolerance range of the rupture disc.

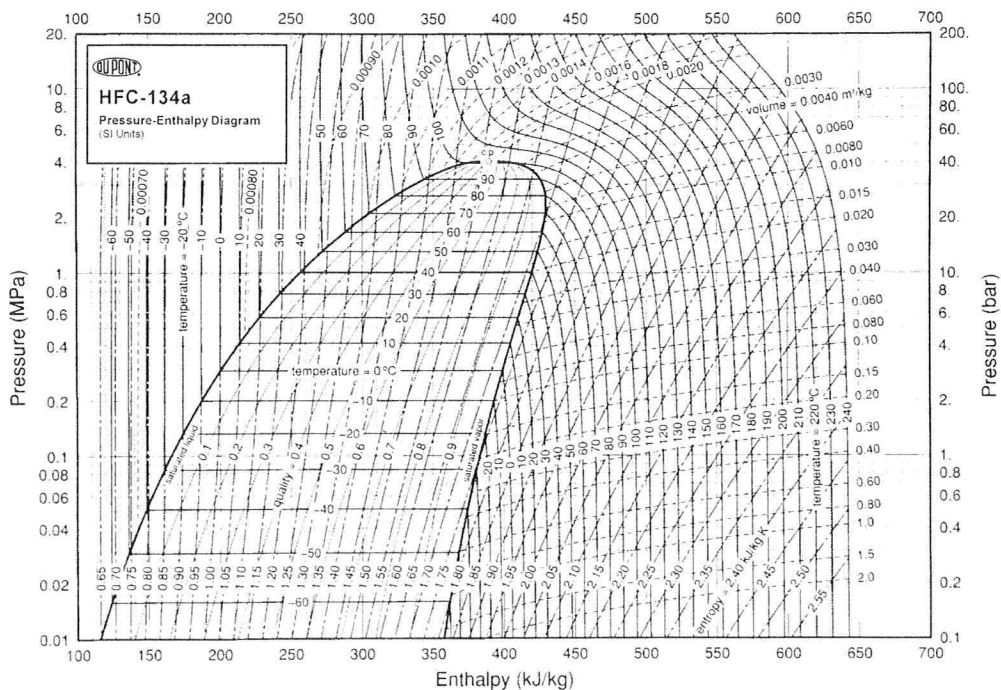


Figure 4-1. R-134a Pressure-Enthalpy Diagram (DuPont, 2005)

Unfortunately, it was discovered that the low temperatures required could not be sustained in the pressurised liquid reservoir and the subcooled state could not be achieved for the low-pressure experiment. Thus, an alternative commissioning experiment was devised, requiring a much-reduced volume of R-134a. A small-scale test section was designed and built, and pictorial view of the design is shown in Figure 4-2. The design was based on a half-inch diameter steel pipe and a glass tube attached at the bottom end to permit flow visualisation. In order to achieve the necessary low temperatures, a cooling pipe enveloped the steel pipe and the glass tube was immersed in an ice-salt bath. The cooling pipe carried a diluted ethylene-glycol solution (40% by volume) from a refrigerated bath pumping unit at temperatures down to $-15\text{ }^{\circ}\text{C}$. The freezing point of this concentration of ethylene-glycol solution is $-25\text{ }^{\circ}\text{C}$ at near atmospheric conditions.

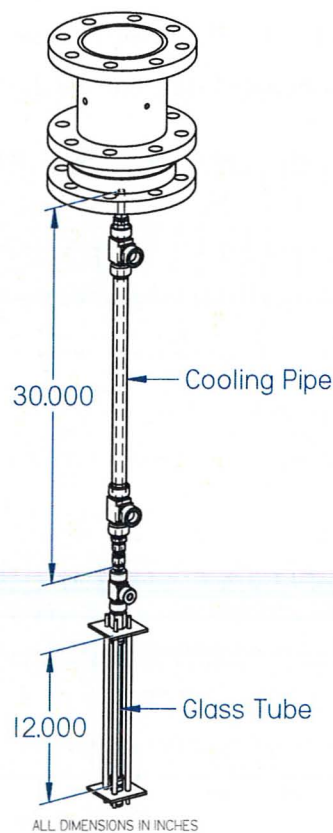


Figure 4-2. Small-Scale Test Section

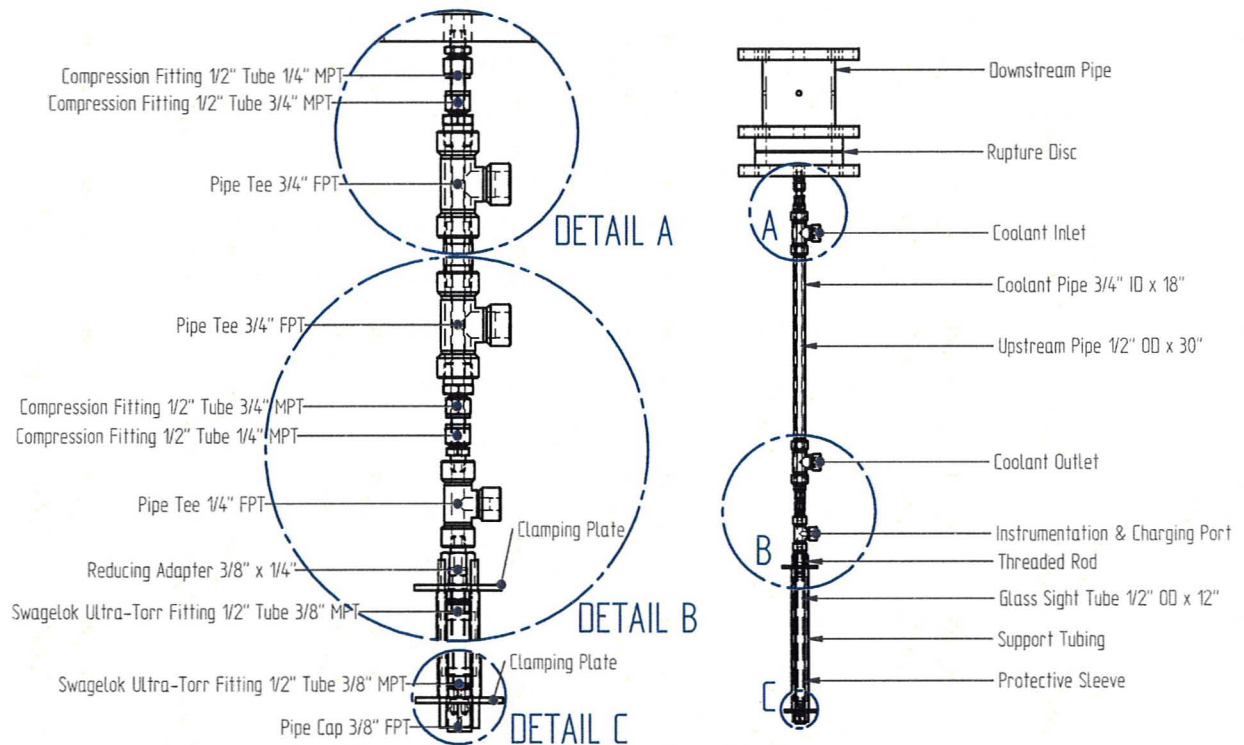


Figure 4-3. Reduced Scale Blow-Down Rig Components

An advantage of having a reduced scale experiment is that the volume of refrigerant is very small, approximately 140 ml, compared with over 20 litres for the full-scale rig. This meant that the liquid reservoir was much easier to chill and the commissioning tests could be performed under favourable conditions. Thus, the operation of various system components could be evaluated without risk of significant loss of R-134a, should there be a structural failure. Knowledge and experience gained from the test results could then be applied towards the large-scale experiments. Figure 4-3 displays the components of the small-scale test section in detail.

Quartz glass tubing of 12 mm outside diameter and 1 mm wall thickness was chosen to serve as the glass sight tube. The maximum allowable internal pressure at low temperatures was determined to be 90 psi based on the internal pressure relationship (12):

$$S = \frac{P \cdot r_i}{t} \quad (12)$$

where S is the hoop stress, r_i is the inside radius, and t is the wall thickness. Because of unpredictable thermal effects, and the possibility of surface scratches or abrasions on the tubing acting as crack propagation sources, a one-inch diameter acrylic protective sleeve was inserted around the quartz glass tubing, to minimise consequences of potential structural failure. The glass tube was connected to a pipe cap at the bottom and to the steel tube at the top using Ultra-Torr vacuum fittings supplied by Swagelok. These fittings are constructed from stainless steel, and include O-rings designed to provide seals on glass and metal tubing. The nut on the fitting body is knurled to permit finger-tight assembly, which helps avoid damaging the glass tubing by over-tightening.

One difficulty encountered while mounting the glass tube in the vertical position involved the bending stresses applied by other components of the test section, which were large enough to break the tip of the glass tube on more than one occasion. In order to prevent this from happening, the design as shown incorporates a stiff support system composed of four threaded rods, four identical lengths of hydraulic steel tubing, and two clamping plates, designed to carry the entire bending load around the sight section. This helped maintain the structural integrity of the quartz glass tubing. The entire rig upstream of the rupture disc was covered in foam pipe insulation, but for the sight section. A static pressure sensor and a thermocouple were mounted in the instrumentation port, which was also used to deliver refrigerant into the test section. Three commissioning tests were carried out on the reduced-scale test rig to evaluate the pressurisation and vacuum system as well as the instrumentation and data acquisition system.

4.2.1 First Commissioning Test

In the first commissioning test, the accumulator was not used. Instead, the liquid R-134a was allowed to heat up slightly by increasing the temperature of the coolant, and this raised the pressure sufficiently to burst the rupture disc. When the refrigerant was

initially charged to the test section, film condensation was observed on the inner walls at the top of the glass sight tube, and boiling bubbles were visible at the bottom. The pressure sensor registered a decrease from the initial charging pressure of 40 psi down to 26 psi. The saturation temperature corresponding to this pressure is $-13\text{ }^{\circ}\text{C}$. The temperature registered by the thermocouple decreased from $16\text{ }^{\circ}\text{C}$ to $5\text{ }^{\circ}\text{C}$, which was misleading, as it was taken in a superheated vapour environment in which there wasn't much convective or conductive heat transfer taking place. The thermocouple provided more representative temperatures of the R-134a thermodynamic states when the junction was in contact with liquid. Before the R-134a was charged, the refrigerated bath unit was allowed to reach steady-state while operating at maximum cooling capacity, with an outlet coolant temperature of $-16\text{ }^{\circ}\text{C}$ and a return temperature of $-15\text{ }^{\circ}\text{C}$.

The test section was then charged with more R-134a, again to a pressure of 40 psi. Further condensation occurred, and the liquid level in the glass sight tube rose. The pressure finally settled at 31 psi. The cycle of charging and allowing near steady-state conditions to develop was continued, and the pressure of the liquid refrigerant gradually increased to 40 psi, at a temperature of $-1\text{ }^{\circ}\text{C}$. The targeted coolant temperature was then incrementally increased towards $0\text{ }^{\circ}\text{C}$, allowing the liquid R-134a in the test section to heat up, pressurise, and eventually reach the 45 psi required to trigger the two-phase blow-down.

The pressure data obtained are shown in Figure 4-4, and temperature histories are shown in Figure 4-5 and Figure 4-6. Figure 4-4 shows the reservoir pressure decreasing from the initial pressure towards equalised conditions over the course of 5 seconds. The pressure downstream of the rupture disc does not show much pressure rise because the test section contains such a small volume of refrigerant compared to the capacity of the vacuum tank. For this set of experiments, dynamic pressure data is not available, due to difficulties encountered with the DAQ system. Figure 4-5 shows the blow-down temperature response at the thermocouple locations, and the sudden expansion from 20 to $-86\text{ }^{\circ}\text{C}$ was captured in 66 milliseconds, as shown in Figure 4-6.

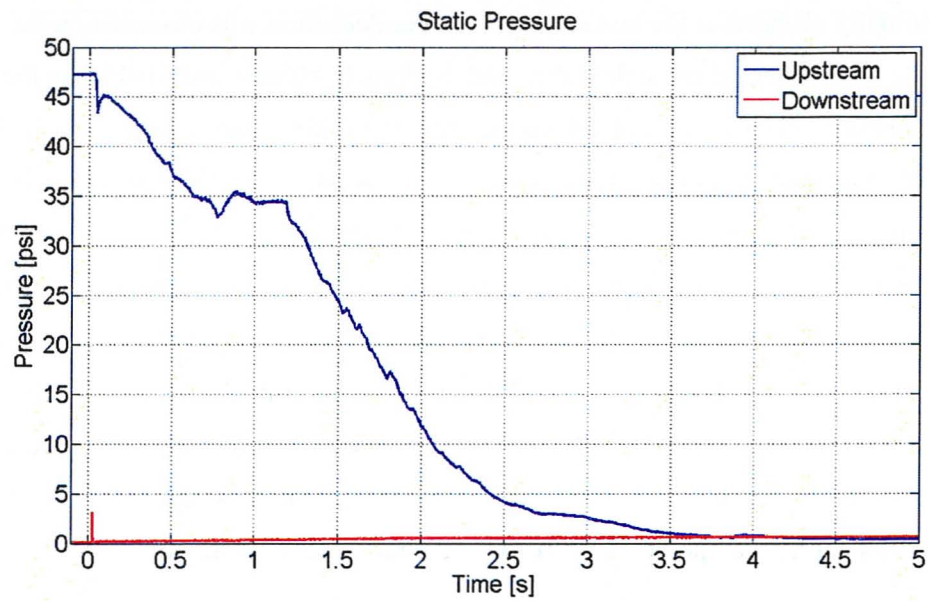


Figure 4-4. Static Pressure vs. Time (1st Test)

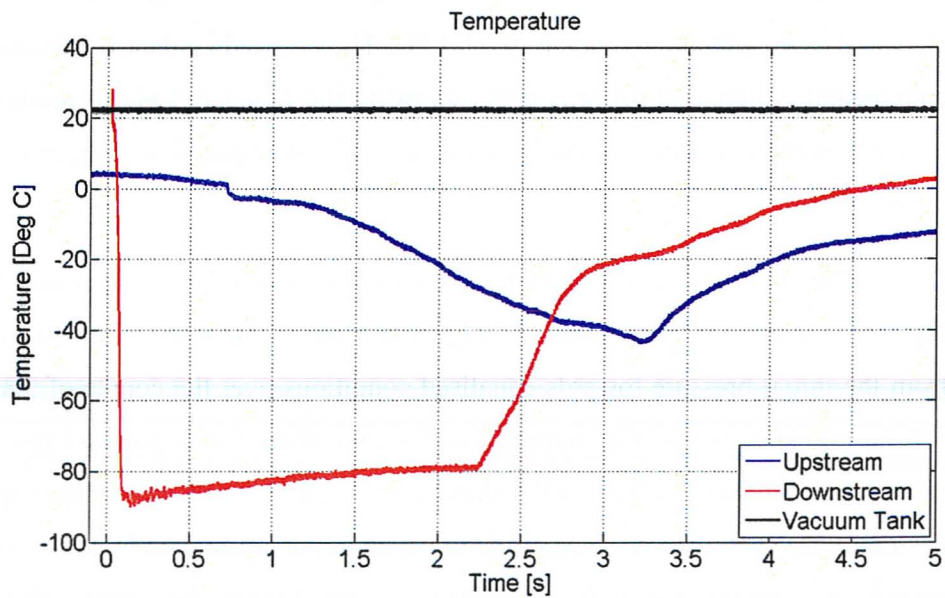


Figure 4-5. Temperature vs. Time (1st Test)

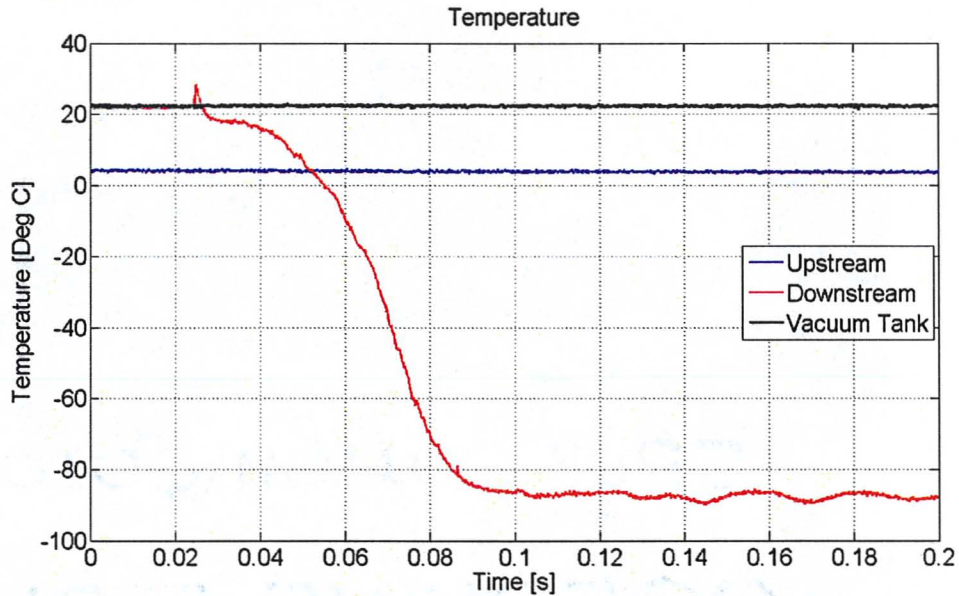


Figure 4-6. Temperature vs. Time (1st Test; 0.2 s Timescale)

The response of the static pressure sensors to the sudden depressurisation, shown in Figure 4-4, arrived after a finite time delay of 37 milliseconds for the upstream sensor, and 24 milliseconds for the downstream sensor. This delay in the response is attributed to the duration of the rapid pressure change behaviour, which cannot be captured by the static pressure sensors. Overall, the test was very successful in evaluating the experimental procedures including initially purging the entire rig down to a vacuum, charging the system with refrigerant, controlling the temperature and pressure for the desired blow-down, and demonstrating the function of the data collection and recording system. Given the small volumetric quantities being dealt with, the charging procedure was very sensitive, and large peaks in pressure could be produced by opening the charging valves slightly more than what was needed. Confidence was gained in the design and its feasibility was demonstrated. A photograph of the experimental setup for the reduced-scale experiment is shown in Figure 4-7.

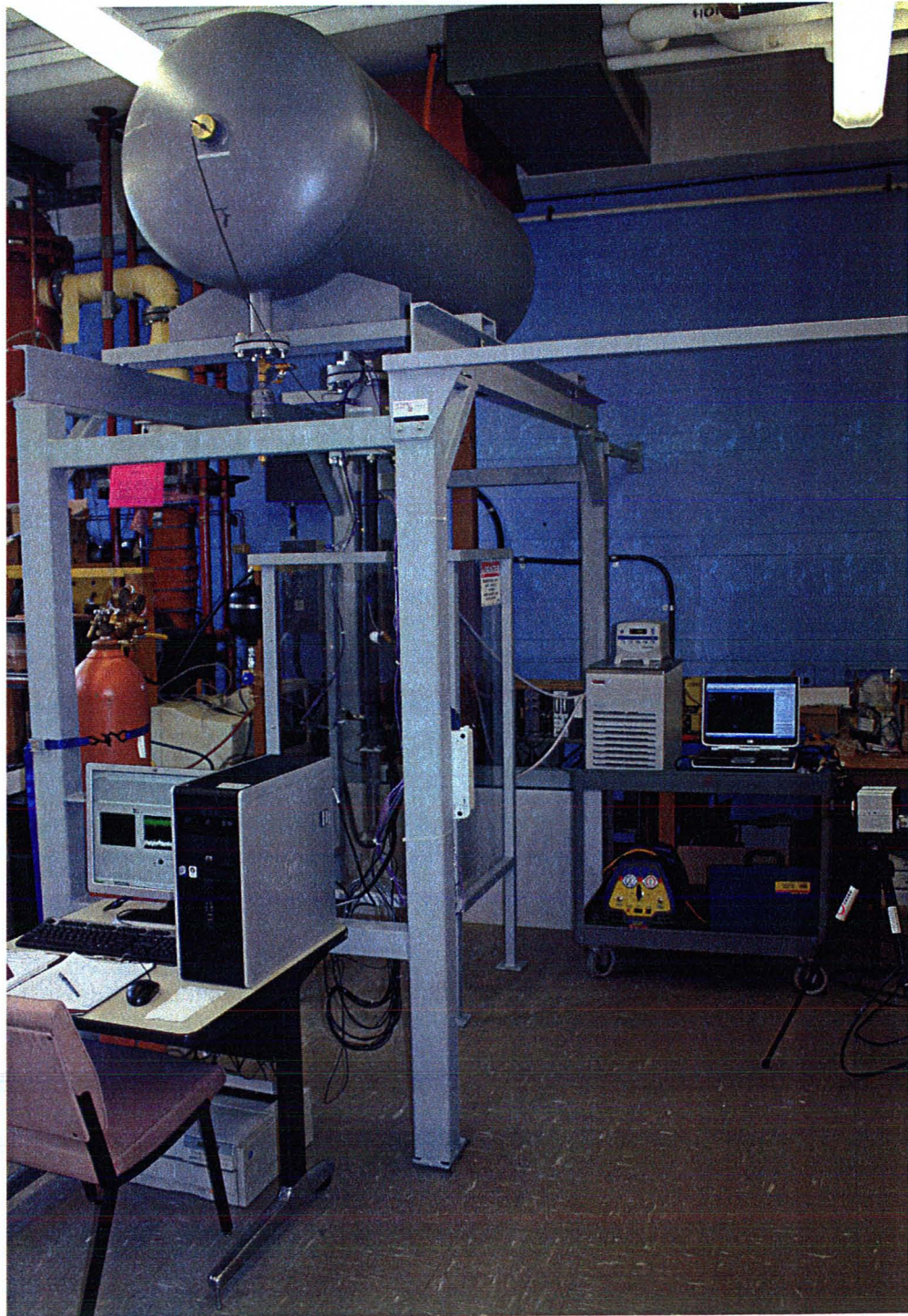


Figure 4-7. Photograph of Small-Scale Experimental Setup

4.2.2 Second Commissioning Test

Knowledge gained from the first commissioning test was applied in the preparation of a second commissioning test by incorporating some changes that aimed to improve the experimental set-up. The main difference between the two tests was the introduction of the accumulator and nitrogen cylinder to provide better control over the pressurisation process for activating the blow-down. The other objectives of this test were to attain more accurate rupture disc burst pressure, acquire more representative temperature results, and obtain some qualitative images of the blow-down flow.

The investigation of the rupture disc behaviour was of particular interest in this test. The rupture discs are designed to rupture at or below the rated pressure, with a $\pm 5\%$ tolerance. In the first commissioning test, the rupture disc burst at a pressure difference of about 47 psi, as shown in Figure 4-4. Although this value still falls within the $\pm 5\%$ tolerance for these discs (rated at 45 psid), the burst pressure was expected to be much closer to the 45 psid for which the disc is rated. It is suspected that cyclic loading placed on the disc during leak testing procedures as well as the continuous cycles of R-134a charging during the first commissioning test contributed towards work-hardening of the rupture disc material, producing a higher burst pressure than the design pressure. In order to avoid a similar reoccurrence, it was decided that for all future tests, the operating pressure upstream of the rupture disc would not exceed 90% of the rated burst pressure, until the final pressurisation step for triggering the blow-down.

Instead of having the temperature and pressure sensors mounted in the charging port of the test section, as dictated by the initial design, individual ports for both sensors were inserted just above the glass sight tube top clamping plate. Therefore, the thermocouple could be installed such that the tip of the junction was just inside the flow area of the blow-down, with the static pressure sensor directly above it, and the charging port above that. The intended objective of this new setup was to achieve a faster temperature response of the thermocouple by having the tip directly in contact with the

blow-down flow, as opposed to having it a couple of inches away in the charging port. Figure 4-5 indicates that the upstream temperature only reduced to $-45\text{ }^{\circ}\text{C}$. By placing the thermocouple in the new location, a more accurate representation of the actual upstream temperature was expected. Finally, the ice-salt bath in which the glass tube was immersed in the first test was removed for this test, in order to provide better capability for high-speed imaging. Given the low temperatures achieved in the first test, it was deduced that the removal of the ice-bath would not significantly alter the thermodynamic state of the liquid refrigerant.

The experiment proceeded in exactly the same manner as the first test. The system was initially purged to vacuum, and R-134a was gradually charged into the liquid reservoir and allowed to condense and settle, before more R-134a was added. The only difference to the first test was the inclusion of the accumulator, which allowed the R-134a to fill the lower compartment of the accumulator. Unfortunately, the addition of the nitrogen bottle and accumulator system to the blow-down rig produced some unanticipated behaviour. As the R-134a was condensing inside the rig, with the pressure reducing from 39 to 36 psi, and without any refrigerant being introduced into the system, the system pressure spiked without any prior notice and the sudden pressure increase was enough to burst the rupture disc, causing a premature blow-down.

Although there was no quantitative data obtained for this test due to the unexpected nature of the blow-down, a qualitative description of the blow-down was captured using a high-speed video camera system. Still blow-down images captured at 2000 frames per second are shown in Figure 4-8. The sudden pressure rise was attributed to the connecting hoses for the accumulator system, which have a comparable volume to the blow-down upstream rig. Since the accumulator hoses were not insulated and contained pathways in which the liquid R-134a could be trapped at temperature conditions above the saturation temperature, thermodynamically unstable volumes of R-134a outside the test section produced pressure pulses that propagated towards the test section, which were eventually large enough to burst the rupture disc.

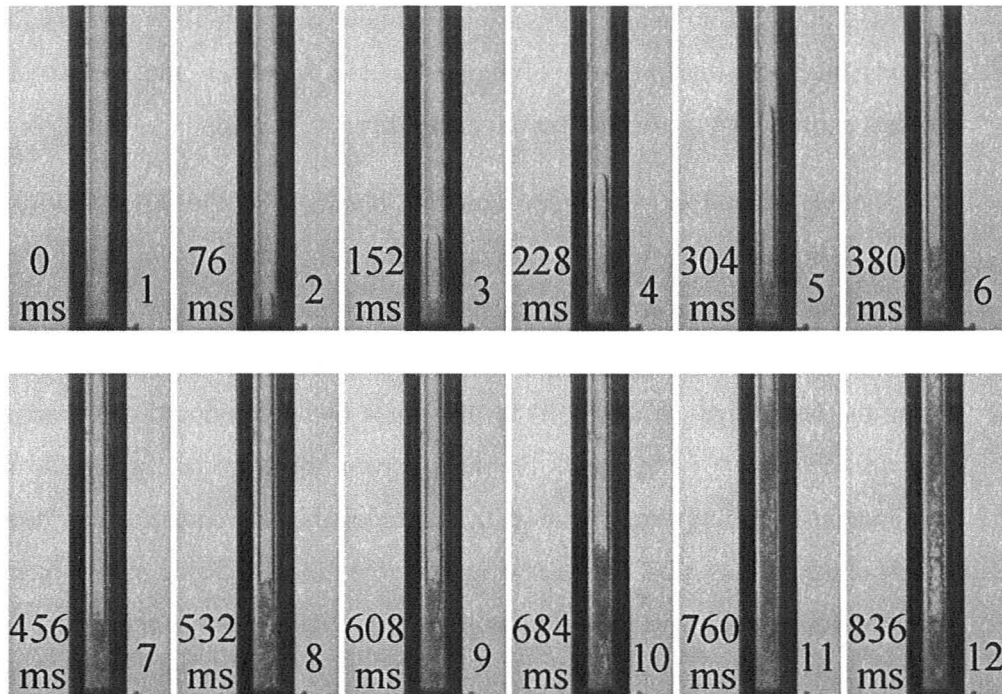


Figure 4-8. High-Speed Images of Low-Pressure Blow-Down

High-speed images obtained for the initial stages of the transient are presented in Figure 4-8. The dark region at the bottom of each frame depicts the compression fitting shown in Figure 4-3 and represents the bottom of the glass tube. Image 1 shows the test section initially filled with saturated liquid R-134a. The ensuing images show the subsequent blow-down transient and the accompanying phase-change phenomena. Images 2 and 3 display a coherent vapour slug forming at the bottom of the reservoir, moving upwards towards the rupture location. An intermittent bubbly boiling regime can be seen expanding in images 4 to 6, trailing the initial slug, which is also increasing in size as it is propelled upwards due to the existing pressure gradient. The leading head of the slug departs from the viewing area of the camera lens in image 7, and the intermittent boiling region shows a subtle decrease in rate of growth in images 8 to 10. Images 11 and 12 show a rapid flow regime transition from the previous slug – bubbly regime towards an intermittent flow pattern exhibiting vigorous boiling. This pattern consisting of

dispersed bubbly flow and the occasional annular or churn flow persists for about 3.5 seconds until the total volume of liquid R-134a vaporises and the experimental rig consists entirely of superheated vapour at equilibrium.

A high-speed video camera recording obtained for the third commissioning test and not included in this text was virtually identical to that shown in Figure 4-8, which indicates that the phase change mechanisms observed are consistent and repeatable with respect to the experimental set-up. The counter-current annular flow configuration seen during the later stages of the blow-down is most likely composed of vaporising flashing flow in the bulk of the fluid, pressure driven towards the break location, and a simultaneously falling liquid film at the walls of the flow area, driven downwards by gravity. Buoyancy is most likely driving the large pipe-sized slug shown in images 2-10, which indicates that there is no slip present at the liquid-vapour interfaces. Furthermore, the blow-down flow consists mostly of small bubbles mixed with liquid, with a low void fraction. The possibility of slip effects in such flow regimes is very small.

4.2.3 Third Commissioning Test

In order to avoid the phenomena encountered during the second test, the accumulator was re-located to the closest possible position to the blow-down rig charging port. By minimising the lengths of piping required to connect the accumulator to the pressurised reservoir, and isolating the accumulator until the system was ready for the final pressure increase to produce the blow-down, the R-134a was maintained at stable thermodynamic conditions throughout the liquid pressure reservoir. For this test, the operating pressure was kept below 80% of the rated burst pressure (36 psi). Apart from these changes, the experimental set-up and procedure were identical to that of the previous test. With the R-134a pressure at 36 psi, the valve isolating the accumulator was opened, allowing the R-134a to occupy the lower compartment of the accumulator. The

nitrogen bottle was then used to pressurise the upper section of the accumulator and, over the course of about 30 seconds, the necessary pressure to rupture the disc was attained. The results acquired are shown in Figure 4-9 and Figure 4-10.

The disc ruptured closer to the expected 45-psi mark, and the upstream temperature and pressure data was more representative of the upstream physical state of the refrigerant during the blow-down as a result of the improved sensor locations. The pressure initially dips below the corresponding equilibrium saturation pressure, recovers to a value below the rupture pressure, and then reduces towards the equilibrium pressure of the vessel. The time required for equalised thermodynamic conditions to be established represents the duration of the transient behaviour. The upstream temperature response shown in Figure 4-10 indicates that the temperature of R-134a closer to the bottom of the reservoir decreased to about $-76\text{ }^{\circ}\text{C}$ around 5 seconds after rupture, which is the time after which all of the liquid R-134a had been converted to vapour. It appears that during the flashing stage which displays pressure recovery and vapour expansion behaviour, the superheated liquid temperature remains constant, and only begins to decrease once the pressure recovery is complete. Downstream of the rupture disc, saturated temperature conditions were established in less than 0.1 seconds, and the response time of the thermocouple in capturing this event was quite satisfactory.

The success of this test signalled the completion of the small-scale commissioning phase of the project. Two-phase blow-downs were produced at identical low-pressure conditions, first by allowing the liquid refrigerant to gain enough heat to rupture the disc, and a second time by compressing the liquid refrigerant using an accumulator and nitrogen bottle system. Pressurisation using the nitrogen gas cylinder produced a well-controlled rapid blow-down, a method that can be easily transferred for application in the large-scale test section. The data collected by the pressure and temperature sensors for both tests were similar and demonstrated functionality of the data collection system. The next step in the project was to commission the large-scale rig by producing a 65-psi blow-down without any obstruction to the flow.

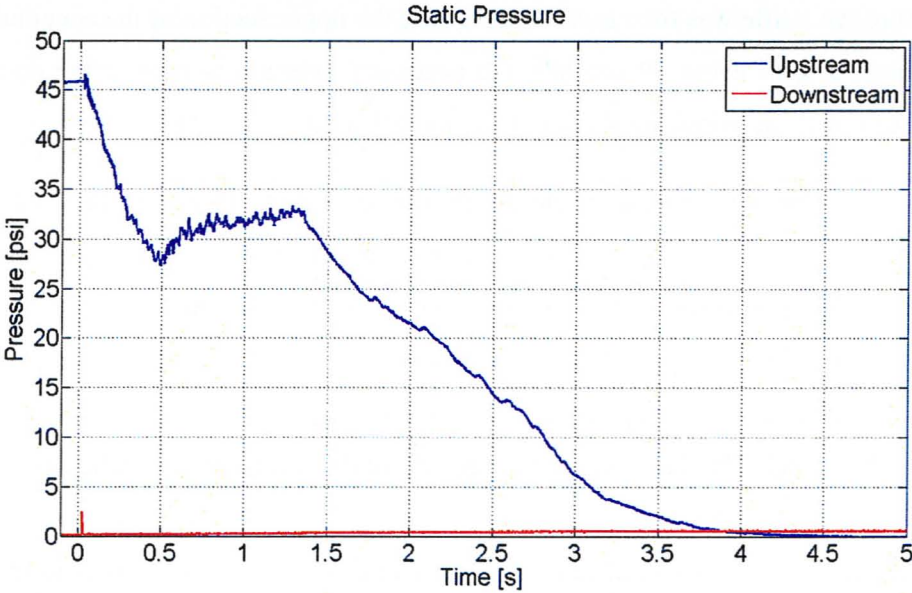


Figure 4-9. Static Pressure vs. Time (3rd Test)

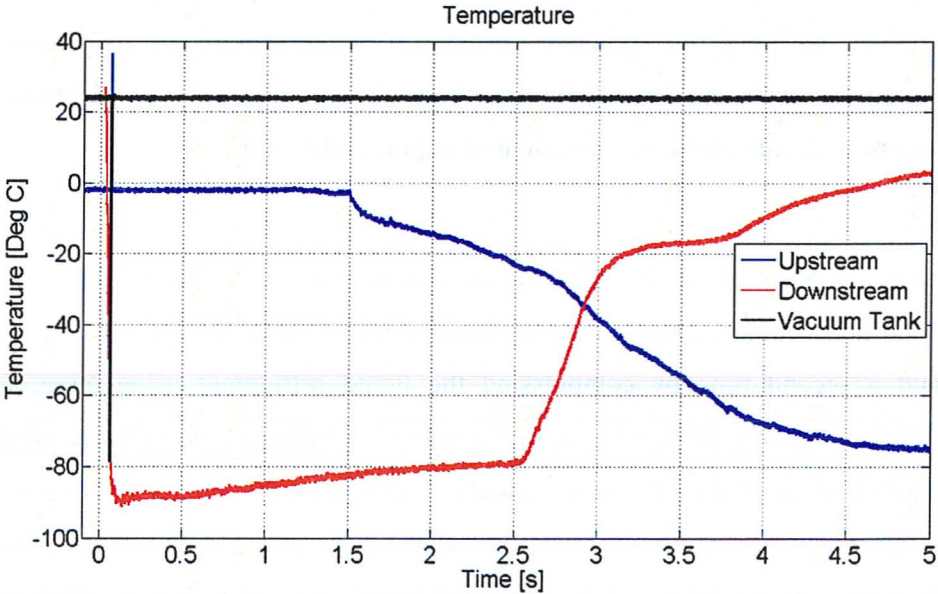


Figure 4-10. Temperature vs. Time (3rd Test)

4.3 Large-Scale Tests

In order to cool down the upstream section of the rig sufficiently below the saturation temperature of R-134a at 65 psi, which corresponds to 12.3 °C, a coolant loop was designed such that the cooling components could be installed without altering the original experimental rig design. A high-purity base mineral oil was chosen as the heat transfer fluid for the moderate-pressure commissioning tests. Mineral oil is a transparent, colourless, non-reactive oil of a relatively low cost. The advantages associated with mineral oil include unaffected visibility for high-speed imaging purposes, as well as prevention of oxidisation of steel surfaces in the rig and coolant circuit. The thermal properties of mineral oil are presented in Table 4-1. During the commissioning experiments, the temperature of the mineral oil ranged between 5-12 °C, and the properties of the mineral oil in this temperature range, as shown in Table 4-1, make it a suitable fluid for the current heat transfer application.

Table 4-1. Thermal Properties of Mineral Oil

Temperature T (°C)	Density ρ (kg/m ³)	Specific Heat c_p (J/kg-K)	Thermal Conductivity k (W/m-K)	Kinematic Viscosity $\nu \times 10^6$ (m ² /s)
0	882	1805	0.1344	185
20	873	1878	0.1330	49

The mineral oil is cooled in a metallic reservoir that is submerged in an ice bath, in an annular configuration. The ice bath tank has a diameter and height of 2 feet, and the mineral oil reservoir is just below 2 feet tall with a 15-inch diameter. All the hose connections in the coolant loop are made using clear polyvinyl chloride (PVC) tubing of 1-inch outside diameter and ¾-inch inside diameter. A ¾-horsepower, 3450-RPM

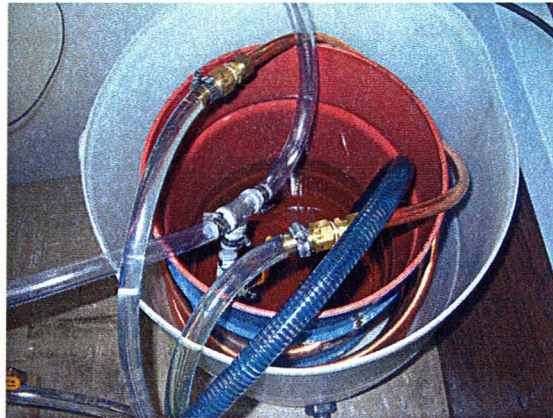


Figure 4-11. Mineral Oil Reservoir

centrifugal pump circulates the mineral oil at a flow rate of about 30 L/min. The pump is primed before operation to prevent air ingestion, and draws mineral oil from the reservoir through a 1-inch PVC suction hose, with a bronze foot valve installed at the suction end eliminating back-flow and loss of prime. The unidirectional foot valve design is based on a stainless steel spring with an O-ring seal on a tapered seat, and is always kept below the surface of the mineral oil inside the reservoir to avoid entrainment of air bubbles in the flow. The mineral oil is then circulated through 50 feet of $\frac{3}{4}$ -inch copper tubing in 22-inch diameter coils, fully submerged in the ice-water mixture, and then flows through the rig cooling system and back into the mineral oil reservoir. A photograph of the ice bath tank and mineral oil reservoir system is shown in Figure 4-11 and a schematic of the coolant loop is shown in Figure 4-12.

The cooling system branches into two main subsystems, and the flow is throttled using gate valves such that suitable flow rates are maintained throughout the entire loop. The pipe section just upstream of the rupture disc is cooled by tightly wrapping PVC tubing around the pipe walls, and the transition sections with viewing windows were enveloped by an acrylic sleeve design, such that optical transparency is retained. A schematic of the cooling system displaying the mineral oil inlet and outlet ports is shown in Figure 4-13, and a photograph is shown in Figure 4-14.

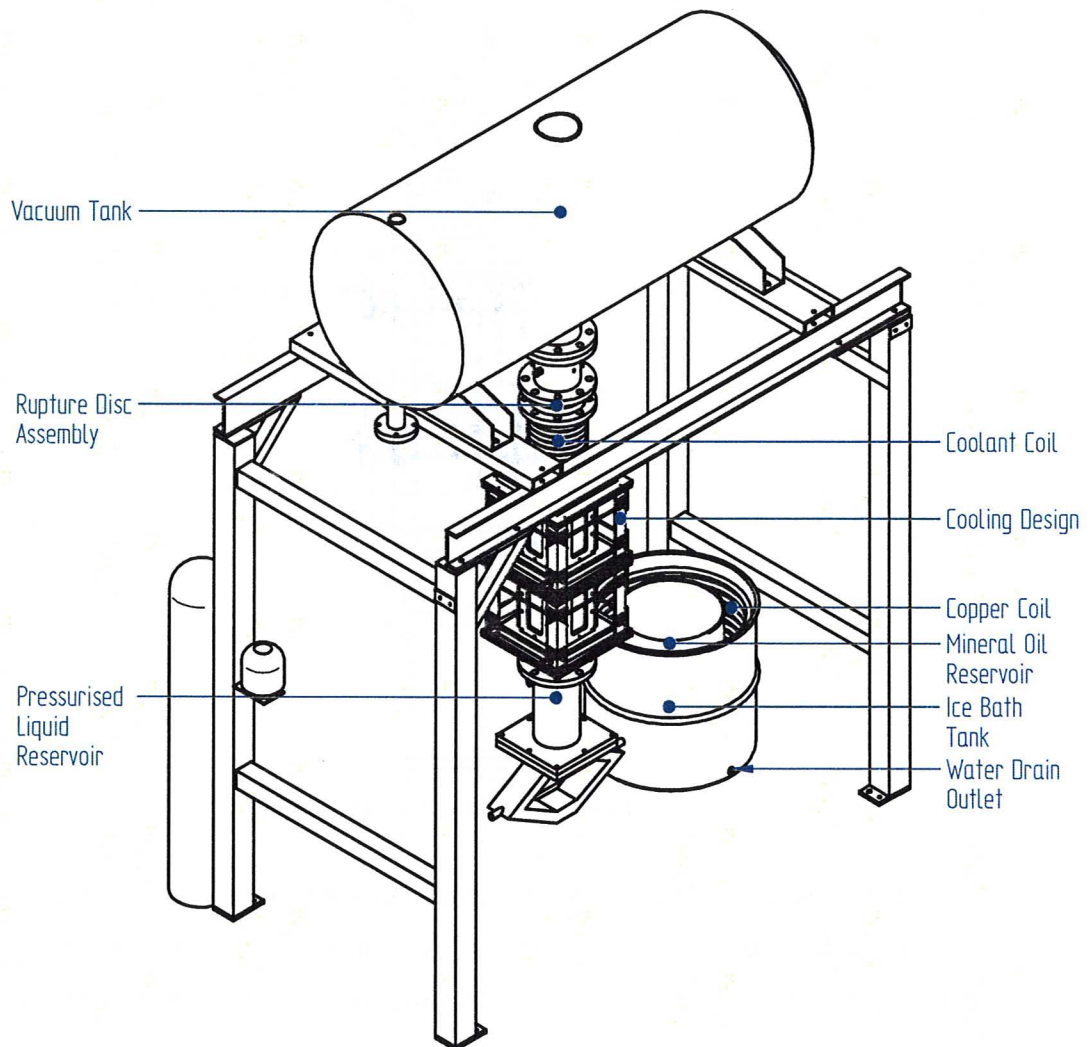


Figure 4-12. Coolant Loop Components

The transition sections cooling design is comprised of an acrylic casing placed between a pair of aluminium flanges. A schematic of the assembly configuration is shown in Figure 4-15. The bolthole pattern in the aluminium flanges is identical to that in the steel square flanges used in the original rig design. Aluminium ribs were attached onto the flanges to position and constrain the acrylic casing. The aluminium flange surfaces are in simultaneous contact with the acrylic top and bottom surfaces, as well as

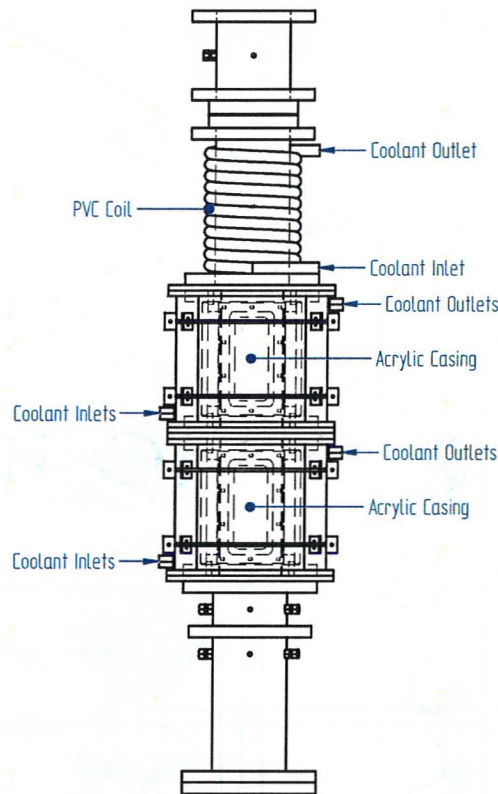


Figure 4-13. Upstream Cooling System

the transition section top and bottom flanges. Consequently, the height of the acrylic cases was machined to match the height of the transition section that it enveloped, so as to ensure that the compressive force provided by the aluminium flange creates an effective seal. A 0.125-inch thick 60-durometer nitrile gasket was used to seal between the aluminium and the acrylic, instead of the 0.0625-inch thick 65-durometer neoprene gasket material used on all other mating surfaces. The softer rubber material ensures that the load transferred to the acrylic is relatively small compared to the load transferred to the steel sections, since the nitrile undergoes a larger compression in comparison to the neoprene. The difference in thickness between the gaskets was accounted for in the machining of the acrylic cases, and they were made 0.125 inches shorter than the height of the steel transition sections.



Figure 4-14. Photograph of Cooling System Design

The acrylic cases were manufactured by bending a ½-inch thick acrylic sheet around two corners into a square U-shape, and bonding a flat acrylic sheet of the same thickness to the open side, producing a consistent square tubing geometry. The inlet and outlet ports were drilled and tapered pipe threads were tapped such that the PVC hoses could be clamped on reducing adapters fastened into the acrylic sheets. The tapping and bending processes place residual stresses on the acrylic material at the corners, and these combined with surface scratches and abrasions due to contact with sharp-edged steel surfaces during installation and removal rendered the acrylic cases highly vulnerable to brittle fracture. Through a trial circulation of mineral oil, it was discovered that when placed under compressive axial loading between the flanges, the acrylic cases were incapable of withstanding the hydrostatic pressures exerted by the mineral oil. Thus, the corners were reinforced using aluminium angle that clamped firmly onto the acrylic case, with threaded rods allowing for adjustable positioning and clamping force.

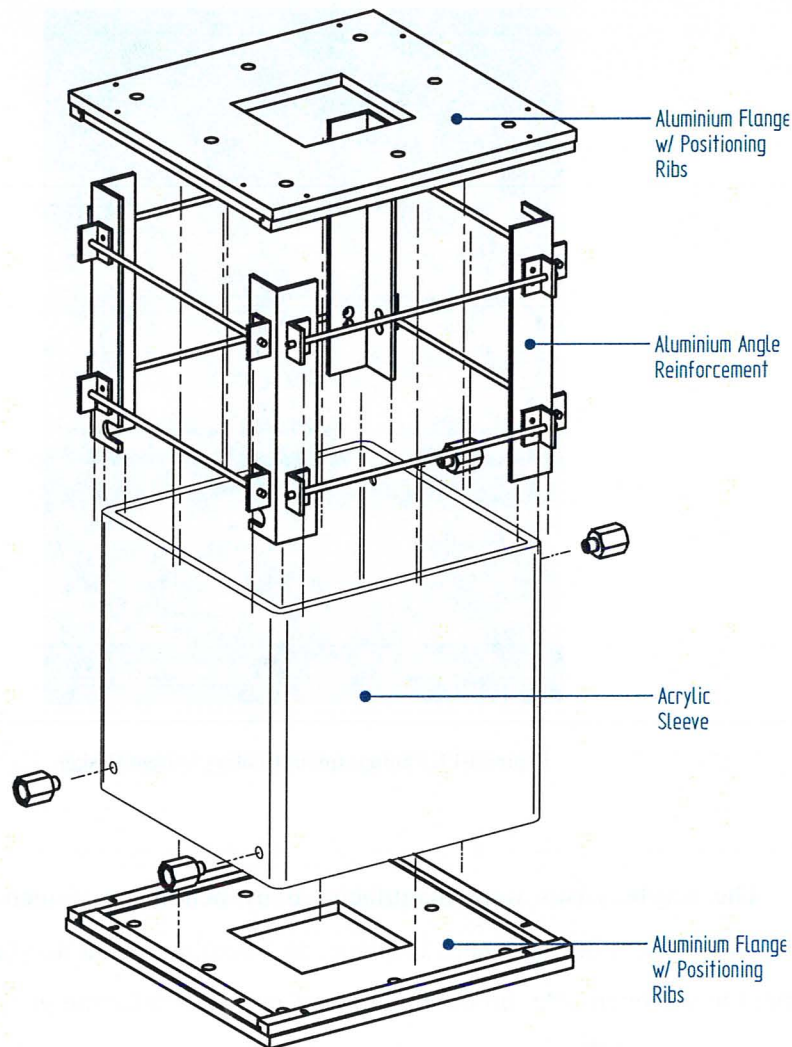


Figure 4-15. Cooling Design Assembly Configuration

The compressive sealing force on the cooling sections and transition sections was applied by eight ½-inch zinc-plated steel threaded rods 31 inches long, torqued to about 50 ft-lbs. In order to prevent mineral oil leaks through the boltholes in the aluminium flanges, annealed copper washers were manufactured and placed between the coupling nuts that were used to tighten the rods and the outer surface of the aluminium flanges. The open ends of the coupling nuts were then capped and sealed using similar copper

washers. Using this cooling design configuration, the upstream section of the blow-down rig was cooled down to temperatures low enough to establish suitable conditions for the moderate-pressure commissioning tests.

4.3.1 Fourth Commissioning Test

The first large-scale commissioning test proceeded as outlined in the experimental procedure, by first inserting the 65-psi rupture disc and sealing the blow-down rig. Once the entire system had been purged down to a vacuum, the mineral oil coolant was circulated in order to establish the required thermodynamic conditions inside the upstream reservoir section. Through cooling the mineral oil as previously described, a minimum average coolant temperature, which is also the inside temperature of the reservoir walls at steady-state, of 10.5 °C was attained, which was deemed appropriate as it lies below the saturation temperature corresponding to the rupture pressure (12.3 °C). R-134a was charged into the system under these conditions, and the first signs of condensation, in the form of small droplets on the sight glasses and falling liquid films on the inside walls, appeared at an equilibrium pressure of 63 psi. The saturation temperature corresponding to this pressure inside the pressurised liquid reservoir is 11 °C. Since this pressure falls within the $\pm 5\%$ tolerance region of the rupture disc, the charging process had to be performed with extreme care, due to the proximity of the charging pressure to the potential rupture pressure of the disc.

Unfortunately, with less than 0.2 lbs of R-134a in the system, the 63.5-psi pressure on one of the charging cycles was large enough to rupture the disc, producing a premature blow-down, while R-134a was still being added into the reservoir. The burst pressure can be seen in the static pressure sensor data recordings acquired for this test, shown in Figure 4-16, and the temperature recorded is shown in Figure 4-17.

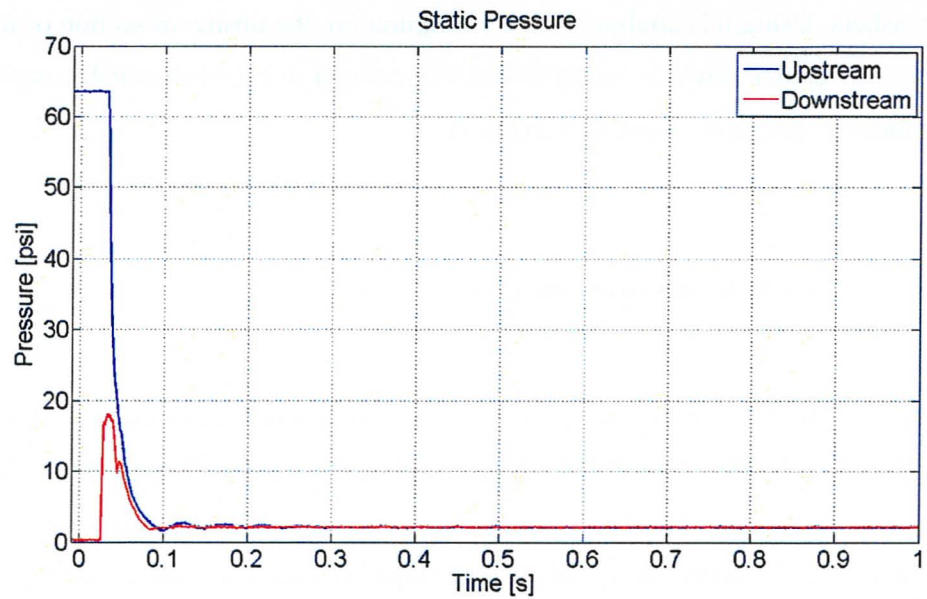


Figure 4-16. Static Pressure vs. Time (4th Test)

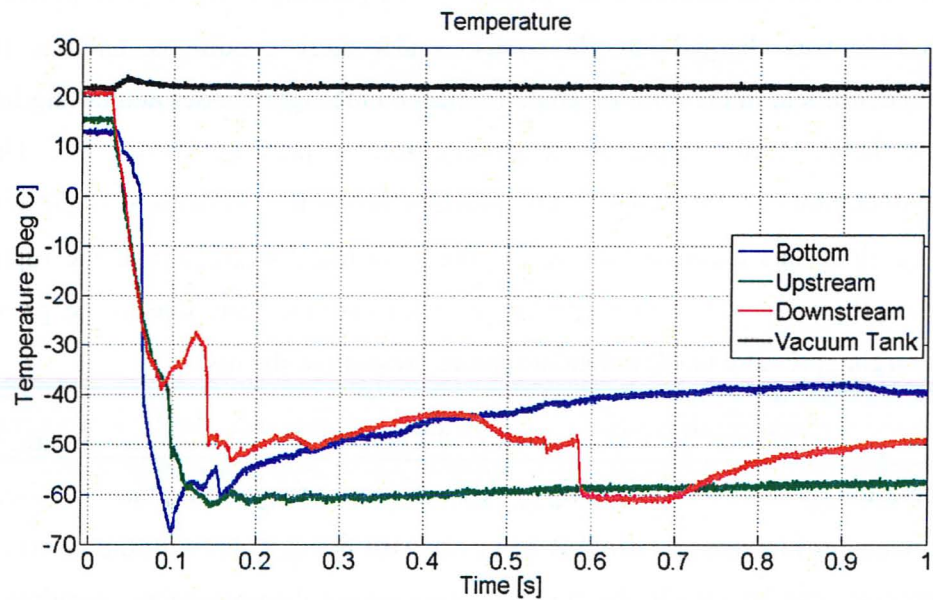


Figure 4-17. Temperature vs. Time (4th Test)

Since there was a very small volume of condensed fluid in the liquid reservoir, very little flashing occurred, and this blow-down essentially displayed single-phase vapour blow-down characteristics. The upstream pressure dip was very steep, and the downstream pressure rose quickly, with an equalised pressure established throughout the system in about 100 milliseconds, as shown in Figure 4-16. The temperature just upstream of the rupture disc, shown in Figure 4-17, indicates that the vapour is highly superheated just before rupture. After the premature blow-down was produced, the vapour R-134a expanded to a temperature of $-68\text{ }^{\circ}\text{C}$. Since the R-134a charging valve remained open when the blow-down happened, the introduction of additional R-134a during the initial stages of the blow-down influenced the system dynamics by producing irregular behaviour, which explains the random fluctuations in temperature visible in Figure 4-17.

After this experiment, it became clear that the coolant temperature was too high, and that lower temperatures were required in order to perform satisfactory two-phase blow-down commissioning tests. In order to improve the heat transfer between the cooling ice bath mixture and the mineral oil, the ice bath was manually agitated at frequent intervals, and the temperature of the pool of mineral oil inside the reservoir was brought down to $1\text{ }^{\circ}\text{C}$ in this fashion. Thus, a second large-scale commissioning test was performed, for which the temperature of the mineral oil was reduced to the minimum possible value with the same cooling design configuration.

4.3.2 Fifth Commissioning Test

This experiment proceeded in an identical manner to the previous one, by first inserting the appropriate disc, sealing the system, and purging the upstream and downstream sections to a vacuum. The mineral oil coolant was then circulated and allowed to reach steady-state conditions, at which the coolant average temperature was

about 5 °C. With these initial conditions established in the upstream liquid reservoir, R-134a charging commenced, and condensation occurred at an average pressure of 52 psi, corresponding to a saturation temperature of 6 °C. Since the flow of refrigerant between the R-134a bottle and the experimental reservoir during charging is driven solely by the pressure difference between the two systems, charging was initially very slow, and R-134a was delivered to the pressurised liquid reservoir at an average rate of 0.02 lbs/min. In order to speed up this charging process, the R-134a cylinder was placed inside a warm water bath with a temperature of about 35 °C. Charging proceeded in this manner, until about 7.5 lbs of liquid R-134a accumulated inside the pressurised liquid reservoir. At this point, the pressure inside the pressurised liquid reservoir was about 58.5 psi, which is approximately 90% of the rated pressure for the rupture disc, and the temperature of the liquid R-134a was about 9 °C.

The temperature of the coolant was maintained between 5-5.5 °C, and this prevented pressures of higher than 59 psi from being sustained inside the reservoir. The volume of liquid inside the reservoir at this point was about 2.7 litres, and the height of the liquid column was about 6 inches. With this amount of pressurised liquid R-134a available inside the upstream section, it was considered appropriate to initiate the blow-down. Thus, the R-134a charging valve was closed off, and the accumulator lines were opened up such that the upstream section could be pressurised using the nitrogen cylinder and accumulator system. In order to trigger the blow-down, the accumulator was required to provide a compression of 6 psi. Unfortunately, it was discovered after several attempts that the accumulator could only provide a pressure increase of 2 psi per compression, due to the limited volume available in the bottom compartment of the accumulator. Figure 4-18 shows a few attempts to pressurise the R-134a towards rupture pressure, with a maximum of 2 psi achieved each time. At this point, the coolant was drained in order to raise the temperature, and therefore, pressure of the liquid R-134a, and attempts to rupture at 61, 62, and 63 psi still did not provide enough of a pressure boost to rupture the disc. While trying to overcome these difficulties, a premature rupture was eventually triggered again at a pressure of about 64 psi, while the charging valve was still open.

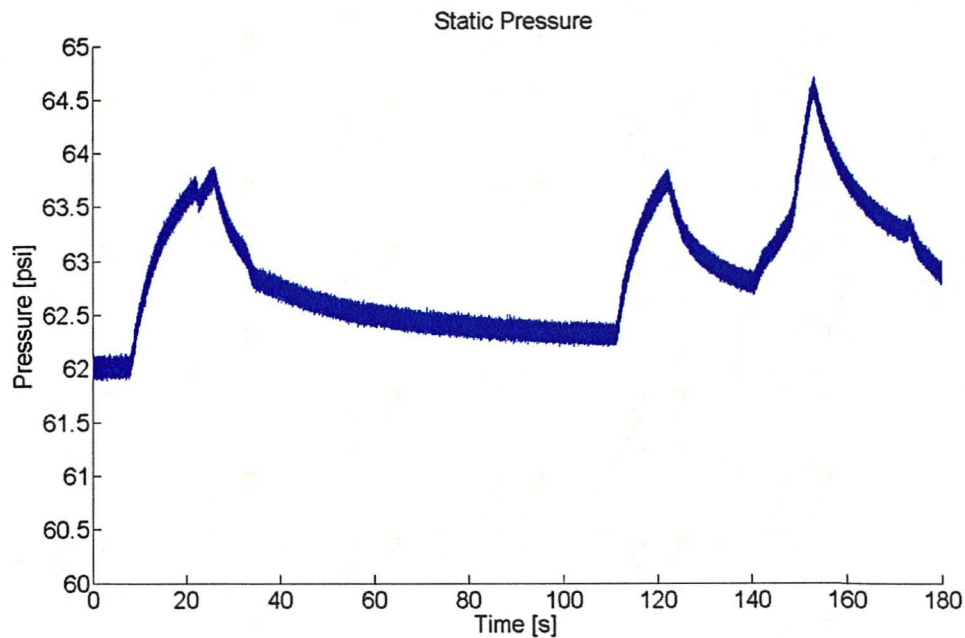


Figure 4-18. Sample Accumulator Pressurisation Attempt

The problems encountered in this test were due to the excessively low temperatures established inside the pressurised liquid reservoir. With temperatures relatively far below the saturation temperature, and a relatively large volume of vapour in the upstream section, it was difficult to raise the pressure to a point from which the accumulator could be used to provide the final compression required to initiate the blow-down. The pressure response, especially in the first few hundred milliseconds, shown in Figure 4-19, is potentially affected by the continued charging while the rapid depressurisation was taking place. The initial temperatures recorded, shown in Figure 4-20, display the temperatures falling rapidly, recovering slightly, and falling towards the minimum temperature recorded, before finally recovering steadily. The long-term temperature response, shown in Figure 4-21, is typical of the expected two-phase behaviour, with an initial rapid temperature change quickly succeeded by a recovery process at saturation temperatures corresponding to the local pressures.

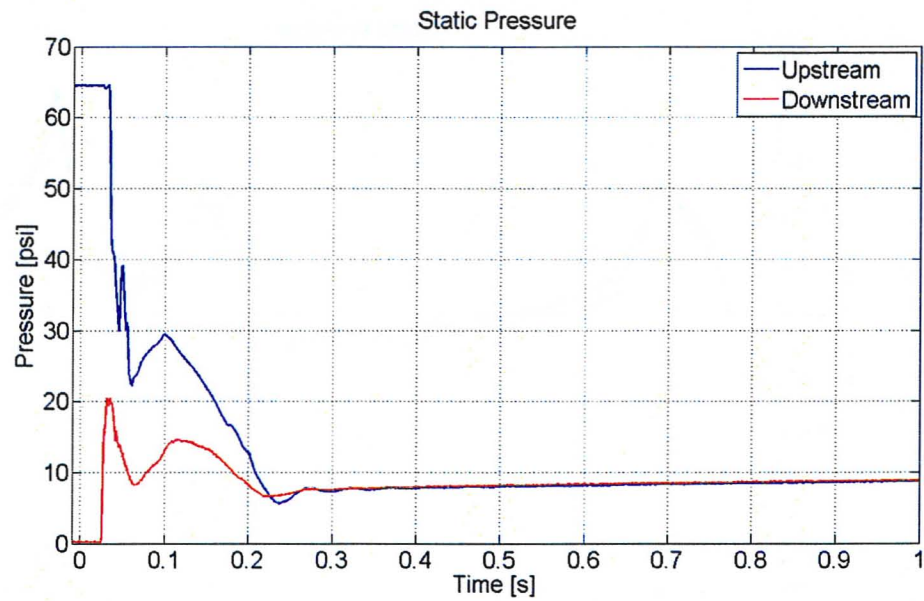


Figure 4-19. Static Pressure vs. Time (5th Test)

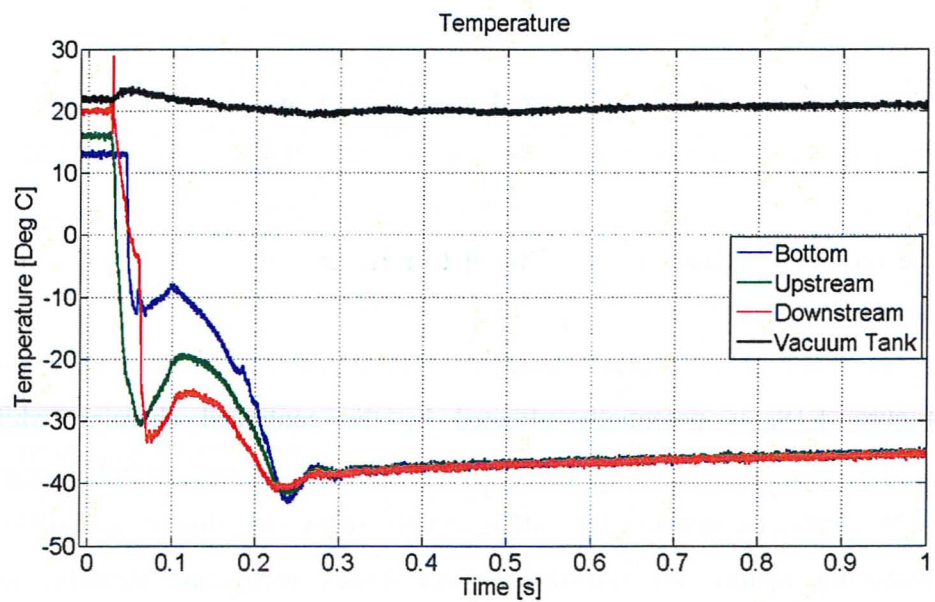


Figure 4-20. Temperature vs. Time (5th Test)

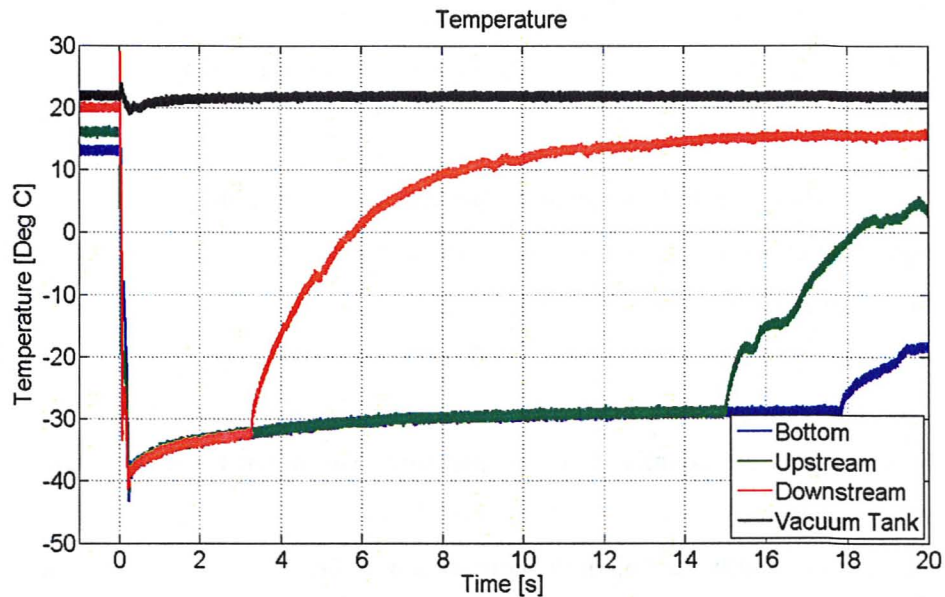


Figure 4-21. Temperature vs. Time (5th Test; 20 s Timescale)

4.3.3 Sixth Commissioning Test

The final commissioning test was performed with a coolant temperature of about 7 °C, such that the temperature of the R-134a inside the pressurised liquid reservoir was low enough to provide adequate conditions for subcooled charging, and high enough to permit precise pressure control such that the accumulator could be used to trigger the blow-down. For this experiment, dynamic signal acquisition was incorporated, and dynamic rapid pressure response was obtained for the blow-down. Furthermore, a high-speed video camera was set-up to capture visualisations of the two-phase blow-down flow. The experiment proceeded in an identical manner to the previous tests, and 15.5 lbs of R-134a, corresponding to a volume of about 5.6 litres (11 inches column height), were charged into the system before it was decided to attempt to initiate the blow-down through nitrogen pressurisation of the upstream section. The system behaviour was very similar to that of the previous test, and the accumulator would only provide an additional

2 psi per compression. Therefore, the ice water mixture was replaced by a warm water bath, raising the temperature of the mineral oil and gradually heating the R-134a inside the pressurised reservoir.

While the R-134a temperature was increasing, the pressure eventually became high enough to rupture the disc using the accumulator, producing a controlled two-phase blow-down without introducing any additional fluid to the system. Figure 4-22 displays the static pressures recorded for the blow-down, with a rupture pressure of about 64.3 psi. The upstream pressure decreases rapidly, then remains temporarily constant, and then falls towards the equalised system pressure. The downstream pressures spikes upward when exposed to the flashing fluid, then drops rapidly, before recovering and falling at a slower rate, finally settling at the equalised pressure.

The temperature response shown in Figure 4-23 is very similar to that observed in the previous commissioning tests. The fluid initially follows an isothermal path, and the delay time associated with the phase change varies between the different locations, with the liquid phase requiring a longer time before the temperature drops. The decrease happens very rapidly, and is most likely a representation of the vapour phase temperature as the fluid flashes. Between 50 and 100 milliseconds after rupture, the temperature recovers by about 10 °C, probably as a result of the superheated liquid flow. The temperature in the rig then decreases at a relatively slow rate for about 200 milliseconds, and the minimum temperature achieved at 300 milliseconds is almost equally distributed throughout the rig. At this point, steady-state conditions are established, and the temperatures follow the equilibrium saturation path of the remaining fluid, until vaporisation is complete. The temperature in the vacuum tank shows a couple of sudden drops at about 300 and 500 milliseconds after rupture, probably due to the arrival of an expanding volume of fluid at the thermocouple location. The bottom thermocouple also displays an irregular increase in temperature beginning at about 150 milliseconds, and this is most likely indicative of the temperature of a superheated liquid slug entrained in the flow.

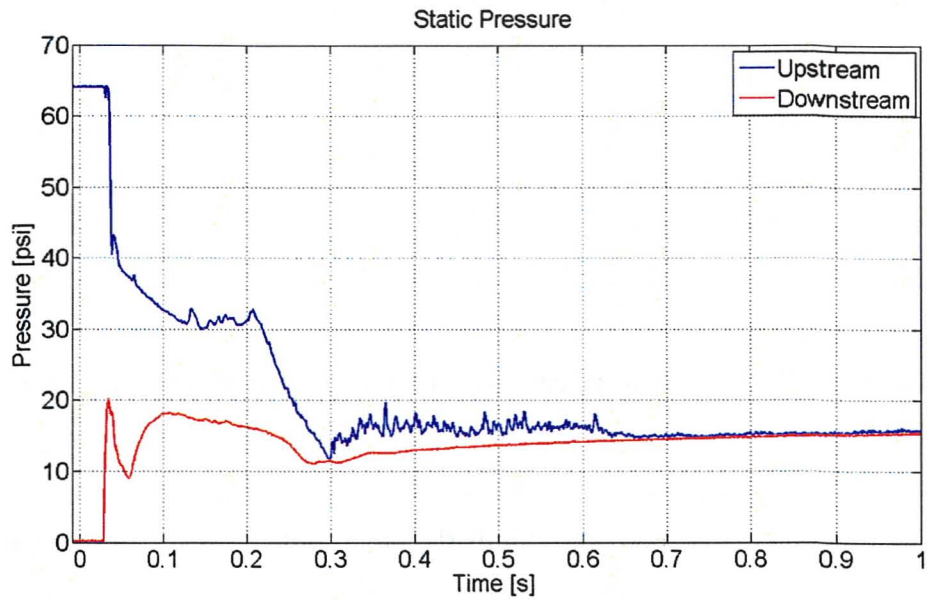


Figure 4-22. Static Pressure vs. Time (6th Test)

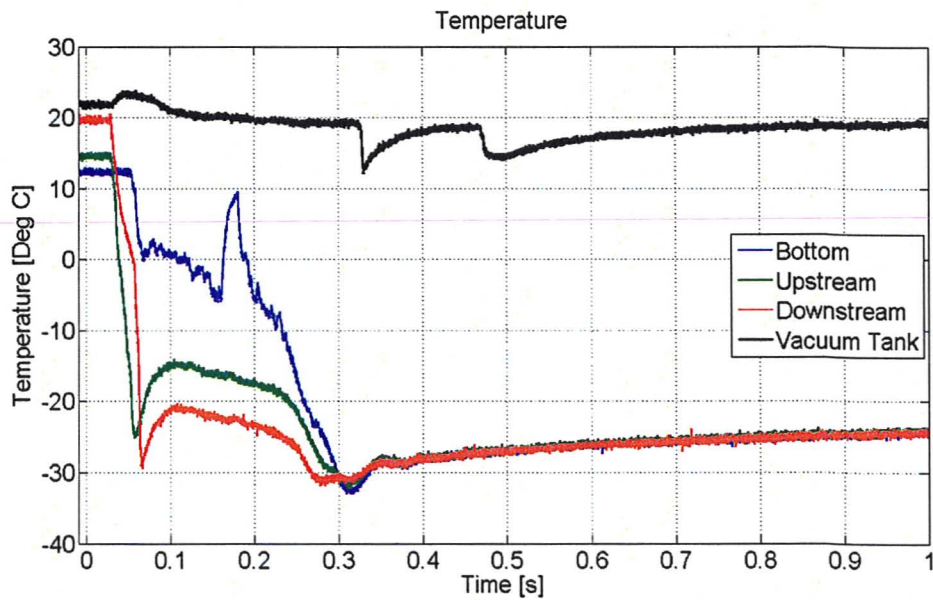


Figure 4-23. Temperature vs. Time (6th Test)

The first set of experimental rapid pressure response data was obtained for this test using the dynamic pressure transducers. The raw data corrected to the initial pressures before rupture is presented in Figure 4-24, and the pressure changes in the first few milliseconds are presented in Figure 4-25. The low-frequency response of these sensors is determined by the discharge time constant of 1.80 seconds. When a steady-state step input is applied, the sensors respond within 2 microseconds, and the output signal discharges towards the quiescent level at a rate determined by this discharge time constant. The measurement accuracy deteriorates for events of a longer duration. For instance, in order to obtain a measurement accuracy of 1%, it is necessary that the time during which the pressure changes is less than 1% of the discharge time constant, which in this case is 18 milliseconds. Similarly, an event that occurs over 90 milliseconds will have a 5% error inherent due to the time constant of the sensors. The dynamic signal in this test was influenced by the low-frequency response of the NI-4472 data acquisition card, which has a discharge time constant of 46.8 milliseconds, owing to a relatively high AC -3 dB cut-off frequency of 3.4 Hz. A thorough explanation and detailed analysis of the discharge time constant effects on the results is included in Appendix C.

The behaviour of the pressure transducers in the first couple of milliseconds after disc rupture, from Figure 4-25, is not understood. The large pressure spikes appear to indicate the development of acoustic shockwaves and pressure rarefactions. However, the polarity of the signals is opposite to what would be expected, as the initially pressurised upstream sensor registers a sudden increase in pressure, and the downstream sensor initially under vacuum conditions displays a pressure reduction of -73.5 psi. After the initial 3 milliseconds, the pressure response is physically explicable, with the upstream pressure dropping to about 21 psi, and the downstream pressure increasing to about 19 psi, both within a few milliseconds. The pressure at the bottom of the liquid reservoir only begins to drop after 7 milliseconds, to about 49 psi, and the pressure inside the vacuum tank is not significantly affected by the blow-down, with the pressure increasing intermittently, with maximum amplitude of about 13 psi.

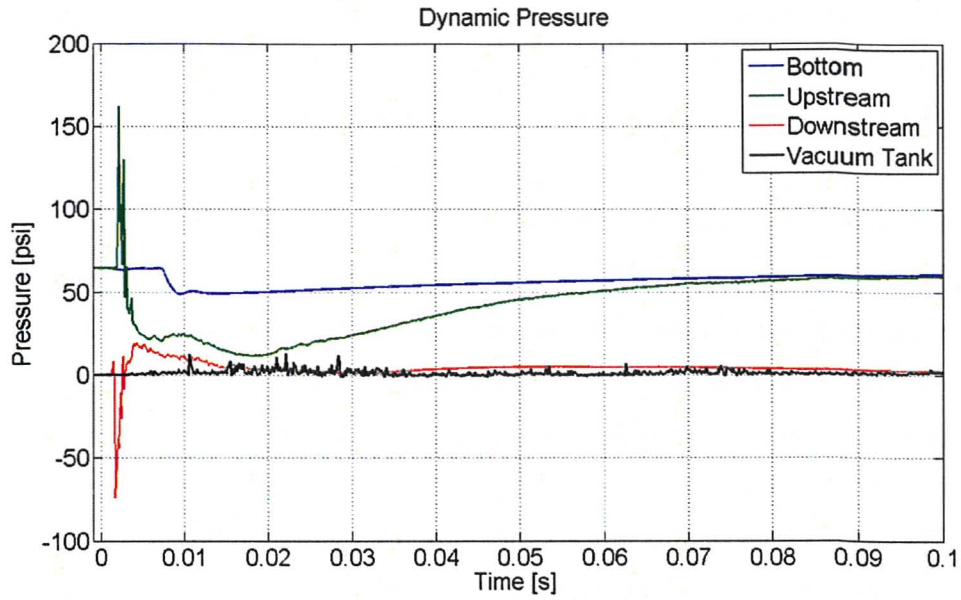


Figure 4-24. Dynamic Pressure vs. Time (6th Test)

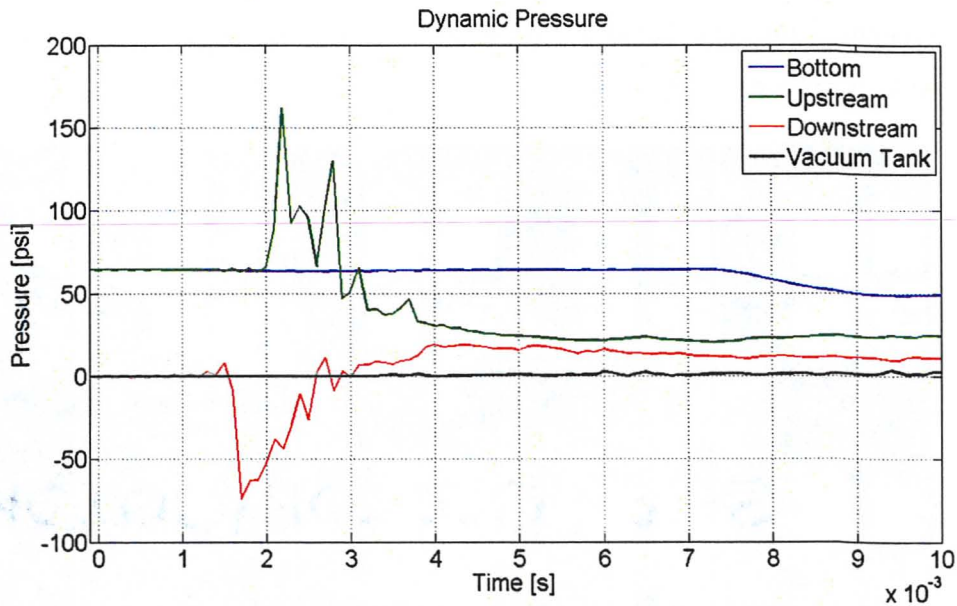


Figure 4-25. Dynamic Pressure vs. Time (6th Test; 0.01 s Timescale)

The blow-down was captured with a high-speed camera at a frame rate of 2,000 frames per second. Figure 4-26 displays images obtained during the early stages of the blow-down. Unfortunately, due to the configuration of the cooling design, the viewing area of the sight glasses is vertically split at the centre by a threaded rod that was needed to seal the upstream section of the blow-down rig. Initially, the vapour bubbles inside the liquid show signs of growth, through a darkening of the shadows on the bubble contours, suggesting an initiation of heterogeneous nucleation throughout the liquid R-134a, with the existing bubbles serving as the main nucleation sites. It is difficult to determine the precise instant at which the disc opens in relation to the flow visualisations, and the instant of rupture was matched to the first perceived bubble interface perturbation. Throughout the initial 5 milliseconds of the visualisation, the bubble growth behaviour continues at a seemingly increasing rate. The nucleation gains significant intensity between 7 and 8 milliseconds after the first signs of transient behaviour, which corresponds to the time at which the pressure at the bottom of the pressurised liquid reservoir begins to drop, as shown in Figure 4-25. Vigorous heterogeneous boiling throughout the bulk liquid is visible at 9 milliseconds, immediately followed by the explosive phase change.

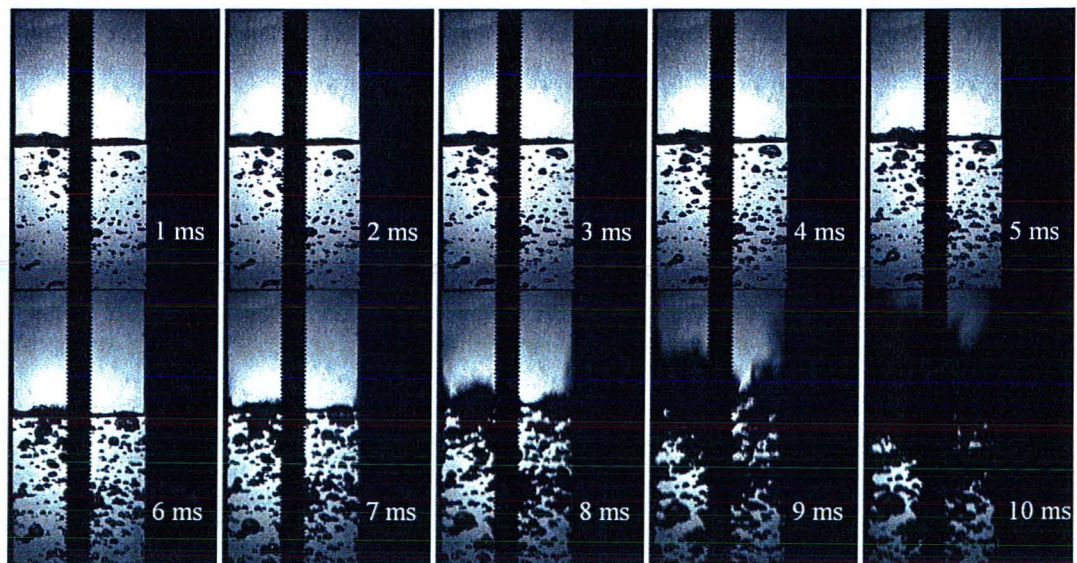


Figure 4-26. High-Speed Images of Initial Stages of Moderate-Pressure Blow-Down

The pressure just upstream of the rupture disc falls considerably between 10 to 20 milliseconds after rupture, shown in Figure 4-24, coinciding with the violent phase change that begins in the last couple of images in Figure 4-26. Unfortunately, due to the magnitude and intensity of the bulk-boiling phenomenon, the backlighting technique, consisting of a light source opposite the camera lens illuminating the test section from behind, was unable to deliver enough brightness to capture a visualisation of the flow between 10 and 300 milliseconds after disc rupture. Figure 4-27 shows high-speed images spanning the entire flashing process. Images 2 and 3 do not display any visualisation of the flow. Flow visibility is regained in image 4, and highly intermittent bubbly flow can be observed. The intensity of the flashing is reduced in images 7 and 8, and there seems to be an annular flow regime developing, with counter-current liquid films falling on the outside of the flow area, at the sight glasses. The liquid on the windows remains visible throughout images 10 to 12, with the inner core fluid vaporising, and during the final second of the blow-down, represented in images 13 to 16, all of the remaining liquid changes to the vapour phase.

The phenomena displayed in the visualisations can be identified and compared to the physical pressure and temperature results provided in Figure 4-22 and Figure 4-23. The transient temperature drop requires about 300 milliseconds to completion, and according to the temperature results, steady state is established before 375 milliseconds, corresponding to image 4. Thus, flow visualisations of the transient stage of the blow-down were not captured. Between images 4 to 6, the static pressure fluctuations about a constant value are indicative of a high degree of mixing between the separate phases, and the equalised pressure at saturation conditions is established throughout the rig after image 6. The physics are in agreement with the observed behaviour, in that the flow is highly intermittent in images 4 to 6, and a more uniform annular flow configuration is established in image 6, which remains until the end of the blow-down. The long-term temperature data, not included in this text, indicates complete vaporisation after 3.5 seconds, which is again in agreement with the visual evidence in image 16.

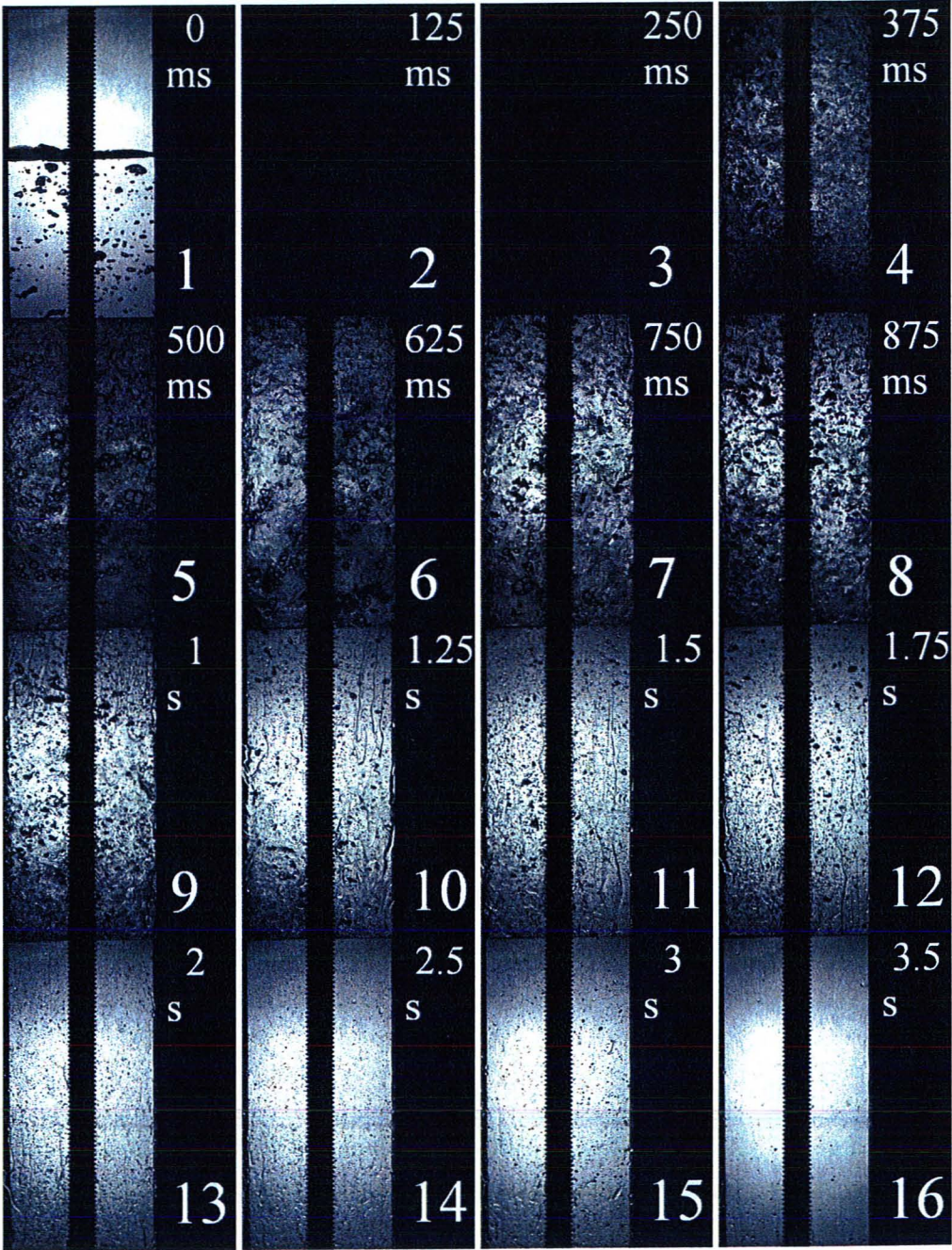


Figure 4-27. High-Speed Images of Moderate-Pressure Blow-Down

4.4 Thermodynamic Analysis

In order to properly analyse the fluid behaviour following the sudden break of the rupture disc, the steady-state conditions upstream of the rupture disc before the sudden depressurisation is imposed need to be accurately determined. Furthermore, given the significance of the phenomena occurring during the first few milliseconds following disc rupture, displayed in Figure 4-25, establishing an objective and repeatable method of determining the precise instant of rupture disc opening is very important. A good estimate of the starting point of the blow-down in the time domain allows for an improved evaluation of the physical phenomena such as signal phase lags, time delays associated with wave propagation speeds, and liquid volume effects. The distances travelled by the pressure waves generated at the disc location immediately following the burst towards the locations of interest, such as measurement points and wave reflection boundaries, need to be identified. This necessitates a thermodynamic analysis of the pressurised fluid inside the reservoir, such that important parameters including liquid level and speed of sound can be estimated.

4.4.1 Determination of Initial Liquid Volume

The initial height of the liquid volume inside the blow-down rig just before the disc ruptured in the last commissioning test was determined through a thermodynamic analysis of the R-134a at its temperature and pressure conditions, and a detailed description of the analysis procedure is provided in this section. The uncertainties related to the mass, pressure, and temperature measurements and the relevant calculations are given in Appendix D. In order to simplify the calculations and establish generalised initial conditions that could be applied for all subsequent experiments, some assumptions were incorporated into the analysis.

The accumulator that is used to pressurise the liquid refrigerant is initially filled with vapour, which is steadily driven out by the expansion of the accumulator diaphragm due to pressurised nitrogen. The blow-down initiates near the end of this pressurisation, after the majority of the accumulator is filled with compressed nitrogen gas. For the initial conditions calculations, the accumulator was assumed to be completely filled with nitrogen, and the vapour refrigerant content was considered negligible. In the worst-case scenario, the accumulator would be filled entirely with vapour R-134a, which amounts to a total volume of 2.80 litres. The connecting lines between the accumulator and the pressurised reservoir, and between the R-134a bottle and the charging port, were also assumed to have negligible volumes. The liquid and vapour densities were assumed to be constant throughout the respective domains, and were calculated based on the measurements obtained at the sensor locations. Although the blow-down rig was designed such that the flow area upstream of the rupture disc is constant, there is a small discrepancy between the internal cross-sectional area of the pipe and square transition sections. An average constant flow area was used in the calculations, based on the volume and length of the upstream section.

For subcooled blow-downs, an average temperature was calculated for the liquid and superheated vapour phases from a short time period just before disc rupture. The liquid static pressures were also obtained in the same manner. For saturated blow-downs, such as the last commissioning test, the temperature of the liquid was assumed to be that of 0 quality at the corresponding pressure conditions. The density of the liquid is determined from the temperature and pressure, and a preliminary liquid column height, H_l , is then calculated based on Equation (13):

$$H_l = \frac{m_0}{\rho_l A} \quad (13)$$

The vapour pressure can then be obtained by subtracting the hydrostatic pressure from the measured liquid pressure as shown in Equation (14):

$$P_g = P_l - \rho_l g H_l \quad (14)$$

where g is the gravitational acceleration. From the vapour pressure, the mass of the vapour phase can be determined using ideal gas considerations, as shown in Equation (15):

$$m_g = \frac{M_{R134a} P_g A (H_0 - H_l)}{RT_g} \quad (15)$$

where M_{R134a} is the molar mass of the refrigerant, and R is the ideal gas constant. The vapour mass is then subtracted from the total mass yielding the liquid mass as shown in Equation (16):

$$m_l = m_0 - m_g \quad (16)$$

From the liquid mass, a new liquid height can then be determined from Equation (17):

$$H_l = \frac{m_l}{\rho_l A} \quad (17)$$

The refined value obtained for the liquid height is then substituted back into Equation (14) and the parameters are solved iteratively until convergence is attained. The sonic velocities for the liquid and vapour phases can then be determined using Equations (18) and (19) respectively:

$$a_l = \sqrt{\frac{K}{\rho_l}} \quad (18)$$

$$a_g = \sqrt{\frac{c_p \cdot P_g}{c_v \cdot \rho_g}} \quad (19)$$

where K is the bulk modulus of the fluid, c_p is the specific isobaric heat capacity, and c_v is the specific isochoric heat capacity. The initial conditions computed for the last commissioning test are presented in Table 4-2. The same procedure was applied in the analysis of all the subsequent experiments in order to establish the initial thermodynamic conditions of the system.

Table 4-2. Initial Steady-State Thermodynamic Properties for 6th Commissioning Test

Phase <i>l or g</i>	Pressure <i>P</i> (kPa)	Temperature <i>T</i> (°C)	Density <i>ρ</i> (kg/m ³)	Volume <i>V</i> (L)	Mass <i>m</i> (kg)	Sonic Velocity <i>a</i> (m/s)
Liquid	443	12.0	1250	5.6	6.7	566
Vapour	440	14.6	21	16.2	0.3	147

4.4.2 Determination of Rupture Disc Burst Instant

A methodology has been implemented that permits determination of the opening instant of the rupture disc based on the analytically determined thermodynamic conditions of the pressurised fluid inside the blow-down rig. Barták (1990) concluded systematically that the propagation velocity of the depressurisation wave during the initial stages of a blow-down does not differ from the local sound velocity, which forms the basis of the current approach for establishing the time of rupture. It must be noted that the computed estimates for the speed of sound are only valid for a short period of time directly following disc rupture, and are unsuitable beyond the point of significant vapour generation in the liquid domain. The effect of vapour production on the speed of sound is substantial, the sonic velocity being lower in a two-phase mixture than in a liquid or vapour phase alone. As the void fraction increases with the development of the blow-down flow, the sonic velocity estimates are expected to deteriorate. The damping also increases as a result of vapour formation, which slows down and reduces the amplitude of the travelling pressure waves. From the speed of sound, the time required for pressure wave propagations is calculated based on the distances from the locations of the events of interest and the corresponding measurement locations. Figure 4-28 displays computed times after disc rupture for the main compression waves, rarefactions, and pressure reflections.

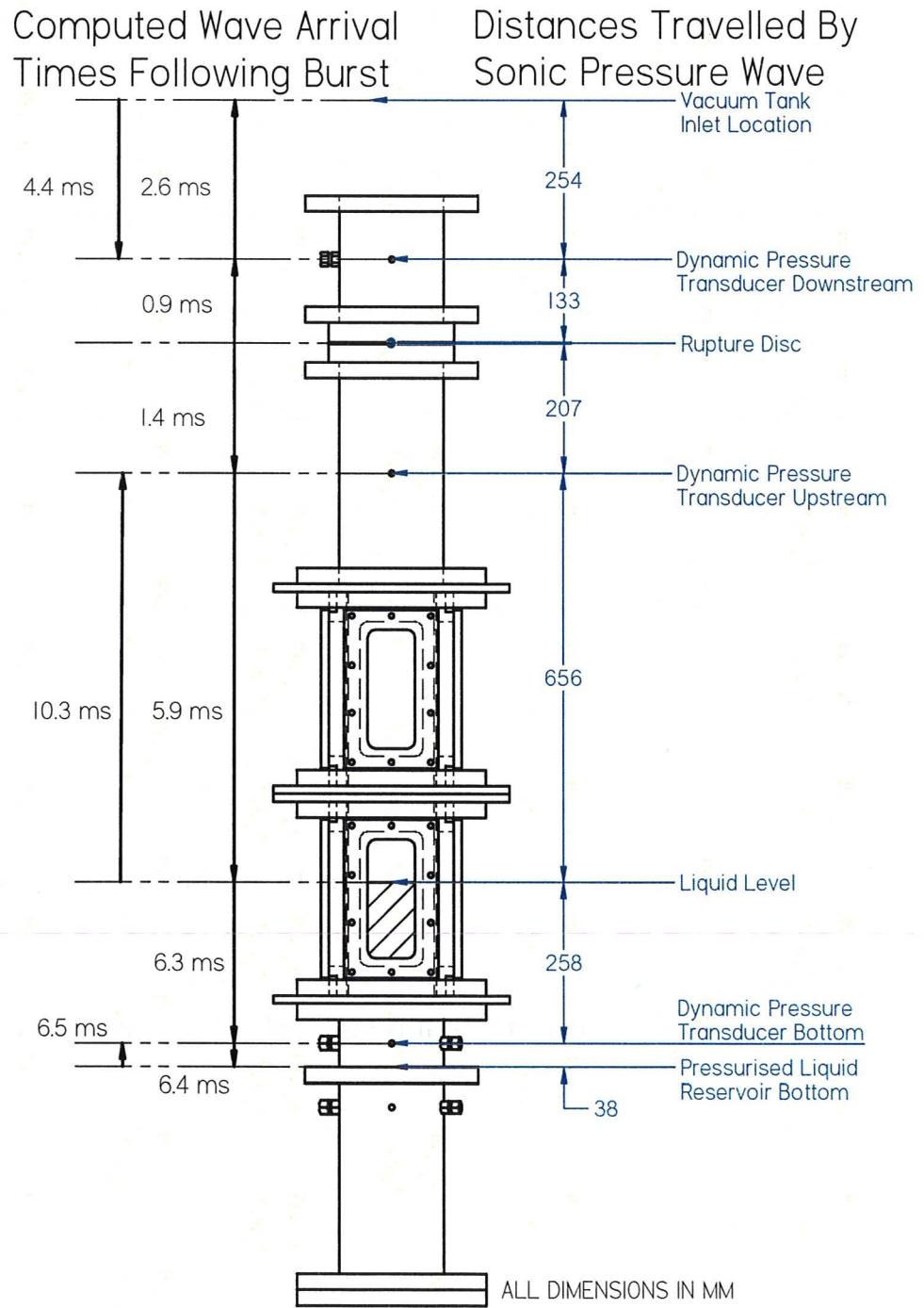


Figure 4-28. Wave Propagation Times for 6th Commissioning Test

The estimated time required for the wave generated at the rupture disc to arrive at the dynamic pressure transducer directly downstream of the rupture disc is 0.9 milliseconds, as indicated in Figure 4-28. Consequently, the first significant rise in the mean pressure signal was set to occur 0.9 milliseconds after the initiation of the transient blow-down. The noise in the pressure signal is about ± 0.003 psi, and the first detectable pressure rise was usually of the order of 0.2-0.3 psi. This procedure was found to be highly repeatable for all subsequent experiments, and provided a consistent means of accurately establishing the acquired signals in the time domain. The determination of the starting time of the transient then allows for methodical evaluation of important post-blow-down phenomena. The mean pressure signal behaviour at the instant of rupture was found to be very similar across all experiments, unaffected by factors such as the signal sampling rate and the initial pressure magnitude. Therefore, the error associated with the rupture time for all experiments is governed by the identification of the increase in the mean pressure signal, which, based on the minimum sampling rate of 10 kHz, corresponds to ± 0.2 milliseconds. The importance of objectively determining the instant of bursting of the disc is further demonstrated since the uncertainty is of the same order of magnitude as the timing of the wave propagation rates.

The pressure signals obtained about 1.7 to 2.1 milliseconds just before the rise in the mean pressure for the experiments sampled at 10 kHz displayed peculiar periodic diverging oscillations that are not fully understood. These effects were not present for experiments sampled at 30 kHz. It is suspected that this behaviour is a product of data acquisition aliasing effects, since the signal oscillates about an average value of 0 psi and there are no other oscillations present. As previously mentioned, the increase in the mean pressure signal showed consistent repeatable behaviour across all experiments, and the sinusoidal oscillations do not introduce any additional error in the determination of the rupture time. It is difficult to apply a similar methodology for the identification of the rupture instant on the flow visualisations, and the starting point was usually set to match the first frame to display a sudden perturbation in the fluid. A comparison with dynamic signals obtained in terms of pressure behaviour and observed phenomena indicates that

the vapour generation occurs within a couple of milliseconds of the recorded pressure drop in the liquid, but an objective uncertainty analysis cannot be established with confidence.

The depressurisation wave is estimated to arrive at the bottom liquid pressure transducer about 6.3 milliseconds following rupture as shown in Figure 4-28, and Figure 4-25 indicates a decrease in pressure beginning about 7 milliseconds after the opening of the disc. The deviation between the pressure recorded signal and analytical propagation estimate is attributed mostly to the uncertainties involved in the determination of the initial conditions. Figure 4-28 also illustrates that the rarefaction wave arrives at the upstream pressure transducer 1.4 milliseconds following rupture, 0.5 milliseconds later than the downstream pressure transducer measures a compressive pulse. This 0.5 milliseconds phase difference between the two pressure transducer measurements due to the delay in the arrival of the sonic pressure wave is visible in Figure 4-25. The downstream sensor displays a sudden pressure drop at exactly 1.7 milliseconds, and the upstream sensor displays a sudden pressure rise at exactly 2.2 milliseconds after rupture. The cause of this unexpected pressure response is investigated in Section 6.3.3.

4.5 Overview of Commissioning Results

Upon the successful completion of the sixth commissioning test, the commissioning phase of the project was brought to a close. Important experience was gained through carrying out the commissioning experiments, and the knowledge obtained was directly transferrable towards the realisation of the experimental phase of the research project. Through successfully controlled tests, the experimental concept of the rig design was demonstrated, and confidence was gained in the feasibility of the experimental rig for simulating steam generator blow-downs and studying the ensuing transient tube-loading phenomenon. From a mechanical and structural safety perspective,

the commissioning tests showed that the experimental rig was capable of withstanding moderate pressures without any perceptible signs of failure. The most critical components in the experimental set-up were the quartz sight glasses, and upon post-commissioning visual examination, the windows displayed no indication of stress-related mechanical aggravation or crack propagation.

Winters and Merte (1979) identified a characteristic length L/D , where L is the length of the section containing the pressurised fluid, and D is the flow pipe diameter. The blow-down flow behaviour can be predicted based on this characteristic length, which represents the volume to break area ratio. For large characteristic lengths, the flow is expected to demonstrate equilibrium thermodynamic behaviour, and a deviation from thermal equilibrium is expected for smaller values, in pipes less than about 5 to 10 diameters long. The small-scale commissioning rig has a characteristic length of 84, whereas the large-scale ratio is about 7.3. Therefore, the blow-down is expected to occur mostly at equilibrium for the small-scale configuration, and some non-equilibrium effects such as pressure undershoot and mechanical slip are expected for the large-scale configuration. The small and large-scale flashing behaviour differed significantly, most notably in the intensity of bubble generation, as well as the duration of the flashing relative to the available pressurised volume. The rates of depressurisation, liquid temperature drop, and phase change in the small-scale commissioning tests were much slower, especially considering that the volumes were about 40 times smaller than those of the large-scale commissioning tests. Despite these significant differences, the widely discussed pressure undershoot phenomenon was barely noticeable in the dynamic liquid pressure response of the large-scale commissioning tests.

Most of the liquid blow-down studies available in the published literature have investigated vessels that are initially filled with liquid, reporting very rapid wave propagation rates and, in many cases, such as experiments performed by Edwards and O'Brien (1970) and Alamgir and Lienhard (1981), very significant non-equilibrium behaviour. Deligiannis and Cleaver (1996) performed blow-down experiments in

partially filled vessels, and reported a much slower rate of depressurisation of the liquid domain compared to full liquid vessel blow-downs, due to the lower speed of sound in the vapour domain. This is in line with the computed estimates of wave propagation rates provided in Figure 4-28, which show that the rarefaction wave arrives at the liquid-vapour interface 6 milliseconds after the opening of the rupture disc. Thus, there is more time available for the superheated liquid to nucleate than there would be if the vessel was entirely filled with liquid, which explains why the pressure undershoot behaviour was not very significant.

The behaviour of the rupture discs was explored in depth for the commissioning tests, and vital experience was acquired with regards to pressurisation using the nitrogen gas cylinder and accumulator, especially concerning the steady-state thermodynamic considerations prior to controlled blow-down initiation. The instrumentation, particularly the thermocouple and static pressure sensors, satisfactorily demonstrated the function of the data collection and recording system. The dynamic pressure signals however were not fully explained, and some modifications to the signal conditioning and acquisition methods were implemented in the subsequent experimental stage in order to provide improved low-frequency response, potentially providing further insights into the physical mechanisms taking place. Overall, the commissioning tests fulfilled their intended purpose, and the tube loading experiments with the test section installed were ready to be performed.

Chapter 5 – Experimental Results

The experimental phase of this project was designed to improve the understanding of dynamic loading of steam generator tubes during sudden depressurisation of a stagnant volume of fluid inside a steam generator. The liquid height inside the vessel, or specifically, the location of the liquid free surface with respect to the tube bundle is an important parameter that necessitates investigation. Since the initial conditions inside the steam generator prior to the postulated SLB may vary, it was desired to study the variation in dynamic loading behaviour when the tube bundle is fully submerged in the liquid water region, as opposed to the steam region above the liquid free surface. As such, two tube loading experiments were to be performed, with the liquid-vapour surface lower and higher than the tube bundle respectively for each test. In order to study the effects of volume of liquid independently, two other experiments were to be performed, with small and large volumes of liquid inside the pressurised liquid reservoir, without the test section installed, under similar thermodynamic initial pressure conditions. The experiments were all carried out using the high-pressure 85-psi rupture discs. The experiments without the test section installed are very similar to the previous moderate-pressure commissioning tests, and similar behaviour was expected.

Since the saturation temperature of R-134a at the rupture pressure of 85 psi is 20.8 °C, the experiments could be performed under ambient conditions without any additional cooling. The experimental technique was essentially identical to that of the large-scale commissioning tests, with some changes implemented in the data collection system. The NI-4472 data acquisition card has a frequency response that is acceptable for dynamic measurements that occur at high frequencies, but does not allow for investigation of phenomena with lower frequency response characteristics. Since the long-term behaviour of the transient was of interest in this study, the data acquisition card was DC-coupled, bypassing its cut-off frequency, and two Piezotron couplers (Kistler

model 5134) were used to provide excitation power and signal conditioning for the piezoelectric sensors. With a -3 dB cut-off frequency of 0.036 Hz, and a discharge time constant of 4.42 seconds, it was possible to capture events that did not occur at very high frequencies, limited only by the low cut-off frequencies of the sensors.

5.1 First Experiment

The experimental phase of the project commenced with a simple pipe blow-down without any obstruction to the flow in the pressurised region. The blow-down was triggered using the nitrogen cylinder and accumulator system, and a total compression of about 4 psi was produced, which initiated the pressure relief on the rupture disc. The initial steady-state conditions for the first experiment are provided in Table 5-1 and the static pressure results are shown in Figure 5-1. The response to the sudden depressurisation happens with a time delay of just below 100 milliseconds, after which a reasonably rapid physical response is depicted. The upstream static pressure response shows a rapid pressure decrease that is almost linear, and the pressure recovers after about 10 milliseconds, followed by a ‘quasi-steady’ pressure plateau that is maintained for about 150 milliseconds, and finally the pressure falls towards the equalised conditions signifying the end of the transient.

Table 5-1. Initial Steady-State Thermodynamic Properties for 1st Experiment

Phase <i>l or g</i>	Pressure P (kPa)	Temperature T (°C)	Density ρ (kg/m ³)	Volume V (L)	Mass m (kg)	Sonic Velocity a (m/s)
Liquid	554	19	1230	4.5	5.5	534
Vapour	551	23.2	26	16.4	0.4	147

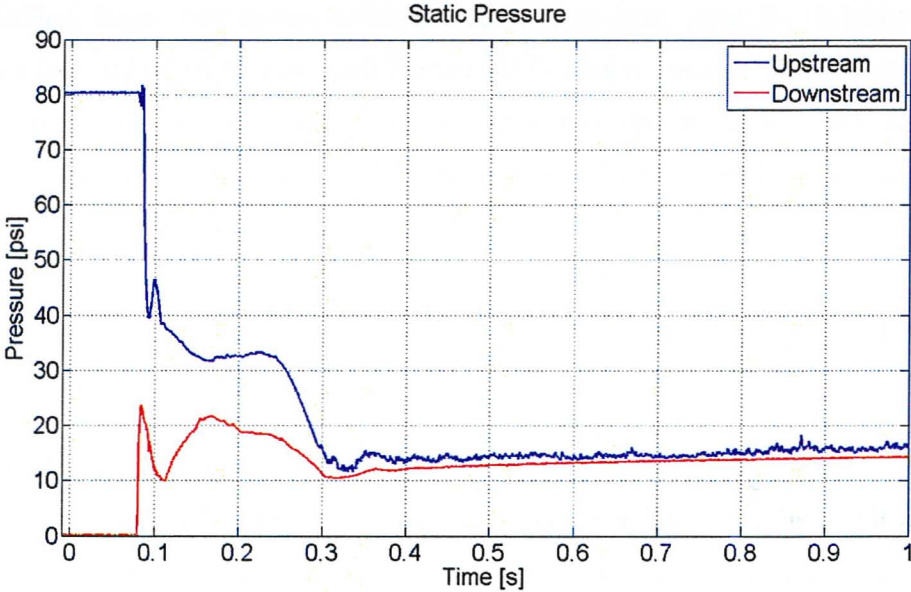


Figure 5-1. Static Pressure vs. Time (1st Experiment)

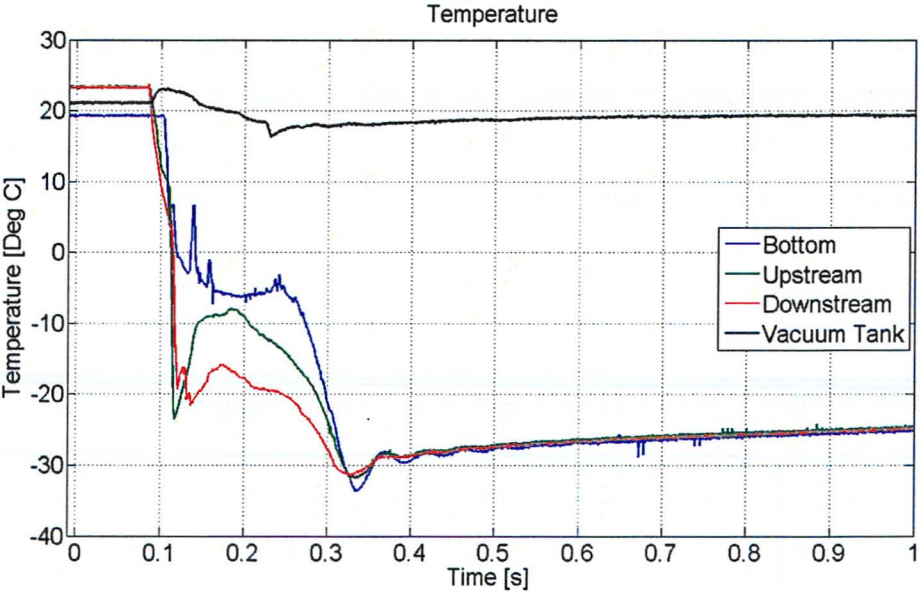


Figure 5-2. Temperature vs. Time (1st Experiment)

The temperature results are presented in Figure 5-2. It is interesting to note that the temperature response seems to follow the same time frame as the static pressure, in that the response is delayed by almost 100 milliseconds, followed by about 150 milliseconds of transient behaviour, after which the steady-state saturation conditions are established. Figure 5-2 depicts distinct differences in response time between the vapour and liquid phases during the initial stage of the blow-down. The three locations initially containing vapour above the liquid free surface, just downstream of the rupture disc, and inside the vacuum tank, all show a transient response initiating at about the same time. The thermocouples inside the blow-down rig indicate a vapour expansion accompanied by a temperature reduction from 23 °C to about -23 °C. Both thermocouples then register a rise in temperature, with a larger increase indicated by the lower of the two thermocouples, due to a higher amount of superheated liquid in the vicinity. The vacuum tank initially sees a small rise in temperature associated with pressure increase, followed by a small temperature reduction below initial conditions.

The liquid temperature response at the bottom of the reservoir lags the other temperature drops by about 15 milliseconds, which is most probably due to the period of time that was required for the phase change to occur at this thermocouple location. The temperature drop is interrupted by occasional peaks, presumably due to the thermocouple junction coming into contact with superheated fluid for finite periods of time, in between the vapour temperature measurements. At the end of the transient flashing, at about 0.35 seconds, the temperatures proceed towards saturation conditions corresponding to the pressure, and this signals the end of the transient two-phase blow-down temperature response.

The dynamic pressure response is plotted in Figure 5-3 on the same timescale as the previous static pressure and temperature curves. Figure 5-4 presents a close-up of the first 10 milliseconds after rupture for identification of the dynamic pressure behaviour in the early stages of the transient. Beyond the discharge point, the pressure changes are too slow to be captured, and the drifting signal has been omitted from the plots.

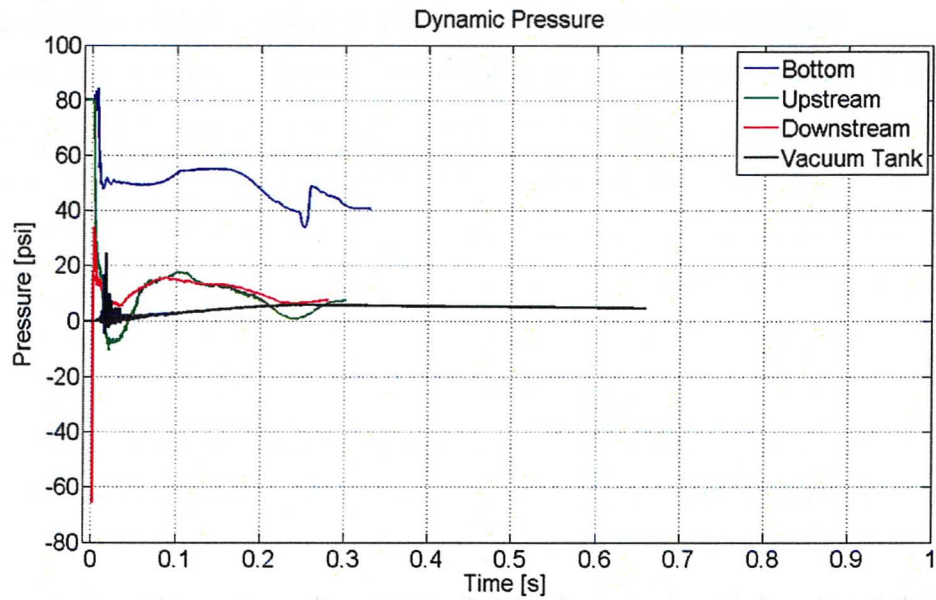


Figure 5-3. Dynamic Pressure vs. Time (1st Experiment)

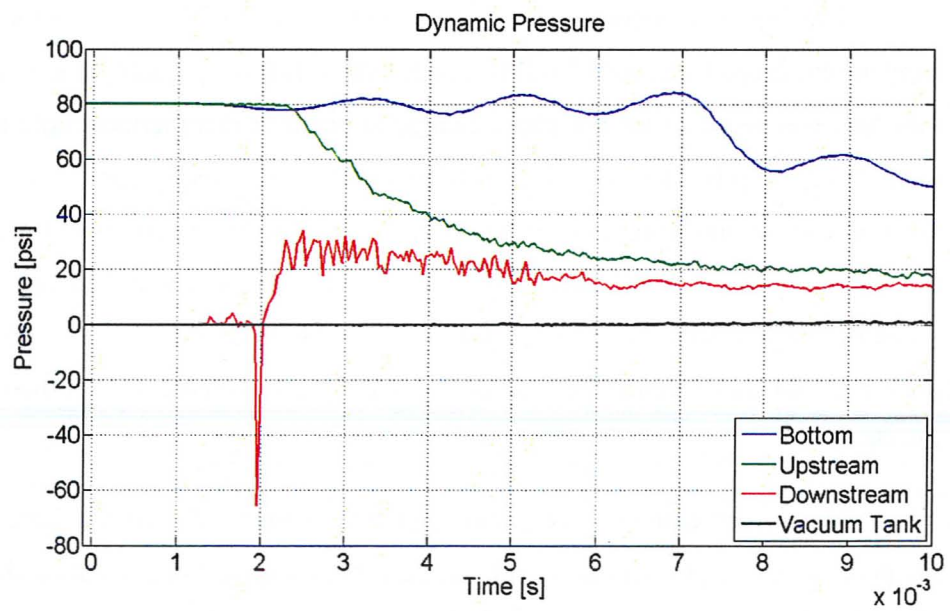


Figure 5-4. Dynamic Pressure vs. Time (1st Experiment; 0.01 s Timescale)

The time at which the sensor signals begin to discharge corresponds approximately with the time at which the static pressure signals show the pressures beginning to follow a steady-state path. From Figure 5-3, the pressure transducer signals at the bottom of the pressurised liquid reservoir and at the vacuum tank appear to be capturing the physical pressures during the blow-down, but the two pressure transducers closer to the rupture disc show intriguing behaviour, especially during the first few milliseconds after rupture. The bottom pressure in Figure 5-4 shows a few small fluctuations in pressure immediately after rupture, followed by a steep pressure drop to about 55.7 psi, which then recovers to about 61.6 psi and drops again in less than 10 milliseconds, and then remains almost constant at about 55 psi for 200 milliseconds. The behaviour seems appropriate for rapid depressurisation pressure response, but the pressure magnitudes are different from those indicated by the static pressure sensor.

The vacuum tank pressure transducer shows some relatively small-amplitude high-frequency pressure spikes between 10 and 35 milliseconds after rupture, but the overall behaviour seems to indicate a practically insignificant transient pressure increase in the tank, which validates the suitability of the design in replicating a SLB to atmospheric conditions, in that the receiver pressure should not affect the blow-down. The pressure transducer just downstream of the rupture disc, initially in vacuum, shows some strange behaviour. Immediately after rupture, there is a slight increase in pressure, followed by a sharp spike downward, reaching -65.5 psi absolute pressure. The pressure then increases as would be expected, to about 30 psi, accompanied by high-frequency fluctuations, and settles at about 15 psi for about 150 milliseconds. The negative pressure spike is not physically believable, and clearly deviates from the real pressure inside the blow-down rig. The pressure transducer directly upstream of the rupture disc does not show any immediate pressure spikes, but also falls to pressures below absolute zero, before settling at about 13 psi. The strange dynamic pressure data is suspected to be a product of transient acceleration and thermal effects, which are analysed more rigorously in Section 6.3.

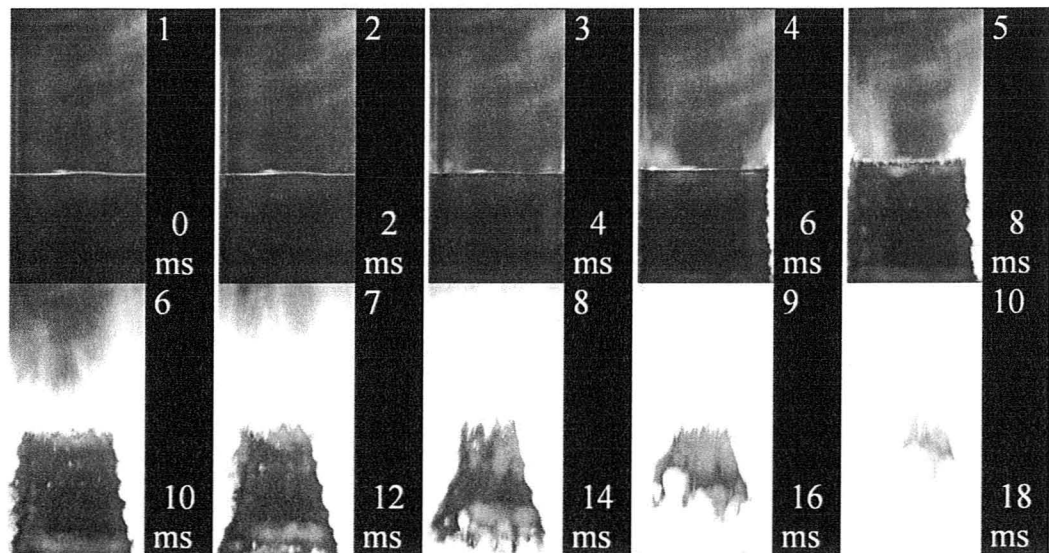


Figure 5-5. High-Speed Images of Initial Stages of 1st Experiment

It is likely that the huge volume of vapour generated during the early stages of the blow-down was responsible for significant loss of light transmission in the last commissioning test, such that the light did not pass through the two-phase medium into the camera lens, and subsequently, no image was recorded. In order to eliminate these effects, a front-lit configuration was employed in this experiment, such that the light would reflect off the liquid-vapour interfaces back to the lens, and the camera would capture the flashing flow. Figure 5-5 shows the high-speed images obtained during the initial stages of this blow-down experiment. Images 2 and 3 display flashing inception at the liquid free surface and at the vertical steel walls, and the vapour growth moves towards the bulk fluid as shown in images 4 and 5. Image 6 shows the development of clear wavy patterns along the interface between the growing vapour region and the apparently static liquid centre, probably as a result of shear layer instability.

In images 7 and 8, a substantial quantity of vapour that probably nucleated at the bottom of the reservoir can be seen arriving at the bottom of the frame. Meanwhile, the liquid upper surface does not seem to move at all. In image 9, the majority of the R-134a

in the frame is composed of vapour, and this flashing growth continues vigorously into image 10, eventually occupying the entire frame. The large amount of bubbles generated reflected a large amount of light back towards the camera lens, effectively saturating the picture, preventing the images from adequately depicting the blow-down process. Thus, once again, the attempt to capture a flow visualisation of the blow-down was partly unsuccessful, this time due to an overwhelming light intensity being reflected back into the camera. In a continuation of the previous images, Figure 5-6 shows high-speed images of the behaviour after the initial phase change mechanism takes place. The flashing intensity appears to decrease between images 12-15, before the vapour concentration increases again saturating the picture in images 17 and 18. Image 19 shows a decrease in the rate of vaporisation, and this continues through images 20-26.

After about 400 milliseconds, steady-state conditions are attained, and the remaining mixture at saturated state continues to vaporise under equilibrium conditions. Unfortunately, not much information could be gained from these images since the reflections off the liquid-vapour interfaces produced strong white spots on the frames, and it was therefore difficult to identify the physical mechanisms taking place. The densely distributed white spots visible in images 19-26 represent liquid droplets entrained in the flashing flow. The droplets originate from the centre of the flashing flow area, and splash outwards towards the pipe walls and sight glasses. Images 21 and 22 display some liquid films falling downwards at the sight windows. This observed counter-current annular flow pattern is very similar to that observed for the last commissioning test after the transient stage of the blow-down was complete. Between 10-60 and 200-280 milliseconds after rupture, the pressure difference between the sensors dictates that the flow should accelerate downwards away from the break location, or at least decelerate. The flow visualisations indicate that during these times, the flow is accelerated upwards towards the break, further casting doubt on the validity of the dynamic pressure results. These images are useful for determining the time periods between the different phase change mechanisms, and, to some extent, the degree of flashing and bubble growth.

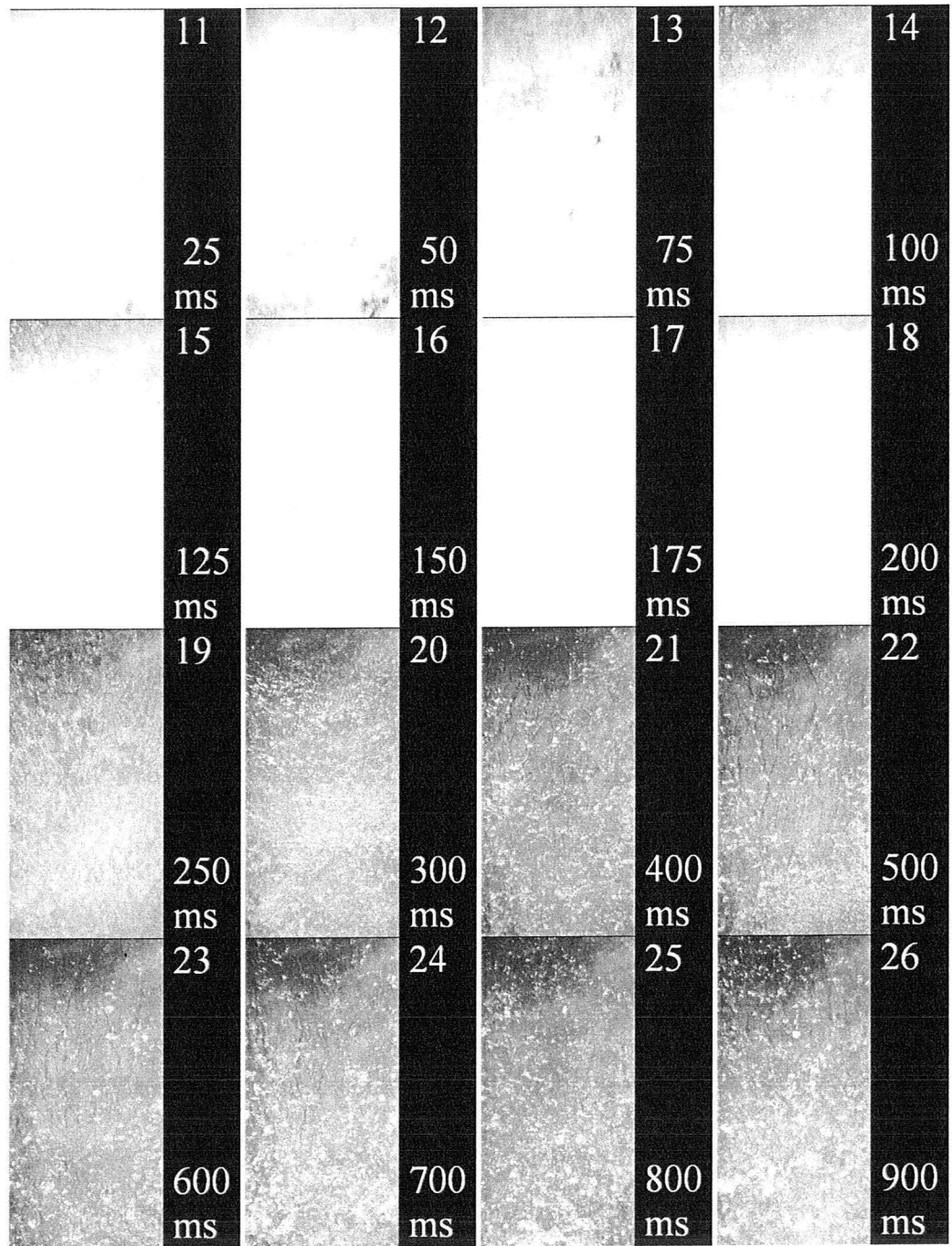


Figure 5-6. High-Speed Images of 1st Experiment

5.2 Second Experiment

The second experiment was a large-volume subcooled pipe blow-down. All of the previous tests, with the exception of the third small-scale commissioning test, were saturated blow-downs. The remaining experiments were all performed under subcooled initial conditions. The steady-state conditions are given in Table 5-2 and the static pressure plot in Figure 5-7. The time delay before response is similar to that of the first experiment, after which the upstream pressure falls rapidly, and the downstream pressure sharply spikes upward. The upstream pressure shows a period of little change in pressure lasting for about 200 milliseconds, before steady-state conditions are established at about 0.45 seconds. The pressure magnitudes established during the plateau region are larger than the previous experiment by more than 10 psi. Another clearly observable difference between the static pressure responses of the first two experiments is that the duration of the transient stage is about 100 milliseconds longer for this experiment.

The temperature response in Figure 5-8 is similar to that of the first experiment. The time frame corresponds well with the static pressure again, and despite the vapour initially expanding to lower temperatures, the temperatures at the beginning of the equalised stage are higher than those recorded in the first experiment. The liquid temperature response was slower than the previous experiment, and the initial recovery occurred at a higher temperature. In the vacuum tank, a substantial amount of expanding vapour was large enough to lower the temperature by 15 °C.

Table 5-2. Initial Steady-State Thermodynamic Properties for 2nd Experiment

Phase <i>l or g</i>	Pressure <i>P</i> (kPa)	Temperature <i>T</i> (°C)	Density ρ (kg/m ³)	Volume <i>V</i> (L)	Mass <i>m</i> (kg)	Sonic Velocity <i>a</i> (m/s)
Liquid	579	16.2	1240	11.5	14.3	548
Vapour	572	21.7	28	10.3	0.3	146

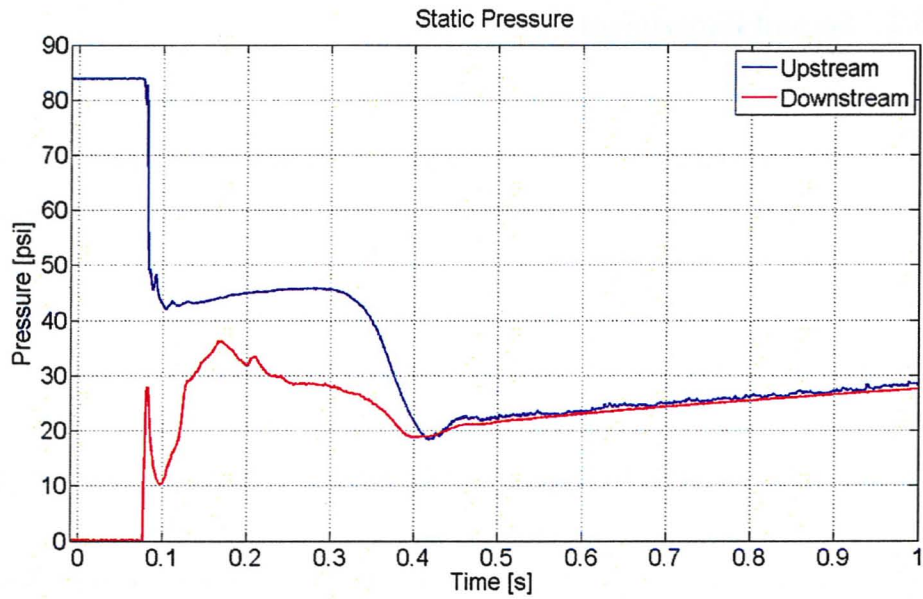


Figure 5-7. Static Pressure vs. Time (2nd Experiment)

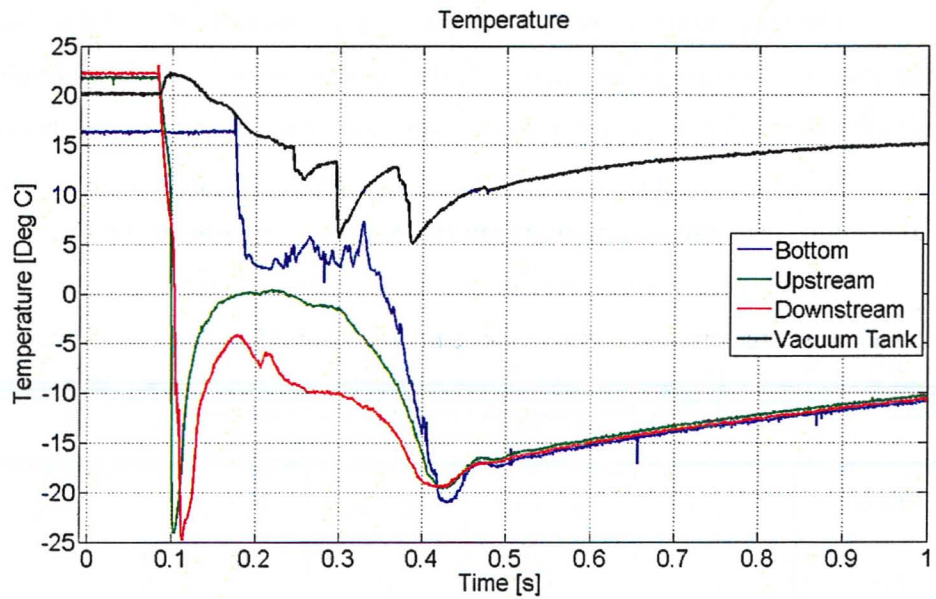


Figure 5-8. Temperature vs. Time (2nd Experiment)

The dynamic pressure response is presented in Figure 5-9 and Figure 5-10. The transient lasts longer for this experiment than the previous one, which was expected since there is more than twice the amount of liquid being depressurised. Again, the dynamic pressures in the liquid reservoir and the vacuum tank line up well with the predicted behaviour, whereas the dynamic pressure signals closer to the rupture disc display strange behaviour, especially during the first few milliseconds after rupture. A distinct difference in behaviour for this experiment compared to the previous one is the prominence of the high-frequency oscillations in the pressure just upstream of the rupture disc. The pressure amplitudes in this experiment were higher than those for the previous test. The bottom pressure transducer in particular shows stronger pressure undershoot behaviour, where the pressure is initially reduced to about 47.6 psi, lower than the previous experiment, before recovering to a pressure of about 60.2 psi, which is greater than the previous experiment.

The observed behaviour can be attributed to volume effects. Since the liquid level is closer to the rupture disc, the time required for the pressure wave to arrive at the liquid interface is shorter. The incompressibility of the liquid phase results in a relatively rapid rate of decompression (Winters and Merte, 1979). The faster depressurisation occurs, the greater the pressure undershoot, and the greater the violence with which flashing takes place (Alamgir and Lienhard, 1981). The pressure transducers directly upstream and downstream of the disc also display increased magnitudes of pressure response compared to the previous test, albeit with a stronger unexplained behaviour in the first few milliseconds. Nevertheless, disregarding the high-frequency oscillations and the reduction of pressures below absolute vacuum, the two pressure transducers record rapid pressure changes in response to the sudden burst, and the subsequent recovery pressures are comparable to each other in magnitude, with the upstream pressure lying between the recovery pressure of the bottom liquid reservoir and the downstream pressure sensor. The receiver pressure of the vacuum tank increased dynamically by about 9.9 psi during the transient. It is clear that the large volume of R-134a is producing non-negligible pressure increases inside the vacuum tank, as should be expected.

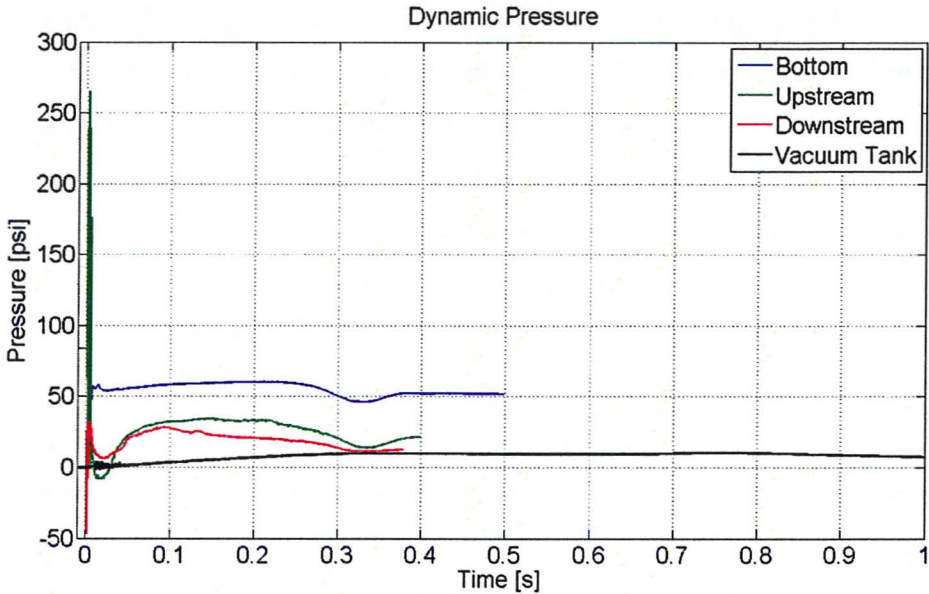


Figure 5-9. Dynamic Pressure vs. Time (2nd Experiment)

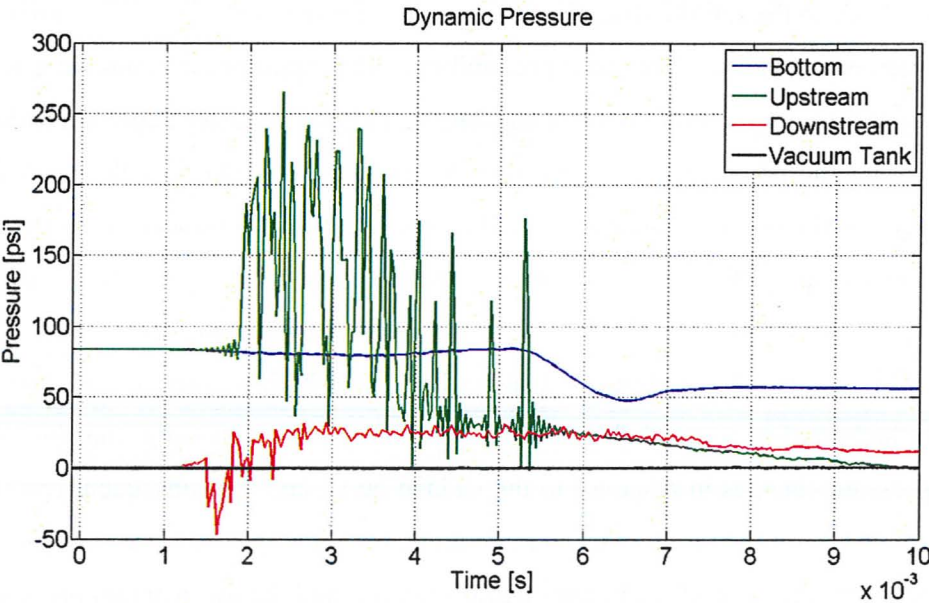


Figure 5-10. Dynamic Pressure vs. Time (2nd Experiment; 0.01 s Timescale)

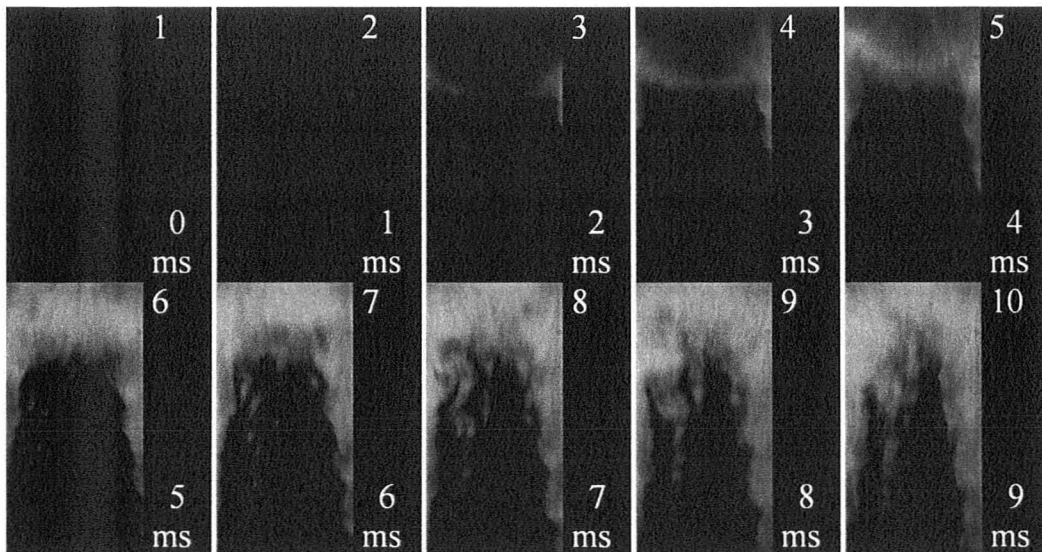


Figure 5-11. High-Speed Images of Initial Stages of 2nd Experiment

The high-speed camera set-up for this experiment was similar to the previous experiment, with the light intensity significantly reduced. Although the low light intensity made it very difficult to separately identify the initial phases, it was hoped that the problems associated with high light intensity and lens saturation would be surmounted, and high-speed visualisations of the blow-down flashing flow could be captured. As a result, the captured video showed very limited information with regards to physical conditions before and after the transient phase change, but the vapour expansion and pressure driven acceleration were adequately captured, as shown in Figure 5-11 and Figure 5-12. Image 2 shows the first signs of vapour formation, and the vapour region grows in images 3-5. The pressure driven vapour expansion originating at the walls continues to propagate into the bulk liquid, and upwards towards the break in images 6-10. Images 6 and 7 show signs of nucleation within the bulk fluid, probably originating at the surfaces of small bubbles. The expansion of these generated voids towards the break is clearly identifiable in images 8-10. The mechanism of flashing inception seen in this experiment is very similar to that observed in the last experiment.

In contrast to the previously captured flow visualisations, in which the camera system was unable to capture pictures of the flow between 20 to 250 milliseconds after disc rupture, Figure 5-12 provides insights into the two-phase behaviour of the flashing flow during this thermodynamically transient stage of the blow-down. The explosive phase change that occurred a few milliseconds after the sudden depressurisation was imposed created clouds of very small vapour bubbles, as shown in image 11. The flashing then developed an intermittent pattern predominantly consisting of rapidly accelerating vapour regions surrounded by low quality flow. Wavy streamlines composed of the two-phase mixture flowing upwards are shown in images 13-19. In images 20 and 21, the majority of the liquid had already boiled off, and the flow consisted mostly of vapour, which began to follow a straighter vertical path towards the break location. Beyond this stage, the flashing was limited to small clouds of quickly rising droplets, accompanied by falling liquid films on the outside, such as shown in image 22. Images 23-25 depict bright spots corresponding to droplets of liquid entrained in the flow, falling downwards, and suspended on the sight windows. Due to the low light intensity, the composition of the fluid inside the rig cannot be identified from the pictures once the transient effects are complete.

The physical mechanisms observed in the flow visualisations are in good agreement with the pressure and temperature results in Figure 5-7 and Figure 5-8. In images 11-19, the flashing at the bottom of the liquid reservoir is isothermal. The temperature decreases sharply towards the vapour saturation temperature at about 0.175 seconds, and between images 19-21, the changing flow behaviour occurs at a roughly constant temperature. Between images 21 and 22, at about 350 milliseconds, the mixture attains steady state at saturation conditions. Between images 19-21, the static pressure increases gradually. It may be deduced that during this period, the rate of vapour expansion exceeds the rate of vapour exhaust from the rig, which would explain the change in the flow pattern signifying an increase in the flow quality. The saturated mixture in image 22 signifies the end of the transient, and the absence of distinct liquid-vapour interfaces makes it difficult to identify the subsequent composition of the fluid.

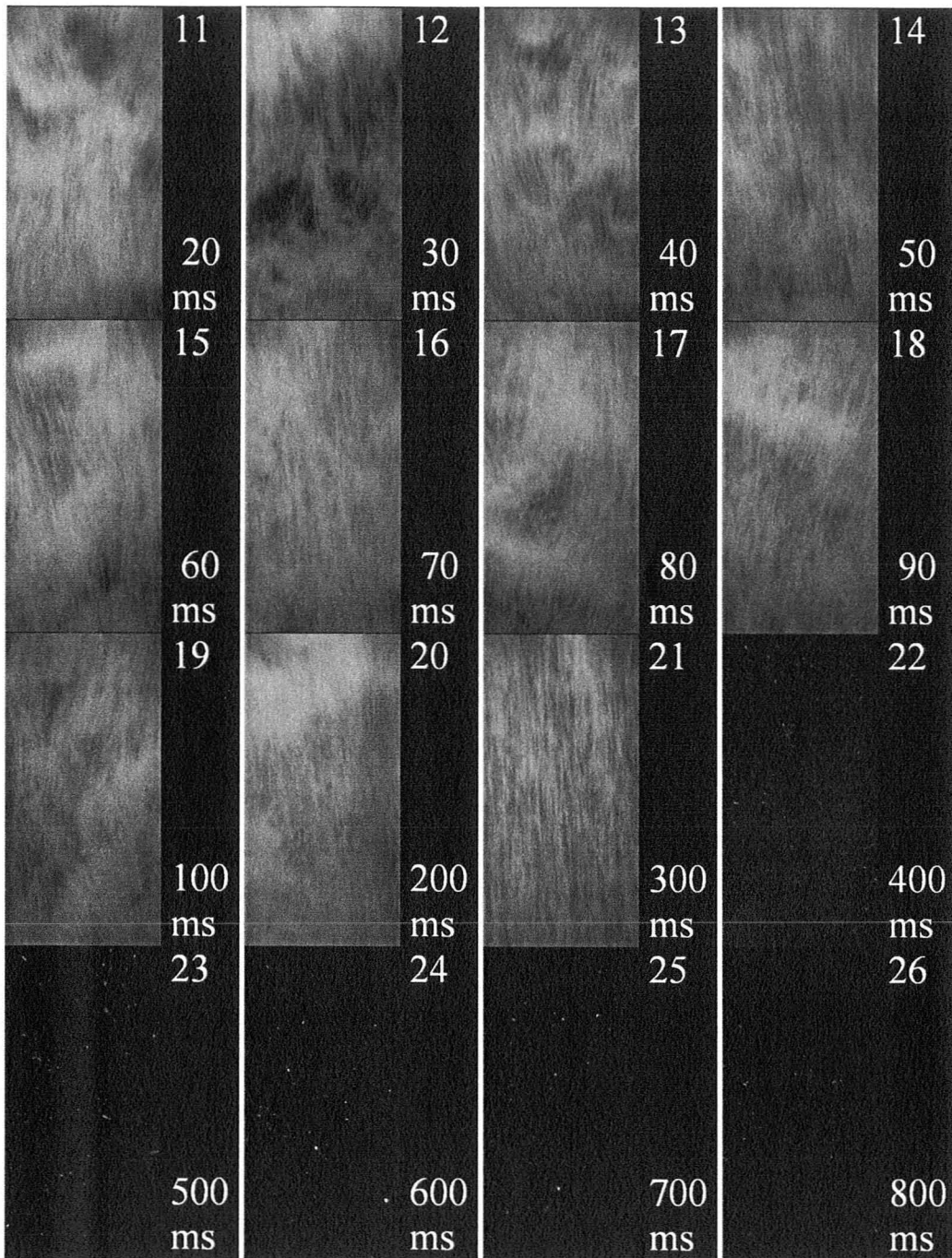


Figure 5-12. High-Speed Images of 2nd Experiment

5.3 Third Experiment

The third experiment represents the first attempt to measure the fluid drag forces exerted on the tube bundle. An equivalent test section height was determined based on volume considerations, and the steady-state conditions are given in Table 5-3. An explanation of the dynamic behaviour of the test section load cells with a detailed description of the calibration procedure and signal polarity is provided in Appendix E. The static pressure recorded is shown in Figure 5-13.

The most remarkable difference between the static pressure response in this experiment compared to the previous two experiments is the signal response time of the depressurisation. The upstream pressure responds with a rapid pressure decrease about 30 milliseconds after rupture, which is less than half of the response time for the previous experiments. The overall static pressure behaviour is different from the previous tests. The recovery pressure is significantly higher, and the region of nearly constant pressure occurs over a much shorter period of time, after which the upstream pressure approaches equilibrium conditions at a slower rate, eventually equalising the upstream and downstream pressures after about 750 milliseconds. The downstream pressure response is also different, in that the pressure spike is not as sharp, and there is no second pressure rise. Instead, the pressure increases steadily towards the equalised conditions. This difference in pressure behaviour is attributed to the pressure drop across the tube bundle during flashing.

Table 5-3. Initial Steady-State Thermodynamic Properties for 3rd Experiment

Phase	Pressure	Temperature	Density	Volume	Mass	Sonic Velocity
<i>l or g</i>	<i>P</i> (kPa)	<i>T</i> (°C)	<i>ρ</i> (kg/m ³)	<i>V</i> (L)	<i>m</i> (kg)	<i>a</i> (m/s)
Liquid	569	17.6	1230	5.5	6.8	541
Vapour	566	20	27	18.3	0.4	145

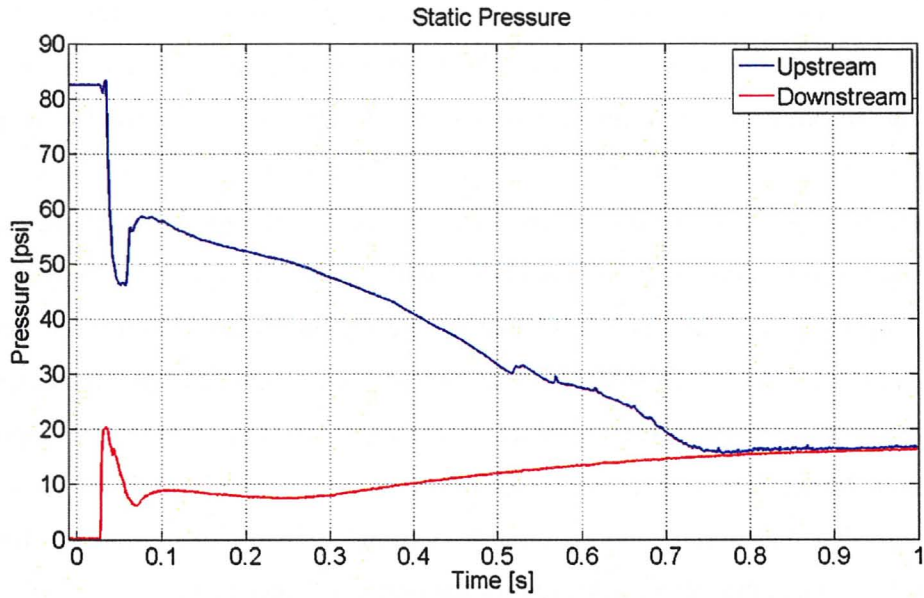


Figure 5-13. Static Pressure vs. Time (3rd Experiment)

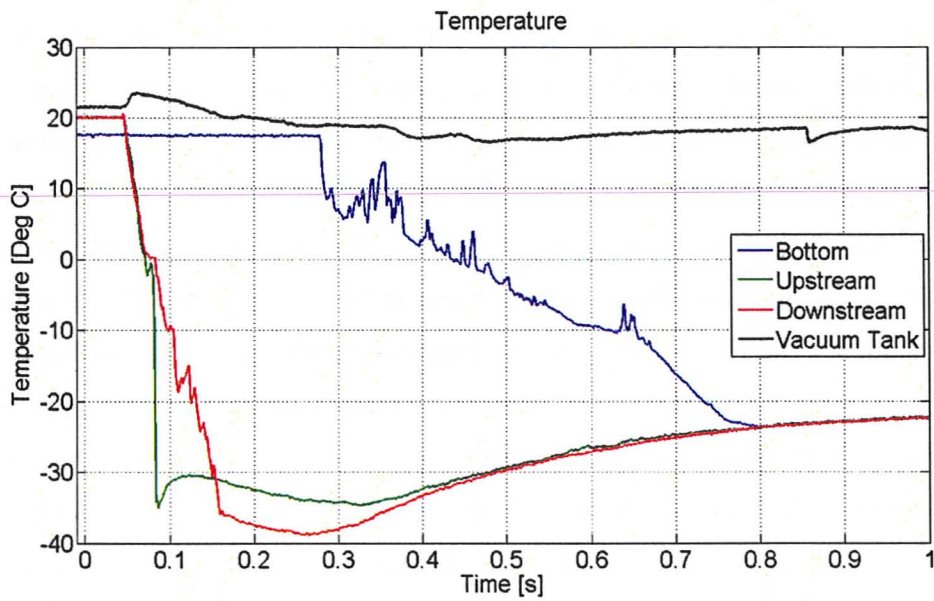


Figure 5-14. Temperature vs. Time (3rd Experiment)

The temperature response is shown in Figure 5-14, and different behaviour caused by the pressure drop across the tube bundle is also demonstrated in these results. The vapour temperature drop responds faster to the break than in previous experiments, but the rate of temperature decrease is slower. On the other hand, the liquid temperature at the bottom of the reservoir remains constant for almost 300 milliseconds, before the sudden temperature drop associated with phase change is displayed. The rate of temperature decrease is also slower for the region initially filled with subcooled liquid, and there is no 'quasi-steady' region as had been observed in previous experiments. The temperature at the three locations on the blow-down rig equalise at approximately the same time as the static pressure sensors at about 800 milliseconds. It is also interesting to note that the thermocouples initially surrounded by vapour registered lower minimum temperatures than those achieved for the previous experiments.

The dynamic pressures are presented in Figure 5-15 and Figure 5-16. There appears to be a distinct difference in transient behaviour between the pressure transducers top and bottom of the tube bundle. The pressure transducer downstream of the tube bundle displays a relatively short period of transient behaviour, whereas the pressure transducer initially surrounded by liquid shows a longer transient duration than any of the results registered in the previous experiments. The initial behaviour shows a relatively broad pressure undershoot which lasts for over 20 milliseconds, and the pressure then recovers slightly before decreasing steadily. The pressure magnitudes are similar to the first experiment, but the pressure remains at the recovery value for a much longer time duration. The high-frequency oscillations on the middle transducers are not as pronounced in this experiment, but the pressure values still fall below absolute vacuum. Figure 5-15 indicates that the downstream pressure is higher than the upstream pressure starting at 10 milliseconds. If this is the case, the flow should be accelerating downwards or at least decelerating. Once again, there is no evidence of such behaviour from the flow visualisations. The lower transient temperatures registered in this experiment may have produced stronger thermal effects on the pressure signals. The vacuum tank barely registers any pressure increase, with maximum amplitude of about 3.5 psi.

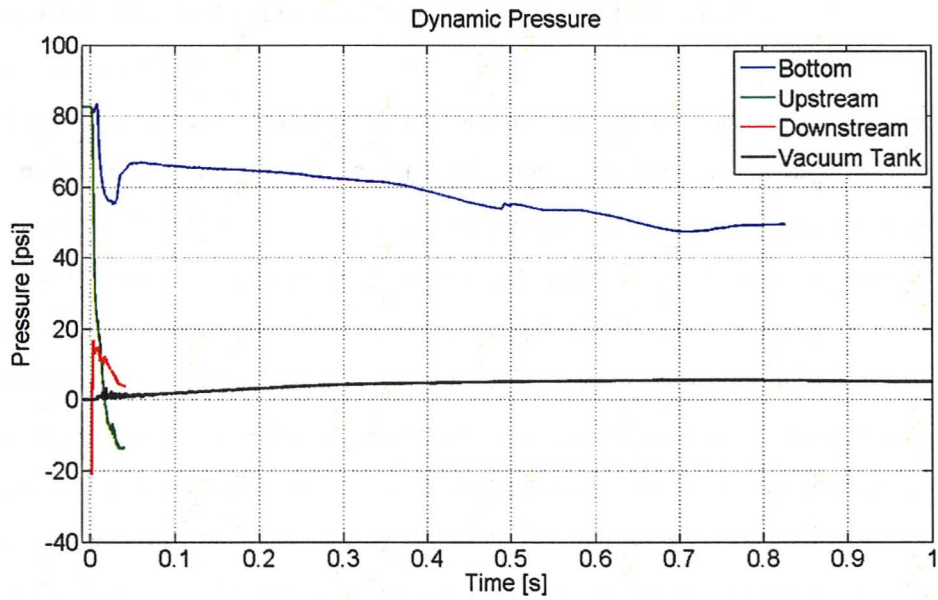


Figure 5-15. Dynamic Pressure vs. Time (3rd Experiment)

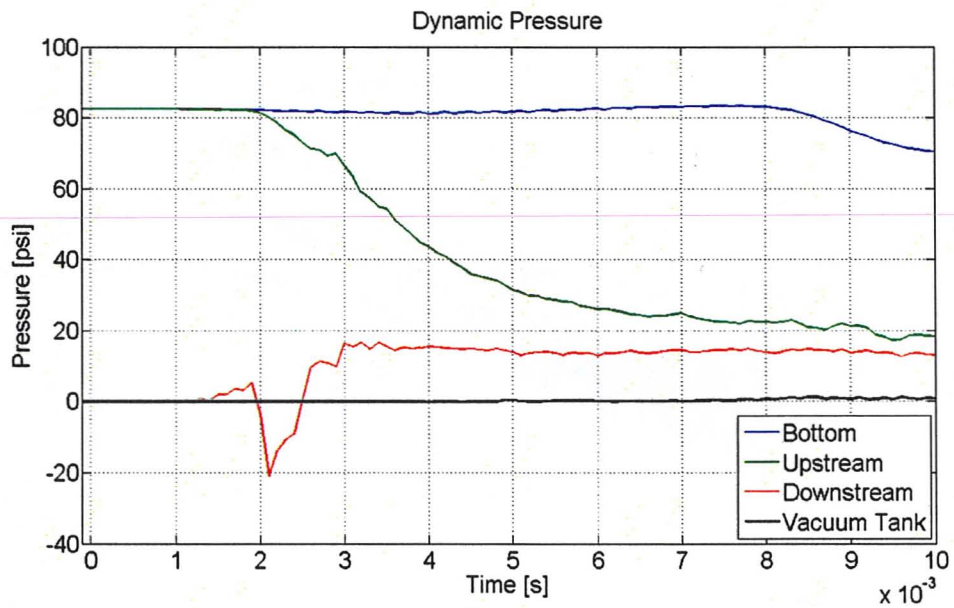


Figure 5-16. Dynamic Pressure vs. Time (3rd Experiment; 0.01 s Timescale)

The dynamic loading results are shown as individual load cell signals in Figure 5-17, and the summed signal of the four load cells is shown in Figure 5-18 and Figure 5-19. There appears to be no evidence of blow-down fluid drag forces in the loading results. Instead, the load cells seemed to capture different phenomena than the drag force measurements required. The signals appear to be very noisy, and the loads shown are in the compressive region, whereas the sensors were expected to measure the loading on the tubes as a tensile force. There appears to be an initial blow-down shock effect in the first 50 milliseconds, followed by a steady increase in the loading up to a maximum point. A Fast Fourier Transform (FFT) analysis of the signal is presented in Appendix F. The oscillations in the signal are a resultant of inertial effects and will be analysed in Section 6.4. It is the mean signal that is of interest in this case, and the mean loading in Figure 5-18 does not appear to have any physical explanation. The physical behaviour depicted in the high-speed visualisation of the flow may provide some clues towards explaining this unanticipated load cell behaviour.

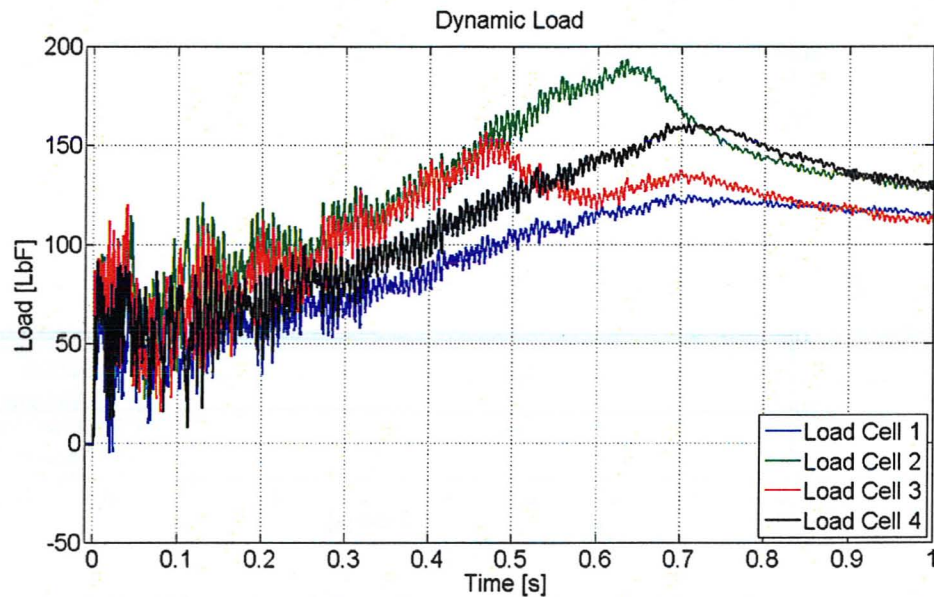


Figure 5-17. Load vs. Time (3rd Experiment – Individual Signals)

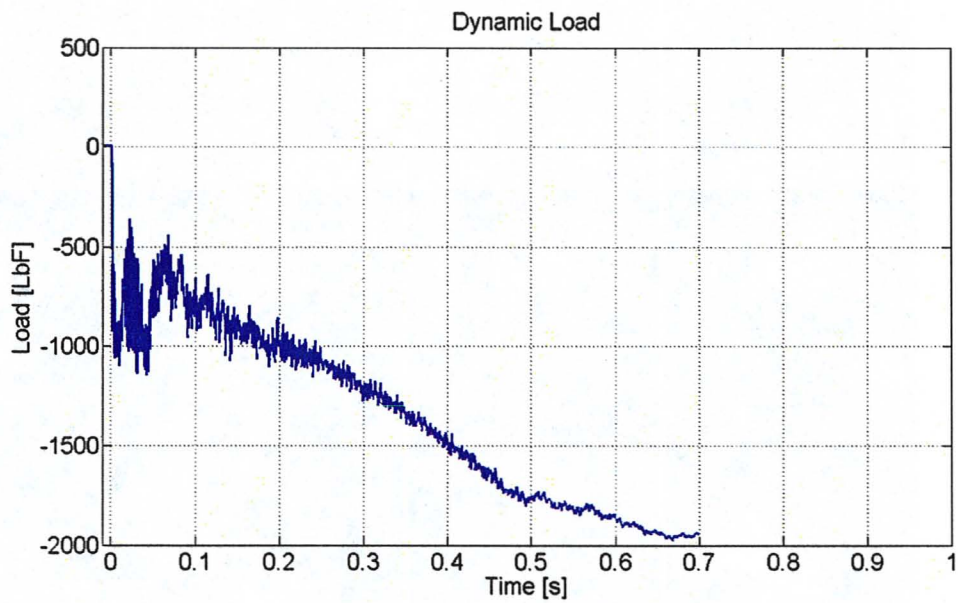


Figure 5-18. Load vs. Time (3rd Experiment – Total Signal)

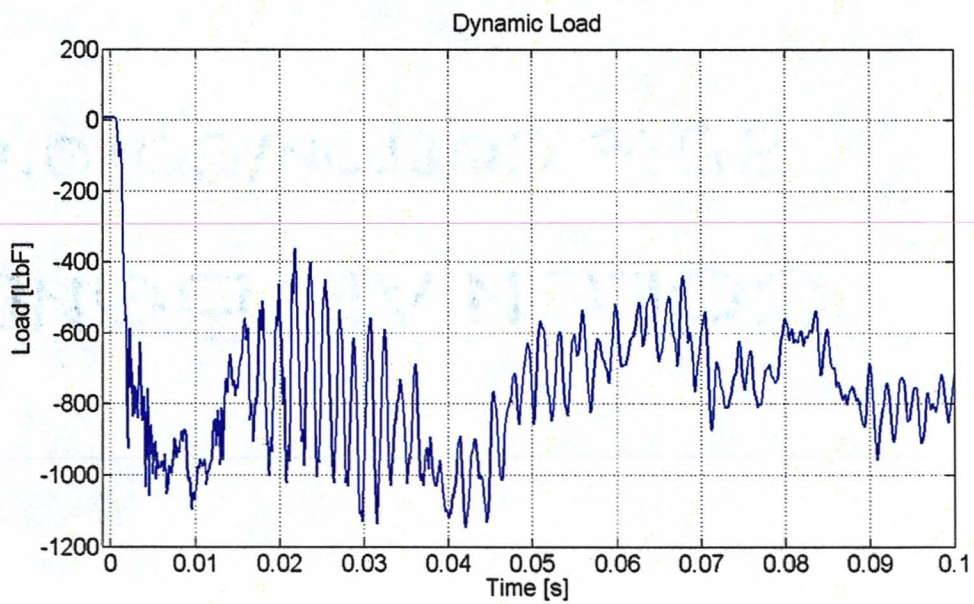


Figure 5-19. Load vs. Time (3rd Experiment – Total Signal; 0.1 s Timescale)

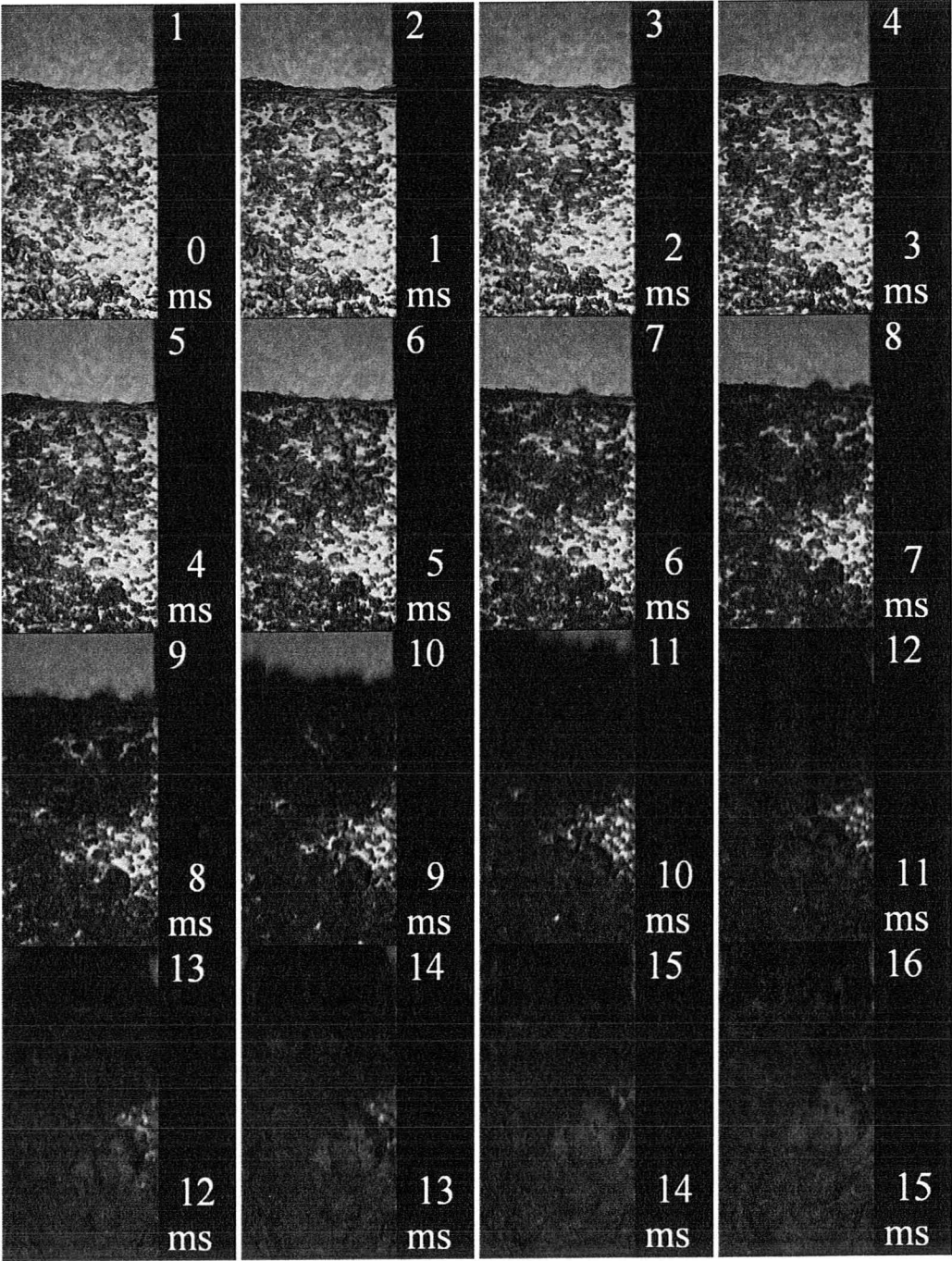


Figure 5-20. High-Speed Images of Initial Stages of 3rd Experiment

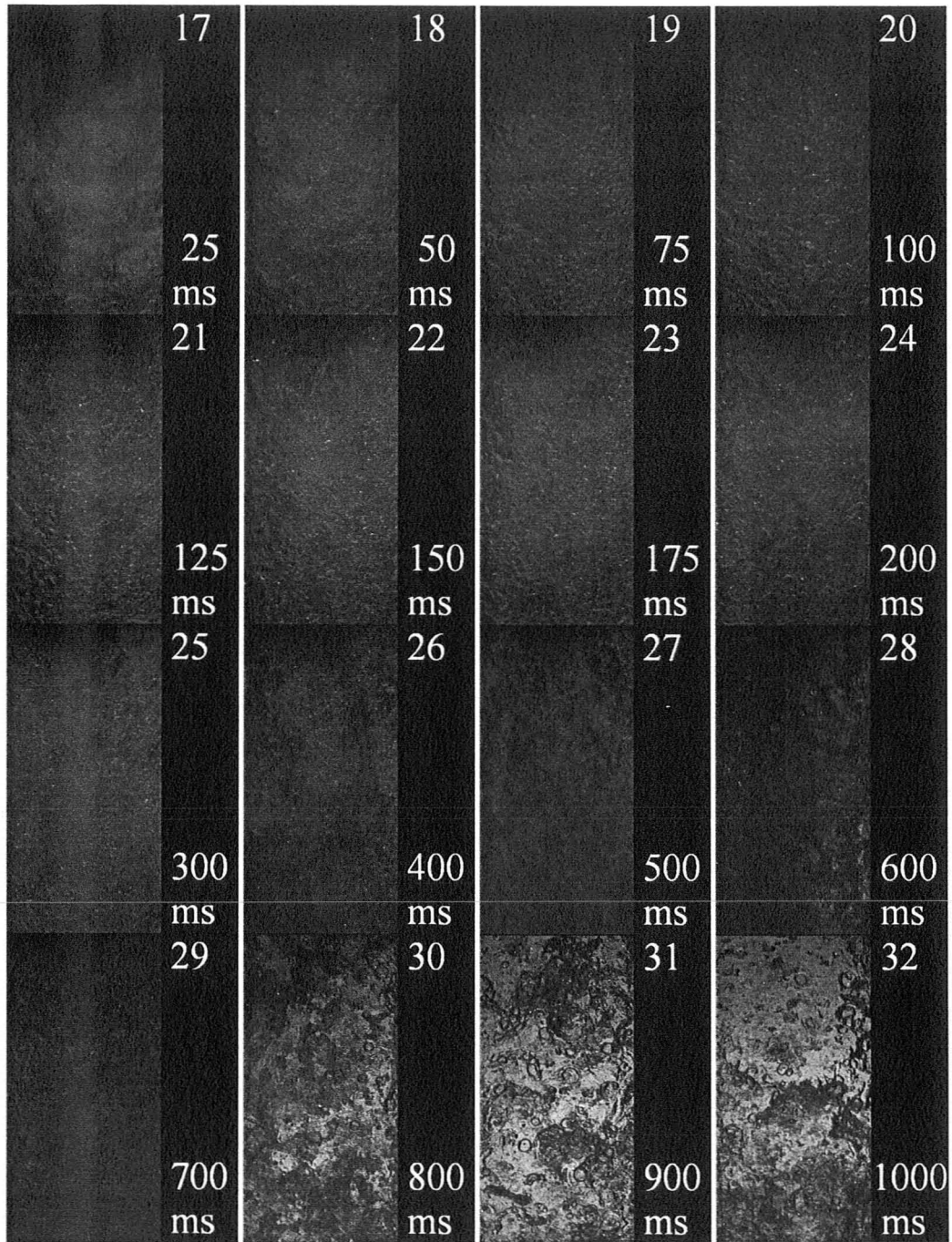


Figure 5-21. High-Speed Images of 3rd Experiment

The high-speed camera system was set-up for this experiment making the best use of the lessons learnt from previous experiments, employing two separate light sources together, with the aim of obtaining a full flow visualisation of the entire blow-down process, including the calm steady-state stage prior to the disc rupture, and the closing stages of the depressurisation. A 250-Watt incandescent halogen lamp light source was used to provide backlighting, sending a bright focussed beam through the blow-down rig into the camera lens. A clear sand-blasted acrylic plate with a translucent white sheet of paper attached to it was placed between the lamp and the viewing sight window to diffuse the light beam, spreading out the light relatively uniformly and eliminating the appearance of the light source as a concentrated point in the flow visualisations. For front lighting, a 200-Watt electronic ballast-powered fluorescent light source with adjustable light intensity was used to reflect light off of the liquid vapour interfaces and back into the camera lens. The light from this source was minimal and normally over-powered by the backlight, but provided useful lighting during the transient phase change, in which the backlight was blocked by the misty two-phase flow. The concept worked successfully, and the blow-down images are presented in Figure 5-20 and Figure 5-21.

The flow visualisations show that the most violent flashing seems to take place during the first 50 milliseconds after rupture, from images 1-18. The subsequent flashing seemingly takes place at a steady state, with some acceleration effects detectable around the time corresponding to images 26 and 29. By image 30, 800 milliseconds after rupture, most of the liquid has boiled off, and there are liquid droplets falling back into the reservoir driven by gravity. Apparently, the rapid vaporisation of the bulk of the liquid has carried some liquid upwards towards the vacuum tank, and as steady-state conditions are approached, some of this liquid falls back in a kind of counter-current annular flow. In Figure 5-18, the loading appears to increase steadily between 100-500 milliseconds after rupture, and the loading rate decreases until about 700 milliseconds, after which loading effects disappear. Curiously, at 400 milliseconds, some acceleration effects can be detected in the flashing fluid from the visualisations, and by 700 milliseconds, the flashing flow was comprised almost entirely of vapour, indicating that the bottom

reservoir had practically no liquid remaining. This is supported by the static pressure and temperature results, which indicate that equalised conditions are established inside the blow-down rig about 750 milliseconds after the break.

It is difficult to determine whether the fluid drag loading is measured by the load cells or is completely overwhelmed by the shock-loads due to vibration and acceleration effects, but it was established through analysis and comparison of the load cell signals with the flow visualisations and results from the other instruments that the phenomena producing the loading are relevant to the sudden depressurisation of the liquid mass. Due to the unanticipated ambiguity in load cell signals, the fourth experiment was put on hold, and it was desired to shed some light on the load cell behaviour before proceeding further with the project. Since the inertial effects were suspected to be the most likely cause of the uncertain load cell signals, an investigation of the shock loading vibration response of the blow-down rig was performed under identical experimental conditions. The third experiment was repeated with the rig instrumented using accelerometers in order to study acceleration effects. The objective was to obtain some insight into the acceleration behaviour of the tube bundle and the blow-down rig frame, with the possibility of calculating the effects of acceleration on inertial loading and subtracting them from the load cell signals, leaving behind loads that result purely due to fluid drag forces.

5.3.1 Third Experiment Retrieval

In order to study the acceleration effects, two accelerometers were employed and the acceleration data was acquired instead of the liquid reservoir and vacuum tank dynamic pressures, due to limited channel availability on the data acquisition card. A piezoelectric accelerometer (PCB model 352A24) was wax-mounted on the tube bundle, and another accelerometer (Kistler model 8638B50) was magnet-mounted onto the blow-down rig. The results are presented in this section.

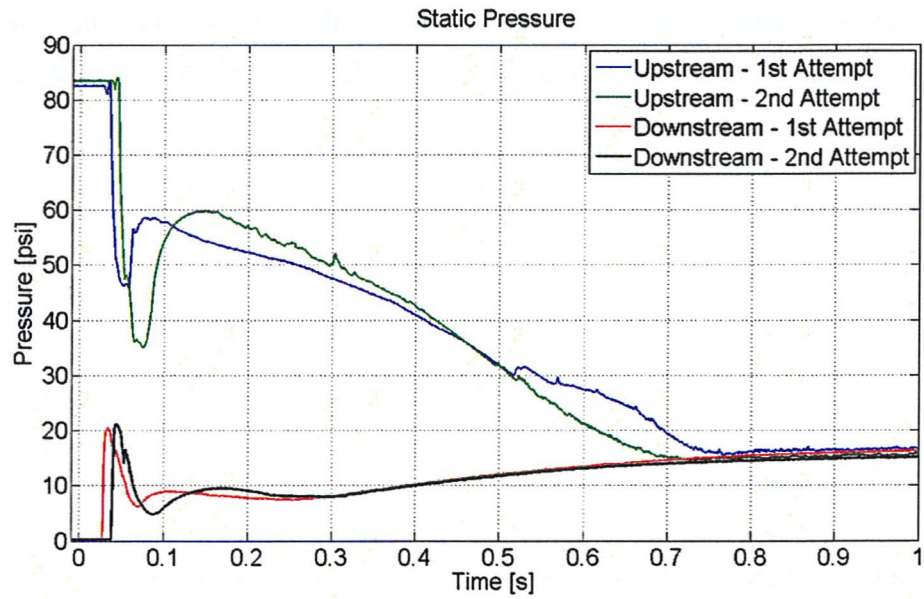


Figure 5-22. Static Pressure vs. Time (3rd Experiment – 2nd Attempt)

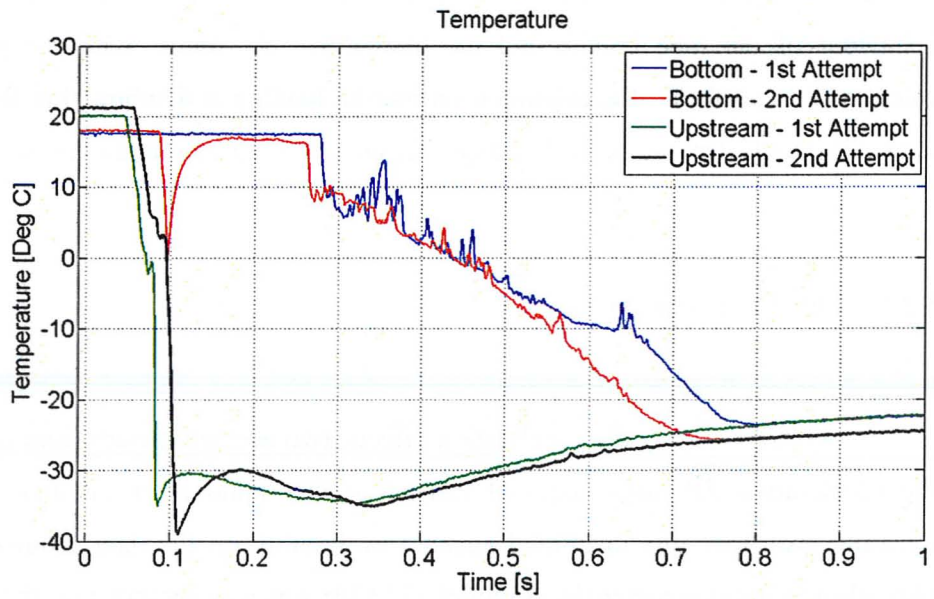


Figure 5-23. Temperature vs. Time (3rd Experiment – 2nd Attempt Upstream)

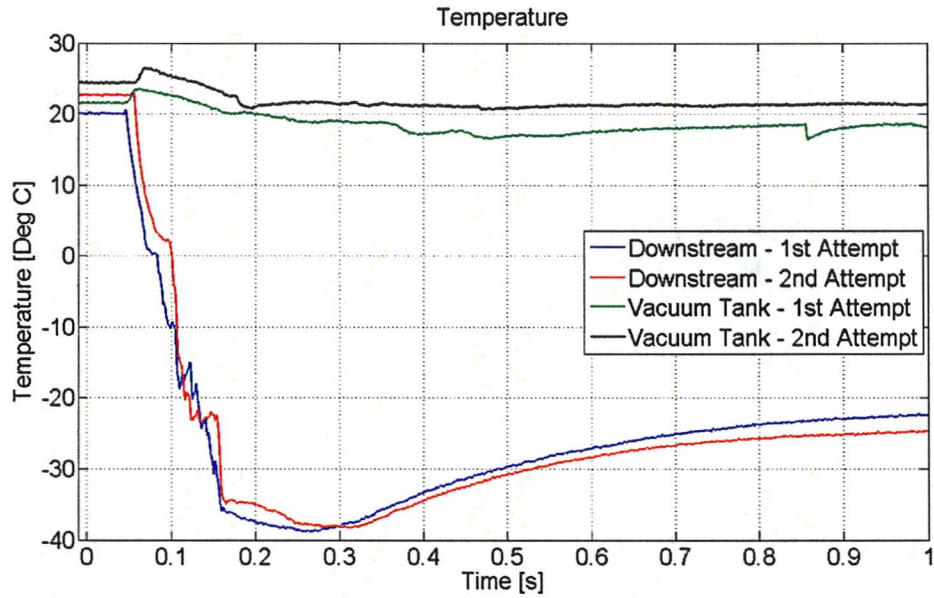


Figure 5-24. Temperature vs. Time (3rd Experiment – 2nd Attempt Downstream)

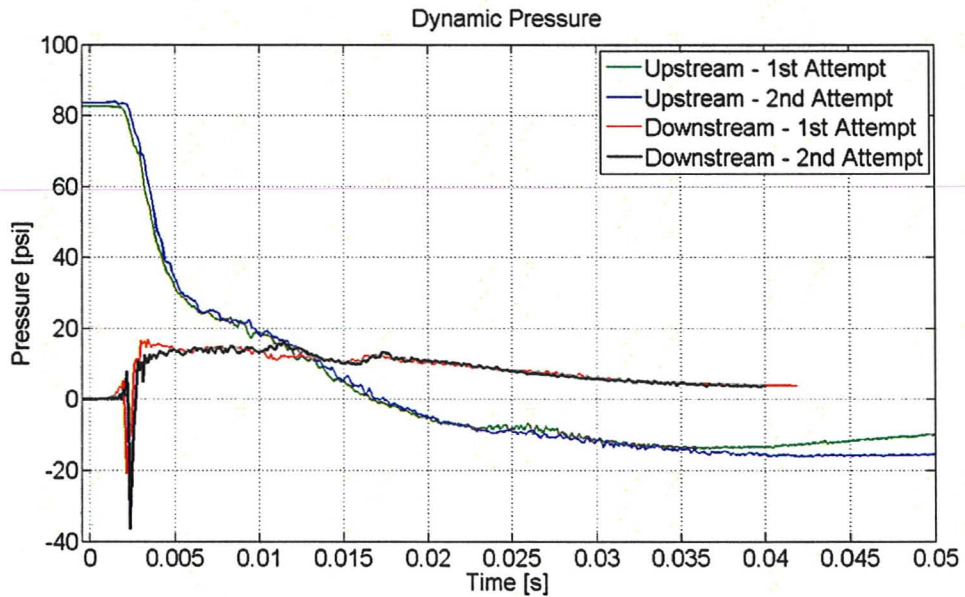


Figure 5-25. Dynamic Pressure vs. Time (3rd Experiment – 2nd Attempt)

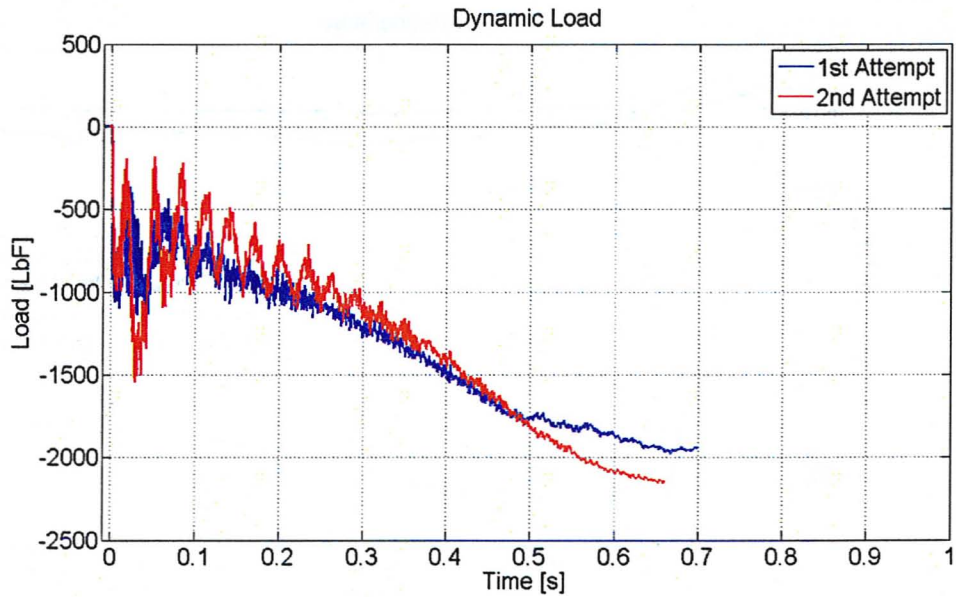


Figure 5-26. Load vs. Time (3rd Experiment – 2nd Attempt)

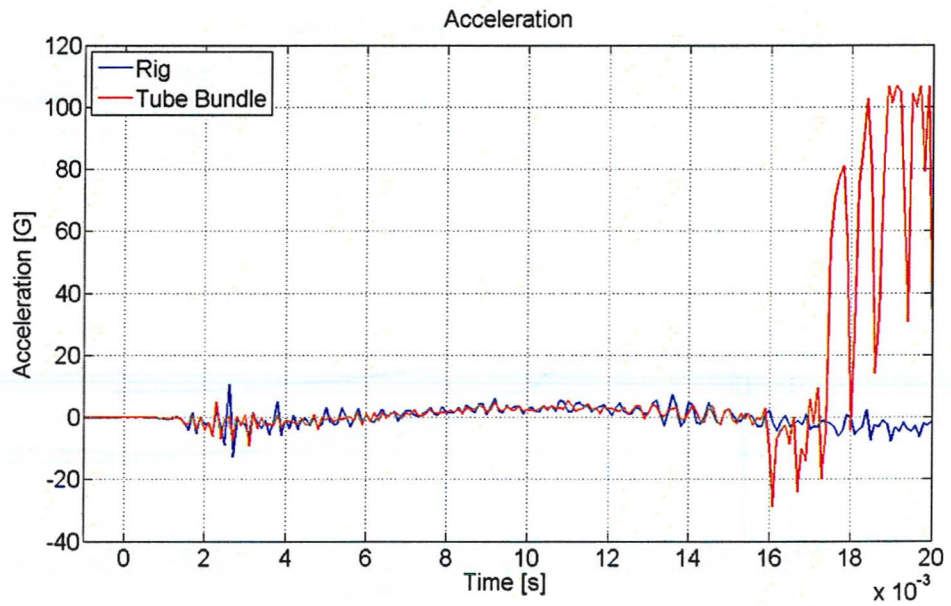


Figure 5-27. Acceleration vs. Time (3rd Experiment – 2nd Attempt)

Table 5-4. Initial Steady-State Thermodynamic Properties for 3rd Experiment – 2nd Attempt

Phase <i>l or g</i>	Pressure <i>P</i> (kPa)	Temperature <i>T</i> (°C)	Density ρ (kg/m ³)	Volume <i>V</i> (L)	Mass <i>m</i> (kg)	Sonic Velocity <i>a</i> (m/s)
Liquid	576	18	1230	5.2	6.4	539
Vapour	573	21.1	28	18.7	0.5	146

The initial conditions were similar to those of the third experiment and are presented in Table 5-4. The static pressure plot in Figure 5-22 is very similar to the static pressure obtained for the original experiment. The magnitude of the pressure dip, and the subsequent pressure recovery, are increased in comparison to the previous experiment. The transient also lasted about 50 milliseconds less than the previous experiment. These differences can be attributed to the slightly smaller amount of liquid R-134a available for depressurisation in this second attempt. In Figure 5-20, many R-134a vapour bubbles originating from the accumulator lines during the steady pressurisation of the stagnant liquid can be seen prior to the sudden depressurisation, serving as nucleation sites for the vapour expansion. In the absence of these bubbles, the availability of nucleation sites is much reduced, which may force the liquid to reach a higher superheat, and hence a stronger pressure undershoot, before nucleation initiates. This could also explain the amplified behaviour observed in this experiment, but no high-speed visualisation was captured to support this theory.

It is also likely that due to three-dimensional effects, the flow conditions are not uniform across the test section and probes at different locations around the test section at the same distance from the rupture disc do not give identical results. For the same reason, such non-equilibrium transients are likely to vary somewhat at a given location from test to test. The temperature results shown in Figure 5-23 and Figure 5-24 are also very similar to those from the previous experiment. A remarkable difference exists in the

bottom thermocouple response around 100 milliseconds after rupture. The temperature seems to follow the expansion associated with the vapour phase, before recovering to indicate the liquid temperature. This behaviour can be justified by the presence of a vapour bubble in the vicinity of the thermocouple junction, either accelerating upwards, or nucleating at the junction itself, resulting in a temperature signal corresponding to the vapour phase. When the bubble escapes and the thermocouple is surrounded by liquid again, the temperature returns to indicate the superheated temperature of the liquid. The dynamic pressure results in Figure 5-25 are similar to those obtained in the previous test, and the magnitudes of the pressures indicate a slightly more violent phase change mechanism.

The load signals from Figure 5-26 are also very similar, with cleaner oscillatory behaviour, and larger load amplitudes. The increased loads can be explained once again by the stronger phase change mechanism associated with fewer nucleation sites. The fact that the transient behaviour lasts for a shorter time duration is attributed to the smaller volume of liquid undergoing depressurisation. The acceleration response is shown in Figure 5-27. The rig has a high stiffness, and its corresponding shock loading did not exceed 10 g's. Since the load cells have a very high stiffness, it was expected that the test section vibration would closely resemble the vibration of the rig. The vibration response in the first 15 milliseconds of the blow-down is in agreement with the expected behaviour in terms of matching the frequency and, to a certain extent, amplitude of the experimental rig acceleration. However, after the first 15 milliseconds of the blow-down, the tube bundle accelerometer signal became unstable and saturated apparently in excess of 100 g. This signal must be considered spurious. Thus, it appears that the rig and the tube bundle do respond to the shock loading caused by the blow-down, but a proper evaluation will have to await a further experiment. A different accelerometer was used for the subsequent experiment, and the irregularity in the acceleration signal was not encountered, providing more useful information of the inertial loading of the test section.

5.4 Fourth Experiment

The last experiment of this project was designed to study the blow-down with the liquid surface above the tube bundle. The accelerometers were again installed instead of the top and bottom pressure transducers. The PCB accelerometer was mounted on the rig, as opposed to the tube bundle, and a different accelerometer (Kistler model 8794A) with a range of ± 500 g was wax-mounted on the tube bundle instead. The initial conditions are given in Table 5-5 and the static pressure record is presented in Figure 5-28.

The time delay associated with the sudden pressure drop is almost 200 milliseconds, about 4 times as long as the previous experiment. The upstream pressure dropped only to about 50.9 psi, quickly recovered to 60.4 psi, and then remained relatively stable at about 54 psi for about 500 milliseconds. The pressure decreased towards steady-state conditions 700 milliseconds after rupture, and the experimental rig pressures equalised shortly after 1000 milliseconds. The downstream pressure initially responded similarly to previous experiments, with the pressure spiking up to 20.2 psi, and then decreasing rapidly towards about 10 psi. Instead of proceeding towards steady-state conditions however, the pressure rose a second time at a slower rate, reaching a peak pressure of 36.3 psi and then falling back to 11.9 psi about 370 milliseconds after rupture, and finally following a saturation path. The observed behaviour demonstrates that equilibrium saturation pressures in both locations are established at different times, with the pressure upstream of the tube bundle requiring a longer period of time.

Table 5-5. Initial Steady-State Thermodynamic Properties for 4th Experiment

Phase <i>l or g</i>	Pressure <i>P</i> (kPa)	Temperature <i>T</i> (°C)	Density ρ (kg/m ³)	Volume <i>V</i> (L)	Mass <i>m</i> (kg)	Sonic Velocity <i>a</i> (m/s)
Liquid	572	17.5	1230	14.6	17.9	542
Vapour	564	21.8	27	9.3	0.2	146

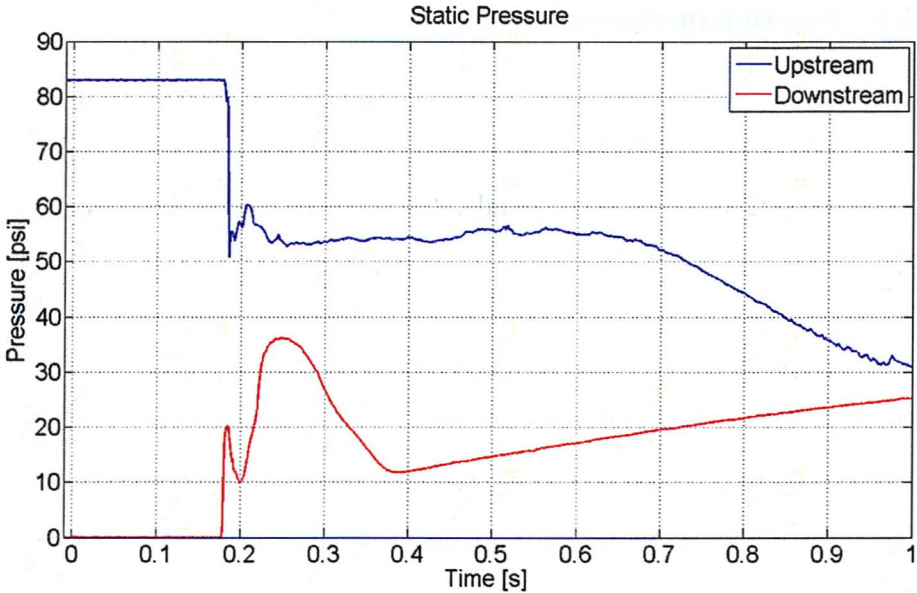


Figure 5-28. Static Pressure vs. Time (4th Experiment)

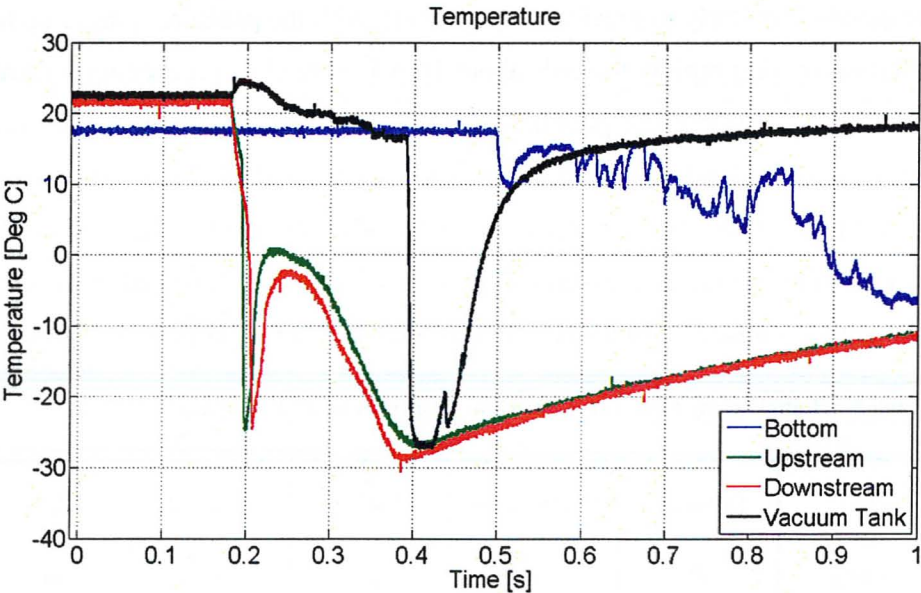


Figure 5-29. Temperature vs. Time (4th Experiment)

The temperature results are shown in Figure 5-29. The differences in thermal response behaviour between this experiment and the previous case are similar to those observed in the static pressure results. The liquid phase temperature response indicates a phase change after more than 500 milliseconds, and the vapour temperatures responded after 200 milliseconds, similar to the static pressure behaviour. The vapour expansion temperatures recorded were not as low as those obtained in the previous case, and the behaviour after the initial expansion is different, with the temperature showing a second temperature decrease beginning about 250 milliseconds after rupture, and reaching a minimum temperature of between -26 to -29 °C at about 400 milliseconds, after which the temperature follows a steady-state path. The vacuum tank temperature dropped to the same minimum temperatures recorded in the rig, indicating that the vapour phase expansion practically occupied the volume of the entire blow-down rig.

The dynamic pressure results are shown in Figure 5-30 and Figure 5-31. From the trends in the static pressure plots, it can be inferred that the bottom pressure transducer that was disconnected for this experiment would have shown a much longer duration of dynamic pressure behaviour, due to the extent of the transient behaviour in the pressurised liquid reservoir region. Similarly, the vacuum tank pressure transducer would be expected to register significant pressure increases due to the significant volume of expanding vapour. The two sets of available pressure results show the same trends as the static sensors, including more rapid yet weaker pressure undershoot behaviour, and a significant ‘quasi-steady’ pressure stage, after which the pressures fall and equalise at saturation conditions.

The dynamic loading results are presented in Figure 5-32 and Figure 5-33. The results appear similar to the previous cases, with a few differences in the details of the behaviour and the magnitudes of the loads. However, since it is difficult to discern the effects of drag loading on the tubes from these results, there is not much room for critical analysis regarding the observed differences in the results. An analysis of the frequency content including a comparison with accelerometer data is presented in Section 6.4.

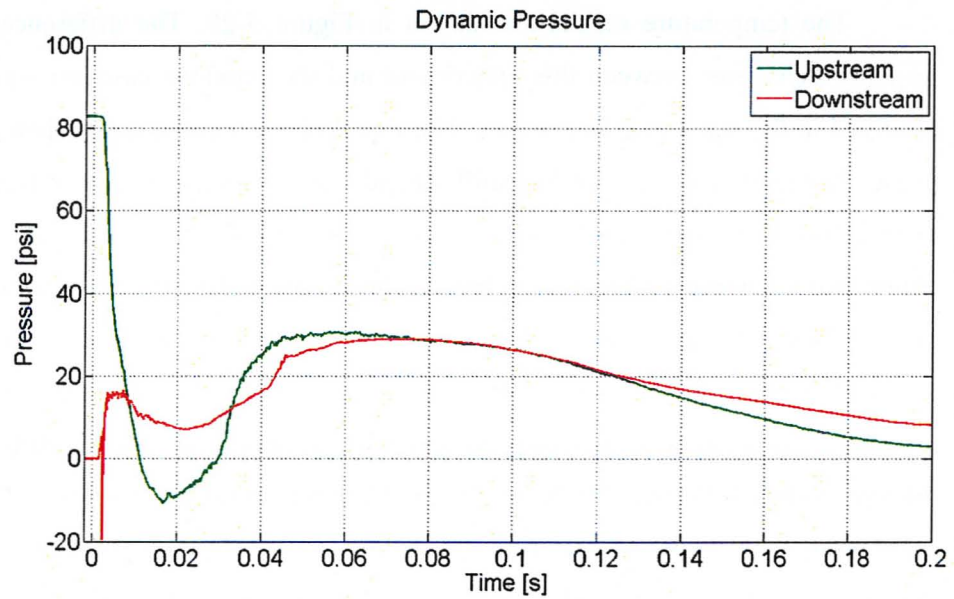


Figure 5-30. Dynamic Pressure vs. Time (4th Experiment)

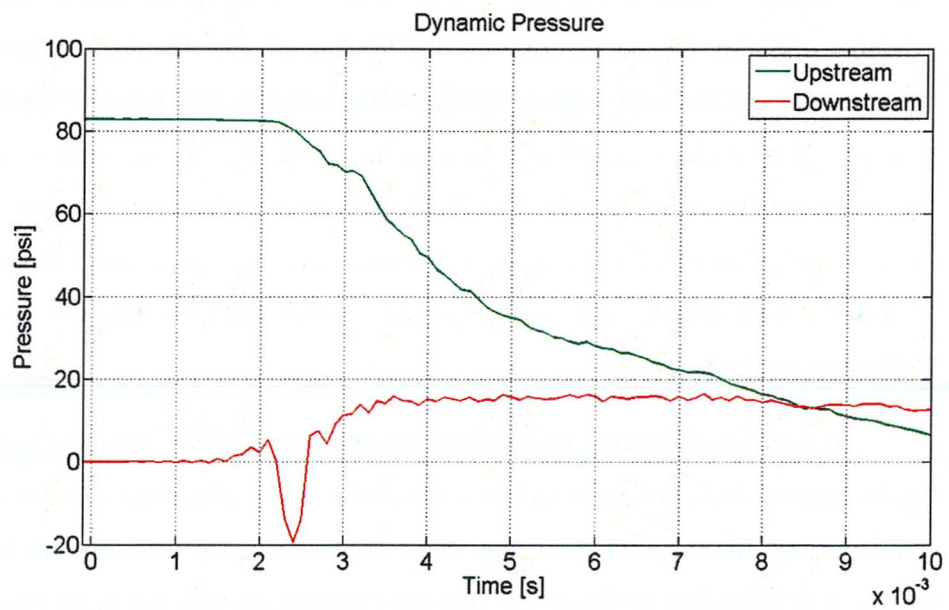


Figure 5-31. Dynamic Pressure vs. Time (4th Experiment; 0.01 s Timescale)

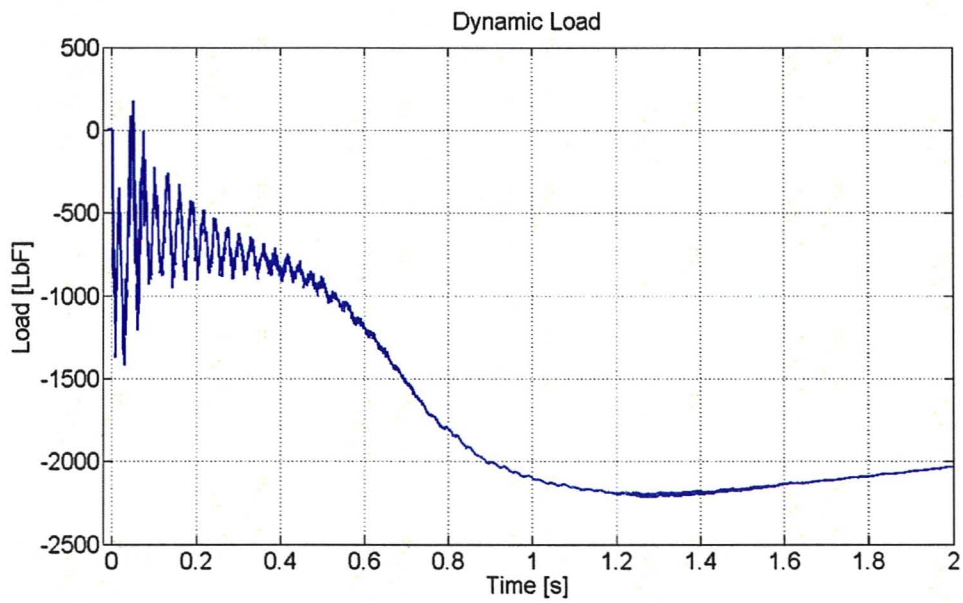


Figure 5-32. Load vs. Time (4th Experiment)

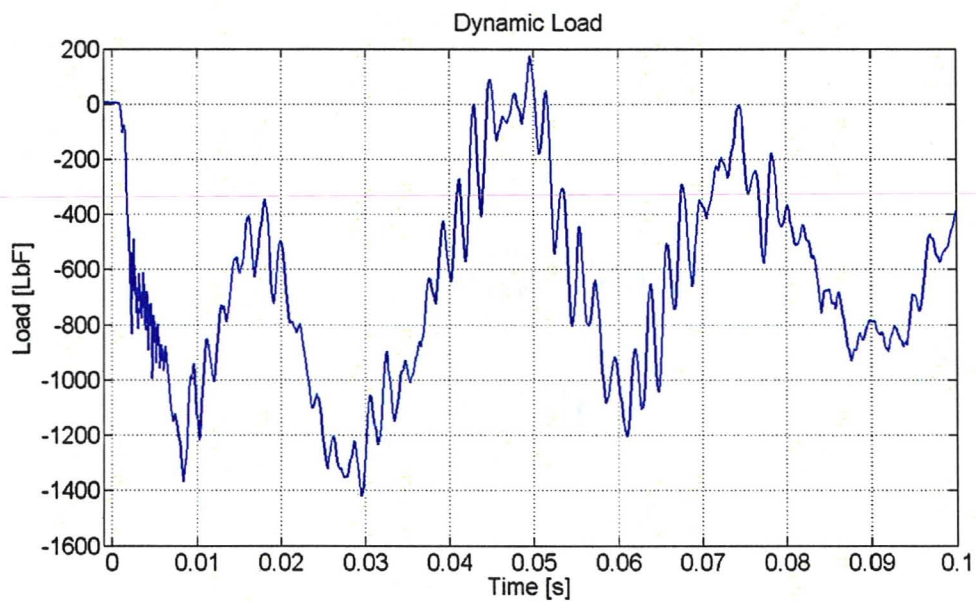


Figure 5-33. Load vs. Time (4th Experiment; 0.1 s Timescale)

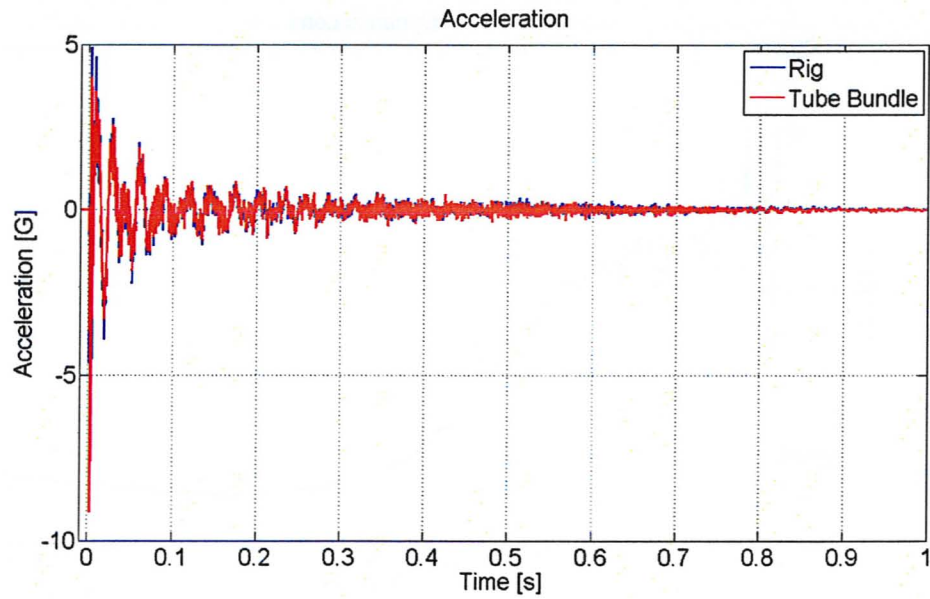


Figure 5-34. Acceleration vs. Time (4th Experiment)

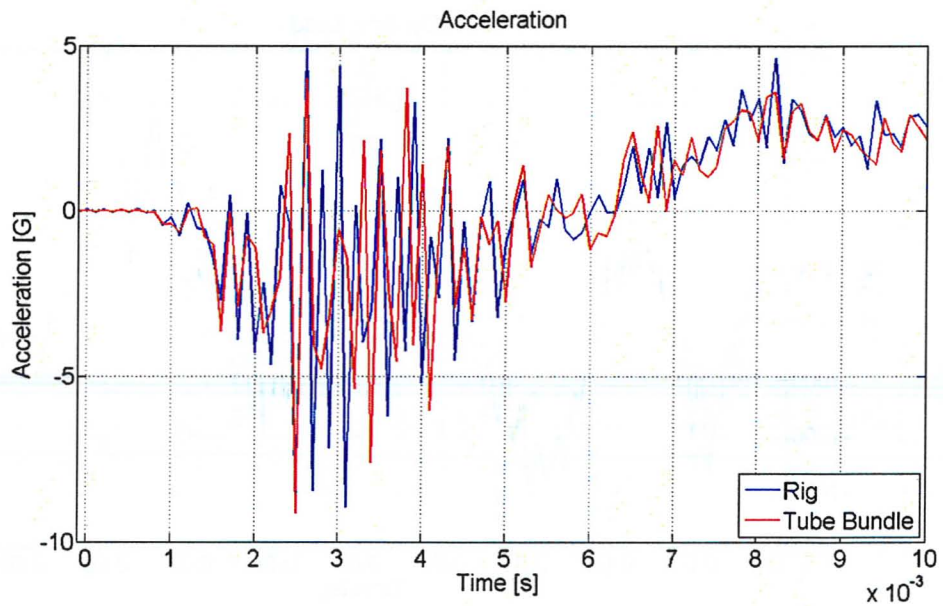


Figure 5-35. Acceleration vs. Time (4th Experiment; 0.01 s Timescale)

Figure 5-34 and Figure 5-35 display the accelerometer signals obtained during the blow-down transient. The acceleration response shows clearly that the peculiar tube bundle accelerometer behaviour in the previous experiment after the first 16 milliseconds was due to faulty signals. The acceleration response registered for the rig and the tube bundle in this experiment are closer to the predicted vibration response based on the design of the test section. The vibration oscillations during the first 300 milliseconds of the transient are of the same frequency and phase, and attenuate together with the same amplitudes. In the first few milliseconds however, the polarities and amplitudes of vibration of the rig and the tube bundle show some minor differences. Flow visualisations captured using the high-speed camera system are presented in Figure 5-36 and Figure 5-37. The depressurisation wave propagates through the fluid during the first three milliseconds, and the first signs of nucleation and phase change are shown in image 3. The vapour growth in image 4 shows similar trends as previous cases.

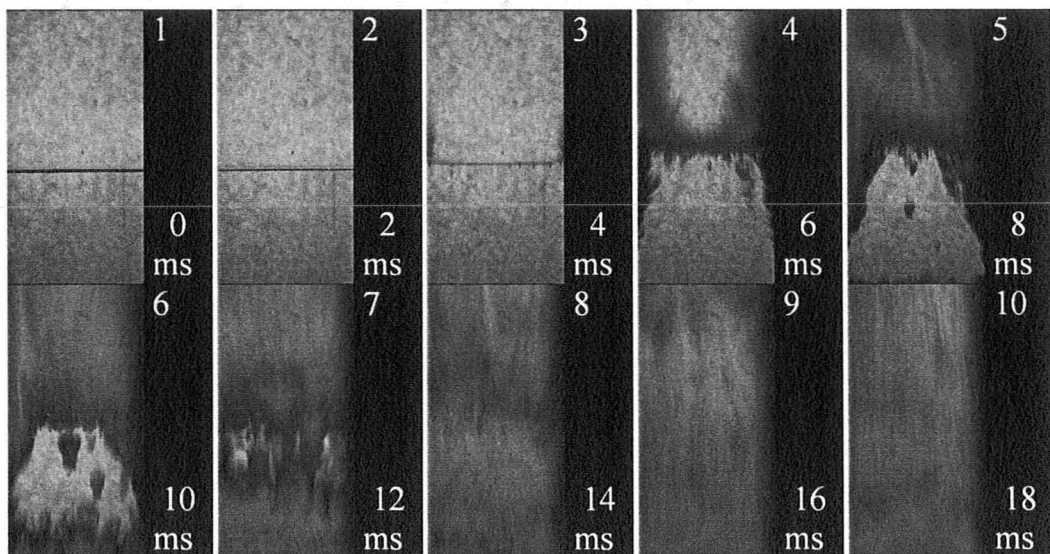


Figure 5-36. High-Speed Images of Initial Stages of 4th Experiment

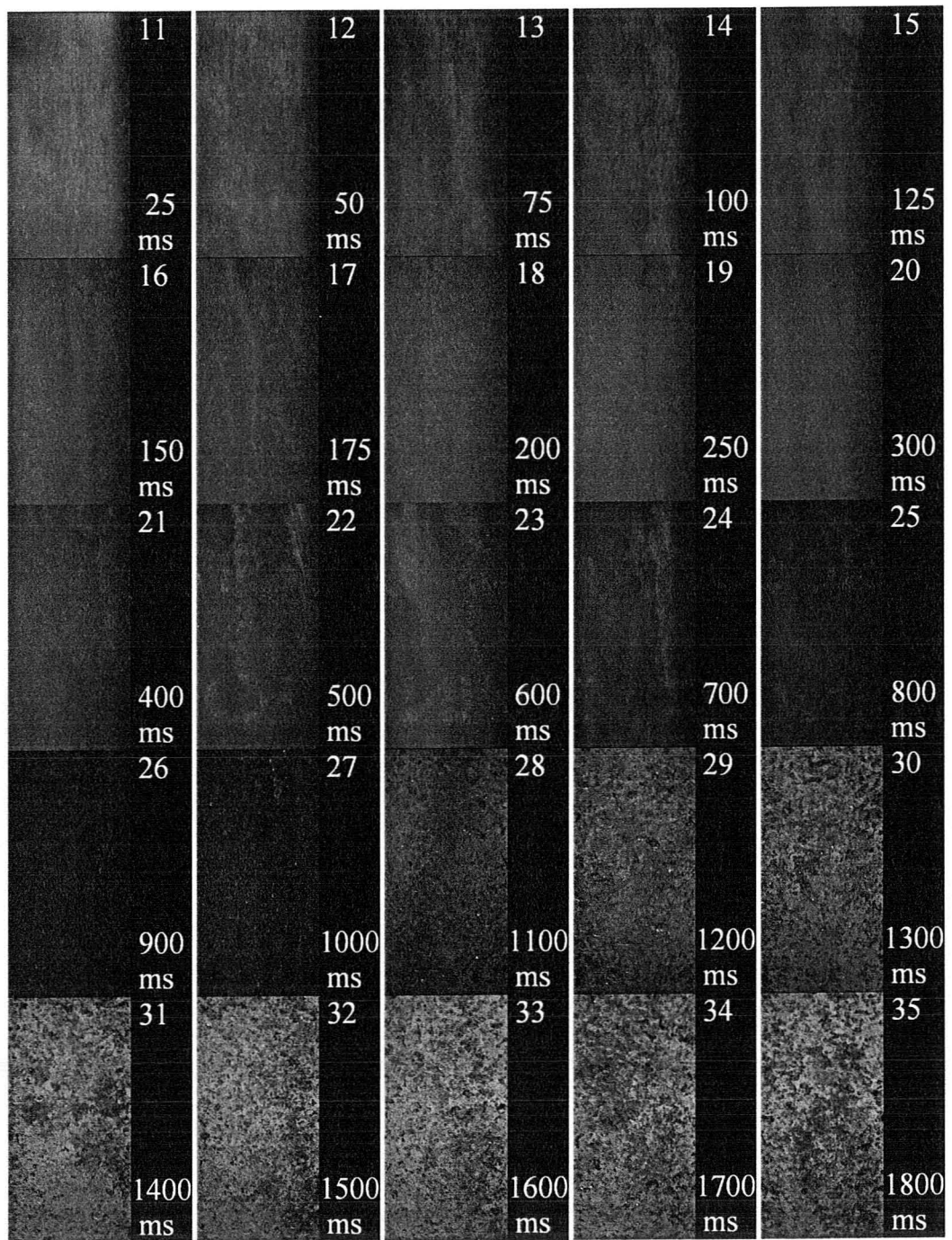


Figure 5-37. High-Speed Images of 4th Experiment

The flashing continues to generate more vapour bubbles initiating at the steel walls and accelerating upwards towards the break. Images 5 and 6 display the arrival of a vapour front from the bulk of the liquid, which could represent the vapour bubbles that nucleated on the surfaces of the tubes. This accelerating cloud of bubbles arrives at the initial liquid surface in image 7, and merges with the vapour clouds creating a vigorously flashing vapour region that continues to accelerate upwards at a very high speed in images 8 through to 11. Images 12 to 14 display a reduction in the violence of the phase change, and show a lower concentration of vapour in the two-phase mixture. The flow pattern appears to change in image 15, and in images 16 to 25, the vapour moves upwards at a higher speed than the liquid, with liquid streams exiting the tube bundle clearly visible as they splash against the viewing window. It seems that the huge pressure drop and significant reduction in flow area created critical flow conditions, with the fluid being choked at the tube bundle, and exiting at the fastest possible flow rate for the majority of the blow-down transient. Images 26 and 27 show the concentration of liquid reducing considerably, with the two-phase flow composed mainly of entrained droplets. Images 28 and 29 display annular flow, and falling liquid films result in a counter-current flow, which persists until all of the liquid has vaporised.

From the flow visualisations, it appears that the majority of the liquid inside the pressurised liquid reservoir had boiled off about 1.1 seconds after the break. Just as was observed for the third experiment, the dynamic load signals corresponding to this time show the compressive loads coming to an end. The effect of fluid drag loading on the tubes is unfortunately undistinguishable from the results. It does not seem that the problem is inertial since the dynamic load oscillations appear to follow the acceleration. Thus, the oscillations on the load results can be explained as inertial, but not the mean trend, which is changing relatively slowly and seems to indicate compressive loading on the load cells. Physically, this does not make sense and cannot be explained by inertia. A detailed frequency analysis is provided in Section 6.4 following up on these views.

It was expected that the flashing flow would initially display pipe blow-down characteristics until the liquid surface reaches the tube bundle, at which point the two-phase flow would behave more like a constricted vessel blow-down. Based on the results obtained from the previous experiments, it is therefore expected that following the initial sharp decrease in pressure, the liquid pressure would follow a ‘quasi-steady’ recovery plateau while the two-phase mixture flashes above the tube bundle, and a slower rate of depressurisation would be demonstrated after the liquid passes through the tube bundle. Unfortunately, due to the absence of reliable dynamic pressure data, attention was shifted towards the static pressure results in attempting to describe the behaviour of the blow-down. The upstream static pressure in Figure 5-28 shows a relatively slow rate of depressurisation beginning at about 650 milliseconds after rupture, which, according to the above reasoning, means that this corresponds to the time at which the liquid passed through the tube bundle. It is not possible however for the fluid to have taken this long to reach the tube bundle, as the liquid temperature in Figure 5-29 indicates a departure from the isothermal superheated state as early as 500 milliseconds after rupture.

The downstream static pressure curve shows a brief recovery pressure plateau between 230-250 milliseconds, before establishing a relatively slow rate of depressurisation that persists until about 370 milliseconds. The thermocouples downstream of the tube bundle show a similar rate of decrease in temperature between 250-370 milliseconds, indicating a relatively constant temperature gradient in the pipe section downstream of the tube bundle. These results imply that the fluid passed through the tube bundle at an estimated time of about 250 milliseconds after the rupture of the disc, and the conditions below the tube bundle past this point in time were independent of the conditions established downstream of the tube bundle. In other words, critical two-phase flow occurred at 250 milliseconds after which the flashing was determined only by the thermodynamic conditions of the fluid upstream of the tube bundle. These findings can be related to the visual observations in Figure 5-37, in which image 19 that corresponds approximately to 250 milliseconds displays the appearance of a larger concentration of choked liquid streams exiting from the tube bundle.

Chapter 6 – Analysis and Discussion

Despite the load cells not supplying any useful information on fluid drag loads during the simulated steam generator blow-downs, the experimental results provided significant insights with regards to the transient thermodynamic behaviour of the fluid undergoing sudden depressurisation. An analysis of the acquired data offers useful descriptions of the predominant physical mechanisms and phenomena taking place, as well as possible explanations for unanticipated trends and developments. This could lead towards possible means of rectifying and eliminating the encountered difficulties in future endeavours, such that more accurate quantitative results can be obtained, and dynamic drag loading on the tube bundle can be measured. In addition to the physical information acquired using the sensors, the high-speed flow visualisations presented a valuable set of qualitative data from which various changing properties of the two-phase mixture, such as void fraction and slip, could be observed and analysed from a visual perspective.

The starting point of the blow-down experiments was the opening of the rupture disc, which subjected the pressurised fluid to a sudden pressure reduction that accelerated the two-phase mixture upwards towards the break location and into the vacuum tank. The initial flow rate is limited by the fluid inertia, and the pressure loss is transmitted as a pressure wave during the subcooled depressurisation. During the transient blow-down, the system can be assumed to be adiabatic, and therefore, the depressurisation follows a path of constant entropy, from the initial subcooled point to the point of flashing inception. When the liquid pressure falls sufficiently below the saturation value corresponding to the initial temperature, in the superheated region, vapour nucleation occurs. The delay time associated with nucleation is dependent on the rate of depressurisation. Following the initiation of the explosive phase change behaviour, the fluid enters a two-phase transition regime during which the vapour-liquid ratio begins to

increase. The degree of superheat at which flashing begins determines the initial conditions of the subsequent blow-down process. Flashing that occurs near the saturation point will display different behaviour than flashing that is delayed until much lower pressures are achieved.

The superheated liquid that is created immediately following the depressurisation exists in a meta-stable state, and the ensuing volume production drives the two-phase mixture towards thermodynamic equilibrium. In a perfectly homogeneous system, nucleation arises spontaneously due to thermal fluctuations and intermolecular interactions, and the flashing displays bulk boiling behaviour. Factors such as surface roughness and liquid impurities increase nucleation heterogeneity, and reduce the time available for pressure relaxation before bubble formation. In such cases, the flashing would occur as liquid-vapour interface boiling, and heterogeneous boiling at liquid-solid boundaries. In real steam generators, the nucleation would occur at the walls due to sizeable surface imperfections, and the same phenomena were seen in the present blow-down experiments. The primary vapour generation mechanisms observed were the activation and growth of bubbles either pre-existing in the bulk liquid, or originating from surface cavities, and vapour generation in the bulk liquid was less evident. Figure 6-1 shows two vapour generation cases with bubbles acting as sites for premature nucleation in the first case and heterogeneous boiling at the vessel walls in the second case.

The images of the initial blow-down nucleation stages displayed clouds of vapour appearing in the liquid suggesting the formation of large amounts of very small bubbles. The appearance of the two-phase mixtures for the remainder of the blow-down as captured by the high-speed imaging system showed some interesting physical behaviour aspects that were clearly distinguishable. The rate of bubble growth is controlled by the transfer of heat from the liquid bulk to the liquid-vapour interfaces. From the flow visualisations, it appears that the rate of bubble growth is very rapid, and the bubbles tend to agglomerate to form continuous regions of vapour that are accelerated towards the break.

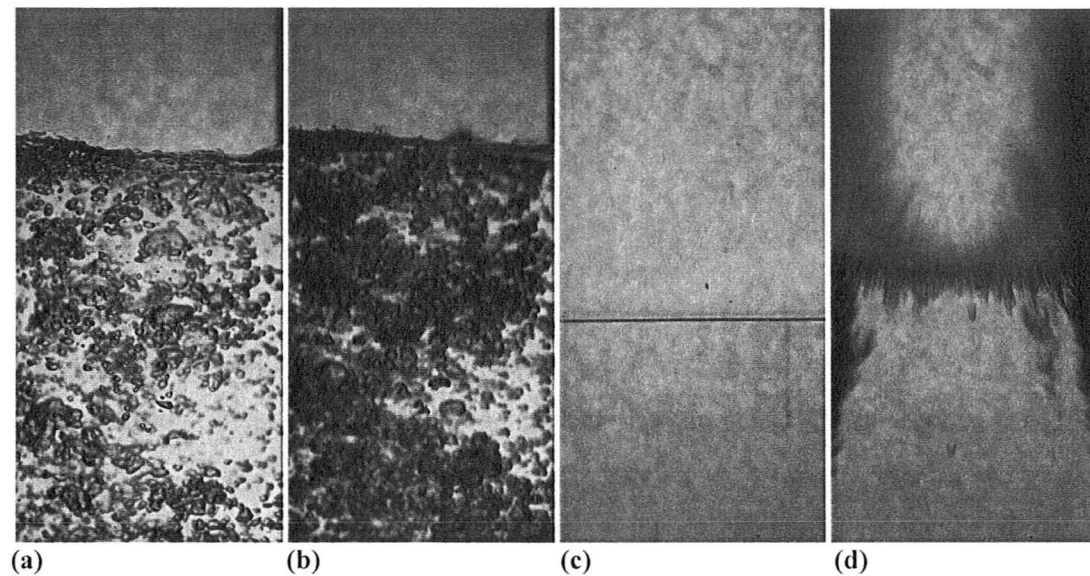


Figure 6-1. Vapour Generation Mechanisms: Interface Boiling (a → b), Heterogeneous Boiling (c → d)

The vapour clouds that formed as a result of the explosive phase change appear to accelerate at a much higher rate than the liquid, seemingly propelling the stagnant liquid upwards during the initial stages of vapour growth. This can be explained by inertial effects between the separate phases, since the density of the vapour is much smaller than that of the liquid phase. The existence of slip provides more space available for the flow, and hence the vapour is accelerated at a higher rate and will have a higher velocity than that of the liquid. The initial stages of the transient are characterised by vigorous boiling and densely populated vapour clouds accelerating upwards. A short period of time later, the void fraction increases sufficiently that the two-phase flow seems to form an accelerating vapour core, containing entrained liquid droplets, that are easier to distinguish towards the final flashing stages. In the last experiment where the flow exiting the tube bundle was captured, the two-phase mixture seemed to flow in an annular configuration, with the vapour region occupying the centre of the flow area, and the liquid displaced towards the walls and the sight windows, with occasional streams of liquid discernibly splashing against the glass. The significant area reduction imposed by

the tubes appears to have choked the flow, and the observed flashing mixture was likely pressure driven towards the break at the critical two-phase flow rate.

6.1 Temperature Results

The thermocouples appeared to perform very satisfactorily throughout the experimental phase of this project. Despite being subjected to significant blow-down mechanical loads and sudden changes in the surroundings, all the thermocouples remained functional and did not require replacement between experiments. It is not clear whether the temperature values are actually correct at a specific point in time, or whether there is a certain error associated with dynamic rise times. The temperature measurements correspond very well with the static pressures, and seem to indicate the presence of transient and steady-states at the about the same times. With regards to temperature spikes associated with vapour growth inside the superheated liquid, or superheated slugs of liquid entrained in a vapour region, the response time appears to be in the milliseconds range. Considering this very rapid thermocouple response to sudden changes in temperature, it is likely that the constant temperature region at the start of the blow-down represents the duration of the isothermal depressurisation of the initially subcooled liquid, and the time required for the boiling vapour front to arrive at the particular thermocouple location.

The following temperature plots show the temperatures obtained for all four experiments at one particular location per plot, with the bottom location (pressurised liquid reservoir) shown in Figure 6-2, the upstream location (between the top sight windows and the rupture disc) in Figure 6-3, the downstream location (between the rupture disc and the vacuum tank entrance) in Figure 6-4, and the vacuum tank location (at the side of the vacuum tank) in Figure 6-5. Plotting the data in this manner facilitates comparison of the effects of changing experimental parameters at the different locations.

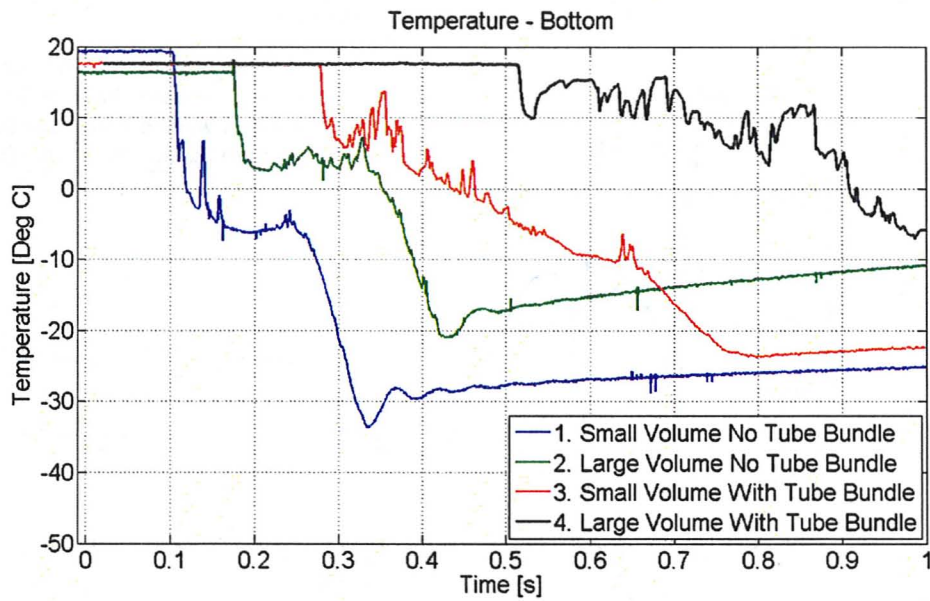


Figure 6-2. Temperature vs. Time (Bottom Location)

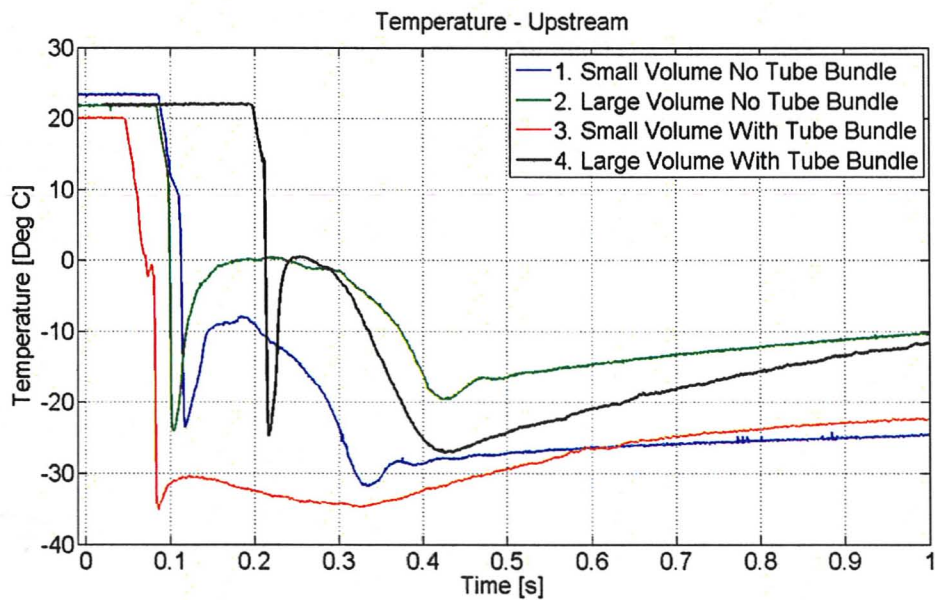


Figure 6-3. Temperature vs. Time (Upstream Location)

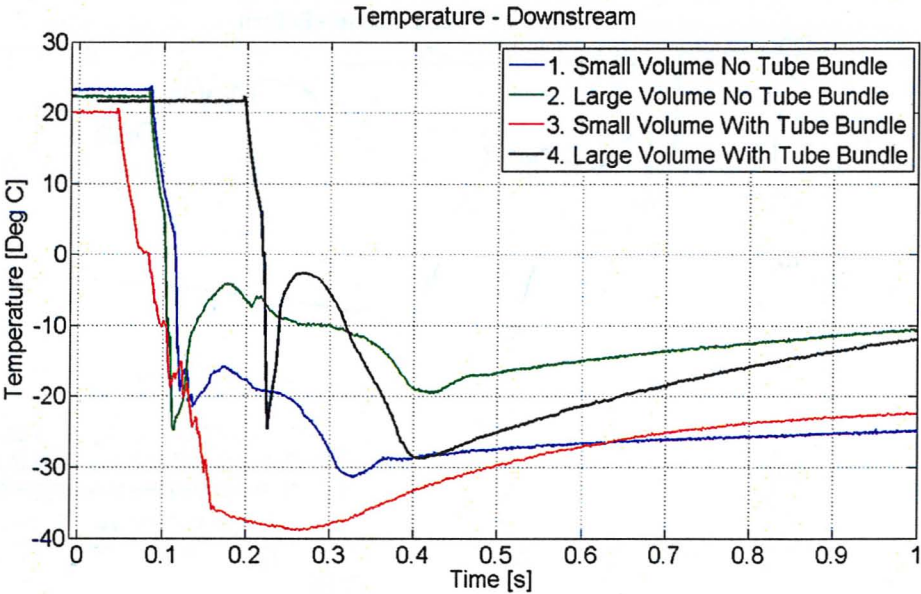


Figure 6-4. Temperature vs. Time (Downstream Location)

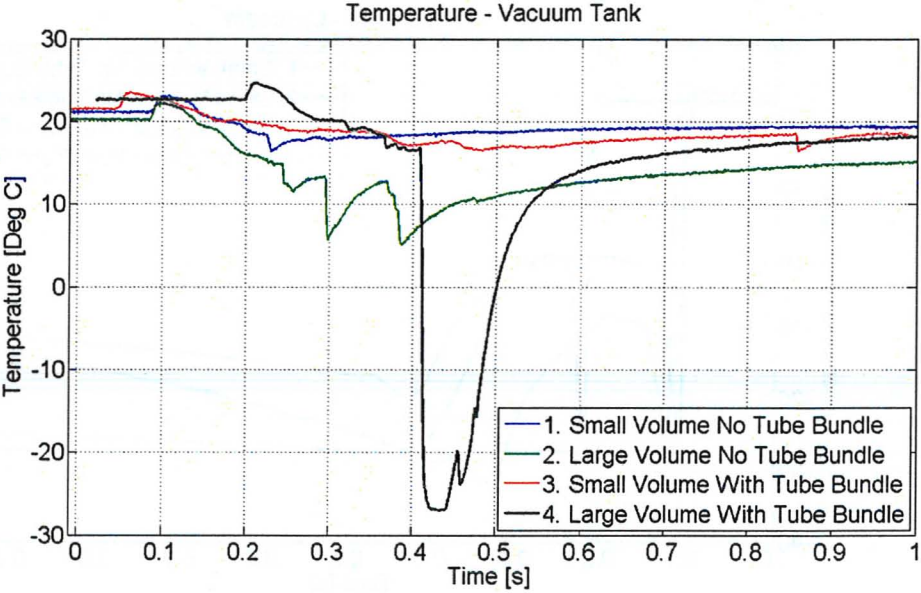


Figure 6-5. Temperature vs. Time (Vacuum Tank Location)

The implications of the thermocouple locations with respect to the temperatures being measured warrant some discussion before the analysis of the results is presented. The ‘bottom’ thermocouple is submerged in the liquid region during all four experiments, and measures the initial temperature of the liquid prior to the blow-down. Once the sudden depressurisation is imposed, the thermocouple measures the temperature of the superheated liquid until a sufficient amount of liquid has vaporised, after which the temperature of the surrounding vapour produced as a result of flashing is measured. The ‘upstream’ thermocouple lies in the vapour region just upstream of the rupture disc in all of the experiments. The temperatures measured are those of the initial vapour prior to depressurisation, the isothermal depressurisation, the vapour expansion, and possibly the superheated liquid slugs accelerated upwards, or falling liquid on the inner wall surface. The ‘downstream’ thermocouple is initially in vacuum, and measures the impinging flow temperature after disc rupture. Finally, the ‘vacuum tank’ thermocouple is situated inside the vacuum tank at the farthest point from the blow-down rig. The vacuum tank was designed mainly to provide enough volume expansion such that the downstream pressure does not affect the transient, and ideally, the temperature in the vacuum tank should not be significantly affected by the transient blow-down.

The effects of volume of liquid and presence of the tube bundle on thermal response can be evaluated based on the plots presented above. The liquid temperature behaviour is displayed in Figure 6-2. The most notable feature is the difference in behaviour caused by the presence of the tube bundle. The temperature response during the first two experiments displays very similar characteristics, and the same applies to the two experiments performed with the test section installed. For the first two experiments, the temperature undergoes a sudden decrease, followed by a quasi-steady stage that accompanies the phase change, and then the temperature decreases at a slower rate than the initial drop towards a temperature minimum, before increasing slightly towards the equilibrium state, following a steady-state saturation path thereafter. In contrast, the temperature behaviour with the tube bundle installed shows a more gradual decrease, with a larger concentration of temperature spikes indicating a higher degree of mixing

between the liquid and vapour phases. This condition persists until steady-state conditions are established, and the temperature follows a saturation path.

There appear to be two perceivable effects of increasing the initial volume of liquid. The first is the longer duration of the early isothermal stage preceding the temperature drop, and the second is the higher temperature for the ‘quasi-steady’ and steady state stages. The influence of volume on the temperature magnitudes is uncertain, as the initial temperature difference before the blow-down was activated between the first and second experiments could also produce similar effects on the subsequent transient. As previously mentioned, the first experiment was a saturated blow-down case, whereas the remaining experiments were all performed under initially subcooled conditions. Additionally, the liquid region in the third experiment contained vapour bubbles that were introduced by the accumulator compression, which served as sites for premature nucleation, and possibly reduced the time available for the depressurisation to reach a higher superheat.

Figure 6-3 shows that increasing the liquid volume results in a higher recovery temperature after the initial dip in vapour temperature. As expected, the higher volume also produces a longer time delay before the first recorded temperature dip for both cases where the test section is installed. For the first two experiments however, both temperatures occurred after the same time delay, and the temperature drop was faster for the larger volume experiment. This behaviour is a result of higher rates of depressurisation established in the liquid region when the liquid surface is initially closer to the rupture disc. As a result, the phase change is more rapid, and the thermocouples respond accordingly. The effect of the tube bundle is only noticeable for the case of the liquid below the tubes, and the temperature response for the liquid above the tubes is very similar to that without any obstruction to the flow. The reason for this is that for the last experiment, there is no pressure area reduction between the liquid surface and the thermocouple location, which essentially replicates the behaviour of the first two experiments. Once a sufficient volume of liquid has vaporised, about 400 ms after

rupture, the temperature increases at a rate that is very similar to that of the third experiment. The temperature recovery is much smaller in the third experiment than the rest, and the transient stage lasts for a shorter time period.

Figure 6-4 demonstrates the same trends as the upstream thermocouple as far as the effect of volume of liquid on vapour recovery temperature is concerned. The first two experiments show similar initial expansion temperatures, and lower temperatures in the subsequent stages of the blow-down, possibly due to limited vaporisation of the superheated liquid flow accelerating from the upstream location towards the downstream location producing a lower mixture quality in the downstream region. The thermocouple response for the liquid level above the tube bundle is almost identical to the response of the upstream thermocouple, indicating that the temperatures between the two locations equalised very rapidly and equilibrium was quickly established downstream of the tube bundle. For the case with the liquid surface initially below the tubes, the initial temperature reduction followed a ragged, saw-toothed fashion, and despite a slower rate of temperature decrease, saturated steady state was established in this region before the bottom thermocouple even registered a change in temperature.

The vacuum tank temperatures, in Figure 6-5, initially respond with a slight increase, associated with the pressure rise due to the opening of the rupture disc. The temperature rise is fastest for the liquid level below the tubes, since equilibrium conditions were established quicker than for the other experiments, and is slowest for the case of liquid level above the tubes, since the tube bundle produces a longer transient than observed for the other cases. The volume effects are noticeable in the temperature response at this location, especially for the last experiment with the largest liquid volume, where a significant vapour expansion is produced, that seems to occupy the entire vacuum tank, almost incorporating it as part of the blow-down rig.

6.1.1 Liquid and Vapour Phase Temperatures

The influence of initial temperature on the blow-down process might be very significant, and some information can be obtained from the temperature response of the first two experiments, the first of which was initially at a saturated temperature, and the second at a lower subcooled temperature. As previously mentioned, the vapour generation is controlled by heat transfer from the liquid to the vapour interface. Therefore, the initial liquid temperature level determines the magnitude of the driving force for the liquid-to-vapour transition. Higher temperatures produce more rapid phase transitions, which result in shorter transients. This effect is observable in Figure 6-2, where the higher temperature produces more rapid phase change, and the lower temperature produces a higher degree of superheating. However, this may also simply be a consequence of increased volume of liquid undergoing depressurisation.

The transient temperatures deviated significantly between the liquid and vapour phases during the blow-down. The vapour phase approached saturated conditions with respect to the system pressure quicker than the liquid phase, which remained superheated as the transition phase change took place. Closer to the end of the depressurisation, the blow-down rig contained a two-phase region near the bottom in which the fluid was vigorously boiling and vapour was being generated, and a much larger void fraction region closer to the rupture disc. Despite increased mixing caused by the explosive phase change, a temperature gradient between the different temperature locations was clearly observed in all the experiments, up until the point at which final temperature equilibrium was established, which was essentially after the pressurised liquid reservoir was practically entirely filled with vapour.

From the high-speed images captured, it is clear that nucleation initiates at the surfaces of the walls, and not on the sight glasses. It seems from the transient temperature results that the thermocouple junctions did not serve as nucleation sites during these experiments either, as the temperatures did not follow the local vapour saturation

temperatures corresponding to the local pressures for the thermocouple submerged in liquid. In the retrial of the third experiment however (Figure 5-23), there did seem to be a sudden drop in temperature that may have been due to the inception of vapour formation at the thermocouple junction, and bubble detachment led to the temperature returning to the initial superheated liquid temperature. For the most part, deviations from the vapour saturation temperature appeared in the form of upward spikes, indicating contact between the thermocouple junction and flowing superheated liquid slugs.

6.1.2 Influence of Volume to Discharge Area Ratio

From the temperature results, and particularly, the behaviour shown in the third experiment, it appears that the degree of departure from thermodynamic equilibrium, reflected in the rate of fluid expansion, is dependent on the volume to discharge area ratio. When the ratio is small, as is the case for the first two experiments, and the last experiment when the liquid surface is above the tubes, the rate of fluid expansion is relatively high. When the liquid surface is below the tubes however, the exit area of the flow is dramatically reduced, which provides sufficient time for mixing and heat transfer between the phases, such that thermodynamic equilibrium is approached quicker, and maintained throughout the latter stages of the blow-down transient. This observation holds true for the depressurisation behaviour as well, and is discussed in Sections 6.2 and 6.3.

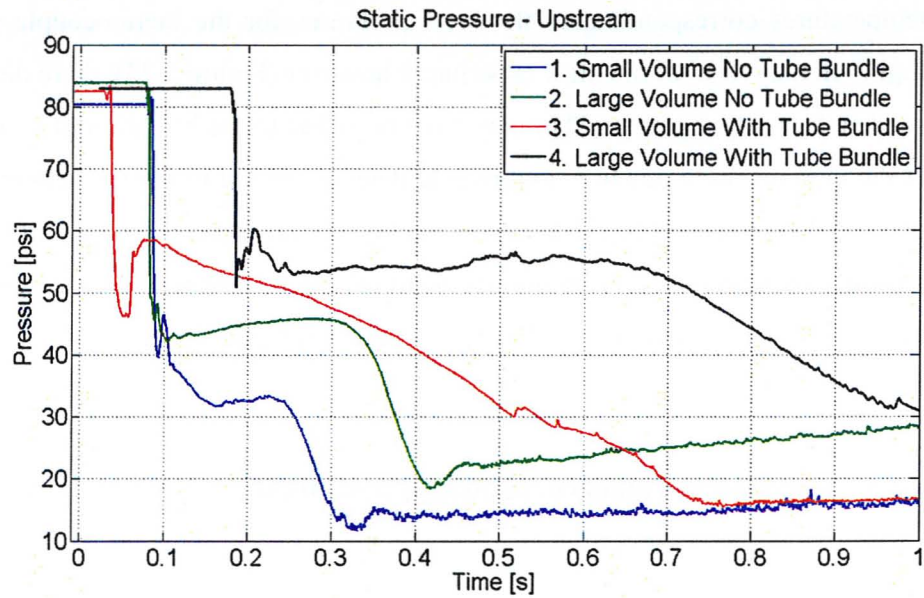


Figure 6-6. Static Pressure vs. Time (Upstream Location)

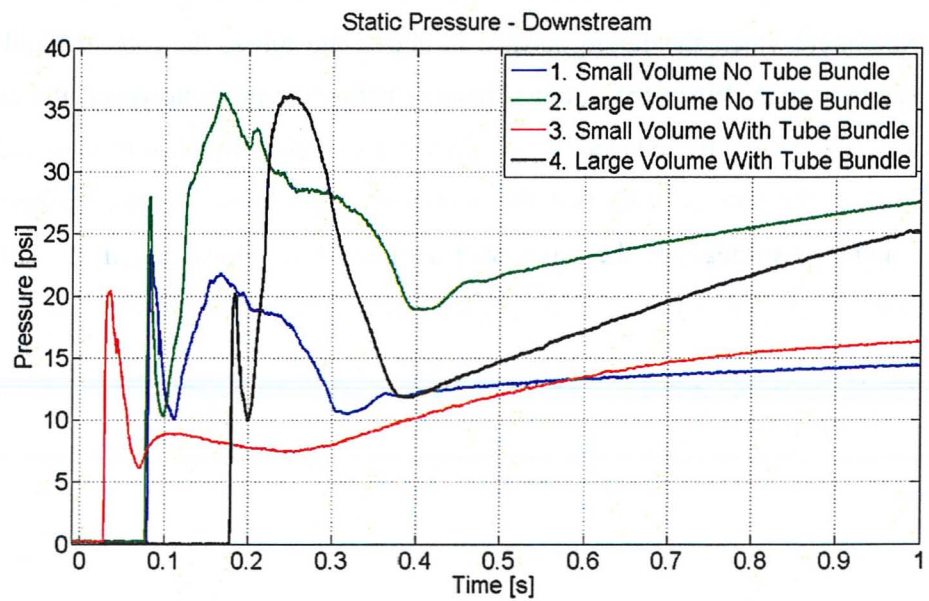


Figure 6-7. Static Pressure vs. Time (Downstream Location)

6.2 Static Pressure Results

Originally, the purpose of the static pressure sensors was limited to providing static pressure values upstream and downstream of the rupture disc, such that the required steady-state thermodynamic conditions and pressure difference between the pressurised liquid reservoir and the downstream vacuum tank could be established, and the sudden depressurisation could be triggered using the accumulator. However, further to the unexpected behaviour of the dynamic pressure transducers, especially at the two locations closer to the rupture disc, the static pressure sensors offered an apparently more reliable alternative for studying the depressurisation behaviour during the blow-down. The overall response of the static pressure sensors matches that of the thermocouples very well, indicating that the pressure behaviour captured was of physical significance.

It must be noted that the magnitudes of the pressures obtained by the static pressure sensors cannot be confirmed with confidence. Since the pressures inside the blow-down rig are changing dynamically, and these sensors are not designed to operate with high-frequency response, they are not expected to capture the non-equilibrium and transient effects with sufficient accuracy. Nonetheless, the behaviour characteristics can be compared, with the relative magnitudes indicative of the effects of the changing parameters on the depressurisation in the closing stages of the transient. The static pressure plots are provided in Figure 6-6 and Figure 6-7. In an analogous manner to the thermocouple plots, the experimental results at one location are all provided on the same plot, and the upstream location in this case actually refers to the bottom location inside the pressurised liquid reservoir.

Figure 6-6 shows that the introduction of the test section in the blow-down rig results in higher recovery pressures following the transient behaviour. The difference in recovery pressures between the first and second experiment also indicates that the volume of liquid influences the magnitude of pressure recovery. This behaviour may also be due to the more explosive phase transition in the second experiment since the liquid was

initially in a subcooled rather than saturated state. The tube bundle also shows an appreciable effect on the rate of depressurisation towards saturated equalised conditions. For the first two experiments, without any obstruction to the flow area, the rate of depressurisation towards saturated equalised conditions is very similar for both cases, with the time delay before the pressure reduction dependent on the initial volume of fluid. For the last two experiments, the rate of depressurisation towards saturation equilibrium conditions is also identical but slower, and the plateau region of quasi-steady recovery pressure is of considerable duration in the last experiment, compared to the third experiment, in which the depressurisation begins almost immediately after the transient undershoot stage without any identifiable pressure plateau.

When the static pressure is compared to the dynamic pressure plots of Figure 6-8 and Figure 6-12, a clear link appears between the amount of time required for the transient behaviour to end, and the time required for the static pressure sensors to respond. The moment the pressure begins to drop on the static plots almost coincides with the end of the rapid dynamic behaviour. This phenomenon is illustrated in more detail in Section 6.3.4 with plots of static and dynamic pressures at the bottom of the rig. It is logical that the dynamic pressure frequencies are too high to be captured by the static pressure sensors, and once they decrease such that they are too slow for the dynamic transducers, the static pressure sensors register a response, in the shape of a response to a step input. It is possible that the observed pressure undershoots, as well as pressure overshoots in Figure 6-7, may have no physical significance, and are simply an artefact of the response of the static pressure sensors to what is perceived as a sudden step input.

The downstream static pressure response in Figure 6-7 is very similar to the thermocouple plots obtained from the locations close to the rupture disc (Figure 6-4). The initial liquid volume has a visible effect on the magnitude and duration of the response, due to the same physical mechanisms previously discussed. Similarly, the tube bundle produces opposite effects on the depressurisation, in that the steady-state pressure is established very quickly for the third experiment, due to a significant reduction in flow

area, whereas the transient takes a relatively long time in the case of the liquid level initially above the tube bundle. Due to the limitations of the static pressure sensors discussed above, analysis of these results is restricted to the qualitative behaviour of the depressurisation during the stages of the blow-down exhibiting relatively slow pressure changes, during which the dynamic pressure transducers did not capture meaningful signals. During the initial transient stages of the blow-down however, the static pressure sensors do not show any change in the pressure response, since the frequencies of the pressure changes are too high.

6.3 Dynamic Pressure Results

The dynamic pressure results are presented in the same location-oriented format, the bottom location in Figure 6-8 and Figure 6-9, upstream location in Figure 6-10 and Figure 6-11, the downstream location in Figure 6-12 and Figure 6-13, and the vacuum tank location in Figure 6-14 and Figure 6-15. Unfortunately, since the accelerometers were employed to investigate acceleration effects in the fourth experiment, there are no corresponding dynamic pressure results available at the pressurised liquid reservoir and vacuum tank locations. It appears that the additional volume of liquid produces a longer duration of transient behaviour at the bottom location, and the presence of the tube bundle substantially increases the duration of the transient even further. It also seems that the insertion of the test section results in higher magnitudes of pressure recovery plateaus. It is interesting to note that the pressure profiles decrease to a minimum point near the end of the obtained results, before the pressures rise and steady state is established. The minimum pressures occur at approximately 250, 325, and 700 milliseconds for the first, second, and third experiment respectively. From the high-speed images, these points in time all coincide with the completion of the liquid flashing stage. For the fourth experiment, this occurs between 0.9 - 1 seconds.

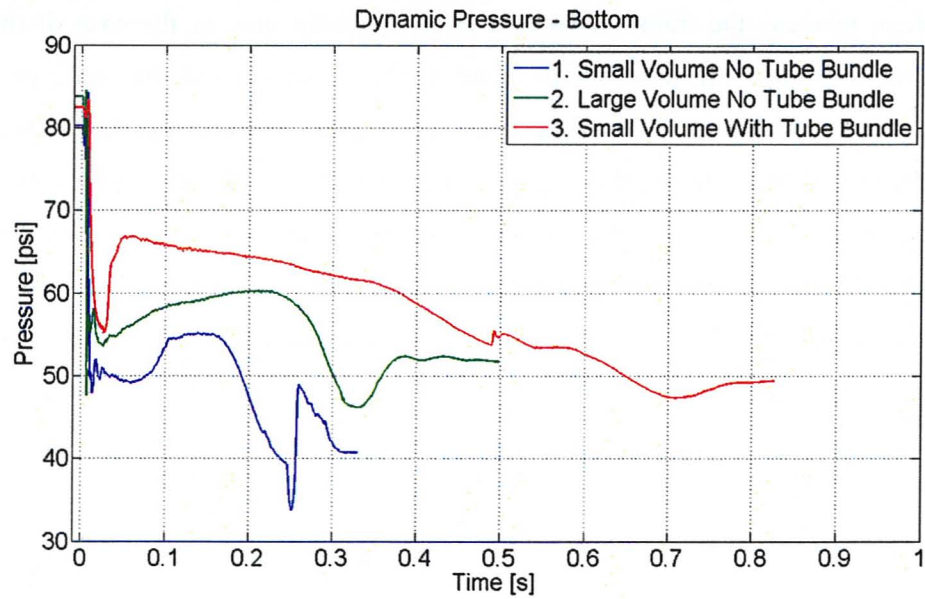


Figure 6-8. Dynamic Pressure vs. Time (Bottom Location)

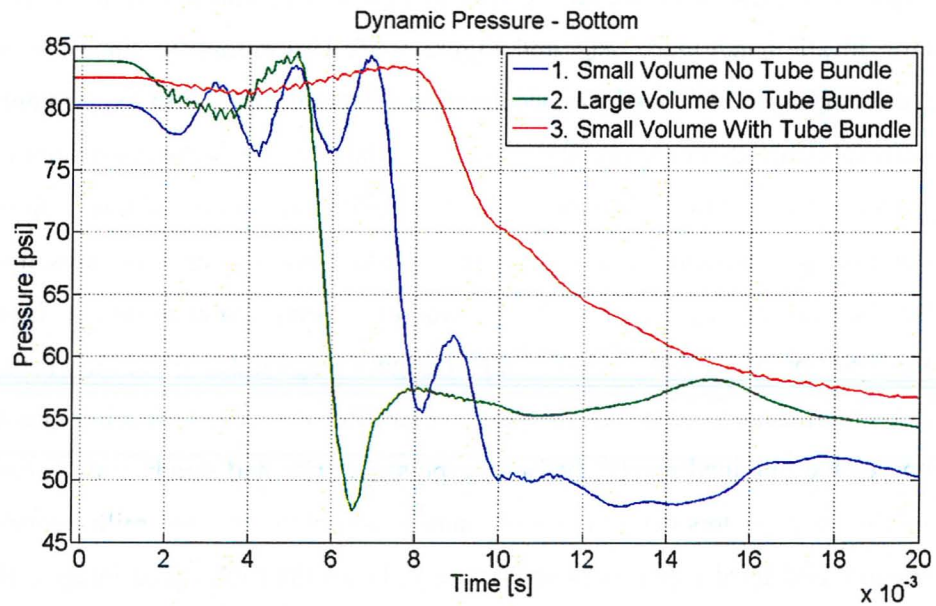


Figure 6-9. Dynamic Pressure vs. Time (Bottom Location; 0.02 s Timescale)

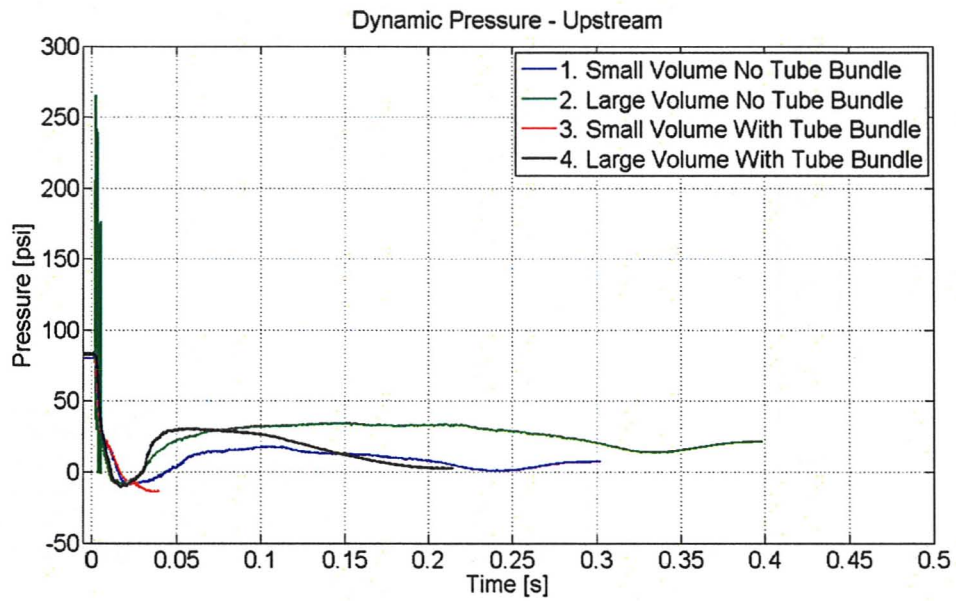


Figure 6-10. Dynamic Pressure vs. Time (Upstream Location)

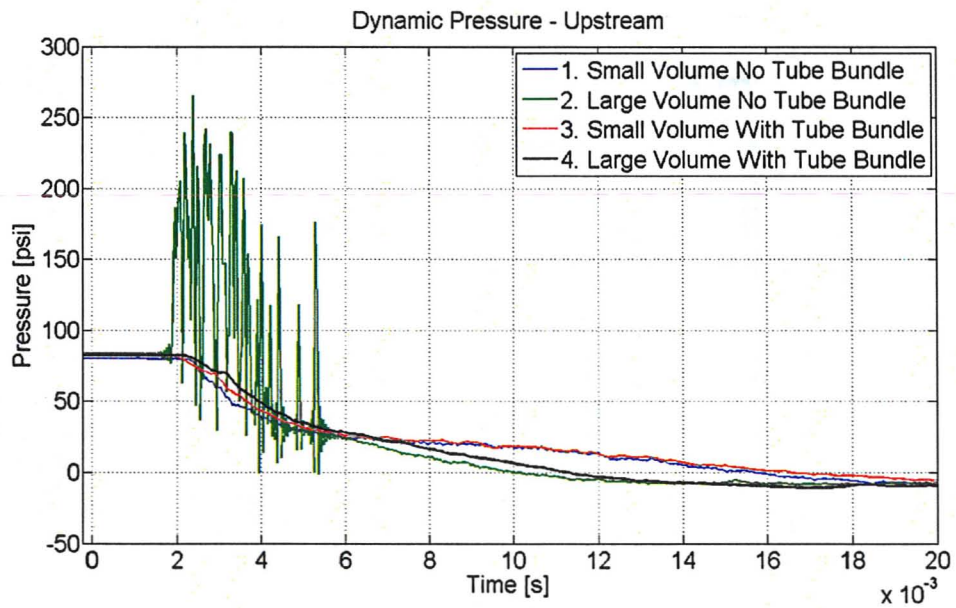


Figure 6-11. Dynamic Pressure vs. Time (Upstream Location; 0.02 s Timescale)

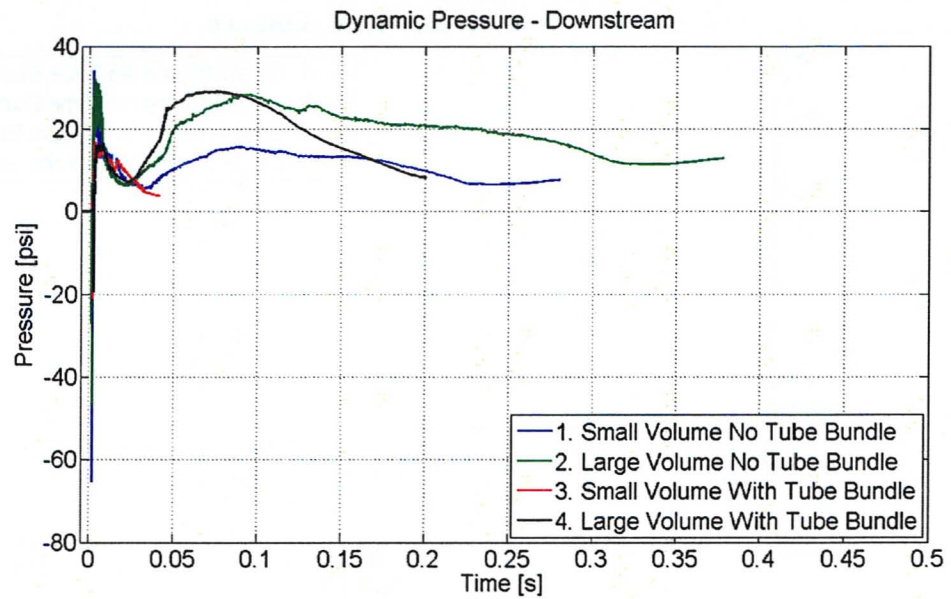


Figure 6-12. Dynamic Pressure vs. Time (Downstream Location)

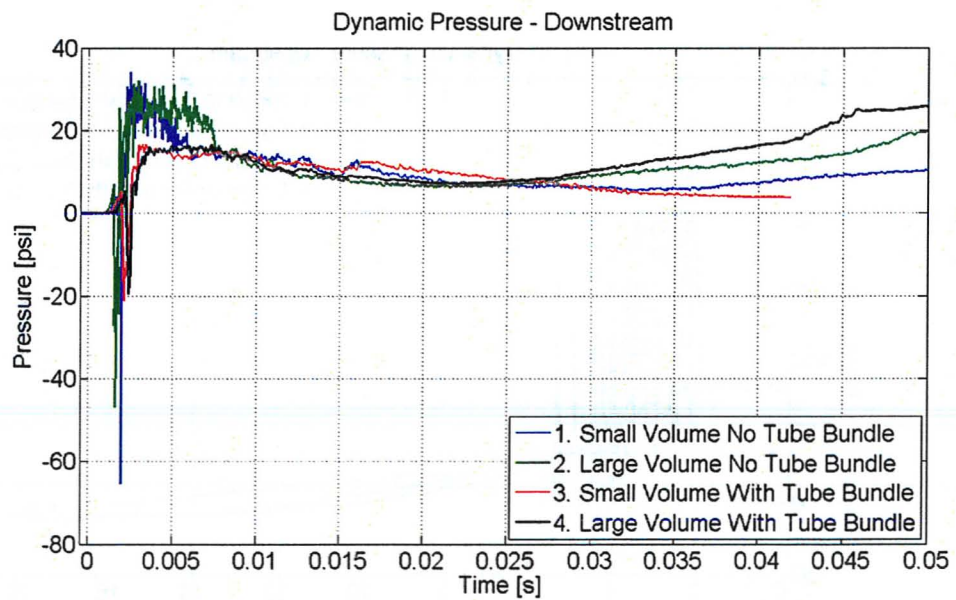


Figure 6-13. Dynamic Pressure vs. Time (Downstream Location; 0.05 s Timescale)

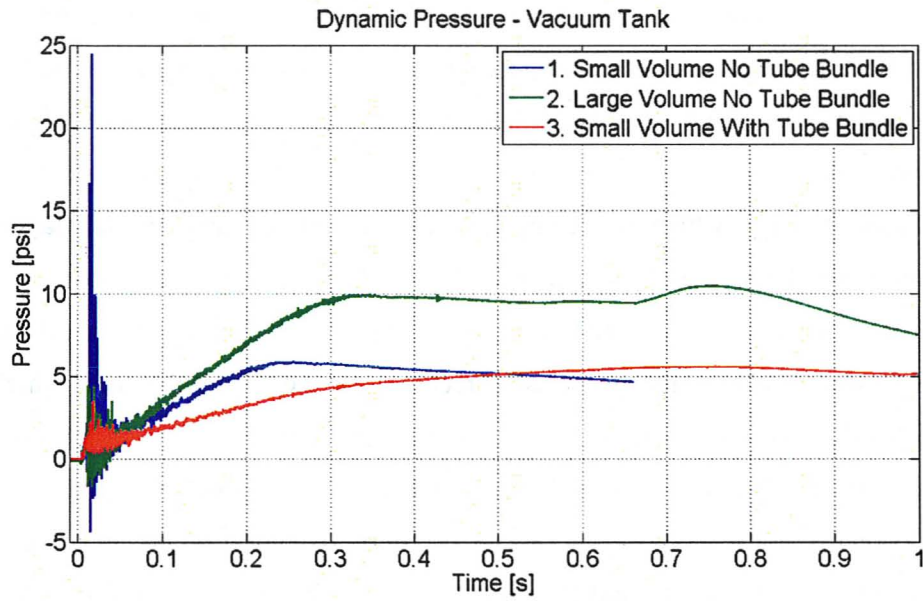


Figure 6-14. Dynamic Pressure vs. Time (Vacuum Tank Location)

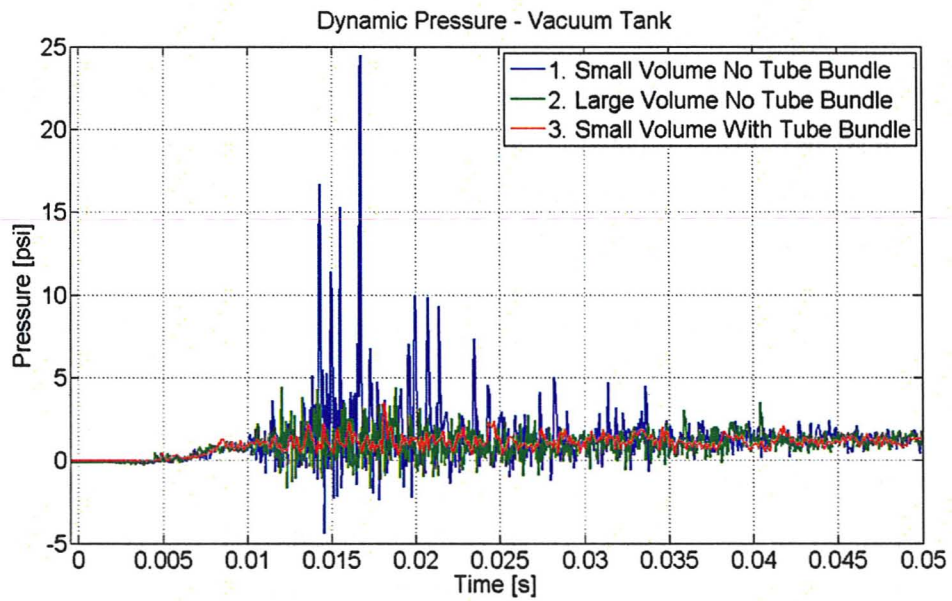


Figure 6-15. Dynamic Pressure vs. Time (Vacuum Tank Location; 0.05 s Timescale)

The pressure undershoot behaviour displayed in Figure 6-9 is remarkably different across the three experiments. The first experiment initially shows some oscillations at high pressure, followed by the pressure undershoot towards 55.5 psi, a pressure recovery to 61.7 psi, and an immediate subsequent pressure reduction towards about 49.9 psi, which is accompanied by a couple of pressure fluctuations and is then maintained for about 60 milliseconds. The second experiment exhibits a more rapid initial depressurisation rate, and a stronger pressure undershoot towards about 47.6 psi, followed by an immediate pressure recovery to about 58.1 psi, after which the pressure steadily increases to about 60.2 psi over the course of 200 milliseconds. The third experiment displays no identifiable pressure undershoot behaviour. Instead, the pressure decreases at a relatively slow rate and remains fixed at a minimum of about 55.9 psi for about 10 milliseconds, and then recovers to a pressure of about 66.8 psi, from which a steady depressurisation takes place until steady state is established. At about 30 milliseconds, where the pressure begins to increase, the high-speed images show the fluid accelerating upwards, accompanied by an apparent increase in the void fraction. When vapour bubbles dominate the bulk of the system, the phase transition takes place mostly through the bubble interface, bringing the pressure to a maximum. Bubble coalescence then changes the flow pattern to liquid droplets entrained in vapour, with low interfacial mass transfer rates. At this point, the pressure inside the rig cannot be sustained, and a gradual depressurisation begins.

A higher initial volume of liquid appears to produce a more rapid rate of depressurisation at the upstream transducer location in the first 10 milliseconds of the transient, as shown in Figure 6-11. Although this behaviour is attributed to the influence of the initial liquid volume, it may also be associated with the physical mechanism of flashing. The second and last experiments were triggered from initially subcooled states, whereas the first experiment was initiated from a saturated state, and the third experiment contained vapour bubbles that may have influenced the flashing and depressurisation behaviour. The effect of initial volume of liquid is more obvious in terms of producing a higher level of pressure recovery following the initial dip in pressure. The initial volume

also affects the duration of the transient. The introduction of the test section produces shorter transients, and steady state is established quicker downstream of the tubes than it would be if there was no reduction to the flow area. Unfortunately, the magnitudes of the pressures obtained at this location cannot be substantiated with confidence, since the pressures are shown to decrease below absolute vacuum at one point or another for all the experiments. In addition, the pressure profile of the second experiment is unique in displaying high-frequency oscillations during the first 5 milliseconds of the transient.

The results shown in the downstream pressure plots in Figure 6-13 are very similar to the upstream results, with a noticeable effect of initial volume on the magnitude of pressure recovery, and a significant reduction of the duration of the transient due to the presence of the tube bundle. The pressures decrease very rapidly below 0 psia in the first two milliseconds of the transient, and it is not clear whether the remainder of the pressure plot actually corresponds with the true local pressure magnitudes. The vacuum tank pressure plot in Figure 6-15 shows high-frequency pressure fluctuations during the initial 35 milliseconds of the transient. It seems that increasing the initial volume of liquid raises the level of dynamic pressure activity inside the tank, as is expected, and the introduction of the tube bundle decreases the rate of pressure increase.

6.3.1 Dynamic Pressure Signal Oscillations

The dynamic results for all but the bottom transducer location display strange high-frequency oscillatory behaviour and questionable pressure magnitudes. Some of the pressures obtained are not physically believable, and it seems that acceleration and thermal transients significantly influence the behaviour of the pressure transducers closest to the rupture disc. The possibility of erroneous measurements being caused by these effects is explored in some detail in Section 6.3.3. The general trends and pressures

obtained for the bottom pressure transducer are more viable in terms of the expected outcomes of the experiments. Therefore, the analysis of the pressure results in this text will revolve mainly around the bottom transducer that is originally submerged in pressurised liquid prior to depressurisation, and reference will be made to the other pressure transducers wherever necessitated by the relevant topics of discussion.

The opening of the rupture disc initiates the depressurisation of the pressurised upstream section of the blow-down rig, and this mechanism is accompanied by the generation of a rarefaction wave that propagates away from the break location towards the pressurised liquid. Following a short time delay after disc rupture, the pressure in the liquid reservoir falls very rapidly below the saturation pressure corresponding to the initial temperature, at a higher rate when there is no flow area reduction upstream to the rupture disc, as illustrated in Figure 6-9. The pressure that responds quicker to the break shows a greater pressure undershoot, and consequently, more violent phase change behaviour is expected. The subsequent nucleation and vapour generation produces an increase in pressure after the minimum pressure is attained. This trend is also observed in the data from the pressure transducers directly upstream of the rupture disc, in Figure 6-10. The magnitude of pressure recovery following the growth of the vapour phase was well below the initial saturation pressure in all of the experiments.

The original dynamic pressure signal under static conditions before the disc opens is essentially a flat signal containing fluctuating noise and pressure perturbations in the range of ± 0.003 psi. The propagation of the rarefaction wave generated by the sudden depressurisation inside the liquid domain is expected to produce a sharp pressure decrease, followed by a pressure recovery due to the vapour expansion. The rarefaction wave broadens as a result of two-phase flow development and the subsequent damping effect. The dynamic pressure trace of the second experiment in Figure 6-9 displays characteristics pertinent to rarefaction wave propagation. However, the signals contain some pressure fluctuations that are difficult to explain. In the second and third experiments, the depressurisation of the superheated liquid was preceded by brief random

pressure fluctuations. The first experiment displays a similar rate of depressurisation as the second experiment, but the oscillations are more pronounced and appear to be periodic. Pressure wave propagation estimates, illustrated in a similar fashion to Figure 4-28, are provided in Appendix G. When there is a smaller amount of liquid inside the pressurised liquid reservoir, the depressurisation wave needs to travel a longer distance before arriving at the liquid-vapour interface.

The early arrival of the depressurisation wave in the case where the liquid level is higher produces a faster depressurisation response because of the time delay associated with the arrival of the pressure wave for the low liquid level case. This slower decompression would allow a longer time for the superheated liquid to nucleate, producing a less violent phase change. The computed rarefaction wave arrival times for the bottom pressure transducer are 6.3, 4.5, and 7.1 milliseconds for the first, second, and third experiment respectively. From the corresponding times and magnitudes of pressure reduction, it is clear that the pressure dips shown in Figure 6-9 represent travelling rarefactions. However, the pressure fluctuations are unlikely to be associated with pressure wave propagation phenomena, since they occur very quickly and the pressure waves would not be able to propagate and reflect in the available times. It may be that the observed oscillations represent inertial vibration effects on top of the pressure response. A frequency analysis presented in Appendix F does not appear to indicate any frequency behaviour related to the vibration of the blow-down rig. It is difficult to establish the influence of inertial effects since the acceleration response of the pressure transducers is not fully understood, and the frequency of vibration of the experimental rig varies from test to test, being largely dependent on the loading of the pressurised liquid reservoir against the scissors jack.

There is also a small possibility that these oscillations are associated with the density fluctuations that activate nucleation sites. They were likely not as pronounced for the slower depressurisation rates because the time available for nucleation made it possible to activate a smaller number of large deterministic nucleation sites. However, the

seemingly periodic nature of the oscillations decreases the likelihood of the pressure fluctuations being caused by nucleation mechanisms. In contrast to the bottom pressure transducer, the pressure changes in the vapour regions did not show very rapid response during the phase transition stage. The second experiment pressure trace is unique in displaying high frequency fluctuations between 2-5 milliseconds after the break, shown in Figure 5-10. Just as previously discussed, this behaviour is unlikely to be caused by pressure wave reflections. The mean pressure follows a similar trend as the other experimental pressure traces, as shown in Figure 6-11, and the peaks are most probably produced by acceleration related effects, similar to those briefly observed in Figure 4-25. The pressure transducer inside the vacuum tank also shows high-frequency fluctuations immediately following the break, and the explanation for such behaviour might lie in highly dynamic pressure activity inside the relatively large volume of the vacuum tank. Analyses of the fluctuations in the frequency domain are presented in Appendix F.

6.3.2 Pressure Wave Propagation Analysis

The dynamic pressure along axial locations inside the pipe is expected to display a rapid pressure change upon the arrival of a travelling pressure wave. Although pressure rarefactions were identified for the first two experiments in the liquid region at the bottom of the reservoir in Figure 6-9, there appears to be no evidence of a travelling rarefaction wave in the vapour region directly upstream of the disc in Figure 6-11. Similarly, the sudden opening of the disc generates a compression pulse downstream of the rupture disc towards the inlet of the vacuum tank. Figure 6-16 shows the pressure signal history in the first 4 milliseconds following rupture at the downstream location. The first experiment pressure data shows a small peak of 3 psi at 1.4 milliseconds, a 4-psi peak at 1.7 milliseconds, and a sharp dip to -65.5 psi at 2 milliseconds. The second experiment peaks at 7 psi at 1.5 milliseconds, and spikes down immediately afterwards to -46.9 psi at 1.6 milliseconds.

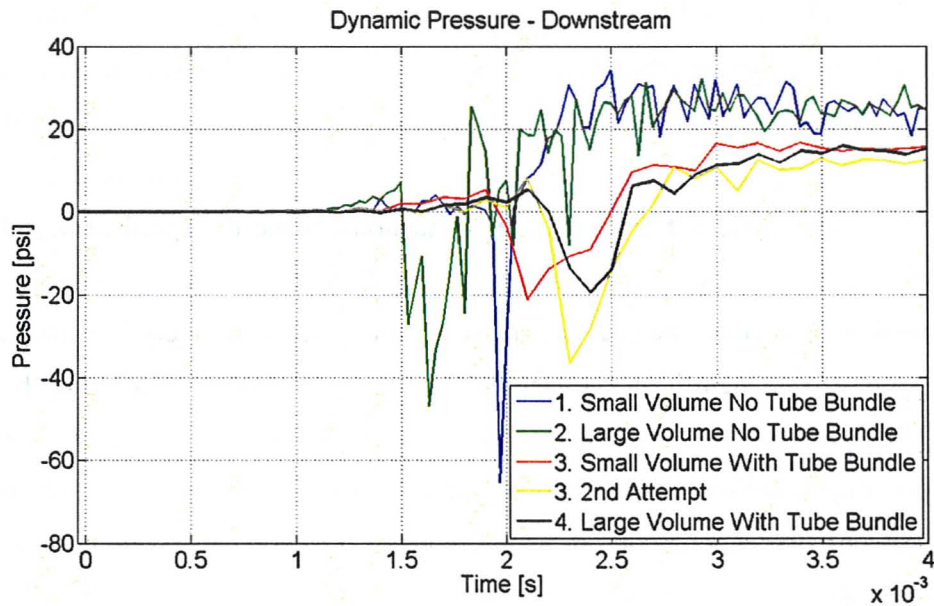


Figure 6-16. Dynamic Pressure vs. Time (Downstream Location; 0.004 s Timescale)

The third and fourth experiments show slightly different behaviour, with 5.3-psi and 5.4-psi peaks at 1.9 and 2.1 milliseconds respectively, followed by a decrease to -21.1 and -19.4 psi at 2.1 and 2.4 milliseconds respectively. The second attempt of the third experiment was included for comparison, and the pressure behaves closer to that observed in the fourth experiment, peaking at 8 psi at 2.1 milliseconds, and dipping to -36.6 psi at 2.3 milliseconds. Following the downward spikes, the pressures return to the positive region and continue to increase as the fluid expands into the downstream segment of the pipe. The negative pressures registered are spurious artefacts of pipe wall acceleration effects. The first two experiments were sampled at 30 kHz, three times higher than the other experiments. This explains the sharp appearance of the downward pressure spikes, compared to the broader dips observed for the slower sampling rates. The initial positive pressures represent the arrival of the compression pulses generated by the opening of the rupture disc.

The ‘water-hammer’ pressure oscillations typical of severe decompressions in relatively incompressible fluids were not present in the results of these experiments. The pressure waves generated were damped out very rapidly by the nucleation and vapour generation that initiates almost immediately after the passage of the depressurisation wave, smoothing out any pressure fluctuations. Since the speed of sound in vapour is considerably slower than in liquid, the rate of depressurisation in the vapour domain is smaller. Therefore, the pressure transducers register a relatively low magnitude pressure pulse, and no significant rarefaction dip is captured further away from the rupture disc. The rarefaction wave was not observed at the bottom pressure transducer for the third experiment in Figure 6-9 because the rate of depressurisation was slower than that of the previous two experiments, providing enough time for the travelling pressure waves to attenuate.

The concept of volume to discharge area ratio discussed for the thermocouples response also applies to the observed dynamic pressure response. When the ratio is smaller, as is the case for the first two experiments, there is not enough time for the heat transfer between the phases to maintain thermodynamic equilibrium, and the rate of depressurisation is very high. When the ratio is increased through the introduction of the tube bundle, the rate of depressurisation is reduced, and thermodynamic equilibrium is established relatively quickly, as shown in Figure 6-9 and Figure 6-10.

6.3.3 Investigation of Erroneous Pressure Measurements

Despite providing valuable information concerning the dynamic pressure behaviour during the transient stages of the blow-downs, the pressure transducers did not behave entirely satisfactorily, and there are some segments of the results that cannot be explained through physical pressures, especially for the two pressure transducers closer to the rupture disc. The occurrence of high-frequency dynamic pressure oscillations observed immediately following the opening of the rupture disc raises the question of

whether the acceleration compensation in the pressure transducers is capable of handling the large shock-loads generated in these blow-down experiments. The direction of the pressure spikes, as well as their timing and duration, offers some valuable clues regarding the possibility of acceleration-related effects in the acquired pressure signals.

When a rarefaction wave passes along a pipe, the relief on the internal pressure could cause the pipe to contract in diameter, and similarly, a compression pulse would produce a sudden pipe expansion. These sudden pipe movements subject the pressure transducers to axial accelerations. Without acceleration compensation, movement towards the flow would produce an increased pressure effect, and movement away from the flow would produce decreased pressure. This exact behaviour is clearly demonstrated in Figure 4-25; the upstream pressure spikes at 2.2 milliseconds and the downstream pressure spikes downward at 1.7 milliseconds. The 0.5 milliseconds phase lag illustrated in Figure 4-28 is associated with the amount of time required for the pressure wave to travel the distance of the sensor location from the rupture disc. An internal accelerometer in the pressure transducers integral with the quartz pressure element cancels unwanted acceleration effects of the sensor diaphragm and end piece masses. The acceleration sensitivity of the sensors is 0.001 Psi/G, but it may be that the acceleration frequencies in the present experiments are above the range of the integrated accelerometers, partly obscuring the acceleration compensation. Edwards and O'Brien (1970) reported similar high-frequency oscillations in a strain gauge transducer that probably did not have acceleration compensation, and frequency oscillations were observed for about 5 milliseconds before the signals agreed with the output of a piezoelectric transducer.

The downward spikes on the downstream pressure transducers were observed in all experiments between 1.5-2.5 milliseconds after rupture, as seen in Figure 6-16. For the upstream pressure transducers, the acceleration effects were only observed in the second experiment. Figure 6-11 shows the pressure fluctuating for about 3 milliseconds, with a relatively higher magnitude of upward positive pressure spikes. The vibration causes the quartz element and some other components inside the piezoelectric transducers

to act as seismic masses, producing measurement error in the pressure signals, limited to the first few milliseconds after rupture. Given the very fast dynamic rise times of the pressure transducers, the signal obtained once the acceleration effects are overcome is expected to represent the actual system pressure. However, Figure 6-10 shows the upstream pressures decreasing below absolute 0 psia between 10-40 milliseconds after rupture. Such behaviour cannot be explained through acceleration effects, and is a result of transient thermal effects on the dynamic pressure transducers. The dynamic pressure signals directly upstream of the rupture disc, and possibly the downstream pressure transducers as well, were substantially degraded by sudden temperature changes produced during the initial stages of the blow-downs.

One of the major effects limiting the accuracy of piezoelectric transducers is their sensitivity to thermal loading effects (Rosseel et al., 1999). Changes in thermal load affect the response of piezoelectric pressure transducers through the corresponding deformation of the transducer and through the resultant effect on the sensitivity. Upon exposure to thermal shock, a temperature gradient is set up in the transducer material and the metal surrounding it. If the corresponding thermal expansion deforms the transducer to the extent that the quartz crystal is touched by this deformation, the pressure transducer registers a response even if the pressure was to remain constant. Therefore, the resulting temperature change and deformation of the transducer in many cases causes a considerable divergence of the transducer response from the actual pressure variation. The transducer sensitivity is affected because thermal load influences the stiffness of the pressure sensing membrane. The sensitivity also changes when the quartz crystal temperature changes. Figure 6-17 depicts a cross-sectional view of the pressure transducers employed in these experiments, with the main internal components labelled. The thermal contractions caused by the sudden temperature drop during depressurisation transients are expected to produce apparent dynamic reductions in pressure. Therefore, the observed pressure reductions below 0 psia can be explained by the thermal contraction of transducers exposed to the rapidly expanding vapour.

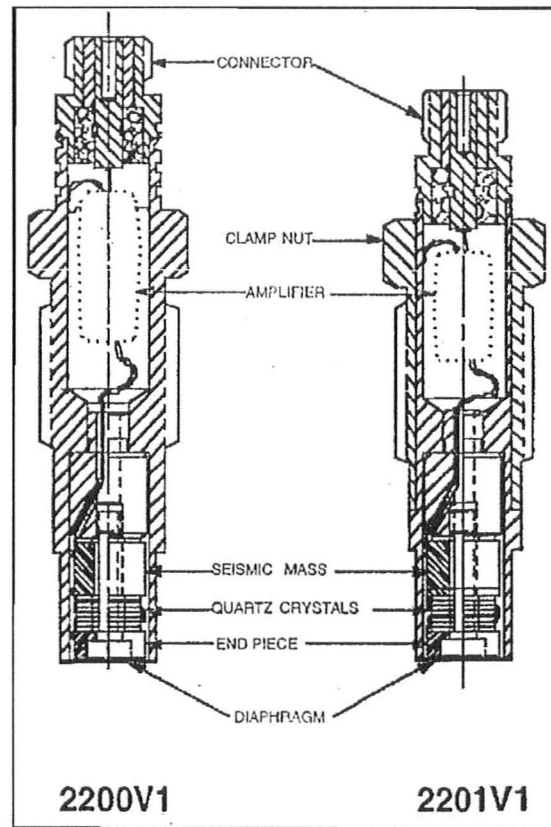


Figure 6-17. Cross-Sectional Representation of Model 2200V1 Dynamic Pressure Sensor

It appears as though covering the pressure sensing membrane of the transducer with a silicon coating that was intended to provide a thermal barrier was not sufficient for insulating the pressure sensor from thermal shock. The thermal insulation coating performed well for the commissioning test, since the pressure signals did not display any detectable thermal loading effects. However, the experimental results indicate that this solution seemingly suffers from limited durability, and the performance of the thermal insulation degraded with continued exposure to depressurisation blow-downs. The degree of severity in pressure measurement error shown in Figure 6-10 is in very good agreement with the timing and magnitude of transient temperature drop at the same location for the corresponding experiments shown in Figure 6-3.

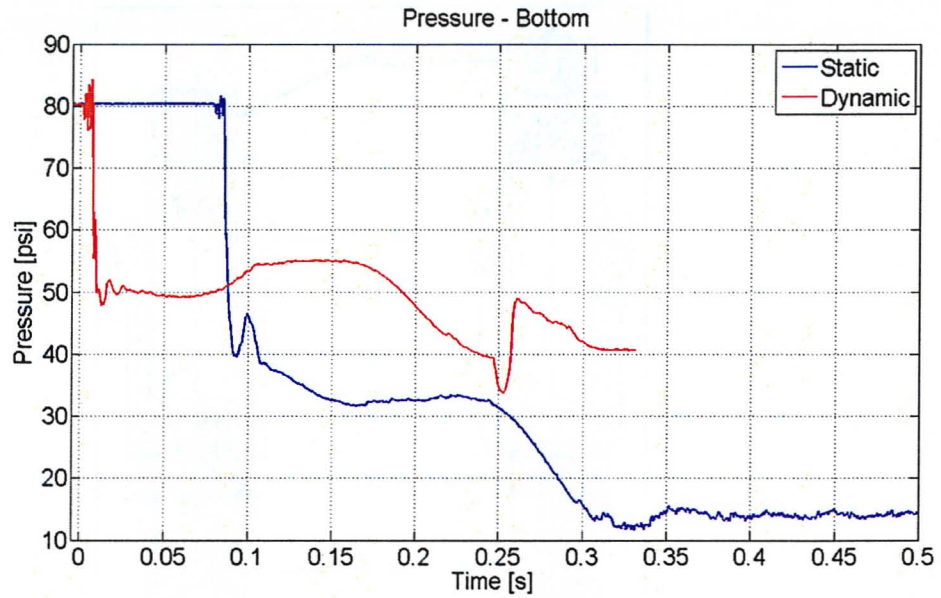


Figure 6-18. Pressure vs. Time (Static Pressure vs. Dynamic Pressure; 1st Experiment)

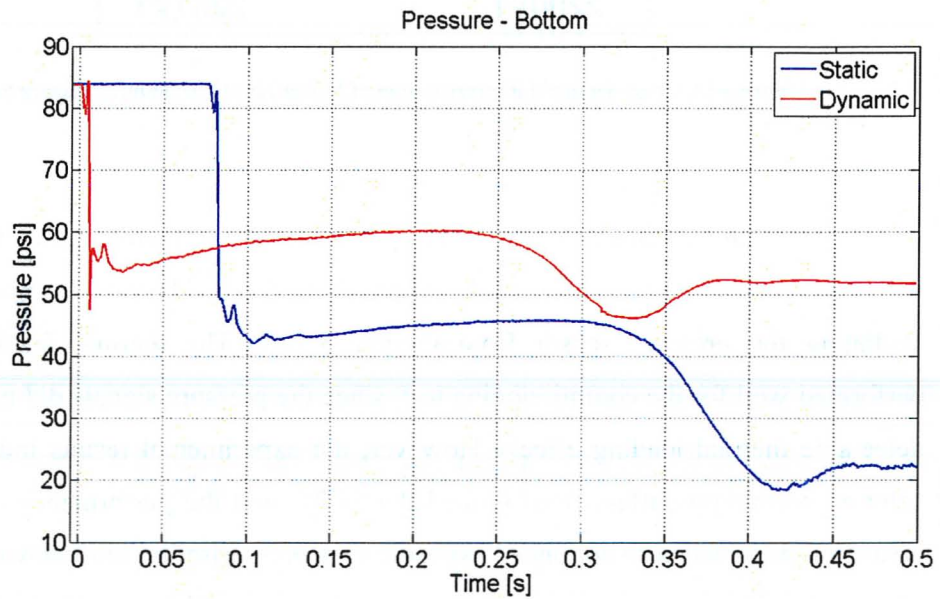


Figure 6-19. Pressure vs. Time (Static Pressure vs. Dynamic Pressure; 2nd Experiment)

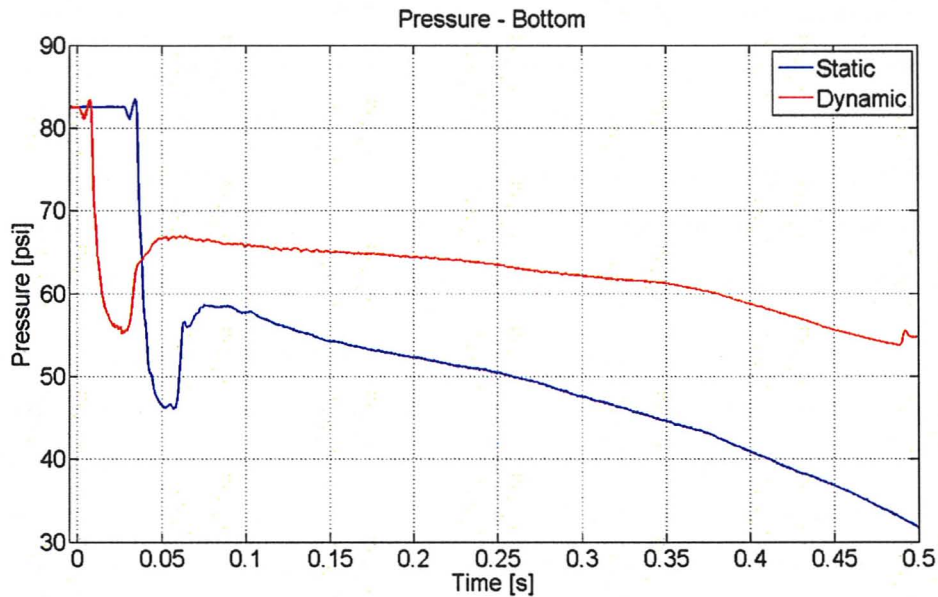


Figure 6-20. Pressure vs. Time (Static Pressure vs. Dynamic Pressure; 3rd Experiment)

6.3.4 Discussion of Static and Dynamic Pressure Results

In order to better illustrate the relationship between the static and dynamic pressure measurements, the static and dynamic pressures at the bottom of the pressurised liquid reservoir for the first three experiments are plotted in Figure 6-18, Figure 6-19 and Figure 6-20. Since the acceleration and thermal shock effects observed for other sensors were not present at this location, the dynamic pressure signal should closely represent the actual pressure variation inside the system during the transient stage of the blow-down. The static pressure sensors respond to the depressurisation after 81, 77, and 28 milliseconds for the first, second, and third experiments respectively. In all of the experiments, this response occurs during the steady recovery of the dynamic pressure signal. Clearly, the dynamically changing pressures are too fast for the static pressure sensor, and the response is sudden with a perception of a step change in pressure. Ultimately, after the transient behaviour is complete, the static pressure reaches saturation

conditions, which agrees very well with the temperature and flow visualisation observations. It appears from Figure 6-18, Figure 6-19 and Figure 6-20 that the static sensors accurately represent the initial pressure conditions before rupture as well as the slowly changing pressures after the transient is complete. However, there is a time delay associated with the response to the rapid transient, after which an amplified change in pressure is immediately produced, overshooting the dynamic pressure signals.

Following the initial sudden response, the overall trends and slopes of the static sensor pressure variations are generally in agreement with the dynamic signals. Furthermore, the phase lag between the two sensors remains consistent throughout the depressurisation, indicating that the static pressure sensors are capable of following the pressure behaviour after a certain time delay, with magnified amplitudes arising from response to sudden pressure changes. From these results, it can be concluded that the static pressure sensors work well except when subjected to an abrupt change in pressure where the time delays and pressure amplitudes are no longer accurately represented. On the other hand, the dynamic pressure transducers react exactly when expected after disc rupture based on the agreement of the calculated rarefaction wave passage times with the registered depressurisations presented in Section 6.3.1. Thus, it appears that these also work well as long as the pressure is changing rapidly enough. The accuracy of the dynamic signal for rapidly changing pressures is expected to deteriorate towards the end of the blow-down where the pressure changes occur at a slower rate, which is demonstrated by the discrepancy between the magnitudes of the dynamic and static pressures after the initial rapid transient is complete. In conclusion, both static and dynamic transducers seem to behave as expected, with the static sensors failing to capture rapid transients, and the dynamic transducers similarly for static pressure variations.

6.4 Dynamic Load Results

The dynamic tube bundle loading results produced by the load cells for each of the two experiments in which the liquid surface relative to the tube bundle was varied are compared in Figure 6-21. The second attempt of the third experiment was selected for comparison with the fourth experiment on the grounds that the dynamic load oscillations are cleaner than those observed in the first attempt of the third experiment, allowing better visual inspection of the behaviour and frequencies. Figure 5-18 also shows a kink in the signal at about 0.5 seconds, which seems to be produced by one individual load cell as identified in Figure 5-17. The load signal in Figure 5-26 does not include any such kinks and the total load is uniform and displays similar behaviour to the signal obtained for the last experiment. It has already been shown that the effects measured by the load cells are not related in an understandable way to the drag loading on the tubes. As such, it is difficult to evaluate the results in terms of the effect of changing the level of the liquid surface with respect to the tubes. Nevertheless, the trends shown in the loading histories contain some physical significance with the respect to the different blow-down behaviour demonstrated in each experiment.

The initial blow-down shock-load is identifiable in the first 10 milliseconds after rupture, producing a drastic increase in high-frequency loading response that extends throughout the first 50 milliseconds of the transient. The load cell response in the first 5 milliseconds of the transient, as illustrated in Figure 5-33, is driven by the shock response of the system to the disc burst. This response is also observed in the accelerometer signals obtained, shown in Figure 5-35. In order to describe the influence of inertial effects on the dynamic load signals, the load cell and accelerometer results were analysed in the frequency domain by computing the FFTs of the signals obtained in the fourth experiment. The frequency content of the signals is compared in Figure 6-22. The frequency peak at 35 Hz is obtained for all signals and clearly represents the first axial natural frequency of the blow-down rig. The smaller peaks that appear at 62, 120, 154,

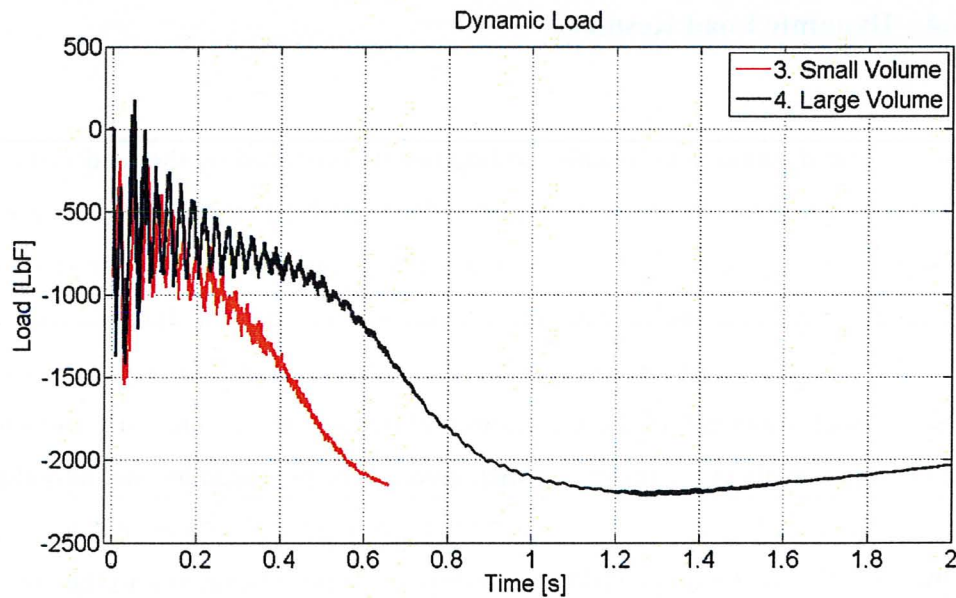


Figure 6-21. Load vs. Time (3rd Experiment vs. 4th Experiment)

and 272 Hz represent different modes of vibration. A frequency analysis of the previous acceleration and load signals is presented in Appendix F, and provides consistent frequencies of vibration. Thus, the oscillations visible in the dynamic loading signals occurring at 35 Hz have been demonstrated to be a result of inertial effects. The mean load signals show the different duration times of the blow-downs and have very similar behaviour but their physical interpretation remains unexplained.

The drag loading on the tubes is expected to produce a tensile force on the load cells that would appear on the calibrated load cell signals as a positive force. However, the loading trend in Figure 6-21 indicates that the load cells are exposed to a compressive force, acting downwards on the tubes. Furthermore, the drag loading was not expected to appear until the flashing fluid flow arrives at the tube surfaces, a finite time period following disc rupture. The dynamic loads registered occurred almost immediately after the opening of the rupture disc, whereas the pressurised liquid in the reservoir did not vaporise until about 3 to 7 milliseconds after the break. The magnitude of the compressive force, the amplitudes of the loading frequencies, and the long-term loading behaviour demonstrated do not seem to be affected by the liquid level inside the blow-

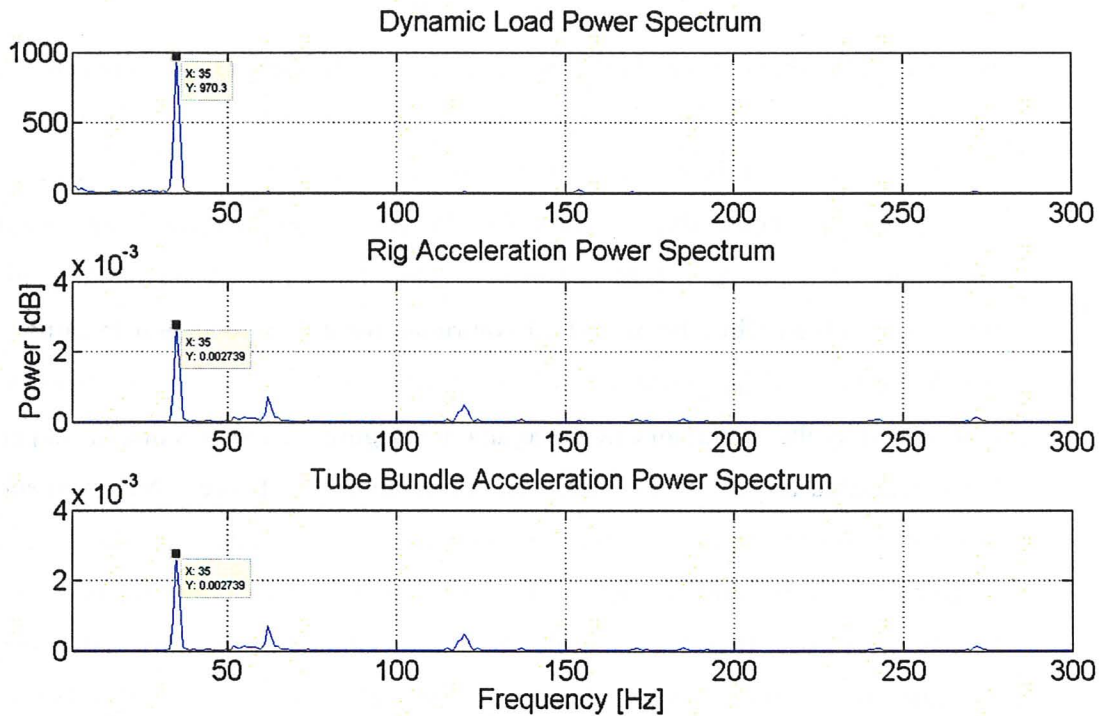


Figure 6-22. Dynamic Load and Acceleration Power Spectra (4th Experiment)

down rig. The only perceivable effect seems to be the extended duration of the loading that is observed for the case with larger volume of initial fluid. The peak value of loading is attained at the point when the liquid phase had completely vaporised. It is possible that the loads measured by the load cells may be related to the thrust force exerted by the pressurised liquid on to the bottom of the reservoir as it flashes upward inside the blow-down rig.

6.4.1 Thrust Force Considerations

The force generated by the expulsion of a suddenly depressurised two-phase mixture, which is the thrust force, can be calculated from Equation (20) (Ardron et al., 1977):

$$F_{CT} = \xi_T \cdot P_0 \cdot A_b \quad (20)$$

where ξ_T is the thrust force coefficient. The thrust coefficient ranges between 1 and 1.25 for saturated blow-downs, and approaches a maximum value of 2 for subcooled blow-downs. Based on this range of thrust force coefficients, the calculated range of theoretically predicted thrust forces for the present experimental subcooled initial conditions from Equation (20) is between 2,400-4,800 LbF. Meta-stability, high void fraction, and high slip ratio would all contribute towards a reduction in thrust loading, which means that the actual thrust load during these experiments is probably better represented by the minimum calculated amount. Figure 6-21 shows that the experimental loads measured are close to the calculated minimum thrust force. An argument can be made that the thrust effects and the subsequent inertial forces of the flashing flow significantly overwhelm the load cell signals such that the drag loads on the tubes become negligible. It is also possible that the magnitude of the blow-down shock-load generates large errors in the load cell measurements, and there are several cases in the literature in which delicate instruments did not operate satisfactorily in the wake of the shock of blow-down initiation. One may point to the neutron densitometer of Allemann et al. (1970) as an example.

6.4.2 Alternative Load Measurement Possibilities

In light of the unsuccessful attempts to measure fluid drag loading on the tube bundle using dynamic load cells, potential alternative methods of measuring the desired dynamic forces are worth some serious thought and feasibility evaluation. When the two-phase flashing mixture flows through the tube bundle past the individual rigid tubes, it tends to physically drag the tube bundle along in the direction of the fluid flow. Seeing as the drag loading is primarily caused by pressure drag, which is related to the dynamic head of the flow, the drag force on the tube bundle can be determined based on the pressure drop across the bundle. It then follows that an alternative solution to obtaining

the dynamic loading characteristics across a sectional model tube bundle is to extract the fluid drag loads from transient pressure drop measurements obtained across the tubes.

Karla and Adams (1980) performed simulation experiments in which the dynamic pressure loading was inferred from the measured dynamic pressure drop. Although they found no significant loading above the steady-state value across the tubes (in contrast to the simulated steam separator region), the observed behaviour changes in the current blow-down experiments due to the significant reduction in flow area in the test section indicate that the pressure drop across the tubes during the transient would be substantial. With the present experimental set-up, the required dynamic loading information cannot be obtained from the pressure measurements. However, the installation of functional, reliable pressure transducers top and bottom of the test section offers a valuable alternative method of determining the drag loading on the tubes during a simulated MSLB.

Another possibility for measuring the drag loading on the tubes is to set up strain gauges such that the drag forces on the tubes can be directly obtained. Strain gauges have no inertial mass so there would be no inertial effects to distort the signals as was observed for the dynamic load cells, and the results of properly calibrated strain gauges would represent a direct instantaneous measure of the load on the tube bundle. The tube bundle supports on which the strain gauges are to be attached would need to be designed carefully with the expected strains accounted for such that sufficient sensitivity in the measurements can be guaranteed. Since the determining factor is the measured strain, the test section supports would need to have a low stiffness such that significant strains could be recorded. Therefore, it is a certainty that the initial shock loading would appear in the signals, but it may be quickly damped out to permit accurate determination of the fluid drag on the tube bundle.

Chapter 7 – Conclusions and Recommendations

In the event of a main steam-line-break (MSLB) loss-of-coolant accident (LOCA), heated pressurised water in the steam generator undergoes rapid depressurisation, resulting in a high-velocity two-phase steam-water flow out of the steam generator. Such a rapid blow-down may induce potentially dangerous transient loading on the tubes in the U-bend region of the steam generator, due to a substantial rise in the pressure drop associated with sudden liquid flashing. There has been much work in the literature investigating the blow-down phenomenon, and particular attention was paid towards predicting the discharged critical flow. Very little experimental research work was performed on the transient tube loading effects during such phenomena, and the available published works are mostly numerical attempts that have produced mixed contradictory results. Hence, tube loading during a MSLB remains a phenomenon that is difficult to predict.

The tubes inside the steam generator represent the boundary between irradiated primary side fluids (deuterium in CANDU steam generators), and the secondary side coolant. Their structural integrity is therefore of utmost importance. This experimental project was devised to study the effect of a simulated blow-down on tube loading, and assist in developing a better understanding of the transient loading and its prediction, such that structural tube failures can be avoided. An experimental rig was designed and constructed such that experimental investigations could be carried out. Using R-134a as a working fluid, the experiments could be performed at ambient conditions, greatly reducing the cost associated with heating and safely containing pressurised water at steam generator conditions. The pressurised liquid was initially charged to a bottom reservoir, and the pressure was relieved through a rupture disc into a vacuum tank that allowed for a minimum expansion ratio of 60:1. Transition sections with sight glasses installed

permitted visual flow observations, and a sectional tube bundle was constructed to simulate the U-tube region in a steam generator.

The rig was instrumented such that thermodynamic behaviour could be investigated through pressure and temperature response, and load cells were installed on the test section for tube loading measurements. A commissioning phase of the project was completed in order to validate the feasibility of the experimental design and prepare for the proper high-pressure experiments to be performed. Through a series of small-scale and large-scale tests, the experimental design concept was verified, and the use of a rupture disc for effective rapid depressurisation and blow-down simulation was demonstrated. The commissioning tests permitted thorough investigation of the instrumentation and data collection system to be conducted, confirmed the structural integrity of the experimental blow-down rig components, and allowed for the development of a well-defined experimental procedure that was implemented in the subsequent experimental phase of the project. The results of the tests were valuable in that the observed blow-down flow behaviour and two-phase thermal-hydraulics could be validated against expected trends and outcomes based on criteria established for similar reported experiments in the published literature. Furthermore, the analysis of the commissioning test dynamic results enabled a methodology for determining the starting time of the blow-down transient to be developed and created a platform for the experimental analysis of transient pressure wave propagations.

Following the commissioning phase of the project, the experimental phase was conducted and the complete set of experimental results is provided in this Thesis. The thermodynamics of the system were assessed, and the effects of various parameters on the blow-down behaviour were established. Unfortunately, it was discovered that large shock-loads associated with the sudden violent nature of blow-downs did not allow proper fluid drag loading measurements to be obtained. Inertial effects produced by the vibration of the experimental rig distorted the load signals by introducing periodic oscillations that were determined using accelerometers, and the mean dynamic loads

remained unexplainable in terms of fluid drag loading phenomena. High-speed flow visualisation methodology was developed which permitted insights into the observed phenomena. The observed nucleation initiated at the liquid-vapour interface of pre-existing bubbles and at the liquid-solid boundaries of the steel surfaces. There was little evidence of homogeneous boiling in the bulk liquid. Slip effects were also noticeable from the flow visualisations, and the temperature and pressure results indicated that the rapid depressurisations produced significant departures from thermodynamic equilibrium.

The degree of departure from thermodynamic equilibrium was dependent on the volume to discharge area ratio. When this ratio is increased significantly by the introduction of the tube bundle into the flow path area, equilibrium conditions were approached. The dynamic pressures reached a minimum point that coincided with the completion of the phase transition from liquid to vapour, after which the pressure inside the rig equalised and began to increase at equilibrium saturation conditions. Significant rarefaction waves generated by the simulated pipe were registered by the dynamic pressure transducer signals only for the fastest rates of depressurisation. Acceleration effects associated with blow-down shock-loads were seemingly beyond the frequency capability of the integrated acceleration compensation in the pressure transducers, which produced strange results and unreliable pressure magnitudes during the first few milliseconds of the transients for the dynamic pressure transducers closest to the rupture disc. Thermal shock due to the rapid expansion of the vapour in the upstream region of the rupture disc substantially degraded the dynamic pressure signals throughout the thermodynamically active stages of the transients.

The experimental rig design is capable of simulating the thermal hydraulics of a steam-line-break (SLB) in a steam generator very adequately, and confidence in the design has been gained through completion of the experimental phase of this project. In order to be able to obtain fluid dynamic tube loading characteristics, an alternative method of measuring the loads may need to be implemented. Potential solutions have been proposed that involve the insertion of additional pressure transducers upstream and

downstream of the test section and strain gauges attached to the test section supports. The pressure drop across the tubes could be monitored, and information regarding the pressure loading on the tubes would be extracted from the results. Alternatively, instantaneous dynamic loads could be measured using properly calibrated strain gauges. In order to obtain reliable dynamic pressure measurements, errors associated with vibration and thermal loads need to be eliminated. The acceleration effects can be controlled by simultaneously measuring the accelerations using accelerometers, and accounting for the vibration by subtracting the corresponding signals from the pressure measurements. Thermal effects can be minimised by ensuring the durability of the insulation coating through reapplication between experiments, installing special adapters designed to minimise thermal effects, or acquiring ‘thermodynamic’ pressure transducers in which the sensitivity to thermal shock is minimised through water-cooling techniques.

References

- Akhtar, S. W., Moon, S. K., Chun, S. Y., Hong, S. D., & Baek, W. P. (2006). Modeling Capability of R134a for a Critical Heat Flux of Water in a Vertical 5 x 5 Rod Bundle Geometry. *International Journal of Heat and Mass Transfer*, 49, 1299-1309.
- Alamgir, M., Kan, C. Y., & Lienhard, J. H. (1980). An Experimental Study of the Rapid Depressurization of Hot Water. *Journal of Heat Transfer*, 102, 433-438.
- Alamgir, M., & Lienhard, J. H. (1981). Correlation of Pressure Undershoot During Hot-Water Depressurization. *Journal of Heat Transfer*, 103, 52-55.
- Allemann, R. T., McElfresh, A. J., Neuls, A. S., Townsend, W. C., Wilburn, N. P., & Witherspoon, M. E. (1970). *Experimental High Enthalpy Water Blowdown From a Simple Vessel Through a Bottom Outlet*. Richland, Washington: Battelle-Northwest, Pacific Northwest Laboratories.
- Allemann, R. T., McElfresh, A. J., Neuls, A. S., Townsend, W. C., Wilburn, N. P., & Witherspoon, M. E. (1971a). *Coolant Blowdown Studies of a Reactor Simulator Vessel Containing a Perforated Sieve Plate Separator*. Richland, Washington: Battelle-Northwest, Pacific Northwest Laboratories.
- Allemann, R. T., McElfresh, A. J., Neuls, A. S., Townsend, W. C., Wilburn, N. P., & Witherspoon, M. E. (1971b). *High-Enthalpy-Water Blowdown Tests From a Simple Vessel Through a Side Outlet*. Richland, Washington: Battelle-Northwest, Pacific Northwest Laboratories.
- Ardron, K. H. (1978). A Two-Fluid Model for Critical Vapour-Liquid Flow. *International Journal of Multiphase Flow*, 4, 323-337.
- Ardron, K. H., Baum, M. R., & Lee, M. H. (1977). On the Evaluation of Dynamic Forces and Missile Energies Arising in a Water Reactor Loss-of-Coolant Accident. *Journal of the British Nuclear Energy Society*, 16 (1), 81-96.
- Ardron, K. H., & Furness, R. A. (1976). A Study of the Critical Flow Models Used in Reactor Blowdown Analysis. *Nuclear Engineering and Design*, 39, 257-266.
- Auvinen, A., Jokiniemi, J. K., Lähde, A., Routamo, T., Lundström, P., Tuomisto, H., Dienstbier, J., Gúntay, S., Suckow, D., Dehbi, A., Slotman, M., Herranz, L., Peyres, V., & Polo, J. (2005). Steam Generator Tube Rupture (SGTR) Scenarios. *Nuclear Engineering and Design*, 235, 457-472.
- Banerjee, S., & Hancox, W. T. (1978). On the Development of Methods for Analysing Transient Flow-Boiling. *International Journal of Multiphase Flows*, 4, 437-460.

Barták, J. (1990). A Study of the Rapid Depressurization of Hot Water and the Dynamics of Vapour Bubble Generation in Superheated Water. *International Journal of Multiphase Flow*, 16 (5), 789-798.

Bhasin, V., Kushwaha, H. S., Mahajan, S. C., & Kakodkar, A. (1993). *Dynamic Analysis of Steam Generator Internals Following Feed Water Line Break / Main Steam Line Break*. Bombay: Elsevier Science Publishers.

Bouré, J. A. (1975). On a Unified Presentation of the Non-Equilibrium Two-Phase Flow Models. In R. T. Lahey, & G. B. Wallis (Ed.), *ASME Symposium Vol. on Non-Equilibrium Two-Phase Flows* (pp. 1-10). Houston, TX: ASME, New York, NY.

Chappidi, P. R., Kannapel, M. D., Vaidya, N., & Singhal, A. K. (1993). *Steam Line Break and Primary Tube Leak Analysis of a Model-F Generator with ATHOS3-MOD1*. Huntsville, Alabama: CFD Research Corporation.

Chun, S. Y., Hong, S. D., Cho, Y. S., & Baek, W. P. (2007). Comparison of the CHF Data for Water and Refrigerant HFC-134a by Using the Fluid-To-Fluid Modeling Methods. *International Journal of Heat and Mass Transfer*, 50, 4446-4456.

Clegg, G. T., & Papadakis, G. (1986). Rates of Evaporation Accompanying the Depressurization of a Pool of Saturated Freon-11. *Chemical Engineering Science*, 41 (12), 3037-3043.

Deligiannis, P., & Cleaver, J. W. (1990). The Role of Nucleation in the Initial Phases of a Rapid Depressurization of a Subcooled Liquid. *International Journal of Multiphase Flow*, 16 (6), 975-984.

Deligiannis, P., & Cleaver, J. W. (1996). Blowdown From a Vented Partially Full Vessel. *International Journal of Multiphase Flow*, 22 (1), 55-68.

Dobran, F. (1987). Nonequilibrium Modeling of Two-Phase Critical Flows in Tubes. *Journal of Heat Transfer*, 109, 731-738.

Downar-Zapolski, P., Bilicki, Z., Bolle, L., & Franco, J. (1996). The Non-Equilibrium Relaxation Model for One-Dimensional Flashing Liquid Flow. *International Journal of Multiphase Flow*, 22 (3), 473-483.

Drai, P., Porterie, B., Monier, P., & Loraud, J. C. (1998). Numerical and Experimental Study of an Accidental Depressurization in an Enclosure Containing High-Pressure Liquid. *Nuclear Science and Engineering*, 129, 246-260.

DuPont. (2005). *HFC-134a Pressure-Enthalpy (SI)*. From DuPont:
http://www2.dupont.com/Refrigerants/en_US/assets/downloads/h39916_hfc134a_pressur_e_enthalpy_si.pdf

- Edwards, A. R., & O'Brien, T. P. (1970). Studies of Phenomena Connected with the Depressurisation of Water Reactors. *Journal of British Nuclear Energy*, 9, 125-135.
- Elias, E., & Chambré, P. L. (1984). A Mechanistic Non-Equilibrium Model for Two-Phase Critical Flow. *International Journal of Multiphase Flow*, 10 (1), 21-40.
- Elias, E., & Chambré, P. L. (1993). Flashing Inception in Water During Rapid Decompression. *Journal of Heat Transfer*, 115, 231-238.
- Faletti, D. W., & Moulton, R. W. (1963). Two-Phase Critical Flow of Steam-Water Mixtures. *American Institute of Chemical Engineers Journal*, 9 (2), 247-253.
- Ferch, R. L. (1979). Method of Characteristics Solutions for Non-Equilibrium Transient Flow Boiling. *International Journal of Multiphase Flow*, 5, 265-279.
- Forrest, C. F. (1995). *Flaw Tolerance of Steam Generator Tubes Under Accident Conditions*. Ottawa: Atomic Energy Control Board.
- Fraser, D. W., & Abdelmessih, A. H. (2002). A Study of the Effects of Flashing Inception on Maximum and Minimum Critical Two-Phase Flow Rates: Part II: Analysis and Modelling. *Nuclear Engineering and Design*, 213, 11-30.
- Gühler, M., Hannemann, R. J., & Sallet, D. W. (1979). Unsteady Two-Phase Blowdown of a Flashing Liquid From a Finite Reservoir. In F. Durst, G. V. Tsiklauri, & N. H. Afgan (Ed.), *Two-Phase Momentum, Heat and Mass Transfer in Chemical, Process, and Energy Engineering Systems: Proceedings of the International Centre for Heat and Mass Transfer Seminar, Dubrovnik. 2*, pp. 781-795. Washington: Hemisphere Publishing Corporation.
- Hall, J. A., & Hall, P. C. (1979). A Multiple Volume Blowdown Experiment and Comparison with RELAP-UK Predictions. *Nuclear Energy*, 18 (2), 141-149.
- Hanaoka, Y., Maeno, K., Zhao, L., & Heymann, G. (1990). A Study of Liquid Flashing Phenomenon Under Rapid Depressurization. *JSME International Journal*, 33 (2), 276-282.
- Hanson, G., & Anderson, J. E. (1969). Subcooled-Blowdown Forces on Reactor-System Components: Calculational Method and Experimental Confirmation. *Transactions of the American Nuclear Society*, 12, 881-882.
- Henry, R. E. (1970). The Two-Phase Critical Discharge of Initially Subcooled or Saturated Liquid. *Nuclear Science and Engineering*, 41, 336-342.
- Henry, R. E., & Fauske, H. K. (1971). The Two-Phase Critical Flow of One-Component Mixtures in Nozzles, Orifices, and Short Tubes. *Journal of Heat Transfer*, 179-187.

Henry, R. E., Fauske, H. K., & McComas, S. T. (1970). Two-Phase Critical Flow at Low Qualities Part I: Experimental. *Nuclear Science and Engineering*, 41, 79-91.

Hutcherson, M. N., Henry, R. E., & Wollersheim, D. E. (1983). Two-Phase Vessel Blowdown of an Initially Saturated Liquid – Part 1: Experimental. *Journal of Heat Transfer*, 105, 687-693.

Isbin, H. S. (1980). Some Observations on the Status of Two-Phase Critical Flow Models. *International Journal of Multiphase Flow*, 6, 131-137.

Isbin, H. S., Moy, J. E., & Da Cruz, A. J. (1957). Two-Phase, Steam-Water Critical Flow. *American Institute of Chemical Engineers Journal*, 3 (3), 361-365.

Jackson, J. F., Ransom, V. H., Ybarrondo, L. J., & Liles, D. R. (1980). *Light-Water Reactor Safety Analysis Codes*. United States: Los Alamos Scientific Lab., NM (USA). Idaho Falls: Idaho National Engineering Lab.

Ju, Y. H., Moulton, R. W., & Garlid, K. L. (1982). Holographic and Photographic Studies of High-Quality Steam-Water Critical Flow. *American Institute of Chemical Engineers Journal*, 28 (4), 597-603.

Kalra, S. P. (1984). Modeling Transients in PWR Steam Generator Units. *Nuclear Safety*, 25 (1), 33-52.

Kalra, S. P. (1990). On the Methodology for Assessing Steam Generator Tube Rupture Safety Margins. *Nuclear Safety*, 31 (2), 187-201.

Kalra, S. P., & Adams, G. (1980). Thermal Hydraulics of Steam Line Break Transients in Thermal Reactors – Simulation Experiments. *Transactions of the American Nuclear Society*, 35, 297-298.

Kendoush, A. A. (1989). The Delay Time During Depressurization of Saturated Water. *International Journal of Heat and Mass Transfer*, 32 (11), 2149-2154.

Kim, Y., & O'Neal, D. L. (1995). A Comparison of Critical Flow Models for Estimating Two-Phase Flow of HCFC22 and HFC134a Through Short Tube Orifices. *International Journal of Refrigeration*, 18 (7), 447-455.

Klingebiel, W. J., & Moulton, R. W. (1971). Analysis of Flow Choking of Two-Phase, One-Component Mixtures. *American Institute of Chemical Engineers Journal*, 17 (2), 383-390.

Krotiuk, W. J. (2004). *Pressurized Water Reactor Steam Generator Internal Loading Following a Main Steam or Feedwater Line Break*. Washington, DC: Office of Nuclear Regulatory Research.

- Leung, L. K., & Dimayuga, F. C. (2007). Measurements of Critical Heat Flux in CANDU 37-Element Bundle with a Steep Variation in Radial Power Profile. *The 12th International Topical Meeting on Nuclear Reactor Thermal Hydraulics*. Pittsburgh, Pennsylvania: Atomic Energy of Canada Limited.
- Levy, S. (1965). Prediction of Two-Phase Critical Flow Rate. *Journal of Heat Transfer*, 53-58.
- Liao, Y., & Guentay, S. (2009). Potential Steam Generator Tube Rupture in the Presence of Severe Accident Thermal Challenge and Tube Flaws due to Foreign Object Wear. *Nuclear Engineering and Design*, 239, 1128-1135.
- Lienhard, J. H., Alamgir, M., & Trela, M. (1978). Early Response of Hot Water to Sudden Release from High Pressure. *Journal of Heat Transfer*, 100, 473-479.
- Majumdar, S., Kanza, K., Oras, J., Franklin, J., & Vulyak Jr., C. (2007). *Sensitivity Studies of Failure of Steam Generator Tubes During Main Steam Line Break and Other Secondary Side Depressurization Events*. Argonne, IL: Argonne National Laboratory.
- Malnes, D. (1975). Critical Two-Phase Flow Based on Non-Equilibrium Effects. In R. T. Lahey, & G. B. Wallis (Ed.), *ASME Symposium Vol. on Non-Equilibrium Two-Phase Flows* (pp. 11-17). Houston, TX: ASME, New York, NY.
- Malnes, D., & Rasmussen, J. (1974). Blowdown Simulation Based on Nonthermal Equilibrium Effects. *Transactions of the American Nuclear Society*, 19, 286-287.
- Meneley, D. (2003,). *Nuclear Safety and Reliability*. From Canteach: <http://canteach.candu.org/library/20032201.pdf>
- Mignot, G., Anderson, M., & Corradini, M. (2004). A Study of Supercritical Fluid Blowdown. *Transactions of the American Nuclear Society*, 91, 226-227.
- Moody, F. J. (1965). Maximum Flow Rate of a Single Component, Two-Phase Mixture. *Journal of Heat Transfer*, 134-142.
- Moody, F. J. (1966). Maximum Two-Phase Vessel Blowdown From Pipes. *Journal of Heat Transfer*, 285-295.
- Moody, F. J. (1975). Maximum Discharge Rate of Liquid-Vapor Mixtures From Vessels. In R. T. Lahey, & G. B. Wallis (Ed.), *ASME Symposium Vol. on Non-Equilibrium Two-Phase Flows* (pp. 27-36). Houston, TX: ASME, New York, NY.
- Nakamura, S., Matushima, T., & Anzai, S. (1984). Transient Characteristics of Flashing Phenomena of Saturated Water in Vessels and Their Method of Analysis. *Heat Transfer Japanese Research*, 13 (4), 1-18.

Organisation for Economic Co-operation and Development. (2008). *Assessment of Computational Fluid Dynamics (CFD) for Nuclear Reactor Safety Problems*. Issy-les-Moulineaux: Nuclear Energy Agency.

Pinhasi, G. A., Ullman, A., & Dayan, A. (2005). Modeling of Flashing Two-Phase Flow. *Reviews in Chemical Engineering*, 21 (3-4), 133-264.

Reinke, P., & Yadigaroglu, G. (2001). Explosive Vaporization of Superheated Liquids by Boiling Fronts. *International Journal of Multiphase Flow*, 27, 1487-1516.

Revankar, S. T., & Riznic, J. R. (2009). Assessment of Steam Generator Tube Flaw Size and Leak Rate Models. *Nuclear Technology*, 167, 157-168.

Riebold, W. L. (1981). Loss of Coolant Accident. In O. C. Jones Jr., *Nuclear Reactor Safety Heat Transfer* (pp. 273–323). Washington: Hemisphere Publishing Corporation.

Riznic, J. R., & Ishii, M. (1989). Bubble Number Density and Vapor Generation in Flashing Flow. *International Journal of Heat and Mass Transfer*, 32 (10), 1821-1833.

Rosseel, E., Sierens, R., & Baert, R. S. (1999). Evaluating Piezo-electric Transducer Response to Thermal Shock from In-cylinder Pressure Data. *Society of Automotive Engineers Transactions*, 108 (3), 1431-1446.

Sami, S. M., & Duong, T. (1989). A Transient Model for Predicting Nonhomogeneous Nonequilibrium Critical Two-Phase Flows. *Nuclear Technology*, 85, 98-108.

Saury, D., Harmand, S., & Siroux, M. (2005). Flash Evaporation From a Water Pool: Influence of the Liquid Height and of the Depressurization Rate. *International Journal of Thermal Sciences*, 44, 953-965.

Sauvé, R. G., Tabatabai, M., Savoia, D., & Kozluk, M. J. (1996). *Bruce 'B' Steam Generators Flow Induced Vibration Analysis Blowdown Conditions Transient Fatigue Evaluation*. Toronto, Ontario: Ontario Hydro Technologies.

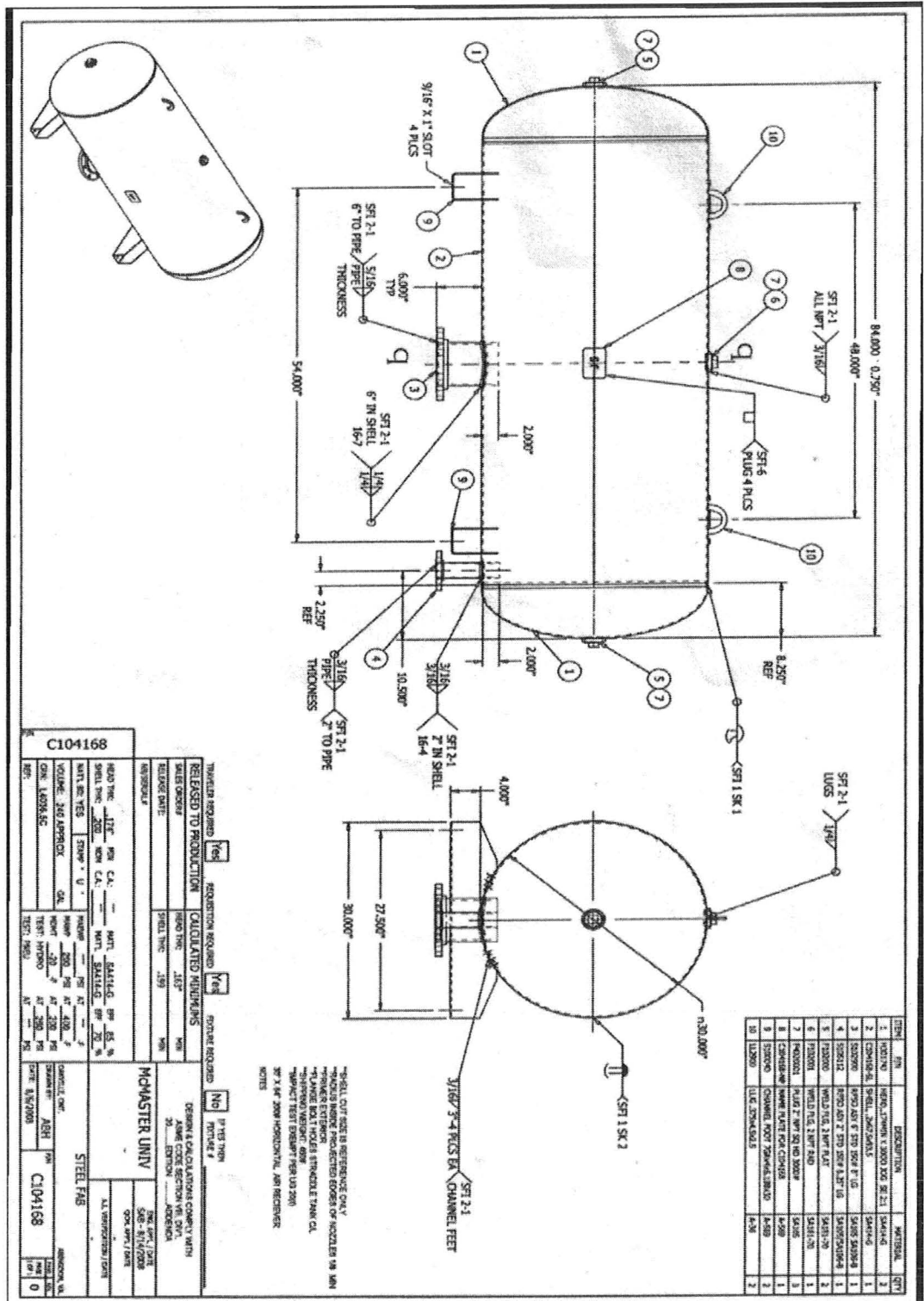
Scheuerer, M., Heitsch, M., Menter, F., Egorov, Y., Toth, I., Bestion, D., Pigny, S., Paillere, H., Martin, A., Boucker, M., Krepper, E., Willemsen, S., Muhlbauer, P., Andreani, M., Smith, B., Karlsson, R., Henriksson, M., Hemstrom, B., Karppinen, L., & Kimber, G. (2005). Evaluation of Computational Fluid Dynamic Methods for Reactor Safety Analysis (ECORA). *Nuclear Engineering and Design*, 235, 359-368.

Schneider, R. E., & Whipple, R. C. (1978). Effect of Subcooled Critical Flow Discharge Model on Hydrodynamic Loads During a LOCA. *Transactions of the American Nuclear Society*, 28, 403.

Sozzi, G. L., & Sutherland, W. A. (1975). Critical Flow of Saturated and Subcooled Water at High Pressure. In R. T. Lahey, & G. B. Wallis (Ed.), *ASME Symposium Vol. on Non-Equilibrium Two-Phase Flows* (pp. 19-25). Houston, TX: ASME, New York, NY.

- Tain, R. M., Groeneveld, D. C., & Cheng, S. C. (1995). Limitations of the Fluid-to-Fluid Scaling Technique for Critical Heat Flux in Flow Boiling. *International Journal of Heat and Mass Transfer*, 38 (12), 2195-2208.
- Wallis, G. B. (1980). Critical Two-Phase Flow. *International Journal of Multiphase Flow*, 6, 97-112.
- Wallis, G. B., & Richter, H. J. (1978). An Isentropic Streamtube Model for Flashing Two-Phase Vapor-Liquid Flow. *Journal of Heat Transfer*, 100, 595-600.
- Weisman, J., & Tentner, A. (1978). Models for Estimation of Critical Flow in Two-Phase Systems. *Progress in Nuclear Energy*, 2, 183-197.
- Winters Jr., W. S., & Merte Jr., H. (1978). Non-Equilibrium Effect in Pipe Blowdown with R-12. In T. N. Veziroglu, & S. Kakaç (Ed.), *Two-Phase Transport and Reactor Safety: Proceedings of the Two-Phase Flow and Heat Transfer Symposium-Workshop, Fort Lauderdale, Florida*. 3, pp. 927-962. Washington: Hemisphere Publishing Corporation.
- Winters Jr., W. S., & Merte Jr., H. (1979). Experiments and Nonequilibrium Analysis of Pipe Blowdown. *Nuclear Science and Engineering*, 69, 411-429.
- Winton, M. L. (1974). Computer Codes for Analyzing Nuclear Accidents. *Nuclear Safety*, 15 (5), 535-553.
- Wu, J. M., & Chuang, C. F. (1984). Consequence Analysis of a Steam Generator Tube Rupture Accident. *Nuclear Technology*, 67, 381-406.
- Yang, J., Jones Jr., O. C., & Shin, T. S. (1986). Critical Flow of Initially Subcooled Flashing Liquids: Limitations in the Homogeneous Equilibrium Model. *Nuclear Engineering and Design*, 95, 197-206.
- Ybarrondo, L. J., Solbrig, C. W., & Isbin, H. S. (1972). The 'Calculated' Loss-of-Coolant Accident: A Review. *American Institute of Chemical Engineers*, 68 (7), 1-99.
- Yoon, H. J., Ishii, M., & Revankar, S. T. (2006). Choking Flow Modeling with Mechanical and Thermal Non-Equilibrium. *International Journal of Heat and Mass Transfer*, 49 (1-2), 171-186.

Appendix A – Vacuum Tank Design Drawing



Appendix B – Specifications and Calibration Certificates

B-2. Static Pressure Sensor – Measurement Specialties U5100

B-3. Dynamic Pressure Transducer – Dytran 2200V1

B-8. Dynamic Load Cell – Dytran 1051V4

B-13. Thermocouple – Omega EMQSS-010E-6

B-14. Data Acquisition Card – National Instruments PCI-4472

B-15. Data Acquisition Card – National Instruments PCI-6221

B-16. Power Coupler – Kistler 5134

B-17. Accelerometer – PCB 352A24

B-18. Accelerometer – Kistler 8794A500



U5100 High Accuracy Pressure Sensor

PERFORMANCE SPECIFICATIONS

Ambient Temperature: 25°C (unless otherwise specified)

PARAMETERS	MIN	TYP	MAX	UNITS	NOTES
Accuracy (combined non linearity, hysteresis, and repeatability)	-0.1		0.1	%Span	1
Long Term Stability (1 year)	-0.1		0.1	%Span	
Total Error Band (over compensated range)			±0.75	%Span	2
Compensated Temperature	-20		+85	°C	
Operating Temperature	-40		+125	°C	3
Storage Temperature	-40		+125	°C	3
Pressure Overload	3X			Rated	
Burst Pressure	4X			Rated	
Vibration (20 to 200Hz)	20			g	4
Shock (11ms)	50			g	5
Pressure Cycles (Zero to Full Scale)	1			Million	6
Weight		96.75		grams	
Media Compatibility	All Materials Compatible with 316 Stainless Steel				

For custom configurations, consult factory.

Notes

- Best fit straight line.
- TEB includes all accuracy errors, thermal errors, span and zero tolerances.
- Maximum temperature range for product with standard cable is -20°C to +105°C.
- Per MIL-STD-810C, Procedure 514.2, Figure 514.2-2, Curve L.
- 1/2 sine per MIL-STD 202F Method 213B condition A.

CE Compliance

EN55022 Emissions Class A & B
 IEC61000-4-2 Electrostatic Discharge Immunity (6kV contact/8kV air)
 IEC61000-4-3 EM Field Immunity (30V/m)
 IEC61000-4-4 Electrical Fast Transient Immunity (1kV)
 IEC61000-4-5 Surge (1kV)
 IEC61000-4-6 Conducted Immunity (10V)
 IEC61000-4-9 Pulsed Magnetic Field Immunity (100A/m)

Pressure Port Options

2 = 1/4"-19 BSP Male
 5 = 1/4"-18 NPT Male
 F = 1/4"-19 BSP Female
 Q = M10x1
 S = M12x1.5
 U = G1/4B DIN 3852
 V = M14x1.5

Others available on request

Electrical Connection Options

1 = 2 ft cable
 4 = Packard Metripak 150
 5 = Bendix PTIH-10-6P
 6 = Hirschmann DIN 43650-C
 D = 4-pin Binder Connector
 M = 1 metres cable
 P = 5 metres cable
 R = 10 metres cable

Others available on request

**SPECIFICATIONS MODELS 2200V1 & 2201V1
DYNAMIC PRESSURE SENSORS**

SPECIFICATION	VALUE	UNITS
PHYSICAL		
WEIGHT	6.0	GRAMS
SIZE (HEX X HEIGHT) MODEL 2200V1	.438 X 1.31	INCHES
MODEL 2201V1	.438 X 1.20	
MOUNTING PROVISION [1]	3/8-24 UNF-2A MALE THREAD	
CONNECTOR, AXIALLY MOUNTED AT TOP	10-32 UNF-2A	
BODY/CONNECTOR MATERIAL	STAINLESS STEEL, HARDENED	17-4 PH
DIAPHRAGM MATERIAL	STAINLESS STEEL	316L
PERFORMANCE		
SENSITIVITY, +20%/-10%	50	mV/Psi
RANGE F.S. FOR +5 VOLTS OUT	+100	Psi
MAXIMUM PRESSURE	1000	Psi
MOUNTED RESONANT FREQUENCY, NOM.	300	KHz
MINIMUM RISE TIME OF INPUT PRESSURE PULSE	2	μSEC
EQUIVALENT ELECTRICAL NOISE FLOOR (RESOLUTION)	.0014	Psi
NON-LINEARITY (ZERO BASED BEST FIT ST LINE METHOD) [2]	±1	% F.S.
ACCELERATION SENSITIVITY, AXIAL DIRECTION	.001	Psi/G
DISCHARGE TIME CONSTANT	2.0	SEC
LOWER -3db FREQUENCY	.08	Hz
ENVIRONMENTAL		
MAXIMUM VIBRATION	5000	G's RMS
MAXIMUM SHOCK	10,000	G's PEAK
TEMPERATURE RANGE	-100 TO +250	°F
MAXIMUM FLASH TEMPERATURE AT DIAPHRAGM	+3000	°F
THERMAL COEFFICIENT OF SENSITIVITY	0.01	%/°F
ENVIRONMENTAL SEAL	HERMETIC	WELDED/GLASS TO METAL
ELECTRICAL		
EXCITATION (COMPLIANCE) VOLTAGE RANGE	+18 TO +30	VDC
EXCITATION CURRENT RANGE [3]	2 TO 20	mA
OUTPUT IMPEDANCE, NOM.	100	Ohms
OUTPUT BIAS VOLTAGE, NOM.	+10	VDC
OUTPUT SIGNAL POLARITY FOR INCREASING PRESSURE	POSITIVE GOING	

SUPPLIED ACCESSORIES

MODEL 6600 SEAL, BRASS, 2 SUPPLIED, BOTH MODELS
MODEL 6507 CLAMP NUT, MODEL 2201V1 ONLY

NOTES:

- [1] MODEL 2201V1 HAS A SEPARABLE CLAMP NUT INSTEAD OF INTEGRAL THREADS ON THE BODY LIKE THE 2200V1. DURING INSTALLATION OF THE 2201V1, THE CLAMP NUT ROTATES INDEPENDENT OF THE BODY. ALL OTHER SPECIFICATIONS ARE SIMILAR.
- [2] PERCENT FULL SCALE, ZERO BASED BEST FIT STRAIGHT LINE METHOD.
- [3] FROM CONSTANT CURRENT TYPE POWER UNIT ONLY. THIS SENSOR **MUST NOT BE CONNECTED** TO A DC POWER SOURCE WITHOUT CURRENT LIMITING, 20 mA MAXIMUM.
- 3 A CALIBRATION CERTIFICATE TRACEABLE TO NIST IS SUPPLIED WITH EACH INSTRUMENT.



Dytran Instruments, Inc.
 21592 Marilla St. Chatsworth, CA 91311 Ph: 818-700-7818 Fax 818-700-7880
 www.dytran.com email: info@dytran.com



CALIBRATION CERTIFICATE LIVM DYNAMIC PRESSURE SENSOR

CUSTOMER: <i>MC MASTER UNIVERSITY</i>			TEST REPORT #: <i>2454</i>			
PURCHASE ORDER #: <i>5559296004</i>		SALES ORDER #: <i>RMA#22644</i>		PROCEDURE: <i>TP2002</i>		
MODEL: <i>2200V1</i>	SERIAL #: <i>2454</i>	TEMP (°C): <i>23.5</i>	HUMIDITY (%): <i>38</i>			
NEW UNIT	RE-CALIBRATION [1] <i>X</i>	AS RECEIVED CODE <i>1</i>	AS RETURNED CODE <i>1</i>			
BIAS VOLTAGE (VDC): <i>8.7</i>		DISCHARGE T.C. (sec): <i>1.80</i>				
CALIBRATION PERFORMED AT <i>30</i> Lb-in MOUNTING TORQUE						
PRESSURE (psi)		SENSITIVITY (mV/psi)		PRESSURE (psi)		
<i>100</i>		<i>48.40</i>				
REMARKS: <i>NONE</i>						
TEST EQUIPMENT LIST - CALIBRATION STATION # 5						
DII #	MANUFACTURER	MODEL	SERIAL #	DESCRIPTION	CAL DATE	DUE DATE
<i>692</i>	<i>FLUKE</i>	<i>45</i>	<i>6976018</i>	<i>MULTIMETER</i>	<i>12/26/09</i>	<i>12/26/10</i>
<i>017</i>	<i>NICOLET</i>	<i>310</i>	<i>IAQ9406710</i>	<i>DIGITAL OSCILLOSCOPE</i>	<i>02/19/10</i>	<i>02/19/11</i>
<i>022</i>	<i>AMETEK / MANSFIELD</i>	<i>T-150</i>	<i>15010</i>	<i>DEAD WEIGHT TESTER</i>	<i>10/01/09</i>	<i>10/01/10</i>
(1) AS RECEIVED / AS RETURNED CODES: 1 = IN TOLERANCE, NO ADJUSTMENTS 4 = OUT OF TOLERANCE > 5% 7 = UNIT NON-REPAIRABLE, RECOMMEND REPLACEMENT 2 = IN TOLERANCE, BUT ADJUSTED 5 = REPAIR REQUIRED 8 = UNIT SERVICEABLE WITH CURRENT CALIBRATION DATA 3 = OUT OF TOLERANCE < 5% 6 = REPAIRED AND CALIBRATED						
(2) THIS CALIBRATION WAS PERFORMED PER MIL-STD-45662A, ANSINCNSL Z540-1-1994, ISO 10012-1 AND IS TRACEABLE TO THE NIST THROUGH TEST REPORT NUMBER: 23938.001. ESTIMATED UNCERTAINTY OF CALIBRATION: 2%. THIS CERTIFICATE SHALL NOT BE REPRODUCED EXCEPT IN FULL, WITHOUT THE WRITTEN PERMISSION FROM DYTRAN INSTRUMENTS, INC.						
CALIBRATION TECHNICIAN: SERGIO AGUILAR				TEST DATE: <i>09/09/10</i> RECOMMENDED RECALL DATE: <i>09/09/11</i>		



Dytran Instruments, Inc.
 21592 Marilla St. Chatsworth, CA 91311 Ph: 818-700-7818 Fax 818-700-7880
 www.dytran.com email: info@dytran.com



CALIBRATION CERTIFICATE LIVM DYNAMIC PRESSURE SENSOR

CUSTOMER: <i>MC MASTER UNIVERSITY</i>			TEST REPORT #: <i>2456</i>			
PURCHASE ORDER #: <i>5559296004</i>		SALES ORDER #: <i>RMA#22644</i>		PROCEDURE: <i>TP2002</i>		
MODEL: <i>2200V1</i>		SERIAL #: <i>2456</i>		TEMP (°C): <i>23.5</i>		
HUMIDITY (%): <i>38</i>		NEW UNIT		AS RETURNED CODE		
RE-CALIBRATION [1] <input checked="" type="checkbox"/>		AS RECEIVED CODE		AS RETURNED CODE		
BIAS VOLTAGE (VDC): <i>8.2</i>		DISCHARGE T.C. (sec): <i>1.80</i>				
CALIBRATION PERFORMED AT <i>30</i> Lb-in MOUNTING TORQUE						
PRESSURE (psi)		SENSITIVITY (mV/psi)		PRESSURE (psi)		
<i>100</i>		<i>48.60</i>				
REMARKS: <i>NONE</i>						
TEST EQUIPMENT LIST - CALIBRATION STATION # 5						
DII #	MANUFACTURER	MODEL	SERIAL #	DESCRIPTION	CAL DATE	DUE DATE
<i>692</i>	<i>FLUKE</i>	<i>45</i>	<i>6976018</i>	<i>MULTIMETER</i>	<i>12/26/09</i>	<i>12/26/10</i>
<i>017</i>	<i>NICOLET</i>	<i>310</i>	<i>IAQ9406710</i>	<i>DIGITAL OSCILLOSCOPE</i>	<i>02/19/10</i>	<i>02/19/11</i>
<i>022</i>	<i>AMETEK / MANSFIELD</i>	<i>T-150</i>	<i>15010</i>	<i>DEAD WEIGHT TESTER</i>	<i>10/01/09</i>	<i>10/01/10</i>
[1] AS RECEIVED / AS RETURNED CODES: 1 = IN TOLERANCE, NO ADJUSTMENTS 4 = OUT OF TOLERANCE > 5% 7 = UNIT NON-REPAIRABLE, RECOMMEND REPLACEMENT 2 = IN TOLERANCE, BUT ADJUSTED 5 = REPAIR REQUIRED 8 = UNIT SERVICEABLE WITH CURRENT CALIBRATION DATA 3 = OUT OF TOLERANCE < 5% 6 = REPAIRED AND CALIBRATED						
[2] THIS CALIBRATION WAS PERFORMED PER MIL-STD-45692A, ANSI/NCSL Z540-1-1994, ISO 10012-1 AND IS TRACEABLE TO THE NIST THROUGH TEST REPORT NUMBER: 23936.001. ESTIMATED UNCERTAINTY OF CALIBRATION: 2%. THIS CERTIFICATE SHALL NOT BE REPRODUCED EXCEPT IN FULL, WITHOUT THE WRITTEN PERMISSION FROM DYTRAN INSTRUMENTS, INC.						
CALIBRATION TECHNICIAN:						TEST DATE: <i>09/09/10</i>
<i>SERGIO AGUILAR</i>				RECOMMENDED RECALL DATE: <i>09/09/11</i>		



Dytran Instruments, Inc.
 21592 Marilla St. Chatsworth, CA 91311 Ph: 818-700-7818 Fax 818-700-7880
 www.dytran.com email: info@dytran.com



CALIBRATION CERTIFICATE LIVM DYNAMIC PRESSURE SENSOR

CUSTOMER: MC MASTER UNIVERSITY		TEST REPORT #: 2457				
PURCHASE ORDER #: 5559296004		SALES ORDER #: RMA#22644				
PROCEDURE: TP2002						
MODEL: 2200V1	SERIAL #: 2457	TEMP (°C): 23.5	HUMIDITY (%): 38			
NEW UNIT	RE-CALIBRATION [1] X	AS RECEIVED CODE 1	AS RETURNED CODE 1			
BIAS VOLTAGE (VDC): 8.7		DISCHARGE T.C. (sec): 1.80				
CALIBRATION PERFORMED AT 30 Lb-in MOUNTING TORQUE						
PRESSURE (psi)	SENSITIVITY (mV/psi)	PRESSURE (psi)	SENSITIVITY (mV/psi)			
100	47.10					
REMARKS: NONE						
TEST EQUIPMENT LIST - CALIBRATION STATION # 5						
DII #	MANUFACTURER	MODEL	SERIAL #	DESCRIPTION	CAL DATE	DUE DATE
692	FLUKE	45	6976018	MULTIMETER	12/26/09	12/26/10
017	NICOLET	310	IAQ9406710	DIGITAL OSCILLOSCOPE	02/19/10	02/19/11
022	AMETEK / MANSFIELD	T-150	15010	DEAD WEIGHT TESTER	10/01/09	10/01/10
<p>[1] AS RECEIVED / AS RETURNED CODES: 1 = IN TOLERANCE, NO ADJUSTMENTS 4 = OUT OF TOLERANCE > 5% 7 = UNIT NON-REPAIRABLE, RECOMMEND REPLACEMENT 2 = IN TOLERANCE, BUT ADJUSTED 5 = REPAIR REQUIRED 8 = UNIT SERVICEABLE WITH CURRENT CALIBRATION DATA 3 = OUT OF TOLERANCE < 5% 6 = REPAIRED AND CALIBRATED</p> <p>[2] THIS CALIBRATION WAS PERFORMED PER MIL-STD-45662A, ANSI/INCSL 2540-1-1994, ISO 10012-1 AND IS TRACEABLE TO THE NIST THROUGH TEST REPORT NUMBER: 23936.001. ESTIMATED UNCERTAINTY OF CALIBRATION: 2%. THIS CERTIFICATE SHALL NOT BE REPRODUCED EXCEPT IN FULL, WITHOUT THE WRITTEN PERMISSION FROM DYTRAN INSTRUMENTS, INC.</p>						
CALIBRATION TECHNICIAN:					TEST DATE: 09/09/10	
SERGIO AGUILAR				RECOMMENDED RECALL DATE: 09/09/11		



Dytran Instruments, Inc.
 21592 Marilla St. Chatsworth, CA 91311 Ph: 818-700-7818 Fax 818-700-7880
 www.dytran.com email: info@dytran.com



CALIBRATION CERTIFICATE LIVM DYNAMIC PRESSURE SENSOR

CUSTOMER: <i>MC MASTER UNIVERSITY</i>			TEST REPORT #: <i>2463</i>			
PURCHASE ORDER #: <i>5559296004</i>		SALES ORDER #: <i>RMA#22644</i>		PROCEDURE: <i>TP2002</i>		
MODEL: <i>2200V1</i>		SERIAL #: <i>2463</i>	TEMP (°C): <i>23.5</i>	HUMIDITY (%): <i>38</i>		
NEW UNIT	RE-CALIBRATION [1]	X	AS RECEIVED CODE	1	AS RETURNED CODE	
BIAS VOLTAGE (VDC): <i>8.7</i>			DISCHARGE T.C. (sec): <i>1.80</i>			
CALIBRATION PERFORMED AT <i>30</i> Lb-in MOUNTING TORQUE						
PRESSURE (psi)		SENSITIVITY (mV/psi)		PRESSURE (psi)		
<i>100</i>		<i>46.60</i>				
REMARKS: <i>NONE</i>						
TEST EQUIPMENT LIST - CALIBRATION STATION # 5						
DII #	MANUFACTURER	MODEL	SERIAL #	DESCRIPTION	CAL DATE	DUE DATE
<i>692</i>	<i>FLUKE</i>	<i>45</i>	<i>6976018</i>	<i>MULTIMETER</i>	<i>12/26/09</i>	<i>12/26/10</i>
<i>017</i>	<i>NICOLET</i>	<i>310</i>	<i>IAQ9406710</i>	<i>DIGITAL OSCILLOSCOPE</i>	<i>02/19/10</i>	<i>02/19/11</i>
<i>022</i>	<i>AMETEK / MANSFIELD</i>	<i>T-150</i>	<i>15010</i>	<i>DEAD WEIGHT TESTER</i>	<i>10/01/09</i>	<i>10/01/10</i>
(1) AS RECEIVED / AS RETURNED CODES: 1 = IN TOLERANCE, NO ADJUSTMENTS 4 = OUT OF TOLERANCE > 5% 7 = UNIT NON-REPAIRABLE, RECOMMEND REPLACEMENT 2 = IN TOLERANCE, BUT ADJUSTED 5 = REPAIR REQUIRED 8 = UNIT SERVICEABLE WITH CURRENT CALIBRATION DATA 3 = OUT OF TOLERANCE < 5% 6 = REPAIRED AND CALIBRATED						
(2) THIS CALIBRATION WAS PERFORMED PER MIL-STD-45662A, ANSI/NCSL Z540-1-1994, ISO 10012-1 AND IS TRACEABLE TO THE NIST THROUGH TEST REPORT NUMBER: 23938.001. ESTIMATED UNCERTAINTY OF CALIBRATION: 2%. THIS CERTIFICATE SHALL NOT BE REPRODUCED EXCEPT IN FULL, WITHOUT THE WRITTEN PERMISSION FROM DYTRAN INSTRUMENTS, INC.						
CALIBRATION TECHNICIAN:						TEST DATE : <i>09/09/10</i>
<i>SERGIO AGUILAR</i>				RECOMMENDED RECALL DATE : <i>09/09/11</i>		

SPECIFICATIONS MODEL SERIES 1051V DYNAMIC FORCE SENSORS

SPECIFICATIONS BY MODEL

MODEL	SENSITIVITY (mV/Lb)	COMPRESSION RANGE (Lbs)	MAXIMUM COMP. (Lbs)	TENSION RANGE (Lbs)	MAXIMUM TENSION (Lbs) [1]	DISCH. TC (Sec)	RESOLUTION (Lb, RMS)
1051V1	500	10	200	10	200	50	.00014
1051V2	100	50	1000	50	500	100	.0007
1051V3	50	100	2000	100	500	500	.0014
1051V4	10	500	10,000	500	500	2000	.007
1051V5	5	1000	15,000	500	500	2000	.014
1051V6	1	5000	15,000	500	500	2000	.07

COMMON SPECIFICATIONS

SPECIFICATION	VALUE	UNITS
STIFFNESS	11.4	Lb/μ In
MOUNTED RESONANT FREQUENCY, UNLOADED	75	kHz
LINEARITY [2]	+/- 1	%F.S.
F.S. OUTPUT VOLTAGE, NOM.	5	VOLTS
MAX SHOCK, UNLOADED	10,000	G's
MAX. VIBRATION, UNLOADED	+/- 5,000	G's
COEFFICIENT OF THERMAL SENSITIVITY	.03	%/°F
TEMPERATURE RANGE	-100 to +250	°F
ENVIRONMENTAL SEAL	EPOXY	
SUPPLY CURRENT / VOLTAGE RANGE [3]	2 to 20 / +18 to +30	mA / VDC
OUTPUT IMPEDANCE	100	OHMS
MATERIAL	STAINLESS STEEL	
WEIGHT	28	GRAMS
MOUNTING PROVISION	1/4-28 x .175 DEEP TAPPED HOLE IN TOP AND BOTTOM SURFACES	
ELECTRICAL CONNECTOR, RADIAL	10-32	COAXIAL

ACCESSORIES SUPPLIED: (1) MOD 6210 STEEL IMPACT CAP, (1) MOD 6204 1/4-28 MOUNTING STUD

[1] Absolute maximum tension. Do not exceed in any case!

[2] Percent of full scale or of any lesser range, zero based best fit straight line method.

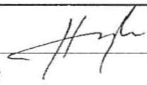
[3] Power these instruments **only** with constant current type power units. **Do not** connect to a source of voltage without current limiting. This **will destroy** the integral IC amplifier.



Dytran Instruments, Inc.
 21592 Marilla St. Chatsworth, CA 91311 Ph: 818-700-7818 Fax 818-700-7880
 www.dytran.com email: info@dytran.com



**CALIBRATION CERTIFICATE
 LIVM DYNAMIC FORCE SENSOR**

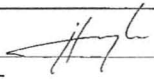
CUSTOMER: SOUND & VIB. SOL. CANADA, INC.		TEST REPORT #: 6423				
PURCHASE ORDER #: J0225		SALES ORDER #: 140912	PROCEDURE: TP1002			
MODEL: 1051V4	SERIAL #: 6423	RANGE, F.S. (Lbf): 500				
NEW UNIT	X	RE-CALIBRATION [1]	AS RECEIVED CODE			
TEMPERATURE (°C): 24		HUMIDITY (%): 28				
SENSITIVITY (mV/Lbf) [2]: 9.9	BIAS VOLTAGE (VDC): 8.5	DISCHARGE T.C. (sec): 2000				
REMARKS:						
TEST EQUIPMENT LIST - CALIBRATION STATION # 5						
DII #	MANUFACTURER	MODEL	SERIAL #	DESCRIPTION	CAL DATE	DUE DATE
956	MOREHOUSE	100,000 LB.	M7828	CALIBRATING MACHINE	09/02/09	09/02/10
977	NICOLET	3091	86DO2912	DIGITAL OSCILLOSCOPE	04/24/09	04/24/10
692	FLUKE	45	6976018	MULTIMETER	12/26/09	12/26/10
[1] AS RECEIVED / AS RETURNED CODES: 1 = IN TOLERANCE, NO ADJUSTMENTS 4 = OUT OF TOLERANCE > 5% 7 = UNIT NON-REPAIRABLE, RECOMMEND REPLACEMENT 2 = IN TOLERANCE, BUT ADJUSTED 5 = REPAIR REQUIRED 8 = UNIT SERVICEABLE WITH CURRENT CALIBRATION DATA 3 = OUT OF TOLERANCE < 5% 6 = REPAIRED AND CALIBRATED						
THIS CALIBRATION IS TRACEABLE TO THE NIST THROUGH TEST REPORT # D897402006 PER MIL-STD-45662A, ANSINC SL Z540-1-1984, ISO 10012-1 DUE 09-02-10. ESTIMATED UNCERTAINTY OF CALIBRATION: 2%. THIS CERTIFICATE SHALL NOT BE REPRODUCED EXCEPT IN FULL, WITHOUT THE WRITTEN PERMISSION FROM DYTRAN INSTRUMENTS, INC.						
CALIBRATION TECHNICIAN:  HUNG LE				TEST DATE: 03/05/10 RECALL DATE: 03/05/11		



Dytran Instruments, Inc.
 21592 Marilla St. Chatsworth, CA 91311 Ph: 818-700-7818 Fax 818-700-7880
 www.dytran.com email: info@dytran.com



**CALIBRATION CERTIFICATE
 LIVM DYNAMIC FORCE SENSOR**

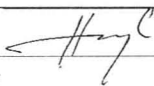
CUSTOMER: SOUND & VIB. SOL. CANADA, INC.			TEST REPORT #: 6424			
PURCHASE ORDER #: J0225		SALES ORDER #: 140912		PROCEDURE: TP1002		
MODEL: 1051V4		SERIAL #: 6424	RANGE, F.S. (Lbf): 500			
NEW UNIT	X	RE-CALIBRATION [1]	AS RECEIVED CODE	AS RETURNED CODE		
TEMPERATURE (°C): 24			HUMIDITY (%): 28			
SENSITIVITY (mV/Lbf) [2]: 10.2		BIAS VOLTAGE (VDC): 8		DISCHARGE T.C. (sec): 2000		
REMARKS:						
TEST EQUIPMENT LIST - CALIBRATION STATION # 5						
DII #	MANUFACTURER	MODEL	SERIAL #	DESCRIPTION	CAL DATE	DUE DATE
956	MOREHOUSE	100,000 LB.	M7828	CALIBRATING MACHINE	09/02/09	09/02/10
977	NICOLET	3091	86DO2912	DIGITAL OSCILLOSCOPE	04/24/09	04/24/10
692	FLUKE	45	6976018	MULTIMETER	12/26/09	12/26/10
(1) AS RECEIVED / AS RETURNED CODES: 1 = IN TOLERANCE, NO ADJUSTMENTS 4 = OUT OF TOLERANCE > 5% 7 = UNIT NON-REPAIRABLE, RECOMMEND REPLACEMENT 2 = IN TOLERANCE, BUT ADJUSTED 5 = REPAIR REQUIRED 8 = UNIT SERVICEABLE WITH CURRENT CALIBRATION DATA 3 = OUT OF TOLERANCE < 5% 6 = REPAIRED AND CALIBRATED						
THIS CALIBRATION IS TRACEABLE TO THE NIST THROUGH TEST REPORT # D6974D2008 PER MIL-STD-45862A, ANS/INC SL Z540-1-1994, ISO 10012-1 DUE 08-02-10. ESTIMATED UNCERTAINTY OF CALIBRATION: 2%. THIS CERTIFICATE SHALL NOT BE REPRODUCED EXCEPT IN FULL, WITHOUT THE WRITTEN PERMISSION FROM DYTRAN INSTRUMENTS, INC.						
CALIBRATION TECHNICIAN:  HUNG LE				TEST DATE: 03/05/10 RECALL DATE: 03/05/11		



Dytran Instruments, Inc.
 21592 Marilla St. Chatsworth, CA 91311 Ph: 818-700-7818 Fax 818-700-7880
 www.dytran.com email: info@dytran.com



**CALIBRATION CERTIFICATE
 LIVM DYNAMIC FORCE SENSOR**

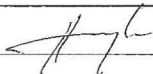

CUSTOMER: SOUND & VIB. SOL. CANADA, INC.		TEST REPORT #: 6425				
PURCHASE ORDER #: J0225		SALES ORDER #: 140912	PROCEDURE: TP1002			
MODEL: 1051V4	SERIAL #: 6425	RANGE, F.S. (LbF): 500				
NEW UNIT	X	RE-CALIBRATION [1]	AS RECEIVED CODE			
TEMPERATURE (°C): 24		HUMIDITY (%): 28				
SENSITIVITY (mV/LbF) [2]: 10	BIAS VOLTAGE (VDC): 8.6	DISCHARGE T.C. (sec): 2000				
REMARKS:						
TEST EQUIPMENT LIST - CALIBRATION STATION # 5						
DII #	MANUFACTURER	MODEL	SERIAL #	DESCRIPTION	CAL DATE	DUE DATE
956	MOREHOUSE	100,000 LB.	M7828	CALIBRATING MACHINE	09/02/09	09/02/10
977	NICOLET	3091	86DO2912	DIGITAL OSCILLOSCOPE	04/24/09	04/24/10
692	FLUKE	45	6976018	MULTIMETER	12/26/09	12/26/10
<p>[1] AS RECEIVED / AS RETURNED CODES: 1 = IN TOLERANCE, NO ADJUSTMENTS 4 = OUT OF TOLERANCE > 5% 7 = UNIT NON-REPAIRABLE, RECOMMEND REPLACEMENT 2 = IN TOLERANCE, BUT ADJUSTED 5 = REPAIR REQUIRED 8 = UNIT SERVICEABLE WITH CURRENT CALIBRATION DATA 3 = OUT OF TOLERANCE < 5% 6 = REPAIRED AND CALIBRATED</p> <p>THIS CALIBRATION IS TRACEABLE TO THE NIST THROUGH TEST REPORT # D6974D2006 PER MIL-STD-45662A. ANS/NCSL Z540-1-1994, ISO 10012-1 DUE 09-02-10. ESTIMATED UNCERTAINTY OF CALIBRATION: 2%. THIS CERTIFICATE SHALL NOT BE REPRODUCED EXCEPT IN FULL, WITHOUT THE WRITTEN PERMISSION FROM DYTRAN INSTRUMENTS, INC.</p>						
CALIBRATION TECHNICIAN:  HUNG LE				TEST DATE: 03/05/10 RECALL DATE: 03/05/11		



Dytran Instruments, Inc.
 21592 Marilla St. Chatsworth, CA 91311 Ph: 818-700-7818 Fax 818-700-7880
 www.dytran.com email: info@dytran.com



**CALIBRATION CERTIFICATE
 LIVM DYNAMIC FORCE SENSOR**

CUSTOMER: SOUND & VIB. SOL. CANADA, INC.			TEST REPORT #: 6426			
PURCHASE ORDER #: J0225		SALES ORDER #: 140912		PROCEDURE: TP1002		
MODEL: 1051V4		SERIAL #: 6426	RANGE, F.S. (Lbf): 500			
NEW UNIT	X	RE-CALIBRATION [1]	AS RECEIVED CODE	AS RETURNED CODE		
TEMPERATURE (°C): 24			HUMIDITY (%): 28			
SENSITIVITY (mV/Lbf) [2]: 9.4		BIAS VOLTAGE (VDC): 8.7		DISCHARGE T.C. (sec): 2000		
REMARKS:						
TEST EQUIPMENT LIST - CALIBRATION STATION # 5						
DII #	MANUFACTURER	MODEL	SERIAL #	DESCRIPTION	CAL DATE	DUE DATE
956	MOREHOUSE	100,000 LB.	M7828	CALIBRATING MACHINE	09/02/09	09/02/10
977	NICOLET	3091	86DO2912	DIGITAL OSCILLOSCOPE	04/24/09	04/24/10
692	FLUKE	45	6976018	MULTIMETER	12/26/09	12/26/10
[1] AS RECEIVED / AS RETURNED CODES: 1 = IN TOLERANCE, NO ADJUSTMENTS 4 = OUT OF TOLERANCE > 5% 7 = UNIT NON-REPAIRABLE, RECOMMEND REPLACEMENT 2 = IN TOLERANCE, BUT ADJUSTED 5 = REPAIR REQUIRED 8 = UNIT SERVICEABLE WITH CURRENT CALIBRATION DATA 3 = OUT OF TOLERANCE < 5% 6 = REPAIRED AND CALIBRATED						
THIS CALIBRATION IS TRACEABLE TO THE NIST THROUGH TEST REPORT # D6974D2006 PER MIL-STD-45662A, ANS/INC SL Z540-1-1994, ISO 10012-1 DUE 09-02-10. ESTIMATED UNCERTAINTY OF CALIBRATION: 2%. THIS CERTIFICATE SHALL NOT BE REPRODUCED EXCEPT IN FULL, WITHOUT THE WRITTEN PERMISSION FROM DYTRAN INSTRUMENTS, INC.						
CALIBRATION TECHNICIAN:   HUNG LE				TEST DATE: 03/05/10		
				RECALL DATE: 03/05/11		

Controls

SQDM

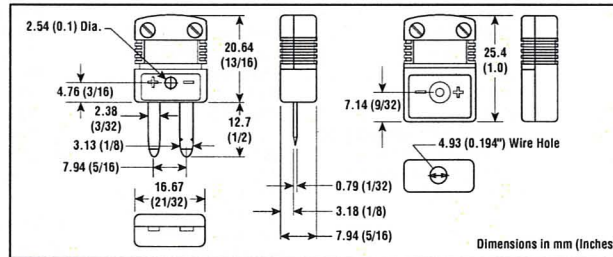
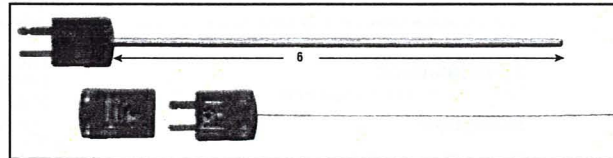
Subminiature Quick Disconnect Molded Thermocouple Probes

- 6 and 12" Lengths in Stock
- Sheath Diameters from 0.010 to 0.125"
- 304 SS or INCONEL® Sheaths
- Grounded, Ungrounded or Exposed Junction
- Color-Coded SMP Subminiature Connector Termination
- Mating Connector and Cable Clamp Included
- Custom Lengths Available
- Available with PFA Teflon® Coating



In Stock:

Model	PCN
JMQSS-062G-6/C	327185
JMQSS-062U-6/C	327193
JMQSS-125G-6/C	327206
JMQSS-125U-6/C	327214
KMQSS-062G-6/C	327222
KMQSS-062U-6/C	327230
KMQSS-125G-6/C	327249
KMQSS-125U-6/C	327257



Dimensions in mm (Inches)
U.S. and International Patents

Specifications and Ordering Information

Thermocouple Alloy	Sheath Dia. (In.)	Model	
		6" Length	12" Length
Iron-Constantan 304 SS Sheath	0.010	JMQSS-010 ^(*) -6/C	JMQSS-010 ^(*) -12/C
	0.020	JMQSS-020 ^(*) -6/C	JMQSS-020 ^(*) -12/C
	0.032	JMQSS-032 ^(*) -6/C	JMQSS-032 ^(*) -12/C
	0.040	JMQSS-040 ^(*) -6/C	JMQSS-040 ^(*) -12/C
	0.062	JMQSS-062 ^(*) -6/C	JMQSS-062 ^(*) -12/C
	0.125	JMQSS-125 ^(*) -6/C	JMQSS-125 ^(*) -12/C
Chromel-Alumel 304 SS Sheath	0.010	KMQSS-010 ^(*) -6/C	KMQSS-010 ^(*) -12/C
	0.020	KMQSS-020 ^(*) -6/C	KMQSS-020 ^(*) -12/C
	0.032	KMQSS-032 ^(*) -6/C	KMQSS-032 ^(*) -12/C
	0.040	KMQSS-040 ^(*) -6/C	KMQSS-040 ^(*) -12/C
	0.062	KMQSS-062 ^(*) -6/C	KMQSS-062 ^(*) -12/C
	0.125	KMQSS-125 ^(*) -6/C	KMQSS-125 ^(*) -12/C
Chromel-Constantan 304 SS Sheath	0.010	EMQSS-010 ^(*) -6/C	EMQSS-010 ^(*) -12/C
	0.020	EMQSS-020 ^(*) -6/C	EMQSS-020 ^(*) -12/C
	0.032	EMQSS-032 ^(*) -6/C	EMQSS-032 ^(*) -12/C
	0.040	EMQSS-040 ^(*) -6/C	EMQSS-040 ^(*) -12/C
	0.062	EMQSS-062 ^(*) -6/C	EMQSS-062 ^(*) -12/C
	0.125	EMQSS-125 ^(*) -6/C	EMQSS-125 ^(*) -12/C
Copper-Constantan 304 SS Sheath	0.020	TMQSS-020 ^(*) -6/C	TMQSS-020 ^(*) -12/C
	0.032	TMQSS-032 ^(*) -6/C	TMQSS-032 ^(*) -12/C
	0.040	TMQSS-040 ^(*) -6/C	TMQSS-040 ^(*) -12/C
	0.062	TMQSS-062 ^(*) -6/C	TMQSS-062 ^(*) -12/C
	0.125	TMQSS-125 ^(*) -6/C	TMQSS-125 ^(*) -12/C
	Nicrosil-Nisil INCONEL® 600 Sheath	0.010	NMQIN-010 ^(*) -6/C
0.020		NMQIN-020 ^(*) -6/C	NMQIN-020 ^(*) -12/C
0.032		NMQIN-032 ^(*) -6/C	NMQIN-032 ^(*) -12/C
0.040		NMQIN-040 ^(*) -6/C	NMQIN-040 ^(*) -12/C
0.062		NMQIN-062 ^(*) -6/C	NMQIN-062 ^(*) -12/C
0.125		NMQIN-125 ^(*) -6/C	NMQIN-125 ^(*) -12/C

1. Specify junction type: E (Exposed), G (Grounded) or U (Ungrounded). To order with INCONEL® sheath, change "SS" in model to "IN". Probes with 0.040" diameter and up are supplied with the connector molded to probe. Smaller sized probes are supplied with removable connector. All type N probes are supplied with removable connector.

Teflon® is a registered trademark of DuPont.

24-Bit, 102.4 kS/s, 8- and 4-Channel Dynamic Signal Acquisition

Specifications

Typical for 25 °C unless otherwise noted.

Analog Input

Channel Characteristics

Number of channels	
NI 4472 Series	8, simultaneously sampled
NI 4474 Series	4, simultaneously sampled
Input configuration	Unbalanced differential
Resolution	24 bits, nominal
Type of ADC	Delta-sigma
Oversampling, for sample rate (f_s):	
1.0 kS/s $\leq f_s \leq 51.2$ kS/s	128 f_s
51.2 kS/s $< f_s \leq 102.4$ kS/s	64 f_s
Sample rates (f_s)	1.0 to 102.4 kS/s in 190.7 μ S/s increments for $f_s > 51.2$ kS/s or 95.36 μ S/s increments for $f_s \leq 51.2$ kS/s
Frequency accuracy	± 25 ppm
Input signal range	± 10 V peak
FIFO buffer size	1,024 samples
Data transfers	DMA

Transfer Characteristics

Offset (residual DC)	± 3 mV, max
Gain (amplitude accuracy)	± 0.1 dB, max, $f_{in} = 1$ kHz

Amplifier Characteristics

Input impedance (ground referenced)	
Positive input	1 M Ω in parallel with 60 pF
Negative input (shield)	50 Ω in parallel with 0.02 μ F
Flatness (relative to 1 kHz)	± 0.1 dB, DC to 0.4535 f_s , max, DC-coupled
-3 dB bandwidth	0.4863 f_s
Input coupling	AC or DC, software-selectable
AC -3 dB cutoff frequency	
NI 4472, NI 4474	3.4 Hz
NI 4472B	0.5 Hz
Overvoltage protection	
Positive input	± 42.4 V
Positive inputs protected	CH<0..7>
Negative input (shield)	Not protected, rated at ± 2.5 V
Common-mode rejection ratio (CMRR)	
$f_{in} < 1$ kHz	>60 dB, minimum

Dynamic Characteristics

Alias-free bandwidth (passband)	DC (0 Hz) to 0.4535 f_s
Stop band	0.5465 f_s
Alias rejection	110 dB
Spurious-free dynamic range	130 dB, 1.0 kS/s $\leq f_s \leq 51.2$ kS/s

118 dB, 51.2 kS/s $< f_s \leq 102.4$ kS/s THD, $f_{in} = 1$ kHz	
0 dBFS input	< -90 dB
20 dBFS input	< -100 dB
60 dBFS input	< -60 dB
IMD	< -100 dB (CCIF 14 kHz + 15 kHz)
Crosstalk ¹ (channel separation), $f_{in} = 0$ to 51.2 kHz	
Between channels 0 and 1, 2 and 3, 4 and 5, or 6 and 7	
Shorted input	< -90 dB
1 k Ω load	< -80 dB
Other channel combinations	
Shorted input	< -100 dB
1 k Ω load	< -90 dB
Phase linearity	$\leq \pm 0.5$ deg
Interchannel phase mismatch	$< f_{in}$ (in kHz) $\times 0.018$ deg + 0.082 deg
Interchannel gain mismatch	± 0.1 dB
Filter delay through ADC	38.8 sample periods

Onboard Calibration Reference

DC level	5.000 V ± 2.5 mV
Temperature coefficient	± 5 ppm/ $^{\circ}$ C maximum
Long-term stability	± 20 ppm/ $\sqrt{1,000}$ h

Signal Conditioning

Constant current source (software-controlled)	
Current	4 mA, $\pm 5\%$
Compliance	24 V
Output impedance	>250 k Ω at 1 kHz
Current noise	<500 pA/ $\sqrt{\text{Hz}}$

Triggers

Analog Trigger

Source	CH<0..7>
Level	-10 to +10 V, full scale, programmable
Slope	Positive or negative (software-selectable)
Resolution	24 bits, nominal
Hysteresis	Programmable

Digital Trigger

Compatibility	5 V TTL/CMOS
Response	Rising or falling edge
Pulse width	10 ns, minimum
Bus Interface	
Type	Master, slave

Power Requirements

+3.3 VDC	
PXI	400 mA, maximum
+5 VDC	
PCI	2.6 A, maximum
PXI	2.2 A, maximum
+12 VDC	120 mA, maximum
-12 VDC	120 mA, maximum

General

Product Name	PCI-6221 (37-Pin)
Product Family	Multifunction Data Acquisition
Form Factor	PCI
Operating System/Target	Windows , Real-Time , Linux , Mac OS
LabVIEW RT Support	Yes
DAQ Product Family	M Series
Measurement Type	Digital , Frequency , Quadrature encoder , Voltage
RoHS Compliant	Yes
Analog Input	
Channels	16 , 8
Single-Ended Channels	16
Differential Channels	8
Resolution	16 bits
Sample Rate	250 kS/s
Max Voltage	10 V
Maximum Voltage Range	-10 V , 10 V
Maximum Voltage Range Accuracy	3100 μ V
Maximum Voltage Range Sensitivity	97.6 μ V
Minimum Voltage Range	-200 mV , 200 mV
Minimum Voltage Range Accuracy	112 μ V
Minimum Voltage Range Sensitivity	5.2 μ V
Number of Ranges	4
Simultaneous Sampling	No
On-Board Memory	4095 samples
Analog Output	
Channels	2
Resolution	16 bits
Max Voltage	10 V
Maximum Voltage Range	-10 V , 10 V
Maximum Voltage Range Accuracy	3230 μ V

4 Channel Voltage Mode Piezoelectric Sensor Power Supply & Signal Conditioner , Type 5134A...



Technical Data

Type	Unit	5134A
Sensor Supply Factory Set	mA	4
Optional	mA	2 ... 18
Gain Setpoints (±0.5 %)		1, 2, 5, 10, 20, 50
(±1 %)		100
Frequency Range (bandwidth -3 dB)		
Gain = 1 (30 kHz filter)	Hz	0.036 ... 30k
Gain = 100 (10 kHz filter)	Hz	0.036 ... 8k
Lowpass Filters		
2-pole Butterworth 2nd order	dB/oct.	-12
Cut-off frequencies (-3 dB)	Hz	100, 1k, 10k, 30k
Frequency accuracy	%	±7
Output:		
Voltage	V	±10
Current	mA	± 5
Impedance	Ω	100
Temperature Range Operating	°F	32 ... 120
Temperature Range Storage	°F	-5 ... 185
Voltage between power & ground	Vrms	<50
Dimensions: with case	in	3.7 x 5.6 x 7.7
Dimensions: without case	in	2.8 x 5 x 7.2
Power 5134A...		
Line voltage	VAC	115 [A0 & A1] 230 [A0 (E)] 230 [A1 (E)]
Line Frequency	Hz	48 ... 62
Consumption	VA	14
Weight (with housing)	kg	1.75

1 g = 9.80665 m/s², 1 Inch = 25.4 mm, 1 gram = 0.03527 oz, 1 lbf-in = 0.113 Nm

Ordering Key

Case		5134A	<input type="checkbox"/>	<input type="checkbox"/>
without case	0			
with case	1			
Power				
110 VAC	-			
220 VAC	E			

5134A_000-332a-01.06

Model Number 352A24	ACCELEROMETER, ICP®		Revision C ECN # 27171
Performance	ENGLISH	SI	Optional Versions (Optional versions have identical specifications and accessories as listed for standard model except where noted below. More than one option maybe used.)
Sensitivity (±10 %)	100 mV/g	10.2 mV/(m/s ²)	RH - RoHS Compliant
Measurement Range	±50 g pk	±490 m/s ² pk	Supplied Accessory: Model RH030A10 Coax Cable, 10 ft (3 m), 3-56 plug to 10-32 plug, RoHS compliant; replaces Model 030A10
Frequency Range (±5 %)	1.0 to 8000 Hz	1.0 to 8000 Hz	Notes
Frequency Range (±10 %)	0.8 to 10000 Hz	0.8 to 10000 Hz	[1] Typical.
Frequency Range (±3 dB)	0.4 to 12000 Hz	0.4 to 12000 Hz	[2] Zero-based, least-squares, straight line method.
Resonant Frequency	□30 kHz	□30 kHz	[3] See PCB Declaration of Conformance PS023 for details.
Broadband Resolution (1 to 10000 Hz)	0.0002 g rms	0.002 m/s ² rms	
Non-Linearity	□1 %	□1 %	
Transverse Sensitivity	□5 %	□5 %	
Environmental			Supplied Accessories
Overload Limit (Shock)	±5000 g pk	±49050 m/s ² pk	030A10 Coax Cable, 10 ft (3 m), 3-56 plug to 10-32 plug. (1)
Temperature Range (Operating)	-65 to +250 °F	-54 to +121 °C	039A28 Removal Tool (1)
Temperature Response	See Graph	See Graph	080A109 Petro Wax (1)
Electrical			ACS-1 NIST traceable frequency response (10 Hz to upper 5% point). (1)
Excitation Voltage	18 to 30 VDC	18 to 30 VDC	
Constant Current Excitation	2 to 20 mA	2 to 20 mA	
Output Impedance	□300 ohm	□300 ohm	
Output Bias Voltage	8 to 12 VDC	8 to 12 VDC	
Discharge Time Constant	0.4 to 1.5 sec	0.4 to 1.5 sec	
Settling Time (within 10% of bias)	<8 sec	<8 sec	
Spectral Noise (1 Hz)	80 µg/√Hz	785 (µm/sec ²)/√Hz	
Spectral Noise (10 Hz)	15 µg/√Hz	147 (µm/sec ²)/√Hz	[1]
Spectral Noise (100 Hz)	4 µg/√Hz	39 (µm/sec ²)/√Hz	[1]
Spectral Noise (1 kHz)	1 µg/√Hz	9.8 (µm/sec ²)/√Hz	[1]
Electrical Isolation (Base)	□10 ⁸ ohm	□10 ⁸ ohm	
Physical			
Sensing Element	Ceramic	Ceramic	
Sensing Geometry	Shear	Shear	
Housing Material	Anodized Aluminum	Anodized Aluminum	
Sealing	Epoxy	Epoxy	
Size (Height x Length x Width)	0.19 in x 0.48 in x 0.28 in	4.8 mm x 12.2 mm x 7.1 mm	
Weight	0.03 oz	0.8 gm	[1]
Electrical Connector	3-56 Coaxial Jack	3-56 Coaxial Jack	
Electrical Connection Position	Side	Side	
Mounting	Adhesive	Adhesive	

Typical Sensitivity Deviation vs Temperature

Entered: EB	Engineer: BAM	Spec Number:
Date: 08/23/2007	Date: 08/23/2007	12320

PCB PIEZOTRONICS
VIBRATION DIVISION

3425 Walden Avenue
Depew, NY 14043
UNITED STATES
Phone: 888-684-0013
Fax: 716-685-3886
E-mail: vibration@pcb.com
Web site: www.pcb.com

All specifications are at room temperature unless otherwise specified.
In the interest of constant product improvement, we reserve the right to change specifications without notice.

K-Shear® Accelerometer – Low Profile, Integral Cable Triaxial Accelerometer, Type 8794A...



Technical Data

Specification	Unit	Type 8794A500
Acceleration range	g	±500
Acceleration limit	gpk	±1000
Transverse acceleration limit	gpk	±1000
Threshold (noise 200 µVrms) nom.	gms	0.002
Sensitivity, ±5 %	mV/g	10
Resonant frequency mounted, nom.	kHz	>80
Frequency response, ±5 %	Hz	2.5 ... 10000
Amplitude non-linearity	%FSO	±1
Time constant, nom.	s	0.5
Transverse sensitivity, nom. (max. 3)	%	1.5
Long term stability	%	±1

Environmental

Base strain sensitivity @ 250 µε	g/µε	0.015
Shock limit (1 ms pulse)	gpk	5000
Temperature coeff. of sensitivity	%/°F	-0.02
Operating temperature range	°F	-100 ... 250
Type 8794A500M5	°F	-65 ... 330
Storage temperature range	°F	-100 ... 300

Output

Bias, nom.	VDC	11
Impedance	Ω	<100
Voltage full scale	V	±5
Current	mA	2

Source

Voltage	VDC	20 ... 30
Constant current	mA	2 ... 18
Impedance, min.	kΩ	100

Construction

Sensing element	Type	quartz-shear
Case/base	material	stainless steel
Degree of protection case/connector	Type	welded
Connector	Type	4-pin pos.
Ground isolated		yes
Mass	grams	7.6
Mounting (ø0.13 hole)	Type	cap screw
Mounting torque	lbf-in	4.4

1 g = 9.80665 m/s², 1 Inch = 25.4 mm, 1 gram = 0.03527 oz, 1 lbf-in = 0.113 Nm

Included Accessories

- 4 mounting screws M2.5x10 mm long Type 431-0475-001
- 4 mounting screws 4-40x3/8" long Type 431-0475-002

Optional Accessories

- Extension cable, 4-pin pos. to 4-pin neg. Type 1578A...

Ordering Key

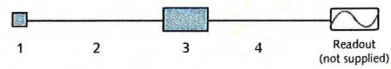
Range	Type 8794A
±500 g	500

Variants

Standard	-
High temperature	M5

Measuring Chain

- 1 Low impedance sensor Type 87...
- 2 Breakout cable, 4-pin neg. to 3x BNC pos. Type 1756B...
- 3 Power supply/signal conditioner Type 51...
- 4 Output cable, BNC pos. to BNC pos. Type 1511



8794A_000-263a-05.08

Appendix C – Discharge Time Constant Behaviour

In order to properly interpret the signals generated by piezoelectric sensors, the signal discharge behaviour needs to be fully understood such that the decay signal can be distinguished from the true dynamic response. The experimental results of the piezoelectric sensors were provided in the text with the decay signal removed, and only the meaningful portion of the signals was kept. The procedure of determining the starting point of decay in the signal will be provided in this section, following an explanation of the pertinent characteristics of piezoelectric low frequency response.

C.1 Quasi-Static Behaviour

The response of a piezoelectric sensor to steady-state events is defined as the quasi-static behaviour. Piezoelectric sensors are effectively AC coupled devices, and do not possess true DC response. Since they do not possess true static response, the quasi-static behaviour is used to approximate static behaviour. Quasi-static behaviour is a measure of the length of time meaningful information is retained after the initial application of a steady state input. Static response in piezoelectric sensors is most closely approximated when the duration of the event represents a very small percentage of the sensor Discharge Time Constant (DTC), which is explained in the following section.

C.2 Discharge Time Constant

The decay of the dynamic signal following a steady-state input is determined by the discharge time constant. The DTC is the time required for a sensor output voltage to discharge 63% of its initial value immediately following the application of a long-term,

steady state input change. A step function input is defined as the type of input obtained by using static means. The step function voltage input is generated by a piezoelectric sensor element in response to a sudden change in the input parameter, such as pressure or force. When the step function is applied, the voltage almost instantly registers the input signal, and then immediately begins to discharge, or decay, exponentially with time. The high-frequency response and rise time properties of piezoelectric sensors are defined by the inherent mechanical design characteristics. For instance, the rise time for the pressure transducers used in these experiments is 2 μ s. The ensuing decay function is provided by Equation (C1):

$$v = V_0 e^{-t/R_G C} \quad (C1)$$

where v is the instantaneous gate voltage, V_0 is the initial voltage, R_G is the gate resistance, and C is the total shunt capacitance. The product $R_G \times C$ represents the sensor DTC, τ , in seconds. Figure C-1 illustrates a decaying signal having retained 37% of its initial value at the time corresponding to one time constant following a step input. In five time constants, the output has essentially decayed to within 1% of zero.

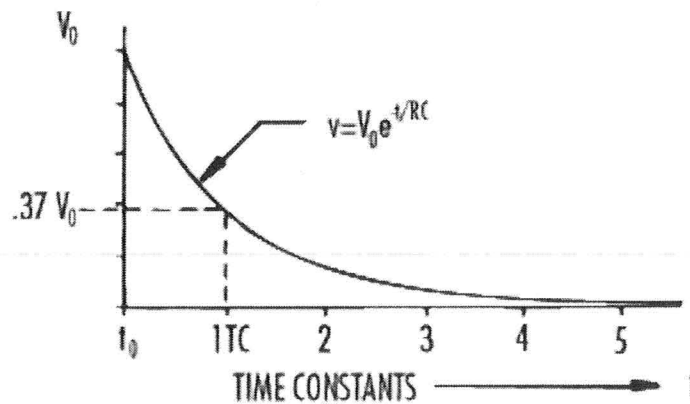


Figure C-1. Discharge Time Constant Output vs. Time

The curve displayed in Figure C-1 is relatively linear until about 10% of the first time constant has passed. Therefore, in terms of measurement deterioration with event duration, it can be concluded that in order to achieve at least 1% accuracy for a quasi-static measurement, the reading must be taken within a time window of 1% of the sensor time constant, and so forth up to about 10% of the time constant.

C.3 Low Frequency Response

The DTC determines the low frequency response behaviour of the piezoelectric sensors. The low frequency response refers to the ability of the sensor to accurately measure a very low frequency input. A Bode plot of the low frequency response of typical piezoelectric sensors is presented in Figure C-2. The horizontal axis is plotted in multiples of the corner frequency. Figure C-2 shows that at the corner frequency, the output from the sensor decreases by 3 dB, or about 30%, from the reference sensitivity. The corner frequency, f_c , also known as the lower cut-off (-3 dB) frequency, is found using Equation (C2):

$$f_c = \frac{0.16}{\tau} \quad (C2)$$

C.4 Description of Discharge Behaviour in the Context of Acquired Results

All AC coupled power units are high-pass filters that can impair the low frequency response and quasi-static behaviour of piezoelectric sensors. For example, in the last commissioning test of the current project, the signal conditioning on the data acquisition card, rather than the dynamic pressure transducer, was the limiting factor for the low frequency system capability. As a result, the dynamic pressures were limited to relatively high frequency response, and the majority of the transient was not captured.

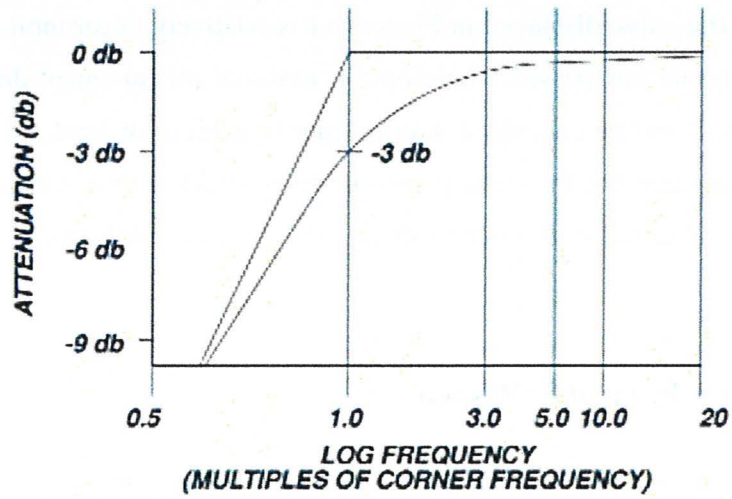


Figure C-2. Low Frequency Response Bode Plot

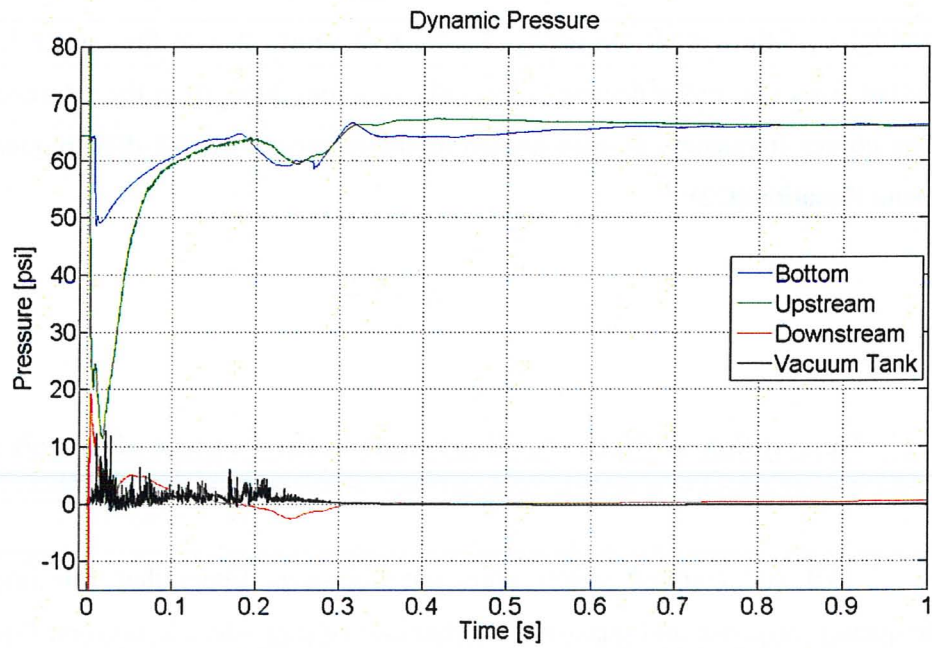


Figure C-3. Dynamic Pressure vs. Time (6th Test; 1 s Timescale)

The dynamic pressures in Figure C-3, apart from the vacuum tank pressure, began to decay as early as 20 milliseconds after disc rupture. The dynamic pressure frequency at this point was below the cut-off frequency of the data acquisition card. Between 200 and 300 milliseconds after rupture, the pressures show some changes in dynamic response. The behaviour during this time period is produced by rates of pressure change that were fast enough to be captured by the data acquisition, and the frequency of the response once again became too slow to be captured after about 350 milliseconds. However, because the signals had already previously begun to decay, the magnitudes of pressures during the signal discharge are meaningless, and the only meaningful portion that can be retained in these signals is the dynamic pressure response immediately following the break. In order to make full use of the low frequency capability of the dynamic pressure transducers, the IEPE signal conditioning was disabled and the data acquisition card was DC coupled for the experimental phase of the project, and a separate coupler was used to provide power output to the sensors. The DTC behaviour of the dynamic pressure transducers can be described in the context of a sample experimental result.

Since the piezoelectric load cells were dynamically calibrated with a step input function, the quasi-static behaviour of the load cells is nicely demonstrated by the calibration curves, such as the one shown in Figure E-2. The dynamic load responds practically instantaneously to the load change, and the signal exponential decay immediately follows. In this case, the DTC of the power coupler, which is 4.4 s, limits the low frequency response of the dynamic load cells. Accordingly, the decay signal is about 37% of the registered load 4.4 s after it is applied, and 22 s later, the signal is practically settled at zero. Since the calibration runs represented step input functions, the signal discharged immediately following the response to the sudden input. In the real experiments however, the transient loading changes dynamically, and it is important to be able to distinguish the true signal changes representing dynamic loading, from the exponential signal decay. The methodology developed for determining the point at which the signals begin to discharge will be described based on a sample experimental dynamic pressure signal.

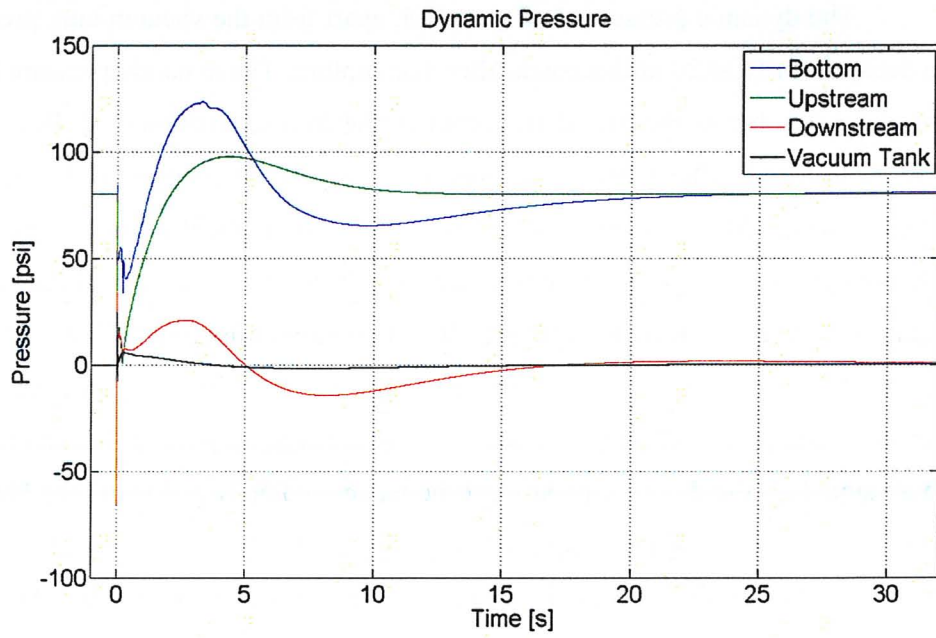


Figure C-4. Long-Term Dynamic Pressure Signal Discharge

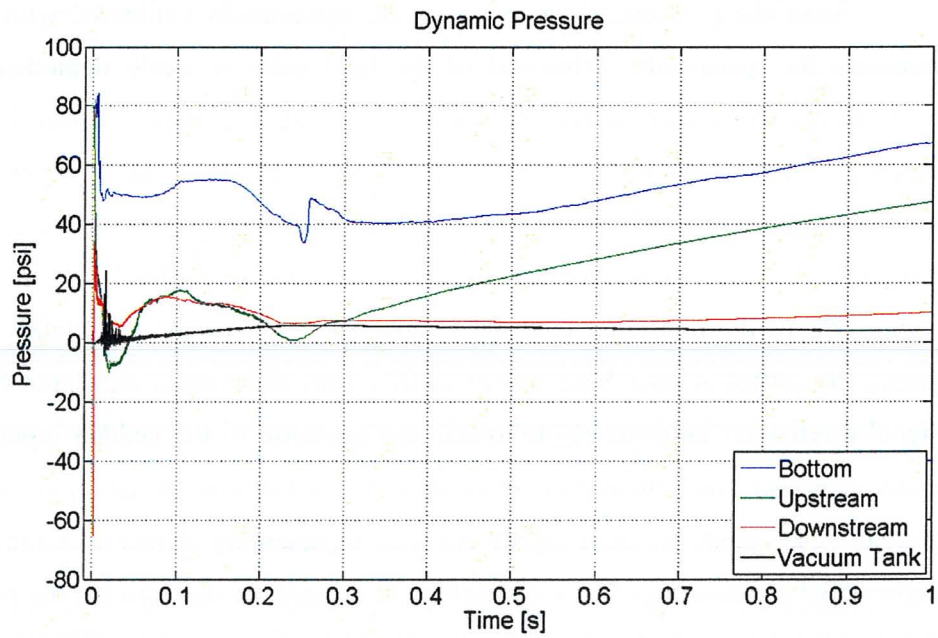


Figure C-5. Short-Term Dynamic Pressure Signal Discharge

The long-term discharge signal is shown in Figure C-4. The signals begin to discharge exponentially shortly after the initiation of the blow-down transient, and it seems that there is some pressure activity inside the blow-down rig around 4 seconds after the break, lengthening the duration of the decay. The DTC of the dynamic pressure transducers is about 2 seconds, and the vacuum tank decay signal is practically settled about 10 seconds, or 5 time constants, following the initiation of the exponential decay. The other signals settle closer to 15 seconds, due to the continuing pressure activity inside the rig. Because the depressurisations were transient in nature, and the pressures continued to change after the blow-down was complete, the decay signals are not expected to exactly match the exponential curve, and some lengthening of the discharge duration is expected. However, as previously mentioned, the magnitudes of the pressures become meaningless as soon as the signals first begin to decay, and the short-term behaviour of the pressure transducers is presented in Figure C-5.

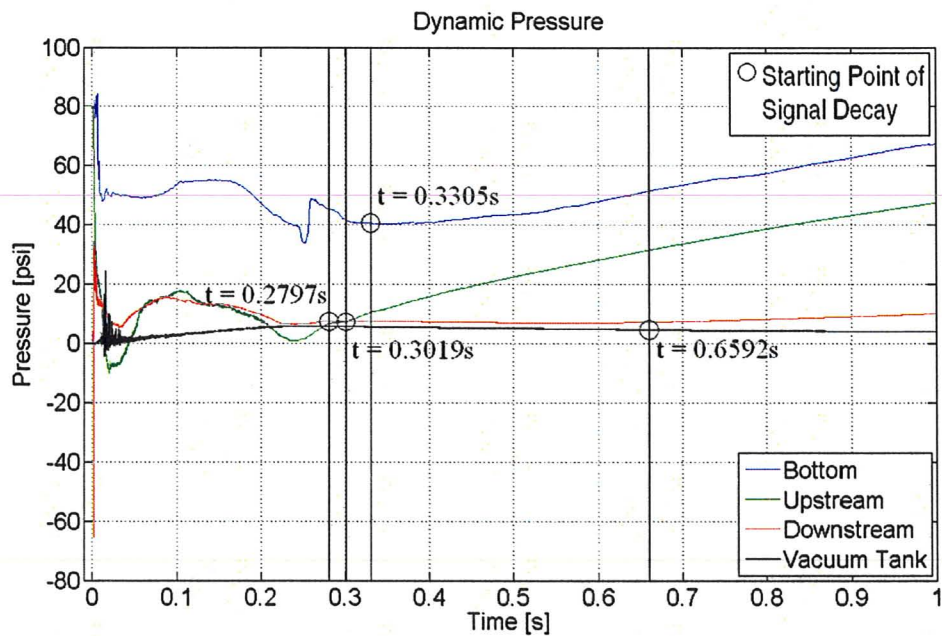


Figure C-6. Determination of Starting Point of Signal Decay

In order to establish the time instant at which the signal begins to discharge, the intersection of the tangent line to the point of inflection at the beginning of the exponential decay curve is determined in MATLAB. The corresponding times for the present sample dynamic pressures are illustrated in Figure C-6. Once the starting point of signal decay is determined, the portion of the signal preceding the discharge point is retained for analysis, and the remainder of the signal is discarded. Due to the rapid transient nature of the blow-downs, and the steady-state nature of the stage that succeeds the flashing, this procedure proved very repeatable across all the experiments, and distinguishing between exponential decay signals and actual dynamic signals was fairly straightforward. The same holds true for the dynamic load signals as well.

Appendix D – Uncertainty Analysis

An analysis of the uncertainties involved in the calculation of the initial thermodynamic conditions and the initial pressure wave speeds based on the uncertainties in the measurements is presented in this section. The overall uncertainty, Δ , of a specific measurement is determined from Equation (D1):

$$\Delta = \sqrt{\sum_{i=1}^n (\delta_i)^2} \quad (\text{D1})$$

where δ_i refers to the separate uncertainties identified for a particular measurement. The uncertainties incorporated in the analysis include the uncertainties inherent to the measurement devices, usually specified by the manufacturer, and additional uncertainties introduced by necessary measures such as calibration procedures and the setting up of the data collection system.

D.1 Pressure Measurements Uncertainty

The uncertainty involved in the pressure measurements obtained using the static pressure sensors includes the calibration uncertainty of ± 0.001 psi, and the non-linearity, hysteresis, and repeatability effects within the sensor itself, specified as $\pm 0.1\%$ of the measurement span range, which is ± 0.3 psi. From Equation (D1), the uncertainty in the pressure readings is found to be:

$$\delta P = \sqrt{(0.001)^2 + (0.3)^2} = \pm 0.3 \text{ psi} = \pm 2 \text{ kPa} \quad (\text{D2})$$

Thus, the error associated with the calibrated pressure signals was practically entirely comprised of the specified uncertainty of the pressure sensor.

D.2 Temperature Measurements Uncertainty

Aside from the cold-junction compensation uncertainty of ± 0.3 °C, there are several factors that can directly contribute towards errors in the thermocouple measurements. These include isothermal error between the cold-junction thermistor and the actual cold junction formed by the thermocouple at the screw terminals of the connector block, variations in ambient temperature, heat dissipation within the connector block module, and conduction along the thermocouple wires. Since the thermocouple signals are in the millivolt range, they are also susceptible to external sources of noise. Power line noise effects were visible when an electronic ballast-powered light source was switched on, and the temperature signal was analysed using a low-pass filter. The thermocouple itself introduces additional errors associated with temperature gradients and metal impurities across the wires, and the total uncertainty is specified as ± 0.85 °C. Therefore, the uncertainty in the temperature readings is found to be:

$$\delta T = \sqrt{(0.3)^2 + (0.85)^2} = \pm 0.9 \text{ } ^\circ\text{C} = \pm 0.9 \text{ K} \quad (\text{D3})$$

D.3 Mass Measurements Uncertainty

The mass of R-134a discharged into the blow-down rig was measured using an electronic charging scale (Yellow Jacket model 68802) with a specified accuracy of $\pm 0.1\%$ of the reading, which yields a maximum uncertainty of ± 0.0181 kg. In addition to the scale uncertainty, the readings were found to fluctuate throughout the charging stages due to the changing volumes, temperatures, and consequently, states of the R-134a inside the pressurised bottle. The maximum uncertainty observed for this behaviour during the experiments is ± 0.03 kg and the total uncertainty in mass readings is found to be:

$$\delta m = \sqrt{(0.0181)^2 + (0.03)^2} = \pm 0.035 \text{ kg} \quad (\text{D4})$$

D.4 Uncertainty of Calculated Quantities

Given the dependence on the pressure, temperature, and mass measurements, the uncertainties in the calculated volumes and sonic velocities of the liquid and vapour refrigerant quantities inside the blow-down rig can be determined from (D5):

$$\delta X = X \sqrt{\left(\frac{\delta P}{P}\right)^2 + \left(\frac{\delta T}{T}\right)^2 + \left(\frac{\delta m}{m}\right)^2} \quad (\text{D5})$$

where X represents the quantity being calculated. The maximum determined uncertainty is $\pm 0.8\%$ for the liquid phase measurements, and $\pm 17.5\%$ for the vapour phase measurements.

The maximum uncertainty found for the liquid volume calculations is ± 0.07 L, and the maximum liquid sonic velocity uncertainty is ± 4.3 m/s. For the vapour phase, the maximum volume uncertainty is ± 1.89 L, and the maximum sonic velocity uncertainty is ± 25.6 m/s. The vapour volume uncertainty is comparable in magnitude to the total volume of the accumulator, which justifies neglecting the accumulator volume in the analysis. Based on the sonic velocity uncertainty, the uncertainty in the calculated time required for the first pressure wave to travel between the rupture disc and the downstream pressure transducer is ± 0.16 ms, which represents the uncertainty in the calculation of the rupture disc opening instant.

Appendix E – Instrument Calibration

The static pressure sensors were calibrated with a pneumatic pressure-vacuum hand pump (Ralston Instruments model DPPV-0000) using a precision pressure calibrator as the pressure reference. The test pump generates pressures from vacuum to 100 psi, and allows for precise pressure adjustment within ± 0.001 psi. The thermocouples were calibrated against the embedded connector block thermistor, which has a specified accuracy of ± 0.3 °C over a 0-55 °C range. Given that the thermocouples are intended to measure rapid transient temperatures in two-phase flow, this calibration was regarded to be sufficient, and the thermocouple signals were deemed satisfactory without the need for further error reduction.

The exact sensitivities of the dynamic pressure transducers are determined using dynamic hydraulic calibration methods prior to their delivery. It is very difficult to calibrate these sensors because of their relatively short discharge time constants (1.8 s), and they were sent to the factory for recalibration midway through the project. The dynamic load cells were also calibrated prior to their delivery, but it was necessary to calibrate the overall loading on the test section, such that the load signals from the load cells could be correlated with the actual loading on the tubes. Since the sensors are designed to measure rapidly changing forces, it was most sensible to calibrate them dynamically. The calibration tests were performed by placing a known load statically on the tube bundle, allowing the signal to discharge completely, and then rapidly removing the load and capturing the resultant step function. The signal polarity is the same as that expected when the tube bundle is forced upwards by the flashing liquid. The load cells were calibrated using 5, 10, and 20-lb weights. Load cells labelled 1 and 4 on the plots are on one side of the bundle, and load cells 2 and 3 are on the opposite side. For illustration purposes, a sample calibration test trace is provided in Figure E-1, and the total summed signal of the four individual load cells is provided in Figure E-2.

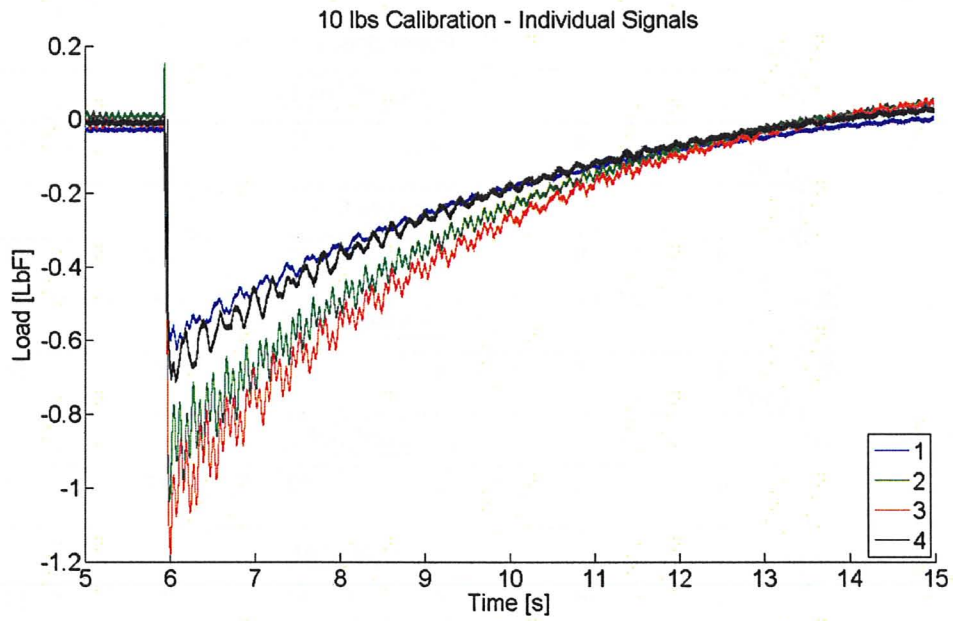


Figure E-1. Sample Calibration Test (Individual Signals)

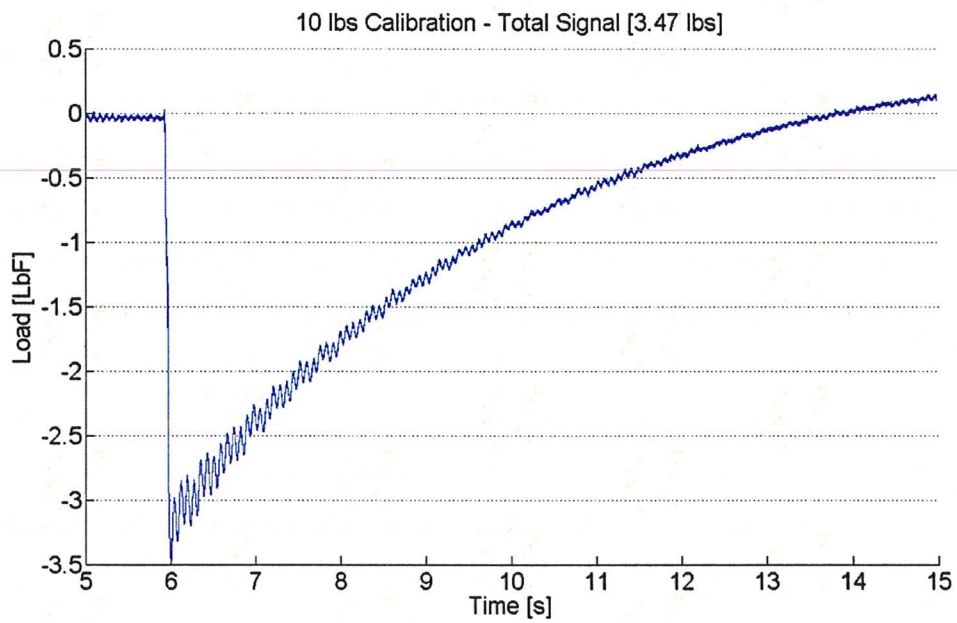


Figure E-2. Sample Calibration Test (Total Signal)

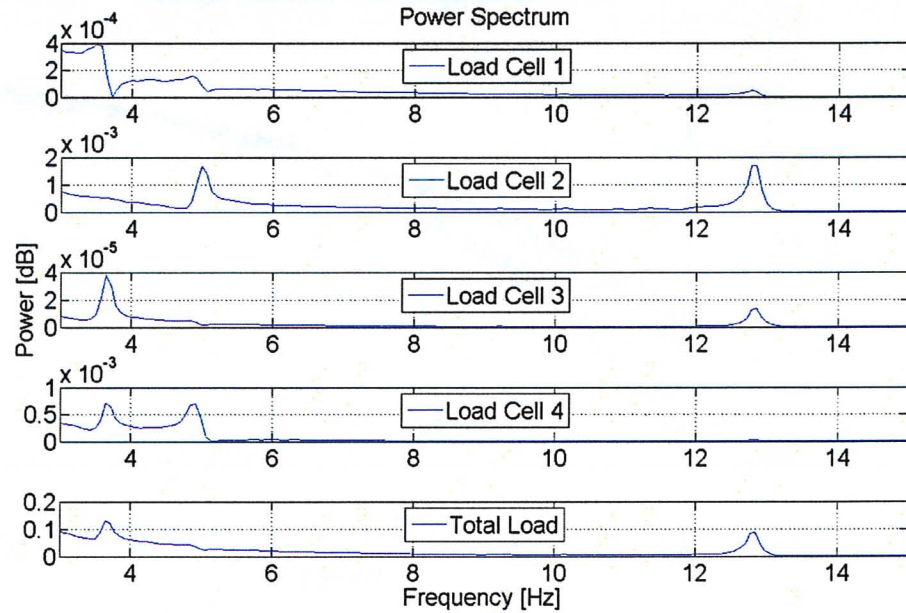


Figure E-3. Frequency Content of Sample Calibration Run

The frequency content of the calibration run shown in Figure E-1 and Figure E-2 is presented in Figure E-3. The individual load cell signals from load cell 2 and 4, which are placed at opposite corners of the test section, display out of phase periodic oscillations at a frequency of 5 Hz, which represents the diagonal rocking mode of vibration for the tube bundle. The summed signal includes inertial oscillations at a frequencies of 3.5 Hz and 13 Hz that represent the planar modes of vibration of the tube bundle parallel to the tubes and in the same direction as the load measurement axis. The individual signals provide some insights into the planar distribution of the loading throughout the tube bundle, whereas the total signal gives the absolute value of the measured loading for the step function. In the context of the experimental loads measured, the individual load cell signals are not useful, and the total loading on all of the four load cells is required to determine the dynamic loading exerted on the tube bundle.

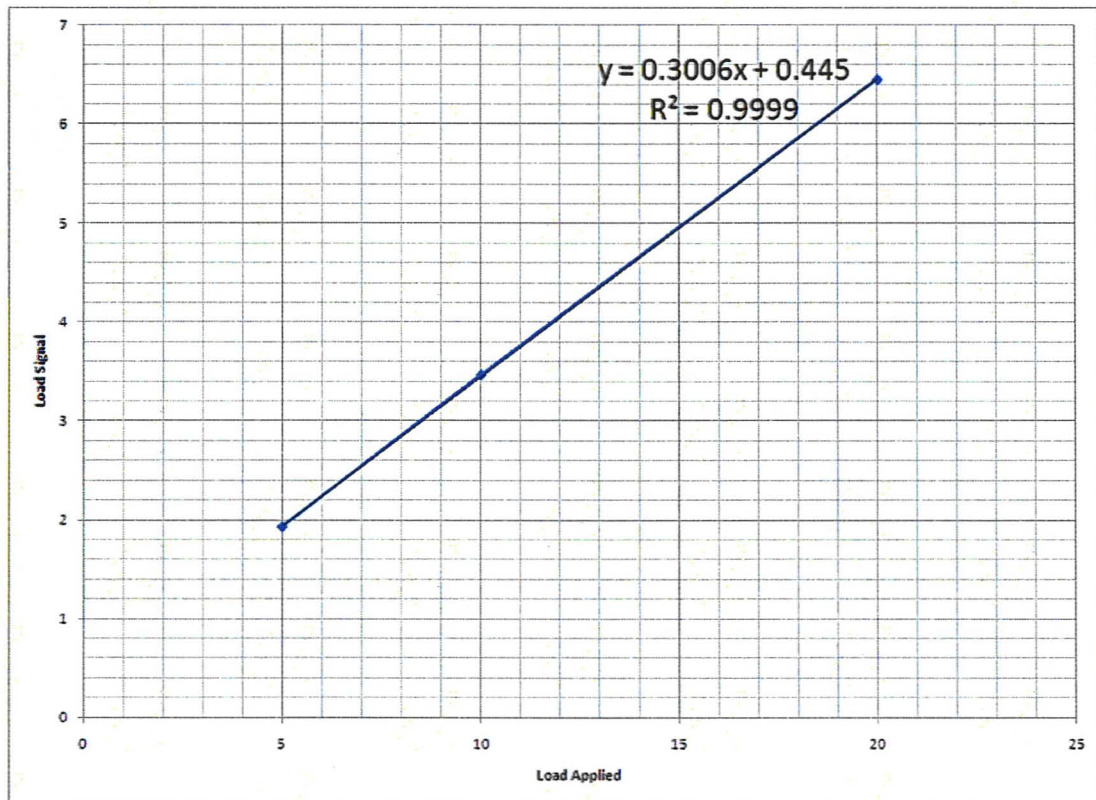


Figure E-4. Test Section Calibration Correlation

In order to calibrate the load signals obtained against the measured loads, the obtained results were plotted on a curve, which is provided in Figure E-4. The three points lined up very well as shown, and the correlation included in Figure E-4 can be used to convert the measured loads into actual loading exerted on the tube bundle. The calibration results of the load cells were found to be highly repeatable, and the linearity of the calibration curve demonstrated the high degree of accuracy and sensitivity with which tube loading was captured, generating confidence in the suitability of the test section design for obtaining load measurements, at least for the calibration test configuration. The calibrated load signals for the three different weights are presented in Figure E-5. The dynamic loading results included in the text were computed such that the true calibrated loads are displayed on the graph, in an analogous manner to the loads displayed in Figure E-5.

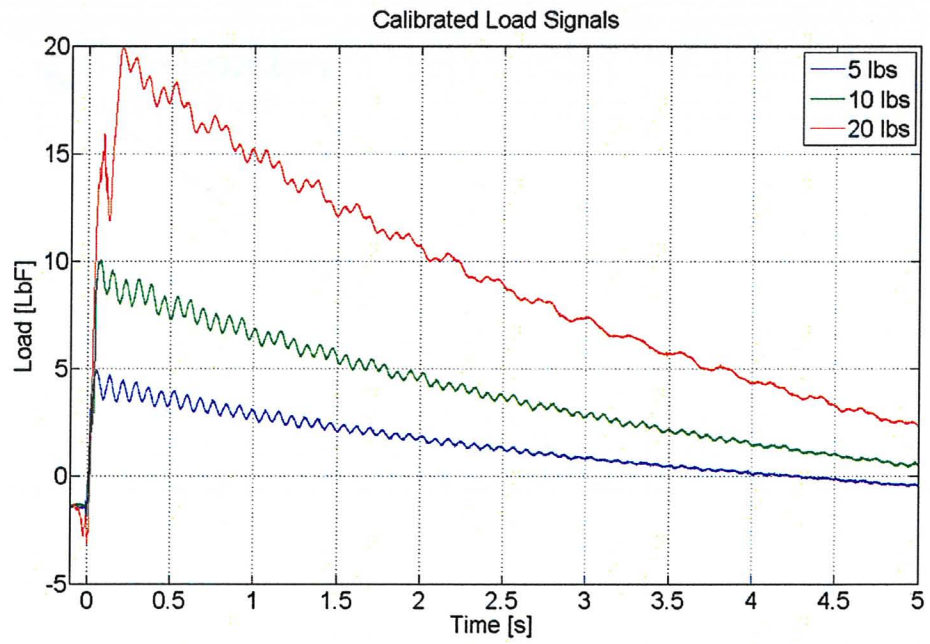


Figure E-5. Calibrated Load Signals

Appendix F – Fast Fourier Transforms

The frequency content of oscillating dynamic signals was studied in order to investigate vibration characteristics of the dynamic behaviour. The main inertial mode of vibration for the dynamic load cell and accelerometer signals in the fourth experiment was found to occur at a frequency of 35 Hz. Although this frequency varies between experiments since it depends on the loading of the scissors jack, the general frequency behaviour of the load cells is expected to remain fairly consistent. The frequency spectra of the relevant signals were plotted such that the consistency in the results could be examined. Figure F-1 shows the frequency domain representation of the dynamic load signal obtained in the third experiment. The frequency peaks shown at 35, 62, 121, and 154 Hz are all consistent with the frequency content of the load signal for the fourth experiment.

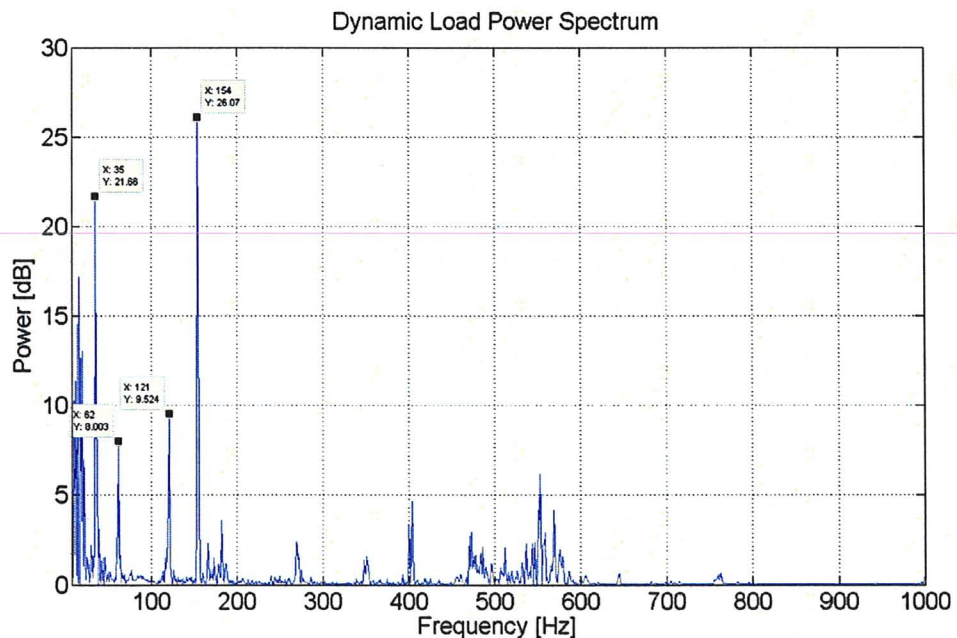


Figure F-1. Dynamic Load Power Spectrum (3rd Experiment)

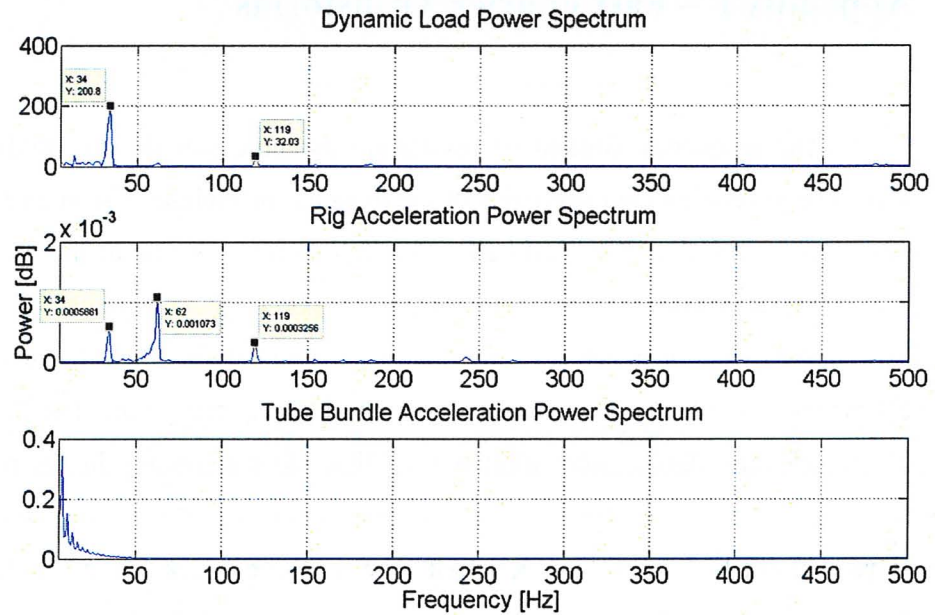


Figure F-2. Dynamic Load and Acceleration Power Spectra (3rd Experiment – 2nd Attempt)

The frequency content of the second attempt of the third experiment, shown in Figure F-2, displays a dominant inertial frequency peak at 34 Hz for the load cells and experimental rig vibration, which is consistent with the previous results. Some frequency peaks are also present at 62 and 119 Hz. The tube bundle vibration in this case did not register any periodic frequencies since the accelerometer malfunctioned shortly after the blow-down was initiated.

The dynamic pressure signals also displayed fluctuating signal response, some of which appeared to be periodic in nature. The analysis of the acquired signals in the frequency domain allows for investigation of the vibration characteristics of the response, in order to determine whether the oscillations were produced by acceleration related effects, or some other unrelated mechanism. The frequency content of the bottom dynamic pressures is provided in Figure F-3.

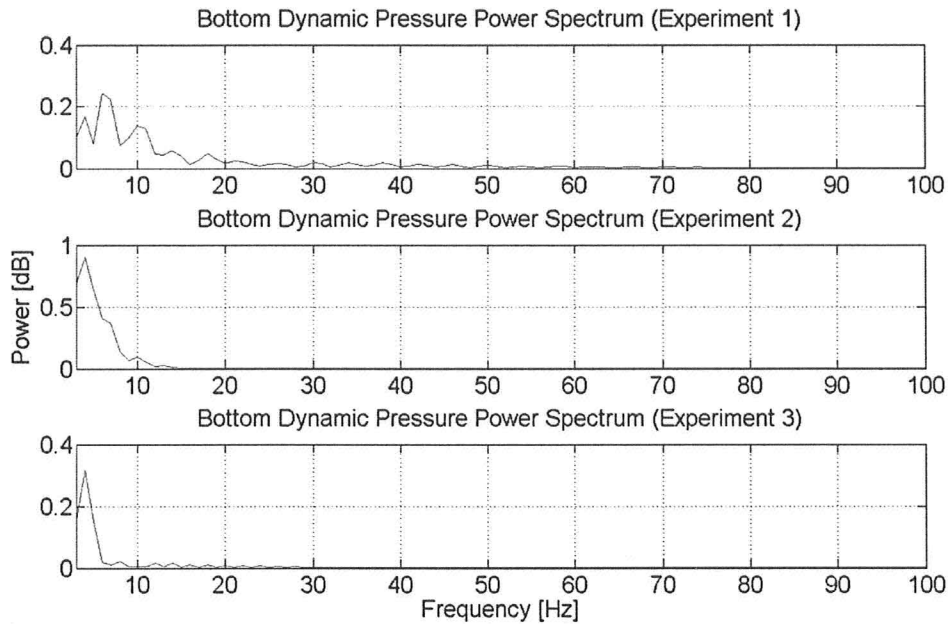


Figure F-3. Bottom Dynamic Pressure Power Spectra

Due to the apparent periodic nature of the oscillations seen in the first few milliseconds after rupture for the bottom pressure transducers, it was suspected that the acquired signal oscillations represented the inertial vibration effects, and the actual pressure should follow the trend of the acquired signal. The power spectra in Figure F-3 do not appear to indicate and significant periodic behaviour in the frequency range of the oscillations seen. As such, the cause of the random fluctuations seen is not fully understood, but it may be that the oscillations did not appear in the frequency analysis because the short duration of oscillating response was not discretised with sufficient resolution. The signal acquired for the upstream dynamic pressure displayed unique high frequency fluctuations about 2-5 milliseconds after rupture. The times and amplitudes of the fluctuations indicate that there is a huge likelihood of the signal behaviour being generated by vibration effects. There is no acceleration component visible in the frequency content of this signal, shown in Figure F-4, and it may be that the interference of the integrated acceleration compensation creates a pseudo-randomly fluctuating signal.

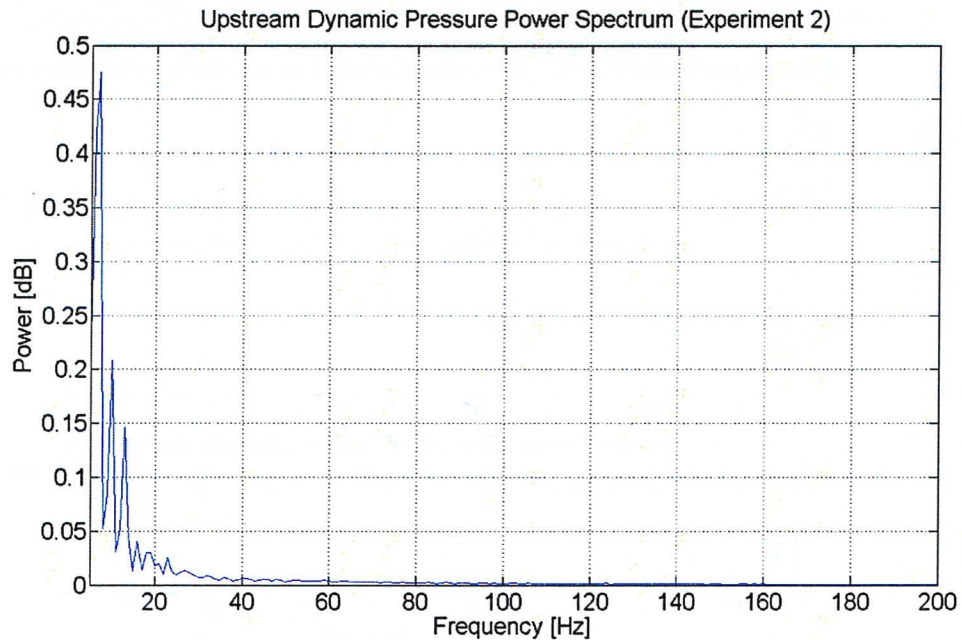


Figure F-4. Upstream Dynamic Pressure Power Spectrum (2nd Experiment)

The dynamic signals acquired from the vacuum tank pressure transducers also displayed some high frequency fluctuations. The analysis of the signals in the frequency domain in Figure F-5 indicates no perceivable acceleration component, which rules out the possibility of the pressure signal being influence by the vibration of the vacuum tank. Thus, with inertial effects having been ruled out, it is most likely that the observed random fluctuation is a product of increased dynamic pressure activity inside the vacuum tank following the opening of the rupture disc. The large volume of the vacuum tank and the relatively small volume of expanding fluid entering the tank create rapidly changing pressures at any particular location inside the vacuum tank. This behaviour produces a noisy signal that is captured by the dynamic pressure transducers, and the mean of the signal indicates the average pressure inside the vacuum tank at a certain point in time after disc rupture. The vacuum tank pressures are not of particular interest in terms of analysing the blow-down depressurisation behaviour inside the experimental rig.

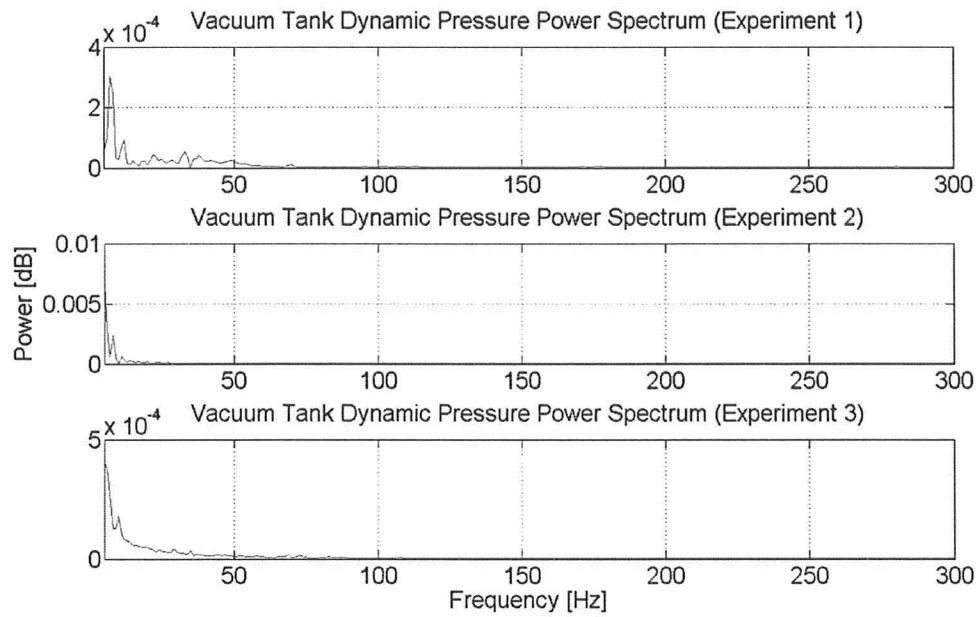


Figure F-5. Vacuum Tank Dynamic Pressure Power Spectra

Appendix G – Wave Propagation Analysis Diagrams

G-2. 1st Experiment

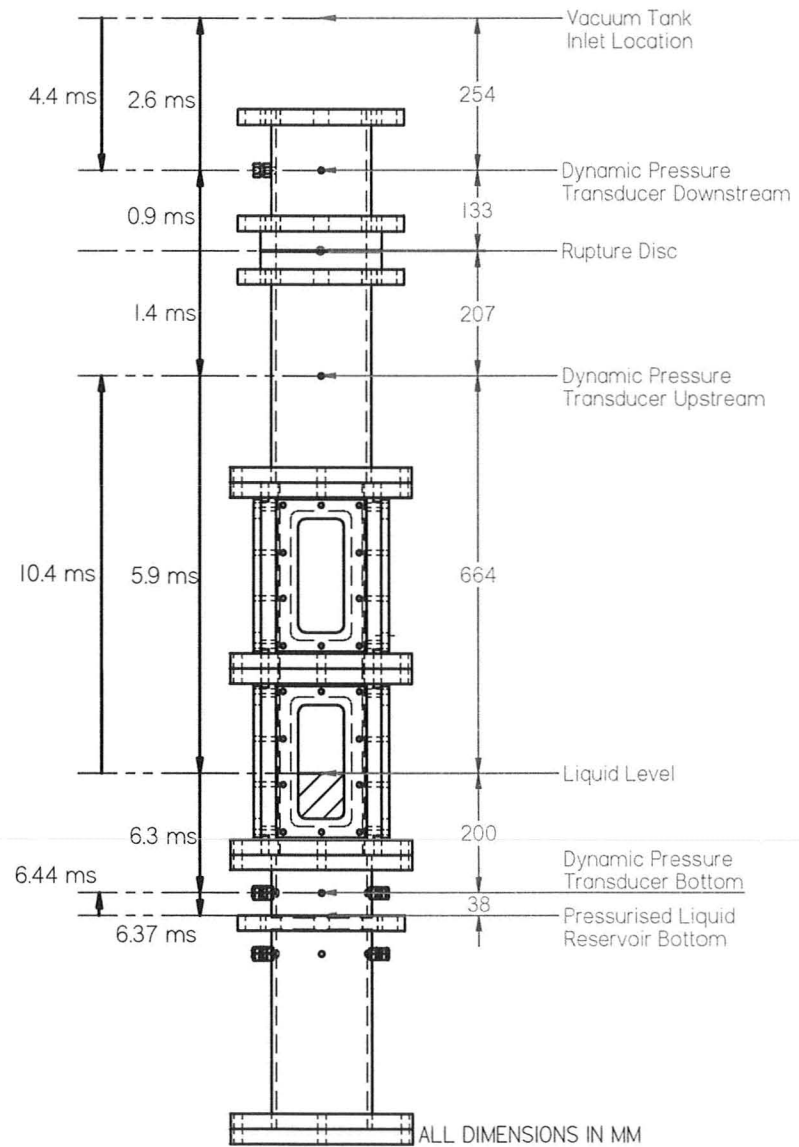
G-3. 2nd Experiment

G-4. 3rd Experiment

G-5. 3rd Experiment Retrial

G-6. 4th Experiment

Computed Wave Arrival Times Following Burst Distances Travelled By Sonic Pressure Wave



Computed Wave Arrival Times Following Burst Distances Travelled By Sonic Pressure Wave

